

Electronic Thesis and Dissertation Repository

8-24-2018 2:00 PM

Synthesis and Drop-on-Demand Deposition of Graphene Derivative Inks for Flexible Thin Film Electronics

Dogan M. Sinar, *The University of Western Ontario*

Supervisor: Knopf, George K., *The University of Western Ontario*

A thesis submitted in partial fulfillment of the requirements for the Doctor of Philosophy degree
in Mechanical and Materials Engineering

© Dogan M. Sinar 2018

Follow this and additional works at: <https://ir.lib.uwo.ca/etd>



Part of the [Nanoscience and Nanotechnology Commons](#)

Recommended Citation

Sinar, Dogan M., "Synthesis and Drop-on-Demand Deposition of Graphene Derivative Inks for Flexible Thin Film Electronics" (2018). *Electronic Thesis and Dissertation Repository*. 5636.
<https://ir.lib.uwo.ca/etd/5636>

This Dissertation/Thesis is brought to you for free and open access by Scholarship@Western. It has been accepted for inclusion in Electronic Thesis and Dissertation Repository by an authorized administrator of Scholarship@Western. For more information, please contact wlsadmin@uwo.ca.

Abstract

This dissertation presents methods for deposition and post-processing of Graphene-Carboxymethyl Cellulose (G-CMC) and Graphene Oxide (GO) aqueous functional inks using a custom drop-on-demand (DOD) printer to fabricate mechanically flexible, non-transparent and transparent thin film electronic devices. Thin films on flexible substrates find use in lightweight, low profile, and conformable electronic devices. Such devices can include chemical sensors, flexible RFID tags, bioelectronics circuits, lightweight electronics for space systems, and transparent electrodes for optoelectronic systems. The goal of this research project is to provide simple methods for fabrication of these devices using environmentally friendly and easy to synthesize functional inks. Therefore, two graphene based inks are utilized; GO and a novel Carboxymethyl Cellulose (CMC) functionalized aqueous dispersion of Graphene, G-CMC. Proposed functional inks are deposited on treated substrates by DOD printing. Deposited thin films were post-processed by use of a muffle furnace or a pulsed laser system. Furthermore, gold doped G-CMC films and G-Silver Nanoprism (G-AgNP) composite inks were developed to enhance film electrical properties.

Inkjet printed films on glass substrates were characterized in terms of their electrical, optical, and mechanical properties. Correlations between film thickness, optical transmittance, and conductivity were investigated. It was possible to deposit homogeneous thin films at 100 nm to 2000 nm thickness. G-CMC films exhibited good scaling of conductance where thicker films had $\sim 660 \Omega/\text{sq}$ sheet resistance. Gold doped and G-AgNP composite semi-transparent films exhibited enhanced conductance with sheet resistances of $\sim 700 \Omega/\text{sq}$ at 35% transparency and $\sim 374 \Omega/\text{sq}$ at 50% transparency, respectively. Laser assisted treatment of samples was conducted to investigate two opportunities; pulsed laser thermal treatment and pulsed laser micromachining on rigid and flexible substrates. Effect of laser parameters was investigated to establish guidelines for thin film thermal treatment and micromachining. Finally, novel flexible sensors and circuits were fabricated to demonstrate task driven performance of proposed materials and methods.

Based on the presented work, proposed methods and functional inks show promise for fabricating simple electronic devices on flexible and rigid substrates. It is believed that presented advances may benefit industrial fields that require scalable and simple thin film fabrication methods.

KEYWORDS: Graphene, graphene-oxide, carboxymethyl cellulose, inkjet printing, laser heating, laser micromachining, doping, flexible electronics, silver nanoprisms

Acknowledgements

I would like to acknowledge the many people who offered me help, guidance, and support throughout my academic career at the University of Western Ontario. First and foremost, I would like to thank Dr. George Knopf, my supervisor, for his guidance and support. Dr. Knopf's confidence in me, his guidance, and patience was crucial. I can gladly say that I could not ask for a better mentor during my PhD career. All I have learned from him, technical and professional, I will carry on to my future career endeavors. I would also like to thank Dr. Nikumb and Craig Dinkel of NRC. Their support and collaboration were critical for my experiments. I am grateful for their assistance.

I would also like to present my thanks to my parents, my mom Tuge and my dad Erdogan. I could not possibly succeed in academia without their support. Their unshakable belief in my capabilities and their support was able to keep me on my feet and push forward. I would also like to thank my extended family as we very close. I would like to thank my sister Muge, my cousin Simten, and my aunts Bilge and Ozge. I would also hope to thank my grandmother Mueyyet. Unfortunately, she passed away long before this day could come. She was always proud of my educational successes and she would be very proud to see me graduate with a PhD degree.

I would like to thank my wife Paulina. She was always supportive of me and always believed in me. She held my hand when I was frustrated and tired. I couldn't have done it without her. I would also like to thank my daughter Ayla. Granted, she was only a couple months old during the last stage of my program, yet her smile was a real motivation in the mornings.

I would like to extend my thanks to Dr. Jun Yang, Dr. Xueliang Sun, and Dr. Amarjeet Bassi for their support and assistance. Thanks to their support, I was able to access critical equipment necessary for me to conduct research. I would also like to thank Surface Science Western and Biotron staff for their assistance in experimental procedures and characterization.

Finally, I would like to thank the University of Western Ontario and its staff as they are a part of my success as much as anyone else.

Table of Contents

Abstract.....	i
Acknowledgements.....	iii
List of Tables	vii
List of Figures.....	viii
Nomenclature.....	xviii
Chapter 1 Introduction.....	1
1.1 The Problem.....	1
1.2 Printed Flexible Electronics.....	3
1.3 Drop-on-Demand Printing and Inkjet Printable Inks.....	4
1.4 Inkjet Printable Functional Materials.....	8
1.5 Thermal Processing of Thin Films.....	11
1.6 Research Motivation.....	13
1.7 Objectives and Scope.....	14
1.8 Overview of the Thesis.....	16
Chapter 2 Review of Graphene and Graphene-Derivatives.....	18
2.1 General Structure and Mechanical Properties.....	18
2.2 Electrical Properties of Graphene and Graphene Oxide.....	28
2.3 Biocompatibility of Graphene and Graphene Oxide	41
2.4 Optical Properties of Graphene and Graphene Oxide.....	43
2.5 Applications of Printable Graphene and Graphene Oxide.....	44
Chapter 3 Chemical Synthesis of Graphene and Graphene Based Dispersions	46
3.1 Methods to Synthesize Graphene Sheets	46
3.1.1 Preparation of Aqueous Graphene Dispersion.....	50
3.1.2 Characterization of Liquid Phase Exfoliation Products.....	52

3.2	Graphene Oxide	61
3.2.1	Preparation of Aqueous Graphene Oxide Dispersion.....	62
3.3	Synthesis of Doped and Composite G-CMC Dispersions	64
3.3.1	Elemental Doping of Films by Self-Assembly	65
3.3.2	Dispersions Based on G-CMC/Silver Nanoprisms.....	67
3.4	Concluding Remarks.....	71
Chapter 4 Thin Film Deposition of Graphene-Based Inks		72
4.1	Experimental Setup and Deposition Parameters.....	72
4.2	Substrate Treatment	80
4.3	Controlling Coffee Ring Effect During Drop-on-Demand Printing.....	85
4.4	Electrical and Physical Properties of Inkjet Printed G-CMC Films	93
4.5	Impact of Au Doping on Film Properties	96
4.6	Electrical and Optical Properties of G-CMC/AgNP Films.....	99
4.7	Concluding Remarks.....	103
Chapter 5 Post Processing of Printed G-CMC and GO films		105
5.1	Furnace Thermal Treatment.....	106
5.2	Pulsed Laser Thermal Treatment.....	108
5.3	Pulsed Laser Micromachining	113
5.4	Concluding Remarks.....	115
Chapter 6 Fabrication of Graphene Based Devices on Flexible Substrates.....		118
6.1	Introduction.....	118
6.2	Fabrication Thin Film Electronic Components.....	118
6.3	Fabrication and Characterization of Interdigitated Capacitive Sensor	123
6.3.1	Experimental Results	127
6.3.2	Mechanical Bending Performance	130

6.4	Fabrication and Characterization of Passive Electrical Filter Circuits	132
6.4.1	Low Pass Filter Fabrication	136
6.4.2	Experimental Results	139
6.4.3	Mechanical Bending Performance	143
6.5	Fabrication and Characterization of G-CMC pH Sensor	144
6.5.1	Hydrogel Synthesis and Device Assembly	144
6.5.2	Experimental Results	147
6.6	Concluding Remarks.....	151
Chapter 7	Conclusions	152
7.1	Thesis Summary.....	152
7.2	Thesis Contribution.....	154
7.2.1	Synthesis of Aqueous Graphene and Graphene Derivative Inks	155
7.2.2	Inkjet Printing of Homogeneous Thin Films	156
7.2.3	Fabrication of Flexible Capacitive Sensors	156
7.2.4	Fabrication of RC Electrical Passive Filters for Signal Control.....	157
7.3	Limitations and Recommendations for Future Work	157
7.3.1	Feature Size and Prospect of Laser Machining/Heating of Thin Films..	158
7.3.2	Optimization of AgNP Geometry	159
7.3.3	Optimization of pH sensitive Hydrogel Sensor	159
7.4	Final Thoughts	159
	Bibliography	160
	Appendices.....	173
	Appendix A - Printhead Control Code.....	173
	Appendix B – Printed Piano Device Code.....	175
	Curriculum Vitae	178

List of Tables

Table 2.1 Comparison of graphite and diamond. Even though both are allotropes of carbon, they exhibit very different properties.....	19
Table 4.1 Typical composition of water based printer inks	77
Table 4.2 Comparison of film thickness (nm) and sheet resistance ($k\Omega/sq$) (Sinar & Knopf, 2018b).	96
Table 6.1 Measured capacitance of several benchmark fluids using IDC#1 (Sinar & Knopf, 2014).	129
Table 6.2 Resistance (R), capacitance (C), time constant (τ) and cut-off frequency (f_c) for printed G-CMC passive filters	137
Table 6.3 Roll-off rate comparison of G-CMC passive electrical filters (Sinar & Knopf, 2018a).	140
Table 6.4 Measured capacitance of fluids using G-CMC IDC (Knopf & Sinar, 2017).....	150

List of Figures

Figure 1.1 Continuous inkjet (left) and drop-on-demand inkjet (right) printers. Unlike continuous inkjet printers, drop-on-demand systems can individually control each nozzle to jet droplets at varying frequencies. 5

Figure 1.2 Piezo printhead (left) and thermal printhead (right) designs are depicted. Piezo crystal can move in Z-direction at any magnitude determined by crystal’s piezoelectric properties and applied potential. Sudden change of Z-direction can eject smaller droplets than nozzle diameter would otherwise allow. Thermal printhead heats up ink with a thin film resistor element. Bubble formation and subsequent eruption ejects ink from nozzle. 6

Figure 2.1 Atomic structure of diamond (left), graphite (mid), and graphene (right). Dashed lines represent van der Waals bonds between layers of graphite..... 19

Figure 2.2 Atomic structure of graphene. In-plane σ -bonds are responsible for graphene’s extreme mechanical strength while electron cloud network formed by vertically extending π -bonds allow a high-speed highway for electrons..... 21

Figure 2.3 Oxidation process of converting graphite into graphene oxide for ink production (Sinar, Knopf, & Nikumb, 2013)..... 24

Figure 2.4 Honeycomb structure of G (Left). Dotted lines, a_1 , and a_2 , define the unit cell. Brillouin zone of G (Right). K and K' define the Dirac points. At these points, Dirac Cones meet..... 31

Figure 2.5 Materials can be roughly categorized into four types based on their energy band structure. Insulators exhibit very large bandgap energies (E_g) that prevent valence electrons’ hopping to conductance band. Semiconductor have smaller bandgap energies. Depending on position of the Fermi Level (E_f), a semiconductor may behave electron (n) or hole (p) like. Metals have overlapping valence and conductance bands. As a result, free electrons are readily available to conduct electricity without needing to hop between bands. In semimetals, E_g is zero but valence and conductance bands do not overlap. Since E_g is zero right at E_f and valence

and conductance bands exhibit completely symmetry (as in the example case shown in this figure), G is regarded as an ideal semimetal..... 34

Figure 2.6 Two possible crystal structures for GNR. (a) Zigzag type edge formation results in metallic behavior. (b) Armchair type edge formation can exhibit metallic (large w) or semiconducting (small w) behavior based on width, w 36

Figure 2.7 Comparison of large area single crystal conductive film (a) and a conductive film formed by deposition of suspended particles (b). For single crystal film, electrons must hop over lattice defects. For deposited suspended particle film, electrons must hop from one sheet to another in addition to lattice defects of each sheet. Distance to hop between sheet-to-sheet is larger than lattice defects. Hence, contact resistance between individual sheets is the major contributor to electrical resistance for printed thin films..... 40

Figure 3.1 TEM images for A4C1 (a), A8C1 (b), A8C3 (c), and A24 (d) samples. A4 samples had large amount of clumped up sheets which indicate inefficient exfoliation. A24 sample had consistently thinner sheets than A8C1 but had smaller lateral dimensions. A8C3 sample had the optimal balance in terms of lateral dimensions and sheet thickness (Sinar & Knopf, 2018b). 54

Figure 3.2 Edge length analysis of A4C1 (a), A8C1 (b), A8C3 (c), and A24 (d) revealed that shorter durations of repeated bath sonication preserves sheet lateral dimensions while 24 hour long single bath sonication resulted in reduced edge lengths (Sinar & Knopf, 2018b)..... 55

Figure 3.3 Electron diffraction pattern (a) and TEM image (b) for A8C3 sample. Intensity profile for $\{110\}$ and $\{210\}$ locations suggest bilayer sheets (Sinar & Knopf, 2018b). 56

Figure 3.4 Raman spectra of select ink samples and raw material. Exfoliation is evident from Raman spectra of exfoliated sheets. Though, determination of layer count requires careful analysis of 2D-mode (Sinar & Knopf, 2018b)..... 59

Figure 3.5 2-Component analysis of 2D-mode shows a clear trend for exfoliation performance of different protocols. For better exfoliated samples (A8C3 and A24-Thin), high frequency component is emphasized compared to stronger low frequency peak of raw material and A4

samples. Due to insufficient exfoliation during 4-hour sonication protocol of A4 samples, these inks were not included in the inkjet printing step (Sinar & Knopf, 2018b)..... 60

Figure 3.6 Both A8C3 and A24-Thin samples exhibited characteristic 4 components of bilayer G sheets (Sinar & Knopf, 2018b). 62

Figure 3.7 Effect of different approaches to doping graphene films with AuCl₃ (Sinar et al., 2016). 66

Figure 3.8 Synthesis of AgNPs start with reduction of silver nitrate salt. Presence of sodium citrate and etching effect of hydrogen peroxide forces elemental silver to assemble in a prismatic form (Sinar, Knopf, & Nikumb, 2017). 68

Figure 3.9 Typical UV-VIS spectra of AgNPs. Transverse plasmon peak intensity can change depending on nanoprism thickness, yet a significant shift on wavelength is not observed. On the other hand, longitudinal plasmon peak red shifts with increasing effective edge length (Sinar et al., 2017)..... 68

Figure 3.10 Synthesis of AgNPs start with reduction of silver nitrate salt. Presence of sodium citrate and etching effect of hydrogen peroxide forces elemental silver to assemble in a prismatic form (Sinar et al., 2017)..... 70

Figure 3.11 TEM Images of AgNPs synthesized with modified method. AgNPs have uniform thickness of ~4 nm. Sharp and robust corners contribute to red shift (Sinar et al., 2017)..... 70

Figure 3.12 UV-VIS spectra of synthesized AgNPs. Due to long effective edge length, absorption in visible spectrum is minimal compared to absorption beyond 750 nm (Sinar et al., 2017). 71

Figure 4.1 Paper feed mechanism of a Canon IP7220 inkjet printer. Office inkjet printers feature rollers to feed paper through and keep it in place during printing process. Regardless of feeding route, paper goes through rollers after inkjet printing. 73

Figure 4.2 Epson 2800 CD/DVD tray. CD/DVD trays allow use of both rigid and flexible substrates. Substrates must be fixed on the surface to avoid shifting during printing and keep flexible substrates from coming into contact with printhead..... 74

Figure 4.3 Epson R2800 Printhead. Under the conical manifolds, there are thick cellulose filters to prevent contaminants from entering printhead assembly. To be able to use this printhead for inkjet print colloidal inks, cellulose filters must be removed. 75

Figure 4.4 C-Beam linear stages with NEMA 23 stepper motors (top). Linear stages can be fixed in 90-degree angle to each other to form an XY coordinate stage (bottom). 76

Figure 4.5 HP C6602 Printhead unit and carriage assembly (left). Inside of HP C6602 printhead (right). During this research, metal mesh filter was not removed as G-CMC sheets were small enough to pass through the filter without causing clogging..... 78

Figure 4.6 Experimental setup for custom XY plotter style printer. Printer was controlled through an Arduino Uno board. Designed circuits were translated into G-Code on the laptop (top). Summary schematic of experimental inkjet printing setup (bottom)..... 79

Figure 4.7 Low pressure air supply can facilitate quick evaporation of deposited ink..... 80

Figure 4.8 Polyelectrolyte coating process. Substrate is cleaned and treated to form negatively charged OH functional groups. Due to charge over compensation, there is a charge surplus after each polyelectrolyte deposition step (steps 3, 4, and 5). 83

Figure 4.9 Conformational changes to a polymer strand can change its physical shape and properties. In a low ionic strength environment (no salt), polymer strands extend (a). Addition of salts masks opposing electrostatic charges on polymer subunits, which results in physical changes to polymer shape (b). If electrostatic charges are completely masked, polymer can collapse on itself and agglomerate (c). 84

Figure 4.10 Marangoni flow (T_0a) and corresponding colloid movement (T_0b) inside a droplet at T_0 and T_1 (a). For a droplet with pinned contact lines, width ($2r$) does not change during evaporation. For larger θ , relative evaporation rate at the edges is larger than droplet center.

Inkjet printing of solvent free aqueous inks on hydrophilic surfaces experience severe coffee ring effect (b) (Sinar & Knopf, 2018b)..... 86

Figure 4.11 Reverse flow towards droplet center can carry dispersed particles and result in a more homogenous film formation. Dotted arrows show the direction of initial flow. Arrows inside the droplet show the reverse flow following the surface tension gradient. 88

Figure 4.12 Repeated printing on previously deposited films result in degradation of film homogeneity. Thin films experience severe coffee ring effect when substrates are not treated with polyelectrolyte coating (a). During the first print cycle on a polyelectrolyte coating treated substrate, ink is deposited on a clean and treated surface, which results in acceptable film quality (b). Next print cycle happens on previously deposited film which has different surface properties than the substrate. High surface tension of aqueous ink results in poor wetting and large isolated droplets form. Resulting film shows very poor homogeneity (c: 2nd print; d: 6th print) (Sinar & Knopf, 2018b). Dotted line represents 1 mm scale. 90

Figure 4.13 Comparison of Water/1-Propanol and Water/Methanol binary solvent systems. Water/1-Propanol system experience only subtle change in surface tension during evaporation. Lack of strong surface tension gradients mean less contribution to edge directed Marangoni flow (Sinar & Knopf, 2018b)..... 91

Figure 4.14 Microscope images of inkjet printed electrodes on PEC treated glass. Addition of 1-Propanol (12% m/m) resulted in slight improvement in homogeneity (a). Further improvements were observed for increasing 1-Propanol mass percentage; 17% m/m (b), 27% m/m (c), 55% m/m (d) (Sinar & Knopf, 2018b). Dotted line represents 1 mm scale..... 92

Figure 4.15 Electrodes inkjet printed using A8C3 ink. Electrode borders are less defined for thicker films due to large droplet volume of C6602 cartridges. Electrodes were printed 10 to 100 times (Sinar & Knopf, 2018b). 94

Figure 4.16 Full topographic scan of first four electrodes. Since LPE-G has lower conductivity than metals, it is important to demonstrate successful deposition of thicker films. Electrode profile shows that coffee ring effect was not present despite multiple printing cycles (Sinar & Knopf, 2018b)..... 95

Figure 4.17 Sheet resistance of inkjet printed electrodes. Electrical performance of A8C1 and A8C3 electrodes were essentially the same. A24 electrodes exhibited measurably higher sheet resistance (Sinar & Knopf, 2018b).	95
Figure 4.18 Inkjet printed Gold Doped G-CMC optically transparent electrodes (OTEs). From left to right; 2, 4, 6, 8, and 10 prints (Sinar et al., 2016).....	97
Figure 4.19 Sheet resistance of films for high temperature treatment (540°C) decrease sharply with increasing film thickness (a). Similar changes were also observed for 420°C treatment (b) (Sinar et al., 2016).....	98
Figure 4.20 UV-VIS spectra for AgNp, G-CMC and G-AgNP inks. Despite the blue shift, characteristic peaks at 330 nm and primary peak near 500 nm are visible (Sinar et al., 2017).	100
Figure 4.21 TEM Images of AgNPs synthesized with modified method. AgNPs have uniform thickness of ~4 nm. Sharp and robust corners contribute to red shift (top). Once mixed with G-CMC, AgNP experience truncation and resemble thin disks. Despite truncated corners, AgNPs preserve their plate-like form (bottom) (Sinar et al., 2017).....	101
Figure 4.22 Inkjet printed G-CMC (left) and G-AgNP (right) films. The number of printed layers used to create the thin films are high-lighted in red and blue on the sample slides (Sinar et al., 2017).	102
Figure 4.23 Sheet resistance of both G-CMC and G-AgNP steadily decreases as number of prints increases. At 6 prints, G-AgNP film is almost 6 times more conductive than G-CMC film (Sinar et al., 2017).....	104
Figure 5.1 Muffle furnace setup used for this research. Argon gas was supplied during treatment to remove oxygen from the furnace chamber.	106
Figure 5.2 Ribbon GO electrodes before (left) and after (right) annealing. Electrodes lose their transparency due to removal of oxygen containing groups during thermal reduction process (Sinar, Knopf, & Nikumb, 2014).....	109

Figure 5.3 The 775 nm, 120 fs laser system used to reduce GO film to rGO (Sinar et al., 2013).	110
Figure 5.4 3-step reduction of a narrow film sample. Laser beam paths overlap as the beam travels from one end of the film to other (Sinar, Knopf, & Nikumb, 2014).....	112
Figure 5.5 Midsection of GO trace before reduction and after laser reduction. Darker zones are due to overlap of laser beams (Sinar, Knopf, & Nikumb, 2014).	112
Figure 5.6 Film thickness is related to the degree of thermal reduction. The laser reduction caused decrease in overall film thickness (Sinar, Knopf, & Nikumb, 2014).....	113
Figure 5.7 Sheet resistance values for GO traces. Higher NP is generally connected to smaller sheet resistance values while sheet resistance values for the same NP differs among different PO and FR parameters (Sinar, Knopf, & Nikumb, 2014).....	114
Figure 5.8 Basic design of microelectrode design.	115
Figure 5.9 Microelectrode trace created by ablating the rGO film around the conductive line. The ablated regions have zero conductivity ($R \rightarrow \infty$). The width of the conductive microtrace is $2.67\mu\text{m}$ (Sinar, Knopf, & Nikumb, 2014).....	115
Figure 6.1 Three different resistor designs (left) and printed G-CMC resistor on polyimide (right) are represented. All resistors have the same width (w) but differing lengths (s). Consequently, resistance of lines decreases from top line to bottom.	119
Figure 6.2 From left to right: thin film inductor, interdigitated capacitor, and parallel plate capacitor components.....	121
Figure 6.3 A simple capacitive sensor can be constructed using a modified parallel plate capacitor design (PPC) and controlled with a microcontroller unit (a). When a conductive foreign object touches the dielectric layer, total capacitance (C_T) of the PPC changes due to addition of C_F capacitive term in parallel to the initial stray capacitance (C_I) (b).	121

Figure 6.4 LED touchpad sensor on polyimide. Contact with touchpad area turns on the SMD LED.....	122
Figure 6.5 Printed seven-key flexible piano device PDMS substrate (left) and its circuit diagram (right). Black rectangles in the circuit diagram represent G-CMC touchpads. Another piano device was also fabricated on a polyimide substrate.	123
Figure 6.6 Basic design of an IDC sensor that responds to dielectric changes in the material under test (MUT) (Sinar & Knopf, 2014).....	125
Figure 6.7 Printed G-CMC patterns on mechanically flexible polyimide substrates (Sinar & Knopf, 2014).....	127
Figure 6.8 Experimental setup for measuring the capacitance of a printed G-CMC IDC submerged in a liquid (MUT) (Sinar & Knopf, 2014).....	128
Figure 6.9 Time response of IDC #1 at the first 40 minutes of submerging into test liquid (DI water – 10 kHz). Capacitance fully stabilizes at 155 th minute mark (not shown in the graph) (Sinar & Knopf, 2014).....	129
Figure 6.10 Capacitance values for IDC #1 and #2 for pure water, pure ethanol, and mixture of water/ethanol at varying percentages (Sinar & Knopf, 2014).....	130
Figure 6.11 Frequency response of IDC #1 and #2 in pure water and pure ethanol. Frequency sweep range was 100 Hz to 1 MHz (Sinar & Knopf, 2014).....	131
Figure 6.12 Extreme folding of 11 cm long Graphene electrode. Baseline sheet resistance was 66 Ω /sq (Sinar & Knopf, 2014).	131
Figure 6.13 Passive 1st-order <i>RC</i> low-pass filter (RC-FO) for attenuating higher frequencies ($f > f_c$) or performing wave shaping (i.e. <i>RC</i> integrator circuit) (Sinar & Knopf, 2018a). ..	133
Figure 6.14 Illustration of cascading two 1st-order RC low pass filters (RC-FO1 and RC-FO2) to obtain a 2nd-order RC low pass filter (RC-SO) (Sinar & Knopf, 2018a).....	136

Figure 6.15 First-order G-CMC low pass filters (a) G-FO1 and (b) G-FO2, and second-order G-CMC low pass filter (c) G-SO circuits and the corresponding inkjet-printed devices based on these designs (Sinar & Knopf, 2018a). 138

Figure 6.16 First order low pass filter performance of RC-FO, G-FO1 and G-FO2. Note that the f_c was same for both G-CMC circuits and roll off rate was lower than the conventional RC low pass filter (Sinar & Knopf, 2018a). 139

Figure 6.17 Comparison of 2nd-order G-CMC low pass filter performance with equivalent conventional RC circuit. Note that the second order filter roll-off rate was roughly twice of first order circuit. As expected, f_c value did not differ between first and second order low pass filters (Sinar & Knopf, 2018a). 141

Figure 6.18 Comparison of transient response for (a) 1st-order RC integrator, (b) 1st-order G-CMC integrator, (c) 2nd-order RC integrator, and (d) 2nd-order G-CMC integrator. As expected, output signal was a square wave (left-side) below f_c . Beyond f_c , signal was converted to a triangular wave (right-side) (Sinar & Knopf, 2018a). 142

Figure 6.19 Due to increase in capacitance of component C (i.e. a foreign object or finger), the frequency response of the G-FO1 changes. With a finger on C component, f_c of G-FO1 shifted from 30.5 kHz to 5 kHz (Sinar & Knopf, 2018a). 143

Figure 6.20 The pH sensitive hydrogel was poured over the IDC area and allowed to anchor the 3D molded zone. After the pour, hydrogel was allowed to crosslink on the hot plate for 6 hours (Knopf & Sinar, 2017). 147

Figure 6.21 The pH sensitive hydrogel on G-CMC IDC before (left) and after (right) drying on hot plate. Anchoring pattern keep hydrogel in place even when hydrogel was completely dry (Knopf & Sinar, 2017). 147

Figure 6.22 Frequency response of IDC biosensor, without the pH responsive hydrogel, to various baseline conditions and solutions (Knopf & Sinar, 2017). 149

Figure 6.23 Frequency response of hydrogel actuated G-CMC IDC biosensor to standardized buffer solutions with various pH (Knopf & Sinar, 2017). 150

Nomenclature

Abbreviations

% m/m	mass percentage
% v/v	volume percentage
AC	alternating current
AFM	atomic force microscope
AgNPs	silver nanoprisms
AQH	anomalous quantum hall effect
C-LPE	Cyclic liquid phase exfoliation
CD-COP	cd/dvd tray fed commercial office printer
CIJ	continuous inkjet
COP	commercial office printer
CRE	coffee ring effect
CVD	chemical vapor deposition
CVD-G	chemical vapor deposition synthesized graphene
DI	deionized
DOD	drop-on-demand
DOS	density of states
ECHA	The European Chemicals Agency
ETPs	electronic trap states
eV	electronvolt
FEDs	flexible electronic devices
FETs	field effect transistor
FR	feedrate
G-CMC	graphene/carboxymethyl cellulose
G-EC	graphene/ethyl cellulose
G-FO	first order graphene electrical filter
GNR	graphene nanoribbons

G-SO	second order graphene electrical filter
HAZ	heat effected zone
HBP	high boiling point
HDP	Hildebrand parameter
HPF	high pass filter
HSP	Hansen solubility parameters
IDC	interdigitated capacitor
LA	longitudinal acoustic phonons
LBP	low boiling point
LCD	liquid crystal display
LI	laser intensity
LP	laser power
LPE	liquid phase exfoliation
LPE-G	liquid phase exfoliation synthesized graphene
LPF	low pass filter
MCU	microcontroller unit
MDSs	materials deposition systems
MUT	material under test
n.n	nearest neighbor
n.n.n	next nearest neighbor
NP	number of passes
OLED	organic light emitting diode
Op-Amp	operational amplifier
OTE	optically transparent electrode
P-COP	paper fed commercial office printer
PEC	polyelectrolyte coating
PPC	parallel plate capacitor
RC	resistor-capacitor
RC-FO	first order <i>RC</i> filter
RC-SO	second order <i>RC</i> filter
REACH	Registration, Evaluation, Authorization, and Restriction of Chemicals

RFID	radio frequency identification
RIP	remote interface phonons
<i>RLC</i>	resistor-inductor-capacitor
RM	raw material
$S \cdot \text{cm}^{-1}$	siemens per centimeters
SVHC	substances of very high concern
ST	scotch tape
T%	transmittance percentage
TB	tight binding
TEM	transmission electron microscope
Ω/sq	ohm per square

Variables and Constants

<i>a</i>	nearest-neighbor c-c spacing
<i>A</i>	area of parallel plates
<i>a₁, a₂</i>	lattice vectors for lattice atom a
<i>b₁, b₂</i>	lattice vectors for lattice atom b
<i>c</i>	speed of light
<i>C</i>	capacitance
<i>C_F</i>	capacitive term due to finger on sensor
<i>C_I</i>	initial capacitance of sensor
<i>C_T</i>	total capacitance
<i>D</i>	dispersive
<i>d</i>	distance between the parallel plates
<i>d_E</i>	electrode transmission line distance
<i>e⁻</i>	electron
<i>E_f</i>	Fermi level
<i>E_g</i>	bandgap energy

E_n	total energy of a particle
f	frequency
f_c	cut-off frequency
h	insulator thickness
H_b	hydrogen bonding
I	electrical current
I_{2D}	2D-mode Raman signal intensity
I_D	D-mode Raman signal intensity
I_G	G-mode Raman signal intensity
K, K'	lattice Dirac points
l	length
m	mass
Ma	Marangoni number
m_e	electron mass
n	number of IDC digits
Oh	ohnesorge number
p	momentum
P	polar
q	momentum relative to Dirac points
r	droplet radius
ρ	resistivity
R	resistance
s	length
t	nearest-neighbor hopping energy
T	time step
U	energy of vaporization
v	velocity
V	voltage
v_e	electron velocity
v_f	Fermi velocity
V_g	gate voltage

V_{in}	input voltage
V_{out}	output voltage
V_{pp}	peak-to-peak voltage
w	width
X_c	capacitive reactance
Z	impedance
γ	surface tension
$\delta_1, \delta_2, \delta_3$	nearest-neighbor vectors
ΔL	roll off rate
ϵ	dielectric constant
ϵ_r	substrate dielectric constant
ϵ_0	permittivity of free space ($\sim 8.85 \text{ F}\cdot\text{m}^{-1}$)
ϵ_a	dielectric constant of air
ϵ_e	energy of an electron
ϵ_s	dielectric constant of human skin at 900 MHz
ζ	viscosity
η	thin film thickness
θ	droplet-substrate interface angle
μ_c	Coulomb scattering
μ_{LA}	longitudinal acoustic phonon scattering
μ_{RIP}	remote interface phonon scattering
μ_t	total electron scattering
π -bonds	in-direct covalent bonds between carbon atoms in graphene lattice
π -orbitals	orbitals of electrons indirectly shared by carbon atoms
M	molar volume of solvent
σ	spin state
σ -bonds	in-plane covalent bonds in graphene
τ	time constant
φ	diffusion coefficient
χ	one unit cell of an IDC
$F(k)$	Fermi equation

Chemicals and Materials

Ag	silver
AgNO ₃	silver nitrate
Ar	argon
Au	gold
AuCl ₃	gold chloride
C	carbon
CMC	carboxymethyl cellulose
CNTs	carbon nanotubes
DMF	dimethylformamide
DMSO	dimethyl sulfoxide
G	graphene
GaAs	gallium arsenide
GO	graphene-oxide
Gr	graphite
GrO	graphite oxide
H ⁺	hydrogen ion
H ₂	hydrogen gas
H ₂ O ₂	hydrogen peroxide
HMDS	hexamethyldisilazane
HNO ₃	nitric acid
ITO	indium tin oxide
Mba	n,n'methylene-bisacrylamide
Na ₂ CO ₃	sodium carbonate
Na ₃ C ₆ H ₅ O ₇	trisodium citrate dihydrate (TCD)
Na ₄ BH ₄	sodium borohydride
NaCl	sodium chloride
Ni	nickel
NMP	n-methylpyrrolidone

O	oxygen
OH	hydroxyl
PDMS	polydimethylsiloxane
PEDOT:PSS	poly(3,4-ethylenedioxythiophene):polystyrene sulfonate
PEG	polyethylene glycol
PEG-PPO	polyethylene glycol/polypropylene oxide
PEI	polyethyleneimine
PET	polyethylene terephthalate
PP	polypropylene
PSS	polystyrene sulfonate
PVP	polyvinylpyrrolidone
rGO	reduced graphene-oxide
rGrO	reduced graphite oxide
Si	silicon
SiC	silicon carbide
SiO ₂	silicon dioxide
STC	sodium taurodeoxycholate

Chapter 1

Introduction

1.1 The Problem

Advances in microelectronics has enabled the miniaturization of various electronic devices. For example, today, a smartphone has more computational capabilities than a room sized computer from 1970s. These smart devices feature number of passive and active components; including sensors, antennas, microchips, resistors, capacitors, inductors, batteries, and transparent electrodes for display systems. Relatively low cost availability of such devices and their high portability mean that smart devices, such as used for medical monitoring, can be integrated into clothing and personal accessories. This level of integration is commonly referred to as wearable technologies. Wearable technologies, as a term, encompasses smart devices that could bend and fold with predictable and controllable consequences on device functionality. Consequently, wearable technologies are inherently flexible electronic devices.

Flexible electronic devices (FEDs) that could conform to non-planar surfaces can positively affect fields of healthcare, medicine, food inspection, environmental monitoring, communication systems, and visualization systems. Through advances in materials science and manufacturing technologies, research on flexible electronics has become a global effort to develop feasible fabrication methods. Researchers of this field face a two-fold challenge; limitations of current fabrication methods and availability viable functional materials. Standard lithographic methods and Chemical Vapor Deposition (CVD) systems are not suitable for direct fabrication of electronic devices on flexible substrates. Any film or device fabricated through these methods must be transferred onto the desired substrate. Thin film transfer methods limit design choices, device dimensions, and introduce defects. Furthermore, environmental impact of harmful etching chemicals causes global concern. Another challenge is availability of functional materials and compounds for creating flexible conductive traces. Metals are susceptible to ductile fracture due to introduction of lattice dislocations with repeated bending. Once density of dislocations reaches a critical point, metal traces fail. A

consequence of geometrically thinner materials is an increased vulnerability to dislocations. A single dislocation will have a larger impact on a 20 atoms thick layer compared to a 1000 atoms thick layer. This means that FEDs that feature very thin metal films may fail sooner than expected due to excessive bending cycles. This is especially true when it comes to fabrication of flexible display systems. Display systems have become an integral part of smart devices. Extremely thin (< 10 nm thick) copper or silver films would provide required electrical conductivity and transparency but fabrication of ultrathin metal films is still very challenging. In addition, ultrathin metal films would quickly fail upon bending due to rapid increase in dislocation density. Industry standard for transparent electrodes, Indium Tin Oxide (ITO), is a brittle material and cannot sustain repeated bending either. In addition, Indium is a scarce element and a major contributor to fabrication cost. Alternatives to ITO electrodes that can be bent repeatedly and transmit visible light are highly desired by the industry.

Novoselov et al. (2004) characterized for the first time how a single layer of a graphite flake would perform electrically, optically, and mechanically when isolated. Resultant one atom thick layer, named Graphene (G), has been shown to possess properties that surpasses known materials. Unfortunately, Geim isolated a single layer G sheet using repeated application of a scotch tape. This method has shown to produce good samples for material characterization; defect and contaminant free pristine G sheets. Yet, it is not controllable or scalable. Large area G sheets can be fabricated by CVD. On the other hand, films are originally on copper substrates and must be transferred on to insulators to be utilized. This transfer process is prone to damage films. High capital and production cost of CVD fabrication results in high per cm square cost G films. Thus, due to numerous technical and financial limitations, CVD-G films have been mostly ignored by the industry.

For a new material such as G to be adopted, synthesis and deposition methods must be well defined. Involved chemicals and raw material must be easily accessible, affordable, and environmentally friendly. Resultant thin films must demonstrate acceptable electrical, optical, and mechanical performance. This thesis attempts define necessary chemicals, methods, and processes to satisfy these criteria while carefully presenting data collected from characterization of thin films and devices to support viability of inkjet printed graphene electronics.

1.2 Printed Flexible Electronics

Printed flexible electronics refer to thin film circuits that are fabricated using one of the available printing technologies on mechanically bendable or stretchable substrates. Initial motivation for flexible electronics was to manufacture flexible solar panels in 1960s (Venugopal et al., 2010). This has led to very thin and light silicon integrated circuits that are more compliant to mechanical stress. Further advances in materials and manufacturing fields have enabled development of micrometer scale functional thin films in the form of transistors, optically transparent flexible conductors, and a whole range of unique electrical component designs (Kim, Maleki, Wei, & Ziaie, 2009; Kim, Xiao, Song, Huang, & Rogers, 2010). When compared to conventional fabrication methods - where deposited features may need to be transferred onto flexible plastics - printing technology allows direct deposition of functional materials in the desired pattern. Printing methods, including screen, gravure, flexo, and inkjet printing, allow room temperature deposition and they lack lithographic process steps. Hence, virtually any material can be used as substrates for direct deposition without generating chemical waste. Inkjet printing has additional advantages over rest of the printing methods. Inkjet printing can deposit films without physical contact to substrate and does not require a production mask. Instead, digital designs can be deposited directly. This allows for quick prototyping and cost free alteration of circuit designs. Inkjet deposited films tend to be thinner than what can be achieved with other printing methods, which is crucial for fabricating highly flexible circuits. Thinner films on flexible plastic substrates are generally lighter in weight which would benefit applications where weight has major impact, such as space exploration.

Despite many advantages that inkjet printing could represent, industrial adoption has yet to happen. As of writing of this thesis, to author's knowledge, no inkjet printed mass production device is available on the market. For printed films in general, most used methods are screen and gravure printing. As a result, most, if not all, inkjet printed devices remain to be prototypes built in labs. Inkjet printing presents several unique problems, and solutions used in other printing methods and lithography do not directly apply. That and low performance of most inkjet printable inks have kept industry from transitioning to inkjet printing.

1.3 Drop-on-Demand Printing and Inkjet Printable Inks

Inkjet printing method refers to drop-by-drop deposition of functional inks to form a thin film with controllable dimensions. Although inkjet printing of functional materials is an emerging technology, the inkjet technology itself was developed during early 1950s and inkjet printers have been extensively used since 1970s. Though initially limited to office use, the technology eventually found place in textile and high resolution image printing. Unlike other printing methods, deposition with inkjet printing lacks direct contact with substrate and can deposit very small amounts of material. Modern inkjet printheads can form droplets in the range of 1 to 250 picolitres and jet these droplets at high precision and accuracy. Resulting films can be as thin as only a few nanometers.

Film deposition with inkjet printing is a repetitive process. Thin films must be deposited layer-by-layer. Depending on desired thickness, more than one print may often be necessary. Hence, precision and accuracy of droplet placement must be very high. State-of-the-art inkjet Materials Deposition Systems (MDSs), such as Dimatix printers from Fujifilm, can achieve down to 25 μm features with high precision and repeatability. Special surface treatment methods were also developed to improve printing resolution. Siringhaus et al. (2000) had achieved features in the 5 μm range by tailoring hydrophobicity of the substrate. Office inkjet printers, which are attractive alternatives to high cost MDSs, can have theoretical feature size of 42 μm (dictated by nozzle pitch and diameter) and a practical feature size around 100 μm on a hydrophilic surface. In comparison, state-of-the-art silicon electronics can achieve features four orders smaller (10 nm as of 2018). Although resolution and robustness of inkjet printers fall short compared to lithography, they can potentially replace lithography where extremely small feature size and accuracy are not required. In fact, most electronic devices used day-to-day do not require a very high level of fabrication precision and resolution. Chemical/biological sensors, transparent electrode arrays for LCD screens, thin film heating pads, capacitive/resistive/inductive passive components, thin film antennas, and circuit board traces are some of the applications where features less than 100 μm would rarely be needed. Inkjet printing can allow quick prototyping of thin film circuits using graphical design software and fabrication of prototypes without the need of a lithographic mask. From an environmental point of view, lack of photoresist and photoresist strip chemicals are definite advantages. Furthermore, flexible plastic substrates can be printed on directly.

Inkjet printers can be categorized as continuous inkjet (CIJ) and drop-on-demand (DOD) printers (Fig. 1.1). CIJ printers continuously jet droplets. These droplets are deflected by an electrostatic field. Deflected droplets form a film on the substrate while non-deflected droplets are collected in a separate tank for reuse. Modern office and material printers work as DOD systems. Compared to CIJ, DOD printers jet droplets as needed. In DOD systems, printer software has full control on droplet generation, as such a single droplet can be jetted at any defined location and time. As a result, DOD printers have superior resolution compared to CIJ printers. On the other hand, CIJ printers print at higher speeds. Hence, they are used in industry for low resolution printing on product packages.

DOD printers are further categorized based on how the droplets are generated. During inkjet printing, a functional ink is either heated to form bubbles or pumped out by use of piezoelectrical crystals. Former method is universally used by thermal printheads while latter is used by piezo printheads (Fig. 1.2). Thermal printheads work by heating an ink to temperatures close 300°C. This heating happens in a span of 1 μ s (HP45 cartridge) to 5 μ s (HP6602 cartridge), depending on printhead design.

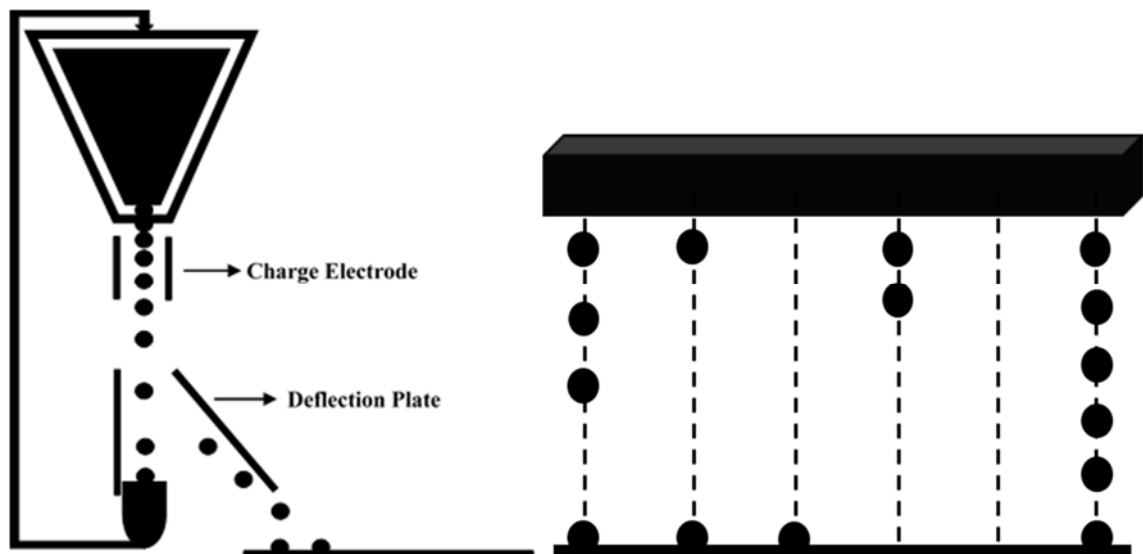


Figure 1.1 Continuous inkjet (left) and drop-on-demand inkjet (right) printers. Unlike continuous inkjet printers, drop-on-demand systems can individually control each nozzle to jet droplets at varying frequencies.

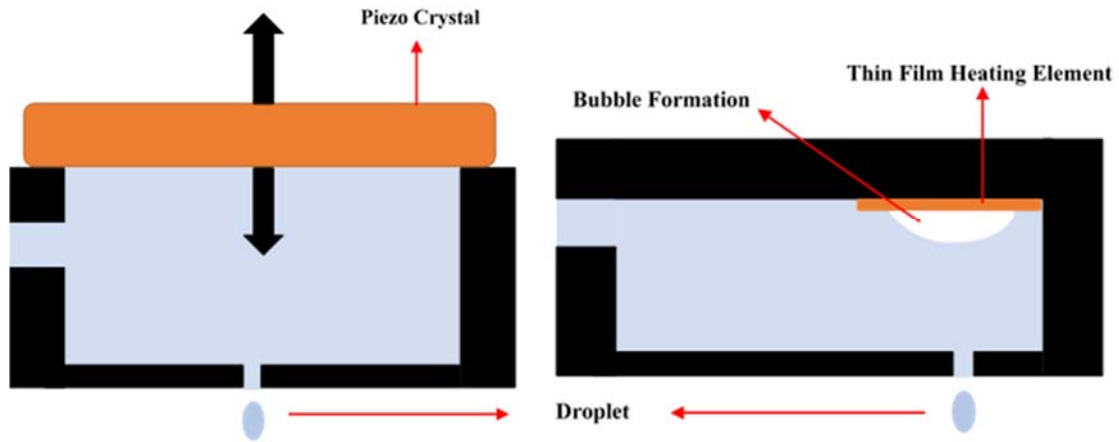


Figure 1.2 Piezo printhead (left) and thermal printhead (right) designs are depicted. Piezo crystal can move in Z-direction at any magnitude determined by crystal's piezoelectric properties and applied potential. Sudden change of Z-direction can eject smaller droplets than nozzle diameter would otherwise allow. Thermal printhead heats up ink with a thin film resistor element. Bubble formation and subsequent eruption ejects ink from nozzle.

Upon heating, formation of microbubbles forces a droplet out of the nozzle. Piezo printheads generate and jet droplets through mechanical action. Piezo crystals can be deformed by electrical signals to create momentum in the liquid to be jetted. As a result, droplets smaller than the nozzle diameter can be pushed out. In addition, purely mechanical action means that deposited material is not exposed to any heat. Hence, piezo printheads are generally preferred for high end MDSs. Piezo printheads can exert smaller maximal force at jetting. Thus, they are prone to clogging and require more strict requirements on ink parameters such as boiling point of solvent and particle size. In comparison, thermal printheads are more rugged and cost effective due to their simple design that involves no moving parts. They can exert larger forces to jet ink and if clogged, can be cleaned in an ultrasonic bath. Yet, droplet size is determined only by nozzle diameter. Consequently, thermal printheads tend to have larger drop sizes compared to piezo printheads.

Once a droplet is jetted from printhead nozzle, it lands on a substrate where it would spread and evaporate. Spread and evaporation directly impacts film formation and can be controlled only indirectly. Film formation by spread and evaporation contrasts methods such as vacuum filtration where there is an external force that guides particles. In inkjet printing, particles self-assemble. Formation of a homogeneous film by self-assembly requires careful

substrate preparation and ink formulation. Methods regarding proper film formation with inkjet printing are discussed in greater detail in Chapter 4.

Jettability is strongly dictated by specifications of printing equipment. Common variables that determine ink jettability are surface tension, viscosity, and particle size (only for colloid dispersions). MDSs tend to put strict limitations on these variables. In example, Dimatix printers require 10-12 cPs viscosity, 32-42 dynes/cm surface tension, and less than 200 nm particles size from printable inks. Considering water has 1 cP viscosity and 70 dynes/cm surface tension, aqueous inks are not printable with this system without using additives. Furthermore, 200 nm is too small for many colloid dispersion formulations. Considering G based dispersions, nanosheets tend to have μm range lateral dimensions and too small G sheets are undesirable, for they tend to perform poorly in electrical conductivity. However, commercial or office inkjet printers have a wider working range for ink properties. Thermal printheads have heating pads near nozzle exit that can superheat ink to temperatures above 300°C. When formulating an ink, heating effect of thermal printheads must be considered. Polymers, biological components, or reactive species may be negatively impacted due to printhead action.

For an ink or any type of liquid to be inkjet printable, it must be jettable by the printhead in a sustained and predictable manner. Solutions are ideal inks when in it comes to inkjet printing. Colloid dispersions must have small enough nanoparticles to avoid clogging. Printhead nozzles can be as small as 20 μm and as large as 80 μm depending on brand and technology. MDSs usually come equipped with very small nozzle diameters. In example Dimatix printheads have 20 μm diameter nozzles. Common commercial office inkjet printers can have nozzle diameters in the range of 30-50 μm while older models can have larger diameters. For example, Canon PJ01080A office inkjet printer was reported to have 65 μm diameter nozzles (Hebner, Wu, Marcy, Lu, & Sturm, 1998). Industrial large character printers tend to have larger nozzle sizes, usually upwards of 60 μm . Particles larger than 1/10th of nozzle diameter are associated with eventual clogging of printhead nozzle or unpredictable jetting profile.

Ink viscosity affects droplet formation and shape directly. In general, viscosity should be as low as possible and less than 20 cP otherwise. High viscosity may result in formation of

a droplet tail or secondary droplets during jetting. This is especially true for thermally actuated printheads as this type of printheads are usually designed to work with water based inks. Surface tension of inks must be adjusted to be higher than 30 dynes/cm. Since printhead ink is held in the tank through pressure balance between nozzle opening and top air vent of cartridge, too low of a surface tension would result in leakage of ink. Maximum surface tension of an inkjet printable ink is determined by printhead technology. Thermally actuated printheads can allow high surface tension liquids to be jetted without problem. On the other hand, piezoactuated printheads may require a lower surface tension to be able to jet.

Boiling point of inks must also be taken into account during formulations. Highly volatile inks can dry at nozzle exit and deposit particles into the orifice, effectively blocking the nozzle. During the studies that have led to this thesis, it was observed that inkjet printing with solvents or solvent mixtures with boiling points less than 90°C was problematic. Based on how volatile the ink is, ink can dry and block nozzle in a matter minutes. For thermal printheads, an exceptionally high boiling point solvent may be unprintable due to difficulty at forming the microbubbles necessary for ink ejection.

1.4 Inkjet Printable Functional Materials

Since printing technology was already well developed by mid 1980s and first examples of inkjet printed conductive films coincide with the availability of inkjet printable functional materials. Based on literature review, inkjet printing of circuits was first investigated by Teng & Vest (1987). Related mathematical models were also studied by Teng & Vest (1988). During this time, inkjet printheads were unable to deposit particulate inks. Hence, metallo-organic solutions were used to fabricate samples.

Brittle nature of metal based films and high conversion temperature requirement of metallo-organic films allowed research on conductive polymers to gain considerable traction. Conductive polymers are soluble. Hence, knowledge base gained from research on metallo-organic inks was transferable. This has resulted in rapid utilization of conductive polymers to showcase direct printing of transistors (Sirringhaus et al., 2000), OLEDs (Hebner et al., 1998), Conductive polymer coated fabrics (Collins & Buckley, 1996), and LCD screens (Shimoda, Morii, Seki, & Kiguchi, 2003). Solution based polymer functional inks lack post-deposition

sintering step and have better mechanical stability in the thin film form. In terms of conductivity, PEDOT-PSS inks are shown to be poor performers (< 10 S/cm) (Jonsson et al., 2003) and have low carrier mobility (Sirringhaus et al., 2000) unless a high boiling organic solvent is present in the mixture. When film morphology improves due to presence of an organic solvent (i.e. dimethylformamide and N-methylpyrrolidone), PEDOT-PSS inks can reach to conductivities viable for printed electronics (Jonsson et al., 2003). Polymer inks have found some application in the commercial field, albeit in the form of thicker films deposited by printing technologies other than inkjet.

Only by early to mid 2000s, metal based nanoparticle inks have become viable options to inkjet print. Inkjet printing of colloid inks is a different problem than printing of solutions. Sustainability of colloid inkjet printing depends on not only solvent properties but also to colloid dimensions and stability. Colloid inks that can easily sediment are practically impossible to inkjet due to nozzle clogging. If colloids are larger than micrometer to few micrometers (depending on nozzle size), nozzles would eventually clog as well. An additional problem specific to metal colloid printing is poor electrical performance in their as printed form. Metal colloids tend to be in spherical form. Films formed by spherical metal colloids do not form an efficient conductive network. Instead, films must be sintered to melt colloids and form a homogeneous layer. Unfortunately, few substrates can withstand high temperatures that would be necessary to sinter relatively large metal colloids (Melting points; copper: 1084.62°C , silver: 961.78°C) (Haynes, 2009). Only solution to this problem is to have nanoparticles less than 25 nm at which point melting point depression occur. Fuller, Wilhelm, & Jacobson (2002) was first to report inkjet printing of very small metal colloids (1 – 100 nm diameter) which could be sintered at a relatively manageable temperature of 300°C .

Carbon based nanomaterial inks have gained considerable popularity with characterization of G in 2004 by Novosolov et al. Due to limitations regarding synthesis of G sheets in bulk amounts, Graphene Oxide (GO), an oxidized variety of G, was first to be used for deposition of thin films. Graphene Oxide can be directly dispersed in DI water and inkjet printed on various substrates. Graphene Oxide is electrically insulating, and deposited GO films must be thermally reduced to recover their conductivity (Huang, Huang, Liang, Wan, & Chen, 2011). Direct exfoliation and dispersion of G in various solvents (NMP and DMF) have been reported. Experiments have confirmed that extended periods of ultrasonication of

graphite in NMP can exfoliate G sheets with relatively low number of defects (Paton et al., 2014). Another approach for direct exfoliation and dispersion of G is use of surfactants. Common surfactants including Tween 85, Pluronic P123, Triton X-100, and Sodium Taurodeoxycholate (STC) (Guardia et al., 2011) can disperse pristine G at large concentrations in aqueous media. On the other hand, most of these solvents and surfactants have not been shown to form into ordered thin films on non-absorbent surfaces. Formation of thin G films have been demonstrated for few studies using inkjet printers (Secor, Prabhumirashi, Puntambekar, Geier, & Hersam, 2013). These G thin films show comparative electrical performance to conductive polymers and demonstrate excellent mechanical and chemical stability.

There are numerous methods to synthesize a stable ink. As mentioned earlier, one method of preparation is use of soluble materials. Solution can be inkjet printed without experiencing stability issues and nozzle clogging. Once solvent evaporates on substrate, non-volatile solutes can form a thin film. Inkjet printing of particulate inks require careful preparation of stable colloids suspensions. Briefly, the aim is to eliminate attractive forces between dispersed materials at which point Brownian motion dominates state of nanoparticles in the liquid media. This can be done either by using a solvent that functional material interacts strongly or by using assistive chemicals that can provide necessary repulsive forces. First approach is to dissolve or disperse functional materials directly in an appropriate solvent. One way to choose appropriate solvent is to compare Hansen Solubility Parameters (HSP), which aims to predict if one material can dissolve in another. Second method is to use surfactants that can adsorb onto material to be dispersed to act as a bridge molecule. Such surfactants are roughly categorized as Ionic and Non-Ionic. Ionic surfactants are composed of a hydrophobic tail, which adsorb onto desired functional materials, and a charged head that creates the electrostatic repulsion necessary to keep particles from aggregating. Non-ionic surfactants are composed of hydrophobic and hydrophilic chains that can adsorb on functional materials and act as a bridge between solvent and particles via molecular forces. In both cases, surfactant must be soluble in the solvent. Another category of surfactants aims to manipulate solubility parameters of the solvent at hand. In example, bile salts can be used to manipulate water solubility parameters and allow stable dispersions of carbon nanomaterials. When a polymer is used as a surfactant, stabilization can happen due to steric repulsion between polymer chains,

total electrostatic charge of the Polymer-Particle system, or both. This phenomenon is sometimes referred as electrosteric repulsion.

Teng & Vest had concluded in their 1987 work that inkjet printer would not replace screen printing immediately but could find use in specialized applications, such as flat-plate solar cells. Interestingly, 30 years later, many journals mirror their words as conclusions. This apparent lack of major progress does not stem from a lack of scientific progress but due to unfeasibility of most solutions presented by researchers to industrial needs. This creates a good opportunity for developing simpler solutions to seemingly complicated problems. Any simple solution investigating DOD printing method's contribution to fabrication industry must also investigate synthesis of easily applicable functional inks.

1.5 Thermal Processing of Thin Films

Thermal processing of deposited thin films may be necessary due to several reasons. If deposited film is composed of metal nanoparticles, it can be melt into a continuous metal sheet. For metallo-organic films, thermal treatment is necessary to initiate the chemical reaction to form elemental metal. In the case of carbon based films, thermal treatment can be used to decompose stabilizing surfactants or remove trapped solvent and other volatile compounds that would be left inside the film. Depending on applicable temperature and nature of stabilizing compound, complete carbonization may be achieved. Yet, most flexible substrates cannot withstand temperatures necessary for carbonization. Common flexible substrate materials rarely withstand beyond 200°C except for polyimide which can be exposed to temperatures up to 400°C for short periods of time.

Minimum processing temperature depends on objective; solvent evaporation, oxygen reduction, thermal decomposition, or melting. When flexible plastics are used as substrates, minimum applicable temperature becomes a limiting factor. For example, a minimum of 180°C is required to reduce GO. This would eliminate some of the cheaper plastics and paper. Furthermore, minimum required temperature may not be enough to produce samples with optimized properties. Graphene Oxide reduction begins at around 180°C, but highest performing rGO cannot be obtained before 600°C. Surfactants may decompose at manageable temperatures, yet their by-products may remain. In example, carboxymethyl cellulose

decomposes at around 320°C. Yet, complete carbonization takes place after 800°C (Chen, Chen, Zhang, & Xie, 2013).

Use of lasers to heat thin films have been proposed and demonstrated over the years. Potentially, lasers could be used for controlled heating or micromachining of thin films. In fact, industry has already been making use of lasers for similar purposes. Welding, polishing, and cutting of metal and non-metal parts are common practices in manufacturing field and experiences in these fields are transferable to processing of thin films. Although there is substantial amount of research studying laser-material interactions, active demonstration is harder to come by among recent publications. It can be argued that, among researchers, lasers are regarded more as industrial tools than research equipment. Heating with lasers is harder to control and quantify compared to oven heating where exact temperature of sample would be known. Indeed, determination of achieved temperature in laser based heating would require a combination of simulation and measured data. State of the art laboratory ovens/furnaces allow very tight control of parameters that lasers do not. As a result, experiments must be performed with great care when lasers are incorporated.

On the other hand, lasers can present a unique opportunity for processing of thin films. Effects of pulsed laser beams on material heating and machining is well documented. Laser beams, when pulsed at high speeds, can heat localized areas on a film with very limited vertical heat diffusion. Which means, theoretically, it is possible to heat surface of a thin layer to a temperature much higher than the underlying plastic or paper substrate could withstand. Sinar et al. had demonstrated both reduction and machining of 1 μm thick GO films without any observable damage to polyimide and acrylic substrates (Sinar, Knopf, & Nikumb, 2014; Sinar, Knopf, Nikumb, & Andrushchenko, 2014). During these experiments, a 120-femtosecond laser was used.

Femtosecond lasers are considered more suitable for machining than heating due to extremely short pulse width. It was shown through experiments that a 150-femtosecond laser can have approximately 2 μm lateral Heat Affected Zone (HAZ) compared to a 7-8 nanosecond laser of same power output which had a 40 μm HAZ (Le Harzic et al., 2002). Although it can vary among different materials, it can be assumed that pulse widths of less than 10 picosecond cause machining of material with negligible thermal diffusion. Larger pulse width laser beams

allow transfer of incident energy to lattice, so heat can be generated and transferred efficiently. Application of (> 10) picosecond lasers for heating thin films to extremely high temperatures can allow synthesis of novel materials or development of novel methods to fabricate high performing devices on plastic and paper substrates.

1.6 Research Motivation

Since its first characterization in 2004, G has been studied as a potential candidate for thin film electronics. At first look, because of G's exceptional mechanical, electrical, and chemical properties, potential fields of application seem unlimited. For example, high conductivity and optical transparency of G means that its thin films can be a cost-effective alternative to Indium Tin Oxide, which is an expensive material due to scarcity of Indium on earth. Graphene's high mechanical strength was also utilized to fabricate flexible transistors that can withstand extreme bending stresses enough to break thin film metal layers. Electronic devices based on G are envisioned to be more durable than polymer electronics due to highly stable chemical structure. In addition to that, G films can non-covalently bond to some chemicals under favorable conditions, which could be beneficial to fabricate sensors. On the other hand, impressive properties of G are only true for defect free, single crystal films. The Scotch Tape (ST) method used by Novoselov et al. (2004) can cleave defect free layers from Gr but it is not applicable to device fabrication. Chemical Vapor Deposition (CVD) and Silicon Carbide Sublimation (SiC Sublimation) can for thin G layers, yet impose restrictions on substrate materials and substantially increase cost per mm^2 film. Hence, it was this research's aim to develop simple, controllable, and straightforward methods to synthesize and deposit graphene thin films through utilizing liquid phase exfoliation and drop-on-demand deposition. Furthermore, derivatives of graphene, graphene oxide, gold doped graphene films, and graphene-silver nanoprism composite films, were also investigated to further expand the possible application field for proposed methods.

In order to utilize G to its full potential, cheap production and controllable deposition methods have to be developed. Initial efforts for intercalating Graphite particles were only partially successful and did not yield high percentage of single layer G sheets. Process of GO synthesis naturally results in monolayer sheets. As a result, GO solutions were used to deposit

thin films. Unfortunately, it was quickly discovered that thermal and chemical treatments could not completely revert GO back to pristine G structure. In fact, resulting material, reduced GO (rGO), had large amounts of defects in its basal plane that could not be fixed. Even though GO has potential use as a semiconductor or variable conductance material, research efforts were redirected to development of bulk synthesis methods for pristine G. A bulk synthesis method for G, liquid phase exfoliation (LPE) by ultrasonication, was first carried over in 2008 (Hernandez et al., 2008). Bulk synthesis of monolayer G sheets from inexpensive mesh Graphite has enabled commercialization of cheap G powders composed of single or few layer sheets. Organic and aqueous G powder dispersions have been used for fabricating thin films by drop casting, spin coating, screen printing, and inkjet printing methods. Although, LPE-G is chemically identical to ST-G and CVD-G, thin films formed by LPE-G sheets are not single crystal structures. These films are composed of individual nanoscale G sheets and have different properties than their single crystal counterparts. Contact resistance between individual G sheets add up to increase bulk resistance. In addition to substantial reduction in conductivity, more exotic properties of single layer, continuous crystal G sheets cannot be observed in LPE-G films. Nature of these properties and how they are observed are discussed in greater detail in Chapter 2. It must be noted that LPE and DOD deposition are compromise methods where simplicity, on-demand fabrication, and scalable processing volume are emphasized over high performance. Hence, a well structured methodology based on these two methods may benefit industry adoption of thin film graphene electronics.

1.7 Objectives and Scope

The core of this thesis is to investigate feasible methods for synthesis of G in bulk amounts and identify necessary parameters for inkjet deposition of synthesized G. Presented methodology will be supported with characterization of deposited thin films in terms of their electrical, optical, and mechanical properties.

Synthesis of G sheet through LPE methods and inkjet printing deposition of resultant dispersion have been investigated by many research teams around the world. On the other hand, a coherent methodology from synthesis to inkjet printing and post processing is harder to come by. Indeed, majority of early work on LPE based G synthesis focuses on synthesis

aspect alone. In these studies, any electrical characterization is conducted on simple vacuum filtered films. Yet, vacuum filter based film fabrication is not applicable in an industrial environment. Furthermore, inkjet printing of dispersions is not straightforward. Formation of homogeneous films through inkjet deposition requires proper ink formulation and careful adjustment of printing parameters. Solvents used for LPE methods are also of concern. Apart from health consequences of toxic solvents, some of them may not even be usable with most inkjet systems. For example, NMP is an efficient solvent that can cause swelling in a wide range of plastics and dissolve adhesives that keep thermal pads in place, effectively damaging printheads from within and possibly contaminating ink with solubles from surrounding plastic parts.

Another issue with available research is use of delicate and expensive lab equipment. MDSs are prime examples of this. High cost and low production capacity of MDSs are not compatible with industrial needs. It also gives the false impression that such high-end devices are necessary to deposit thin film circuits with an acceptable level of controllability and robustness. In fact, one of the main objectives of this study is to show that a non-precision setup can be enough to fabricate application focused circuits and sensors.

During the course of this thesis, following questions will be investigated:

1. Why does G exhibit the touted exceptional electrical, chemical, and mechanical properties?
2. What distinguishes LPE-G from single crystal G sheets?
3. Why does GO behave differently from G?
4. Does LPE damage raw material during processing?
5. Can recycled raw material result in equally well performing functional inks?
6. How can coffee ring effect during deposition be avoided without use of toxic chemicals or hard to control substrate heating methods?
7. Can sensors and circuits fabricated with presented methodology perform as expected?

It is important to note that fabrication of circuits with fine features rivaling photolithography is out of scope of this study. Although high performing films are an ideal objective, this study puts a higher emphasis on industrial feasibility of presented methods from

a manufacturing/fabrication point of view. Based on this, following requirements are expected to be fulfilled:

1. Synthesis method should be scalable, and water based.
2. Final product yield should be higher than previous published works.
3. Synthesized dispersion should be inkjet printable without use of toxic and environmentally dangerous solvents.
4. Synthesized dispersion should be inkjet printable at any thickness without experiencing morphological degradation.
5. Synthesized dispersion should be printable with simple inkjet printing equipment.
6. Inkjet printed devices should function as expected with repeatable results.

In addition to above mentioned requirements, simple routes for modification of film properties are also investigated in this method. Specifically, a simple doping scheme using gold and fabrication of composite G-CMC films featuring silver nanoprisms (AgNP) are investigated. As in the case of inkjet printable G ink, AgNPs were synthesized in the lab under controlled conditions. Overall, as a multi-disciplinary work, topics of thesis include investigation of all aspects of ink synthesis, deposition, and characterization. Major disciplines visited during the progress of this study include; chemistry, materials science, mechanical engineering, and electrical engineering.

1.8 Overview of the Thesis

The remainder of this thesis is organized into 7 chapters. Chapter 2 provides the necessary background on G and GO. Physical structure of G/GO and its impact on mechanical, chemical, electrical, and biological properties are described in detail. It is crucial to understand underlying mechanisms for G's exceptional properties and how these properties relate to dispersion based G. Through a thorough understanding, methods to harness these properties and realistic expectations can be set. In addition, careful analysis of the differences between single crystal G and dispersion based G is necessary to explain how industry can benefit from inkjet printed G devices.

Chapter 3 focuses on common synthesis methods for G dispersions and proposed water based G dispersion. Graphene dispersions have been extensively studied in the last decade and

several efficient methods have been published. On the other hand, use of expensive and potentially dangerous chemicals complicates industrial adoption of these G dispersions. Methods introduced in this chapter provide details for synthesizing environmentally friendly, non-toxic G dispersion in bulk amounts. Furthermore, simple routes for enhancing thin film electrical conductivity through doping and metal nanoparticle addition are also described and related characterization data presented.

Chapter 4 introduces the custom built inkjet plotter printer, substrate treatment protocol, and formulation of inkjet printable inks using the dispersions presented in Chapter 3. Inkjet printing of homogeneous is a multi-dimensional problem where inkjet printing parameters, substrate surface energy and charge, and ink solvent properties all impact film morphology. In this chapter, a polyelectrolyte based substrate coating and use of non-toxic 1-Propanol are described to eliminate coffee ring effect which is a common detriment to thin film homogeneity. Finally, characterization and experimental results are presented for inkjet printed films.

Post processing of printed films is a common step in solution based printed electronics. Even though a sintering step is not possible due to material properties of carbon, thermal treatment can decompose polymeric additives in films and improve bulk conductance. Furthermore, it is often argued that feature size that can be achieved with inkjet printing is too large for higher performance applications. In fact, smallest features that can be achieved by photolithography is many times smaller than what can be achieved with the state-of-the-art materials deposition systems (MDSs). On the other hand, laser micromachining of thin films is a promising method that could compliment inkjet printing. In Chapter 5, theory and experimental results of femtosecond laser micromachining/annealing are described.

Fabrication of an inkjet printed remote capacitive sensor, an electrical passive low pass filter, and a pH biosensor are described in Chapter 6. Theory behind design parameters, fabrication process, choice of substrates, designed circuit patterns, and experimental results are presented in detail. Limitations of presented devices and possible future work are discussed.

Chapter 7 summarizes the contributions of this thesis. Limitations of the research and possible recommendations for future studies are discussed.

Chapter 2

Review of Graphene and Graphene-Derivatives

2.1 General Structure and Mechanical Properties

Graphene is a one atom thick layer of carbon atoms arranged in a hexagonal form. Its basal plane structure does not differ from graphite, which is formed by hundreds of graphene layers stacked on each other and bonded by weak van der Waals forces. When a single or few layers of G is separated from a stack, it exhibits unique properties, which are not observed for graphite. A single layer of continuous G layer exhibits the highest room temperature electrical conductivity known (1×10^8 S/m), very high breaking strength (~ 40 N/m), extremely high Young's Modulus (~ 1.0 TPa), and excellent thermal conductivity (~ 5000 W·m⁻¹·K⁻¹) properties (Novoselov et al., 2004). All these unique properties can be understood, to an extent, by simply studying G's atomic structure. So, in this chapter, atomic structures of G and GO, and their mechanical, electrical, and chemical consequences will be discussed.

Carbon is a member of Group 14 of the periodic table. It has an atomic number of 6. Carbon is the 15th most abundant element on earth and 4th most abundant element in the known universe. It is a highly versatile element and is involved in nearly ten million different compounds. Among purely carbon material, graphite and diamond are the only allotropes that are readily found in nature. However, during the last few decades, several man-made allotropes have been synthesized and characterized; fullerenes, carbon nanotubes, and graphene. In addition, several exotic stable allotropes have been proposed but are yet to be synthesized; penta-graphene and graphyne. Allotropes of carbon exhibit a huge span of properties despite the fact that they are made of the same element. A simple example of this is differences observed between graphite and diamond, which are closely related to G (Table 2.1). Carbon has a partially filled *p* sub shell and requires four covalent bonds to form stable compounds. In diamond, every carbon atom shares an electron with its four neighboring atoms in the three-dimensional space (Fig. 2.1).

Table 2.1 Comparison of graphite and diamond. Even though both are allotropes of carbon, they exhibit very different properties.

Graphite	Diamond
Soft	Hardest material known (Mohs 10)
Self lubricant	Highly abrasive
Good conductor of electricity	Very poor conductor of electricity
Opaque	Transparent
Can be used as thermal shielding	Very good thermal conductor

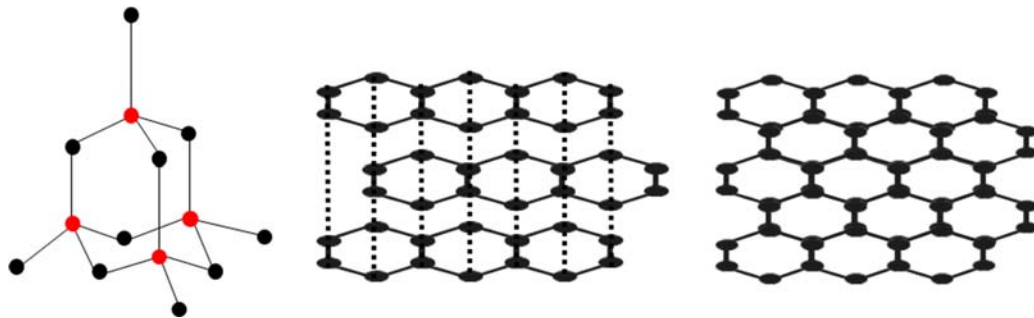


Figure 2.1 Atomic structure of diamond (left), graphite (mid), and graphene (right). Dashed lines represent van der Waals bonds between layers of graphite.

This type of chemical bonding is generally known as a σ -bond and it is the strongest of covalent chemical bonds. Energy required to break σ -bonds of diamond (cohesive energy) is estimated to be around 7.5 eV/atom (Shin et al., 2014). In comparison, metallic bonds have cohesive energy in the range of 1-5 eV/atom. High cohesive energy of bonds that form diamond crystal results in; high melting point, high thermal conductivity, low electrical conductivity, and very high hardness factor. Graphite forms three σ -bonds with its neighboring atoms and one π -bond. The π -bonds are covalent chemical bonds where overlapping atomic orbitals share electrons indirectly. This is a weaker form of covalent bonding and it has important consequences for both G and graphite.

Another type of bonding present in graphite is van der Waals bonds. Van der Waals bonds are the result of intermolecular or interatomic electrostatic forces named after Johannes Diderik van der Waals. Van der Waals forces and subsequent bonds are the result of electric dipole moment of atoms. At any given time, negatively charged electrons and positively charged protons of an atom are in a state of balance. This balanced system can be considered a dipole with slightly separated charges. Product of one of the charges and the distance between positively and negatively charged parts give the electric dipole moment. Van der Waals bond happens when a momentary electric dipole in an atom induces an electric dipole at a nearby atom. This electrostatic bonding is very weak, and its cohesive energy is around 0.1 eV/atom. For solids composed solely of van der Waals bonding, this would result in very low melting points. In the case of graphite, van der Waals bonds are found between stacked G sheets and hold Gr together through electrostatic attraction between sheets. As a result, graphite is a very soft material and a very good lubricant due to almost frictionless slipping of stacked G sheets in graphite flakes.

As it is mentioned, two-dimensional structure of G is not different than graphite. Figure 2.1 represents typical carbon arrangement for G. Each carbon atom has three σ -bonds and one π -bond. From Fig. 2.2a, location of π -bond is not immediately clear and cause confusion for the fact that carbon needs four covalent bonds to be stable. The π -bonds are found vertically up and down on hexagonal ring like structure of G. This effectively creates an electron cloud. In a perfect G layer, π -orbitals are not disrupted and resulting electron clouds merge to create a layer wide electron network. In this network, electrons can move freely which results in the extremely high electrical conductivity of G. The π -orbitals are also what set graphite apart from diamond. Unlike diamond, graphite is electrically conductive, albeit, it is much less conductive compared to G. In graphite, π -orbitals and electron cloud formations exist but are not continuous and perfectly aligned as in the case of G. In diamond lattice, π -orbitals do not exist and all the electrons are tightly bound in σ -bonds.

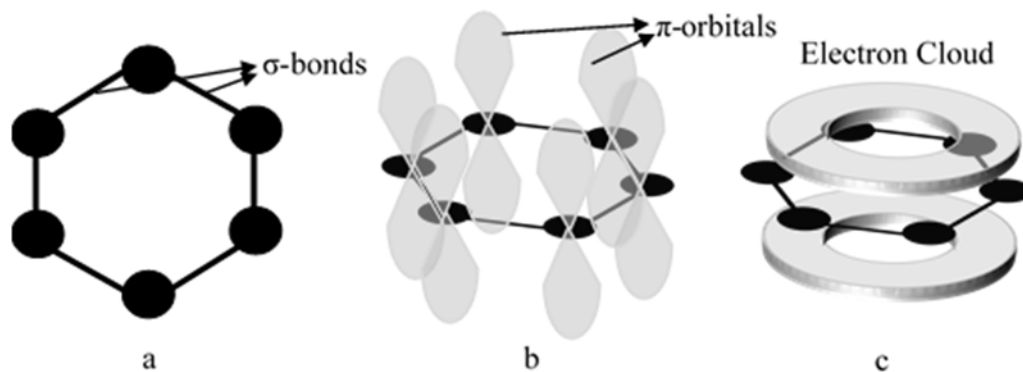


Figure 2.2 Atomic structure of graphene. In-plane σ -bonds are responsible for graphene's extreme mechanical strength while electron cloud network formed by vertically extending π -bonds allow a high-speed highway for electrons.

A single layer sheet of G is solely formed of strong in-plane covalent bonds and exhibits extreme mechanical strength. Through Quantum Monte Carlo study, G's cohesive energy was calculated to be ~ 7.46 eV/atom (Shin et al., 2014). Hence, G has a very high breaking strength (~ 40 N/m), extremely high Young's Modulus (~ 1.0 TPa) while having a relatively low density (2 g/cm³). Theoretically, a perfect single layer of graphene film would be nearly impossible to break while weighing less than 1 mg per m².

A single layer of G is about 0.4 nm thick. Although its thickness has been long expected to be somewhat closer to atomic radii of carbon atom (0.15 nm), perceived thickness may be larger due to G sheet-surface interactions. It has been observed that, unless a higher amount of pressure applied to the AFM tip, perceived G layer thickness can be as high as 1.7 nm (Shearer, Slattery, Stapleton, Shapter, & Gibson, 2016). In that sense, single layer G sheets somewhat float over surfaces they are deposited on. G is hydrophobic, it does not readily form stable colloid dispersions in aqueous media. Binding energy between water molecules is ten times larger than adsorption energy between G sheets and water molecules which causes the perceived lack of interaction between water and G (Leenaerts, Partoens, & Peeters, 2009). In addition, electrostatic repulsion (zeta potential) between G sheets is not high enough to stop eventual agglomeration in aqueous media. Bepete et al. (2016) has recently claimed that lack of water-G interaction is, at least in part, due to dissolved gasses in water. But his work is yet to be repeated and confirmed by other researchers.

Chemical properties of G are direct results of its atomic structure and geometry. Basal plane of G film is composed of σ -bonds and π -bonds both of which are covalent chemical bonds. Although π -bonds (2.84 eV/atom) are weaker than σ -bonds (7.46 eV/atom), basal plane of G has been shown to be chemically inert (Mélinon, Masenelli, Tournus, & Perez, 2007). At room temperature, G shows resilience against chemical attack, either in gas or liquid form. G has been shown to be 100 times more resistant to corrosion than copper and increases resistance against hydrogen peroxide (30%) (Singh Raman et al., 2012). Krishnamurthy et al. (2013) showed that thicker G films (3-4 layers) can provide even better environmental protection for long periods of time (2400 hours) against microbially-induced galvanic corrosion. A more recent work by Krishnamurthy et al. (2015) also showed that G's protection was 10 and 100 fold better compared to Polyurethane and Parylene-C, respectively. An interesting consequence of G's geometry is its increasing chemical reactivity with decreasing thickness. It was observed that vacancy defects can be introduced by exposure to pure oxygen at $\sim 260^\circ$ (Yamada et al., 2014). Compared to Gr, this is a low temperature for oxidation to occur. At higher temperatures, in ambient atmosphere, single layer G films can be damaged at temperatures lower than expected. Sun et al. (2008) exposed single layer CVD-G to a confocal laser beam in ambient air. It was found out that CVD-G film's basal plane was unstable above 500°C while edges were vulnerable at temperature above 220°C . Similar temperature stability trend is also observed for TGA curves of pristine G powder where an initial weight loss at 340°C and rapid weight loss after 500°C were observed (Lv, Yu, Jiang, Chen, & Nie, 2014). Although this is unusual compared to graphite and diamond both of which exhibit excellent stability up to 700°C , it is expected due to high surface area/volume ratio of G. While basal plane of G is very stable, sheet edges can have one or more open bonds. These sites are common targets to attach molecules to stabilize G in various mediums. Unfortunately, they are also vulnerable to environmental attacks more than basal plane since edges with open bonds can be considered defects and they are chemically active. Because of this, G films formed by smaller sheets are more vulnerable to chemical attacks compared to single crystal or large grain CVD-G.

Under right conditions, it is possible to introduce defects to G basal plane. This allows for not only defining limits to its protective capabilities but also for efficiently modifying films to introduce functional chemical sites. Such modifications can change electronic properties of

G and allow fabrication of chemical sensors, doped semiconductors, and insulators. Use of strong acids can modify G basal plane as it was demonstrated by use of Nitric Acid treatment of CVD-G (Kasry, Kuroda, Martyna, Tulevski, & Bol, 2010; Gunes et al., 2010). Chemical gas sensors with extremely high sensitivity ppm levels can be fabricated by intentionally induced basal plane defects. In example, ozone treated G films were shown to outperform pristine G films by 2 folds for NO₂ gas sensing (Chung et al., 2012). More defects sites on basal plane means more particles from environment can be absorbed. Absorbed foreign particles change conductivity of G film which can be measured and related to the environmental conditions.

While nanometer scale vacancy defects and atomic doping can tweak G's properties, extreme modifications to basal plane can change material characteristics considerably. One such derivative of G is called Graphene Oxide (GO) and it has been studied extensively for its unique properties. Graphene Oxide is electrically insulating, optically transparent (due to band gap energy coinciding with visible spectrum), and hydrophilic. It was found out that thermal, chemical, and thermochemical treatments can induce graphitization and recover G like electrical properties. Since synthesis of single layers of GO is a straight forward and well studied problem, researchers commonly used GO for creating functional films in the early stages of G research.

In a typical synthesis of GO, natural graphite flakes are processed through use of strong oxidizers to intercalate and eventually separate layers of single layer sheets. Precursor material, Graphite Oxide (GrO), was first synthesized in 1859 by Benjamin Brodie through treating graphite with fuming nitric acid (Brodie, 1860). This process was very time consuming and required great attention to detail to safely handle involved processes. In Brodie's method, a graphite and potassium chlorate solutions are mixed with strong fuming nitric acid and left in a 60°C water bath for three to four days. After the initially oxidation reaction concludes, synthesized product is washed with clean water, dried in a water bath, and original oxidation process is repeated three more time.

A highly efficient and safer alternative method was developed by Hummers & Offeman (1958) (Fig. 2.3). In Hummers' method, graphite was treated in a water-free mixture of concentrated sulfuric acid, sodium nitrate, and potassium permanganate. Compared to Brodie's

method, oxidation reaction is carried out only once and whole process take mere hours. This method is the current golden standard for GrO synthesis, although slightly modified derivations have been proposed to further increase efficiency and product quality. Once GrO is synthesized, preparation of GO is straightforward. GrO synthesis process readily intercalates graphite layers with water molecules during oxidation. Due to increase in interlayer spacing, GrO particles can be easily exfoliated into single layer GO sheets through mild bath sonication in water for one to two hours.

Although synthesis of GO is a simple process, atomic structure of resulting material is still a matter of debate. Unlike G, GO structure is complex and no unambiguous model exist to this date. There are many challenges regarding development of a universal model for GO structure. First, chemical reactions leading to GrO are not fully understood. Oxidation process of graphite does not simply inject oxygen atoms into the basal plane, it forms several different functional groups on the surface. There is no a consensus on what specific groups are formed during oxidation. Second, method of oxidation, purity of chemicals involved in the process, and source of graphite alter resulting material. Hence, great variety among samples can be observed. This leads to conflicting reports from different research groups. Last, precise analytic methods to identify functional groups on GO without doubt do not exist. Many conclusions come from indirect observations which opens presented data and methodology to interpretation.

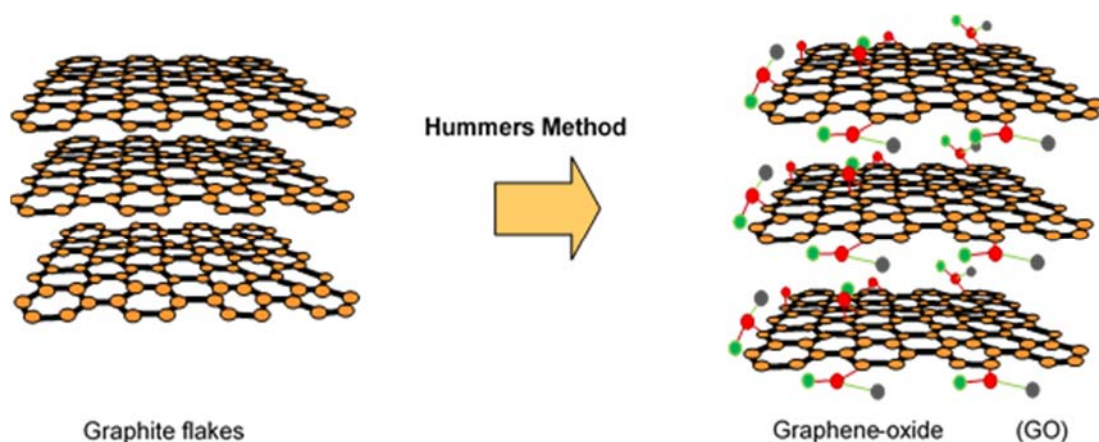


Figure 2.3 Oxidation process of converting graphite into graphene oxide for ink production (Sinar, Knopf, & Nikumb, 2013).

Single layer sheets synthesized by Hummers' method contain several functional groups on their basal plane and exhibit very different properties than pristine G sheets. It is agreed universally that GO surface includes at least tertiary alcohols, epoxides, and a variety of alkenes. It is also observed that ratio of epoxides to alcohols increase with higher levels of oxidation. Exact identity of epoxides is not agreed upon as some models suggest 1,2-ethers while other 1,3-ethers. It is also debated that carboxylic acid groups may exist in very low amounts since they are detected during XPS studies (Dreyer, Park, Bielawski, & Ruoff, 2010). It is also debated if GO has a regular lattice structure or not. Early models generally featured ordered lattice structures. Models by Hofmann and Ruess featured ordered repeat unit with epoxy and hydroxyl groups, respectively (Dreyer et al., 2010). These models were generally accepted until the non-stoichiometric model proposed by Lerf, He, Forster, & Klinowski (1998). According to proposed model, GO surface was amorphous and dominated by epoxides (1,2-ethers) and tertiary alcohols while featuring carboxylic acid groups at low amounts.

An important consequence of epoxides on GO is the observed hydrophilicity. Neutron scattering studies have confirmed that hydrogen bonding between epoxides and water is responsible for GO-Water interaction. Although similar interactions have been observed with several polar solvents (e.g. DMF, Oxolane, and NMP) dispersibility in water is a highly desired property. It has been demonstrated that GO can be dispersed in large enough concentrations (up to 9 mg/mL in water) to be deposited in the form of thin films (Huang, Huang, et al., 2011). Ease of synthesis and deposition of GO fueled research efforts for efficient reduction methods. As of writing of this thesis many chemical and thermal methods have been demonstrated to reduce GO to rGO. General theory of these methods will now be explained in detail.

Graphene Oxide can be reduced by use of common strong reductants. So far, an extensive range of chemicals have been demonstrated to reduce GO; i.e. hydrazine (Park & Ruoff, 2009; Ren, Yan, Ji, Chen, & Li, 2010; Eda, Fanchini, & Chhowalla, 2008), lithium aluminum hydride (LAH) (Ambrosi, Chua, Bonanni, & Pumera, 2012), sodium hydride (Mohanty, Nagaraja, Armesto, & Berry, 2010), sodium borohydride, sodium-ammonia mixture, hydrogen sulphide, and dimethylhydrazine (Eda et al., 2008; Stankovich et al., 2006). Some of these chemicals can react with water (LAH and sodium borohydride), hence require special care when utilized. Hydrazine either in liquid or vapor form is the benchmark chemical for reduction performance and ease of use. In a typical reduction process, hydrazine hydride is

dissolved in GO dispersion. Hydrazine hydride's performance is a function of solution temperature as higher temperatures yield more reduction. In a study by Ren et al. (2010) it was observed that C/O atomic ratio and electrical performance of rGO at 95°C for 3 hours was better than 80°C, 60°C, 15°C treated samples regardless of treatment duration.

Another observation was hydrazine's lack of reactivity towards hydroxyl groups on GO surface. Hydrazine vapor can be used to reduce GO. In a typical vapor based reduction process, prepared GO films are placed in a sealed container with dimethylhydrazine and heated to 80°C for 24 hours followed by additional treatment in N₂ atmosphere for 5 hours at 200°C (Eda et al., 2008). Chemical based reduction of GO is arguably the simplest method to synthesis rGO. On the other hand, it has critical drawbacks. Solution based reduction of GO practically limits treatment temperature to water's boiling point. Also, solution reduced GO becomes hydrophobic like G. Hence, unless reduction was carried on in the presence of a stabilizer or a solvent exchange method utilized, rGO dispersion would lose stability and sediment. An important advantage of vaporized reductants over liquid solutions is possibility of reducing already deposited samples. On the other hand, sample treatment still needs to be in elevated temperatures. Consequently, treatment temperature is limited by substrate temperature stability. Whether solution or vapor based, chemical reduction affects material properties universally and equally, meaning that localized properties cannot be achieved on rGO films. This can be a serious limitation depending on the application. As it will be discussed in the following chapter, a crucial advantage of rGO is its adjustable material properties. Ability of locally adjusting rGO properties could pave the road to fabricate electronic components more sophisticated than simple electrodes. Choice of reductants is critical for reduction performance. Not every reductant can react with every available functional groups on GO surface. Hence, each chemical must be evaluated separately for its reducing capacity. Finally, some reductants are known to dope rGO. For example, n-type doping is commonly observed with hydrazine treated films. Inadvertent doping may eliminate any possibility for further functionalization where specific functional groups are needed on rGO surface, such as selective sensor applications.

Thermal reduction is achieved simply by heating GO samples in film or dispersion form and can be considered the second most common method to synthesize rGO. Compared to chemical reduction, product of thermal reduction is more predictable as reduction process

follows simple thermodynamic assumptions. One can intuitively conclude that treatment would be equally applied to all available functional groups, unlike chemical reduction. Also, bond strength of functional groups differs from each other. Hence, it is expected that certain groups may persist until a threshold temperature is reached. At very high temperatures, by 2100°C, it would be expected that rGO would revert completely back to a perfect crystalline graphite. This last step has been known for a long time and true for even diamond as graphite is the thermodynamically favored form for carbon. Characterization of rGO samples by separate research groups have confirmed these expected results. Research conducted by Bagri et al. (2010) and Seung Hun Huh (2011) has been especially important for understanding how these results come to be. Seung Hun Huh studied XRD and Raman data of GO for treatment temperatures 60 to 2000°C. XRD data of thermal reduction presents a rather study transition for GO pattern (expressed by d_{002} peak at $2\alpha = \sim 15^\circ$) to a graphite pattern (d_{002} at $2\alpha = \sim 26^\circ$). Raman data, on the other hand, shows a transition point where rearrangement of carbon atoms begin (graphitization). Up to 800°C, Raman pattern of rGO resembles of GO with both D-mode and G-mode peaks are expressed. By 1000°C, a sharp increase in I_D/I_G ratio is observed. This observation is in agreement with findings of other research groups (Park & Ruoff, 2009; Bagri et al., 2010).

Functional groups on GO are different than functionalized pristine G sheets where some molecules would be weakly attached to the open bonds available at the nanosheets edges. Functional groups of GO are thought to be inclusive or formed by double bounds (aromatic or conjugated) some of which can be removed only through harsh methods, while others are removed at relatively lower temperatures (hydroxyl groups). When they are removed, they tend to leave defects in the basal plane. GO has low thermal stability and removal of oxygen containing species tend to be in the form of CO and CO₂, not in just pure O₂. This is especially exacerbated at very high temperatures which results in a highly disorder structure with many vacancies left over from reduction. As the temperature is further increased beyond 1000°C towards 2000°C, I_D/I_G ratio completely diminishes, and Raman pattern resembles graphite due to self-repair of graphitic structure through rearrangement. Although, complete reduction of GO is possible through thermal routes, unfortunately, it is commonly used to study reduction kinetics of GO. Since most substrates cannot stand the high temperatures necessary for graphitization, rGO samples usually heated up to 800°C at most. On the other hand, application

of heat is also possible by use of a focused laser beam. A pulsed laser beam can heat GO films without damaging underlying substrate and locally adjust rGO properties. Laser based modifications and micromachining of GO films have also been demonstrated by Sinar et al. (Sinar, Knopf & Nikumb, 2014; Sinar, Knopf, Nikumb & Andrushchenko, 2014). Laser based processing of GO and G samples are discussed in detail in Chapter 5 of this thesis.

During thermal reduction at around 800°C, most -if not all- functional groups would be removed from GO surface. But, vacancies persist since atomic rearrangement cannot take place until > 2000°C. Comparison of resulting rGO and pristine G has not been investigated by any research group so far. While merits of such research can be questionable, certain assumptions can be made to differentiate mechanical, chemical, and electrical properties of the two materials. First, any open bonds on sheet surface will contribute to chemical reactivity. A high chemical reactivity means that rGO sheet would be more susceptible to environmental effects. If temperature is sufficiently increased, oxygen from the environment will react with carbon to produce CO or CO₂. Hence, rGO is also expected to be somewhat thermally less stable. Same logic can be used for mechanical strength. High yield strength of pristine G is a direct consequence of covalent bonds between carbon atoms. If any bonds are missing, it would create a weak zone where further damage could happen to lattice. Finally, broken bonds mean disrupted π orbitals. Subpar electrical performance of rGO samples have been universally documented when compared to pristine G.

2.2 Electrical Properties of Graphene and Graphene Oxide

Electrical properties of G have been at the center of attention since its characterization. In fact, majority of papers on G investigates utilization of its electrical properties through various means. Before discussing G's electrical properties, a crucial distinction must be made between pristine G and rGO. It is common in the literature to find peer reviewed papers that discuss G electronics yet use GO as a starter. It is also common for rGO that was used in those papers to be referred to as G. As discussed in the previous section, GO does not completely revert to G up until 2000°C. In another word, rGO is not G unless thermally reduced at a temperature beyond 2000°C, which is never the case since this temperature is enough to destroy most substrates. Distinction between rGO and pristine G is beyond semantics as rGO's Raman

signature is different from G's. Since their physical structure is different from each other, so are their properties. Hence, for the remainder of this thesis, G specifically stands for pristine G that was synthesized from either a pristine Graphite source or synthesized atom by atom from a carbon source through a verified method (i.e. vapor deposition and SiC sublimation) without oxidative procedures for producing G sheet or sheets. Discussion regarding studies done on samples where GO is the starting material will always refer reduced material as rGO regardless of original author's wording. Another crucial point is impact of G's electronic properties from a printed electronics point of view. Strictly speaking, most unique electronic properties cannot be observed for G films that were printed using particulate ink formulations, unless certain post-processes were to be attempted. This will be discussed in further detail by the end of this section. Regardless, a solid understanding of G's electronic properties is vital for research in this field. Hence, this section will briefly explain electronic structure of a single crystal suspended G sheet, assuming defect free lattice, no doping, and infinite dimensions.

Graphene, since its characterization, has been dubbed the "miracle" material due to its unique properties. Many of G's unusual properties are electrical in nature. A few of these properties can be roughly explained by considering how electrical conductivity occurs among different kinds of materials and by fitting G's structure in this context.

Since electrical conduction can only happen through free movement of electrons, electrical properties of any material directly stem from their physical structure. Ionic solids where there are no free electrons, except due to impurities and holes, are excellent insulators. In metals, valence electrons are not covalently bound but rather shared by the entire solid. Which means valence electrons are free to move around the solid when subjected to an electrical potential. Semiconductors have covalently bonded atoms. Conductivity of semiconductors depend on how tightly electrons are bound to the lattice. Atomic radius of elements is larger for higher periods. A larger atomic radius means less orbital overlap and loosely bound electrons. A result of this is much higher conductivity of crystalline Silicon compared to diamond even though both assume diamond cubic crystal structure. As mentioned in previous section, G's crystal structure can also roughly explain why it can conduct electricity at all. Free electrons in the overlapping π orbitals of G can travel through whole crystal with immense velocities. A single layer of continuous G layer exhibits the highest room temperature

electrical conductivity known (1×10^8 S/m) and a record carrier mobility (2×10^5 cm²·V⁻¹·s⁻¹).

In addition, inadvertent doping of G sheets was observed due to the nature of substrate it was deposited on. These structural peculiarities can be explained by general geometry of a single layer G sheet and simple statistics. In fact, adsorption of foreign molecules from the top side can further affect these properties. Hence, as commonly observed, G films can exhibit slightly different or sometimes contradicting properties according to the method they were deposited or synthesized.

Unlike bulk materials, single layer G sheets have two surfaces and no volume. Thus, underlying substrate directly affects whole sheet's properties. It can go through spontaneous doping, both n and p type, depending on substrate in contact with G sheet. Epitaxially grown G sheets on SiC tend to exhibit substrate induced bandgap, a property that is not necessarily observed for G sheets deposited on other kinds of substrates (Zhou et al., 2007). Also, due to a lack of volume, any inclusion or exclusion from crystal structure would have a profound effect as there is only one route for electrons to flow through; the surface. Method of synthesis can cause damage to G lattice. Films fabricated through defect causing synthesis methods exhibit poor electrical performance. As it will be discussed later in this section, this has important consequences for inkjet printed electronics.

Graphene can be considered a zero-bandgap semiconductor or a semimetal with zero carrier density at Dirac points, depending on the experimental conditions. Electron's in G act like massless particles, show extreme mobility, and can travel long distances without any scattering. Even more unique properties such as anomalous quantum hall effect, photoconductivity, and Casimir effect have also been observed. Most of these properties cannot be immediately deduced from G's crystal structure, but they can be analytically shown to exist. So, derivation of G's energy band structure, its carrier transport properties, and related consequences will be the focus for this section.

Electronic band structure of solids is commonly calculated using tight binding model (TB) approach. TB model suggests that most of the electrons are tightly bound to the parent atom and do not take part in conduction or interact with other atoms. A singular atom located infinitely far from any other would have distinct energy values for each of its electrons. On the

other hand, as two atoms approach each other, wave functions of outer most electron shells begin to overlap. Due to Pauli Exclusion principle, broad energy band formed from this overlapping wave functions split into energy levels that are distinct but almost continuous inside the energy band itself (Griffiths, 2005). Electrons occupying outermost shells can move between energy levels inside the same band which results in conduction (if there are empty energy levels in the band). Meanwhile, electrons closer to the atom preserve their discrete energy values and remain tightly bound to the nucleus. Because electrons cannot have any of the energy values contained within the bandgaps, electrons reside close to nucleus do not conduct electricity or interact with any other atom.

To be able to model electronic band structure of G, its Bravais lattice, lattice vectors, and nearest-neighbor vectors must be defined (Fig. 2.4). Lattice vectors shown in Figure 2.4 are written as

$$a_1 = \frac{a}{2} (3, \sqrt{3}), \quad a_2 = \frac{a}{2} (3, -\sqrt{3}) \quad (2.1)$$

$$b_1 = \frac{2\pi}{3a} (1, \sqrt{3}), \quad b_2 = \frac{2\pi}{3a} (1, -\sqrt{3}) \quad (2.2)$$

$$a \approx 1.42 \text{ \AA} \text{ (nearest-neighbor C-C spacing)}$$

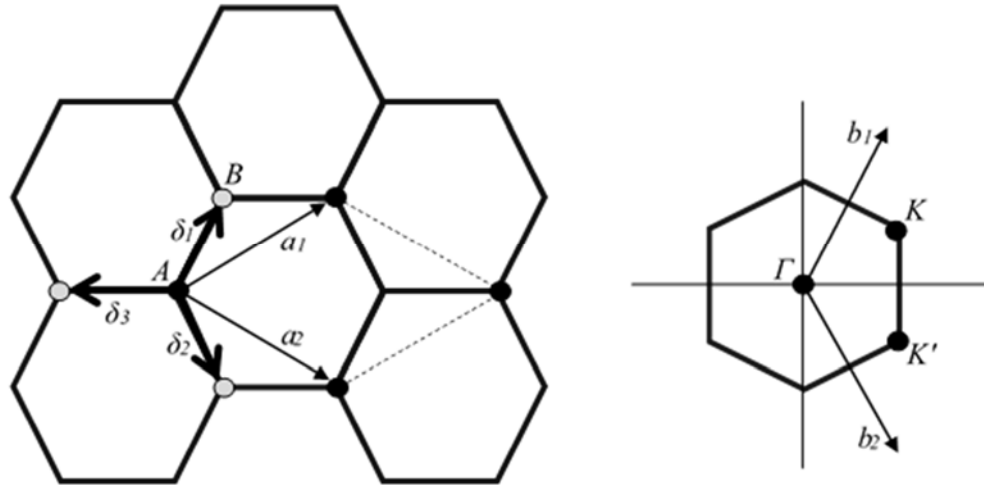


Figure 2.4 Honeycomb structure of G (Left). Dotted lines, a_1 , and a_2 , define the unit cell. Brillouin zone of G (Right). K and K' define the Dirac points. At these points, Dirac Cones meet.

Nearest-neighbor vectors (for sublattice A) are given by

$$\delta_1 = \frac{a}{2} \left(1, \sqrt{3} \right), \quad \delta_2 = \frac{a}{2} \left(1, -\sqrt{3} \right), \quad \delta_3 = a(1,0) \quad (2.3)$$

K and K' points on momentum space are defined as

$$K = \frac{2\pi}{3a} \left(1, \frac{1}{\sqrt{3}} \right), \quad K' = \frac{2\pi}{3a} \left(1, -\frac{1}{\sqrt{3}} \right) \quad (2.4)$$

Considering electrons in π orbitals of G can hop to nearest-neighbor (n.n.) and next-nearest-neighbor (n.n.n.), simple TB Hamiltonian can be written as (Nilsson, Neto, Guinea, & Peres, 2006)

$$H = -t \sum_{\langle i,j \rangle, \sigma} (a_{i,\sigma}^\dagger b_{j,\sigma} + H.c.) - t' \sum_{\langle i,j \rangle, \sigma} (a_{i,\sigma}^\dagger a_{j,\sigma} + b_{i,\sigma}^\dagger b_{j,\sigma} + H.c.) \quad (2.5)$$

$t \approx 2.8$ eV (nearest-neighbor hopping energy)

where i and j denote atoms and σ denotes spin state. If denote orbitals as (i, σ) and (j, σ) , creation operators $a_{i,\sigma}^\dagger$ creates an electron at A (commonly denoted as site R_i). The energy bands from above Hamiltonian were derived by Wallace (1947) in his work, *The Band Theory of Graphite*.

$$E(k) = \pm t \sqrt{3 + f(k)} - t' f(k) \quad (2.6)$$

$$F(k) = 2 \cos(\sqrt{3}k_y a) + 4 \cos\left(\frac{\sqrt{3}}{2}k_y a\right) \cos\left(\frac{3}{2}k_x a\right)$$

In order to find energy band structure at point K and K' of the Brillouin zone, dispersion equation (Eqn. 2.6) has to be expanded using $k=K+q$ relationship and assuming $q \approx 0$. Which means $k = K$ for (Eqn. 2.6),

$$E(q) \approx -\frac{3ta}{2} (e^{-iK_x a}) (iq_x - q_y) \quad (2.7)$$

When $(e^{-iK_x a})$ is extracted to simplify the equation

$$E(q) \approx \frac{3ta}{2} (q_x - iq_y) (1 + O\left(\frac{q}{K}\right)^2) \quad (2.8)$$

Alternatively, (Eqn. 2.8) can be written as follows

$$E(q) \approx \hbar v_f (q_x - iq_y) \left(1 + O\left(\frac{q}{K}\right)^2\right) \quad (2.9)$$

where,

$$v_f \equiv \frac{3ta}{2\hbar} \cong 10^6 \text{ m/s} \quad (2.10)$$

(Eqn. 2.10) is known as the Fermi Velocity. It is quickly clear from (Eqn. 2.10) that dispersion at K and K' (Dirac Points) is independent of electron mass m_e .

It is important to note here that electron hopping can happen only between sublattices A and B . Also, in accordance with k -representation of the first term of (Eqn. 2.5), TB model represents off-diagonal symmetry. This suggests electron-hole symmetry. Since unit cell of G has two atoms and each atom has one electron (with $1/2$ spin), G must be either a semiconductor or semimetal (when undoped and defect free). Moreover, $F(k)$ is zero at K and K' . What this means is that density of states (DOS) at Fermi level for K and K' is zero and in fact energy band is half filled. Hence, undoped and defect free G is an ideal semimetal (Fig. 2.5).

It was shown by Albert Einstein that total energy of a particle can be written in terms of its rest mass (m) and momentum (p)

$$En^2 = (pc)^2 + (mc^2)^2 \quad (2.11)$$

For non-relativistic particles, where velocity v is much smaller than speed of light (c), $(pc)^2$ term is simply classical kinetic energy of a body, $\frac{1}{2}mv^2$. But, for massless particles (relativistic), such as photons, total energy equation of (Eqn. 2.10) is simply

$$En = pc \quad (2.12)$$

Now, (Eqn. 2.9) can be rearranged in matrix form

$$H \equiv \hbar v_f \begin{pmatrix} 0 & q_x + iq_y \\ q_x - iq_y & 0 \end{pmatrix} \quad (2.13)$$

$$\varepsilon(q) = \pm \hbar v_f |q|$$

where q is the momentum relative to the Dirac points. Note that usual case for energy of an electron is $\varepsilon_e(q) = \frac{q^2}{2m_e}$, which is simply the non-relativistic kinetic energy with $q = m_e v_e$ with v_e being electron velocity.

Equations (Eqn. 2.13) and (Eqn. 2.12) are fundamentally similar with Fermi velocity replacing velocity of light, c , in the case of (Eqn. 2.13). Also, considering (Eqn. 2.9) and (Eqn. 2.10), Fermi velocity is independent of momentum and total energy, unlike $\varepsilon_e(q)$. Since (Eqn. 2.13) resembles massless Dirac's Equation instead of Schrodinger's equation, electrons and holes of G are called Dirac Fermions. Hence is the excitement about G, as quantum electrodynamics for massless fermions allow several unique phenomena that wouldn't be possible with ordinary electrons. For example, graphene exhibits anomalous quantum hall effect (AQH). AQH effect can already be observed in other material such as Si and GaAs, but only under strict experimental conditions. On the other hand, AQH effect in G can be observed at room temperature (Novoselov et al., 2005).

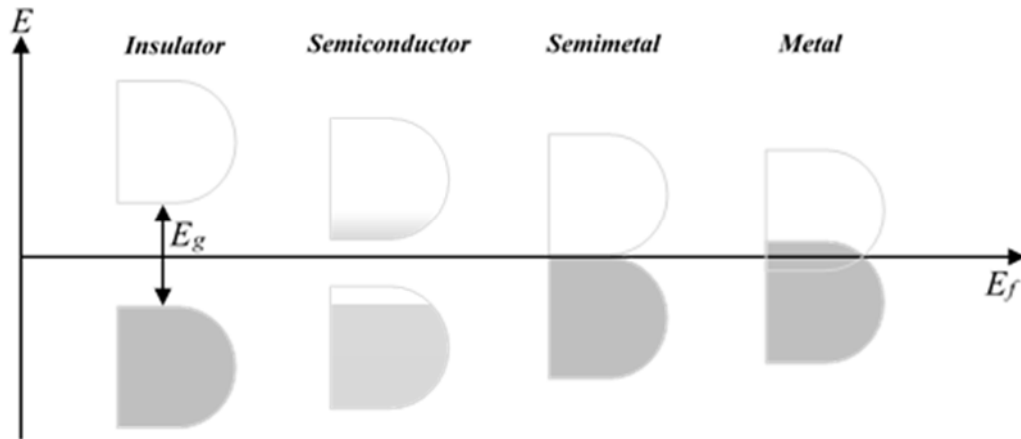


Figure 2.5 Materials can be roughly categorized into four types based on their energy band structure. Insulators exhibit very large bandgap energies (E_g) that prevent valence electrons' hopping to conduction band. Semiconductors have smaller bandgap energies. Depending on position of the Fermi Level (E_f), a semiconductor may behave electron (n) or hole (p) like. Metals have overlapping valence and conduction bands. As a result, free electrons are readily available to conduct electricity without needing to hop between bands. In semimetals, E_g is zero but valence and conduction bands do not overlap. Since E_g is zero right at E_f and valence and conduction bands exhibit completely symmetry (as in the example case shown in this figure), G is regarded as an ideal semimetal.

Another unusual phenomenon is the Klein paradox (Huang, Ruiz-Vargas, et al., 2011). Klein paradox states that relativistic massless particles, such as G's Dirac fermions (at normal incidence), can be transmitted through an electrostatic barrier with a probability of "1" whereas a non-relativistic particle would be reflected (classical mechanics) or dampened (non-relativistic quantum mechanics). An electrostatic barrier does not have to be an ordered structure or a potential wall, in fact lattice disorder can be considered as one. As a result, electrons in G can travel micrometer scale distances with no scattering at all, effectively tunneling through impurities, defects, and topological deformations. Klein paradox (or tunneling) was shown to contribute to high carrier mobility of G sheets on SiO₂. Despite high concentration of charged impurities between SiO₂-G interface, carriers can travel through electrostatic barriers near charge neutrality point (Gate voltage (V_g) zero for defect free, suspended G. V_g shifts based on concentration of impurities) (Huang, Ruiz-Vargas, et al., 2011). Finally, Graphene Nanoribbons (GNR) were shown to have very different electronic properties. GNRs are G sheets that has very narrow widths (< 50 nm). The zigzag edge formation was experimentally shown to be always metallic and less resistive (Fig. 2.6a). On the other hand, armchair edge formation (Fig. 2.6b) was shown to be semiconductive with a bandgap inversely related to the GNR width (Barone, Hod, & Scuseria, 2006).

Although these properties carry great importance for certain applications, discussing them in greater detail would be out of scope for this thesis. Moreover, utilization of these properties for realistic G based devices have been a very challenging task. For example, large theoretical conductivity of single layer G was not possible to achieve without additional steps that complicate fabrication processes. Since single layer G has two surfaces and no volume, it is very susceptible to impurities and defects introduced from the environment. In other words, major limitation to G's conductivity is extrinsic factors, not intrinsic limitations. As a matter of fact, a multitude of scattering sources contribute to reduce G's effective carrier mobility well below the theoretical $2 \times 10^5 \text{ cm}^2 \cdot \text{V}^{-1} \cdot \text{s}^{-1}$ (Chen, Jang, Xiao, & Ishigami, 2008).

As mentioned above, G's resistivity is a result of several sources of scattering. Three major sources of scattering have been identified for G (Hwang, Adam, & Sarma, 2007; Chen et al., 2008); Coulomb scattering due to surface impurities, phonon scattering due to Longitudinal Acoustic (LA) phonons of G, and Remote Interfacial Phonon (RIP) scattering

due to polar optical phonons of the underlying substrate. Combined effect of these scattering mechanisms can be estimated by using Matthiessen's Rule

$$\frac{1}{\mu_t} = \frac{1}{\mu_c} + \frac{1}{\mu_{LA}} + \frac{1}{\mu_{RIP}} \quad (2.14)$$

where mobility values (μ_c , μ_{LA} , μ_{RIP}) represent the mobility of the material if each of them was the only sources of scattering. The well circulated electron mobility (μ_{LA}) figure of $2 \times 10^5 \text{ cm}^2 \cdot \text{V}^{-1} \cdot \text{s}^{-1}$ arises from electron-phonon scattering of a suspended, defect free G sheet. When a defect free and clean G sheet is suspended, mobility limitations due to Coulomb scattering and RIP scattering are nullified ($\frac{1}{\mu_t} = \frac{1}{\mu_{LA}}$). Chen et al. (2008) has experimentally shown that only remaining source of scattering, LA phonons, is independent of carrier density and its contribution to overall resistivity is almost negligible (30Ω). Hence, very high carrier mobility of $2 \times 10^5 \text{ cm}^2 \cdot \text{V}^{-1} \cdot \text{s}^{-1}$ can be achieved. When charged impurities and RIPs are taken into account, carrier mobility can be as low as $1 \times 10^4 \text{ cm}^2 \cdot \text{V}^{-1} \cdot \text{s}^{-1}$ (Ponomarenko et al., 2009). In this context, and as has been experimentally shown by Chen et al. (2008), Ponomarenko et al. (2009), and other researchers, dominant scattering mechanisms for G are Coulomb scattering due to impurities and RIP scattering due to substrate optical phonons. Since main source of impurities on otherwise clean sheets of G is substrate itself, proper substrate engineering may one day increase carrier mobility of G to a lever closer to its intrinsic limit.

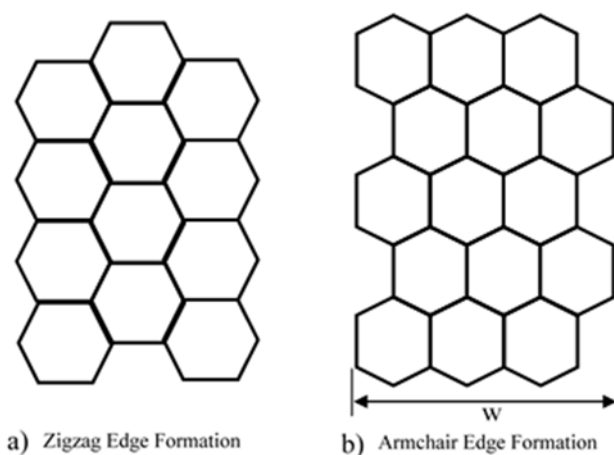


Figure 2.6 Two possible crystal structures for GNR. (a) Zigzag type edge formation results in metallic behavior. (b) Armchair type edge formation can exhibit metallic (large w) or semiconducting (small w) behavior based on width, w .

Notice that (Eqn. 2.14) does not have any terms for disorder scattering due to lattice defects. Fundamental research on G's electronic properties commonly use mechanically exfoliated sheets for experiments. Because G's sp^2 covalent bonds exhibit excellent mechanical and chemical stability, for mechanically exfoliated samples, lattice defects are exceedingly rare. In comparison, CVD fabricated films contain large amounts of lattice defects in the form of microscopic exclusions in the lattice and macroscopic (relatively) scale grain boundaries. Since any disruption of sp^2 network is a lattice disorder, edges of G sheets can be regarded as defect sites. Grain boundaries can be thought as edges in the same context. When a CVD film has grain boundaries, electrons must hop through these "edge" like formations. Huang, Ruiz-Vargas, et al. (2011) showed that grain boundaries can significantly impact total carrier mobility of a CVD-G film. Chemically derived G sheets, namely rGO exhibit even a higher level of lattice disorder. GO synthesis involves harsh processes. Furthermore, thermal or chemical reduction of GO sheets do not fix lattice disorder for lower temperature processes. Zhan et al. (2011) has investigated lattice defect of Graphite Oxide (GrO) and reduced Graphite Oxide (rGrO) samples through I_D/I_G ratio of their Raman spectra. D-mode peak of Raman spectra arises from disruption of sp^2 network. Since G-mode peak represents graphitic structure itself, ratio of the two peaks is a valuable parameter for assessment of lattice defect status. As expected, thermal reduction at 950°C for 30 mins (under Ar/H₂ atmosphere) had not significantly impacted I_D/I_G ratio. In other words, graphitic structure was still damaged. Kaniyankandy et al. (2011) employed ultrafast optical pump probe spectroscopy to study electronic properties of both GO and rGO. Study revealed presence of electron trap states (ETPs). ETPs increase required energy to move an electron or hole in a material, which effectively traps it in place. In Kaniyankandy's work, electron trap states had diminished following reduction with hydrazine hydrate. So, it can be deduced from Kaniyankandy's work and Zhan's Raman data that increase in conductivity for rGO samples is due to elimination of trap states, not rearrangement of lattice structure.

It can be speculated that due to persistence of lattice defects in rGO, research on its electronic properties have been limited, especially compared to G. Reduced GO samples, rather chemically or thermally reduced, have been universally documented to be inferior to G in terms of conductivity. Moreover, to author's knowledge there hasn't been any study or report of any exotic electronic properties relating to GO/rGO. On the other hand, GO/rGO's insulating,

dielectric properties and electronic band structure have been frequently investigated. Discussion on GO/rGO's electronic properties will focus on these aspects.

Compared to G, GO exhibits very low electrical conductivity (Table 2) and is not viable as electrode material. Instead, its feasibility as an insulating material has been frequently investigated. Insulating materials are important components of microelectronic components such as capacitors and transistors. In transistors, highly resistive layers are crucial to prevent current leak. In capacitor design, dielectric constant of insulating layers is major determinant of final capacitance. Regarding dielectric constant of pure non-modified GO films (composed of single and few layers sheets), there have been conflicting reports where some sources claim ϵ more than 10^2 (~ 1 kHz) (Huang et al., 2012; Yousefi et al., 2014) while others report a range of around 3 to 4 (Salomão, Lanzoni, Costa, Debeke, & Barros 2015) which is closer to GrO dielectric constant. In addition, a modified Hummers' method is also reported by Kumar, Pittala, Sanyadanam, & Paik (2015) with a claimed dielectric constant of 648 at 1 MHz. Polymer/rGO nanocomposite formulations as dielectric layers follow a similar trend where different preparations yield very different dielectric properties. Polypropylene/rGO (PP/rGO) composites were prepared by D. Wang et al. (2013). In this study, GO was prepared by a modified Hummers' method and chemically reduced in situ. At high particle load (0.2 Vol%), proposed PP/rGO composite layers exhibited high dielectric constant ($> 10^3$) in a range of 10^2 to 10^4 Hz (D. Wang et al., 2013). On the other hand, PDMS/rGO films prepared by Wang, Nelson, Hillborg, Zhao, & Schadler (2012) exhibited starkly different dielectric properties. In this work, commercially prepared GO particle samples were thermally reduced at temperatures ranging from 70°C to 160°C for 12 hours and then mixed with PDMS. Resulting layers exhibited constant dielectric constant (< 10) for all samples at all particle loads in a range of 10^{-1} to 10^5 except for the sample that was reduced at 160°C (sample S160). The S160 sample showed a similar trend to D. Wang's data where dielectric constant had increased for lower frequencies. This may be due to inefficient thermal reduction for Z. Wang's sample, since it is known that GO reduction usually commences for higher temperatures than used in that study. But, common thermal reduction processes are much shorter than 12 hours, hence extent of the thermal reduction is hard to predict without a more focused investigation. Regardless, it is certain that discrepancies may be explained by differences in preparation and characterization methods which also makes comparison of these studies practically impossible. Nevertheless,

studies that claim high dielectric constants, especially for polymer composite preparations, are very promising and further studies would be highly valuable.

Another prospect of GO is its high proton conductivity. A proton conductor is usually used as solid electrolyte for fabrication of supercapacitors and fuel cells. In this scheme, solid electrolyte transports charge with hydrogen ions (H^+). GO was shown to have a proton conductivity of 10^{-2} S/cm (Karim et al., 2013). In comparison, Nafion's proton conductance is reported to be around 5.4×10^{-2} S/cm (Phair & Badwal, 2006). Although GO has slightly inferior performance, it has better thermal stability and it is cost effective.

Finally, unlike G, GO has a bandgap. More importantly, it has been shown that this bandgap can be adjusted by simply tuning oxidation state of GO. Huang, Li, She, & Wang (2012) investigated effect of oxygen density on rGO bandgap energies in a range of 6.25% to 50%. For the heavily oxidized samples, bandgap was the largest (~ 3.8 eV). On the other hand, for lesser oxidation states, relationship between reduction and bandgap lacked a clear trend. In fact, 25% O/C ratio was found to have smaller bandgap energy than 11% O/C ratio. A direct application of GO bandgap was published by Wu et al. (2008). In this work, Wu et al. (2008) was able to fabricate a G/GO Schottky barrier (0.7 eV). As expected, a moderate thermal reduction process (at 180°C for 16 hours) had reduced barrier height to 0.5 eV. On the other hand, since GO bandgap is not linearly related to oxidation state, further studies would be necessary to see if higher barrier height could be achieved with different reduction parameters.

As explained above, electrical properties of G and its derivative GO are unique. If fully harvested, G could fundamentally impact performance and design of electronic devices. On the other hand, so far, this chapter has focused electronic properties G confined in a single sheet with perfect crystal structure. In practice, large area fabrication of G films has been very challenging. Mechanically exfoliated (e.g. Scotch Tape method) G sheets are microscopic in scale and there are no practical means to control size and shape of exfoliated sheets. CVD-G films are the next best alternative. CVD method allows fabrication of large area films. But, CVD method is not appropriate for high volume fabrication of films due to high equipment and energy cost. Moreover, G film can only be fabricated on metal substrates and must be transferred. Film transfer methods have improved over the course, but defects due to transfer cannot be avoided. Alternatively, suspended sheets can be deposited to form thin films of any

dimension and shape. Synthesis of suspended sheets and related deposition methods are discussed in Chapter 3.

When suspended sheets are deposited on a substrate, they form a film through a network of particles in contact with each other. Figure 2.7 depicts differences between a single crystal film and a film formed by suspended particles. The film in Fig. 2.7a can be thought as a close up of a single crystal G sheet that was mechanically exfoliated or as a large area CVD-G film. For such films, equation (Eqn. 2.14) holds true and total carrier mobility can be calculated using known values for μ_c , μ_{LA} , and μ_{RIP} . For films formed such as Fig. 2.7b, an additional scattering term for sheet-to-sheet hopping has to be considered. An exact value of carrier mobility for sheet-to-sheet carrier transport has not been determined. But since the deposition process for such films is completely random, a study towards studying hopping losses may not have any practical use. Regardless, hopping losses have been shown to be the dominant scattering loss for such films and are the major contributor to the poor performance of printed G electrodes when compared to CVD-G films and mechanically exfoliated G sheets (Wang, Ang, et al., 2010).

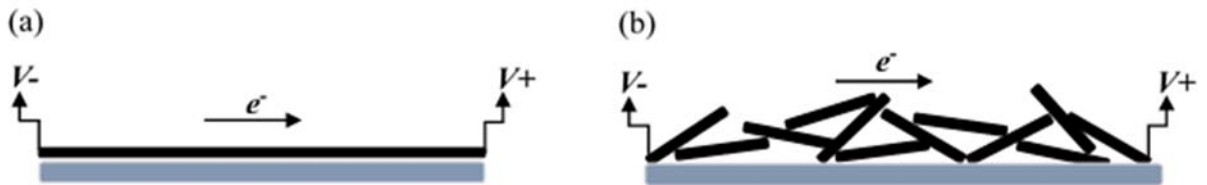


Figure 2.7 Comparison of large area single crystal conductive film (a) and a conductive film formed by deposition of suspended particles (b). For single crystal film, electrons must hop over lattice defects. For deposited suspended particle film, electrons must hop from one sheet to another in addition to lattice defects of each sheet. Distance to hop between sheet-to-sheet is larger than lattice defects. Hence, contact resistance between individual sheets is the major contributor to electrical resistance for printed thin films.

Since mobility reduction due to hopping cannot be avoided, there are only few options for optimizing conductivity of such films. First, use of larger sheets to form films would reduce number of “hopping” an electron would have to do to cover a certain distance. This has been demonstrated by Wang, Ang, et al. (2010) where electron mobility of large rGO sheets (~25 μm) was able to surpass previous studies. Annealing process has been shown many times to increase total conductivity of deposited traces. Depending on the synthesis and deposition process, annealing can increase conductivity through at least one of these effects; removal of residual solvents/surfactants, removal of environmental contamination such as adsorbed humidity, removal of unintentional dopants that may originate from synthesis process, and rearrangement of crystalline structure to correct lattice disorder and possible merge individual sheets (only at very high temperatures $> 2000^\circ\text{C}$). Doping of deposited films can enhance conductivity of film through increasing overall carrier concentration. Gold (Au) and Silver (Ag) doping of both CVD-G and inkjet printed G (Sinar, Knopf, Nikumb, & Andrushchenko, 2016) films have been demonstrated to increase conductance up to 4 times. Substrate engineering methods are known to enhance electrical conductivity of CVD-G films. Coulomb scattering, in example, can be screened out through using layers of high dielectric constant materials over or under G film. To author’s knowledge, substrate engineering methods have not been thoroughly investigated for printed G films and may present an opportunity to further enhance electrical performance.

2.3 Biocompatibility of Graphene and Graphene Oxide

Definition of biocompatibility changes according to the source. Most common definition is based on David F. Williams’ work (Williams, 2008). According to this, biocompatibility can be summarized as coexistence of a material with tissues and able to perform as designed. In the context of this research, and for the sake of simplicity, biocompatibility of a material will be defined as lack of bioresorbance, toxicity, and corrosion. Such complete bio-inertness is ideal for most biological applications where circuits may need to be implanted on the skin, under the skin, or inside human deep tissues. According to leading research, G and GO has been deemed generally biocompatible under right conditions. This opens a wide range of opportunities for application of G based flexible circuits directly on human tissue.

There are several roadblocks when a generalized discussion of nanomaterial biocompatibility must be made. First, surface modulation of nanomaterials can significantly change their biological behavior. In example, CNTs are shown to be biopersistent in their pristine form, yet can be eliminated through renal route if they are functionalized to be water dispersible. Pristine CNTs have also been observed to cause oxidative stress and physical damage to cell membranes (Schrand, Dai, Schlager, Hussain, & Osawa, 2007). Possible genetic damage and interference with immune system were also claimed which put emphasis on importance of proper ways to excrete certain nanomaterials. Depending on the application, each nanomaterial may need to be functionalized to increase dispersibility in a certain solvent, target certain cells in living tissues, or perform different actions. Each modification to pristine nanomaterial must be investigated separately for biocompatibility. Second, it has been shown that different tissues in the same living body can react differently to the same nanomaterial (Jones & Grainger, 2009). Immune cells do not have the same recognition pattern for different organs. As a result, while a nanomaterial performs its duty properly in the lungs, it may cause an immune response in the liver. Third, immune response to nanomaterials differ between species. Iron oxide nanoparticles have been shown to be biocompatible in human cells while they cause inflammation response in rats and mice (Kunzmann et al., 2011). Since most biosafety experiments are exercised on animals, non-transferable results further complicate research on biocompatibility. Finally, geometrical parameters of nanomaterial can significantly change their behavior. Extremely small gold nanoparticles (1.6 nm) are shown to cause cell death through oxidative stress and damage to mitochondria. While same behavior was not observed for larger particles (3.7 nm) despite similar level of penetration into cells. Furthermore, even larger gold nanoparticles were observed to be trapped in liver and lung cells which adds concerns regarding long term accumulation of nanoparticles (Kunzmann et al., 2011).

Biocompatibility of G and GO also suffer from above mentioned difficulties in this research field. Both G and GO are deemed biocompatible by several peer reviewed articles. Utilization of GO for experimental cancer treatments has also been reported (Liu, Robinson, Sun, & Dai, 2008). Yet, GO is shown to cause oxidative stress in the lungs. On the other hand, pristine G does not result in similar oxidative damage. Interestingly, biocompatibility of G was not affected with its dispersibility, although aggregated G did cause mild fibrosis during the

next 21 days (Duch et al., 2011). It should be noted that geometrical parameters of nanomaterials have significant effect on possible damage to living cells through exposure. As 2D materials, G and GO have less chance to penetrate deep into cells compared to CNTs which are 1D nanoparticles. As a result, any direct toxicity may be averted simply due to lack of penetration. An interesting claim by Duch et al. (2011) was that occurrence of fibrosis was not due to toxicity but due to inefficient clearance of aggregated G from cells. This could mean that devices made from non-water dispersible G sheets may persist in body cavities without causing severe degrees of fibrosis or toxicity. Then again, long term effects of this biopersistence would need to be thoroughly investigated in vivo.

2.4 Optical Properties of Graphene and Graphene Oxide

Conductors, such as metals, exhibit strong absorption in visible spectrum due to screening effect of free electrons. Consequently, as thickness of a metal layer increases, transmittance diminishes rapidly. Axelevitch, Gorenstein, & Golan's (2012) investigation on very thin noble metal films shows that a 2 nm thick gold and silver thin film may absorb approximately 30 to 70% of visible light depending on wavelength. In addition, as it was mentioned in Chapter 1, metals are prone to ductile fracture due to occurrence of lattice dislocations through mechanical stress. In a 2 nm thin metal film, lattice dislocations will reach critical density rapidly and result in fracture.

Electrical conductivity happens through different mechanisms in G. As it is discussed in Section 2.3, even though π -orbitals do form a continuous highway of electron cloud, in general, G has less free carrier density compared to metals. It has been experimentally shown that each G layer absorbs about 2.3% of the incident light. Compared to metals, G absorbs all visible wavelengths at a rather consistent amount. Considering that each G layer is about 0.4 nm thick, a 2 nm multilayer G sheet would have an expected absorption rate of 11.5% for all wavelength. Furthermore, thin G sheets are completely flexible and can be folded without breaking C-C bonds. Hence, fabrication of very thin G films has been regarded as the ultimate achievement for fabrication of flexible optically transparent electrodes.

Graphene Oxide is a large band gap semiconductor. Its band gap energy (~ 3.8 eV) results in optically transparency. It has been observed that GO loses its transparency when

reduced through various means. In fact, it has been experimentally shown that level of reduction, band gap energy, and optical transparency are all related. This could potentially mean tunable energy band gap/optical transparency devices. Several studies have demonstrated that such precise control over band gap energy can be possible (Mathkar et al., 2012).

2.5 Applications of Printable Graphene and Graphene Oxide

Unique properties of G and GO make them highly desirable materials for device fabrication. Electrical conductivity and high mechanical flexibility of both single crystal and printed G films can allow them to be used in wearable device fabrication. Conductivity of printed films are poor compared to single crystal G films. On the other hand, use of single crystal, high conductive G films for device fabrication is currently out of question due to excessively high cost and unscalable fabrication process. Yet, for wearable devices that do not require optical transparency, crucial factor is not conductivity but the sheet resistance. Low conductivity issue can be circumvented simply by depositing thicker films. CVD fabricated single layer G films tend to have 300 to 700 Ω /sq sheet resistance. This level of conductance is achievable by printed G films of less than 5 μ m thickness. If protected from environment, this printed film would be bendable. Slippage between individual sheets during mechanical strain would not result in physical damage to the film if it is not stretched to a point where connection between G sheets is interrupted by large gaps.

Unlike simple wearable devices, opto-electronic devices require high conductivity. Nondoped printed G films tend to have high sheet resistance (> 2 k Ω /sq) at low absorbance ($< 30\%$). Yet, several strategies have been devised and experimented on to improve conductivity of printed G films. Elemental doping, nitric acid treatment, and printing in conjunction with unique metal nanoparticles have been demonstrated to reduce printed film sheet resistance by 2 to 10 times. If practical and controllable methods can be identified, printed G films can be used for opto-electronic devices of any kind.

Graphene Oxide as an insulator and dielectric material can find use in component design. It has been suggested that, due to its high ion conductivity, GO can be a good solid electrolyte for supercapacitors (Ogata et al., 2017). Graphene Oxide has also been claimed to possess high dielectric constant (Liu, Galpaya, Notarianni, Yan, & Motta, 2013). Inkjet printed

G/GO/G layers can be as thin as 1 μm which would allow inkjet printing of a very high surface area sandwiched assemblies. Through printing on flexible substrates, flexible energy storage systems could be fabricated. These systems can be used to power wearable technologies.

Finally, G's biocompatibility and high flexibility can be utilized in fabrication of biomedical implants. Combined with flexible G/GO/G supercapacitor assemblies, G based implants could completely replace some of the simple circuitry. If functionalized by piezoelectric materials, G based sensors could be used as track heart rate in real time. If functionalized by active molecules, real time monitoring of critical blood compounds, such as glucose, can be possible.

Chapter 3

Chemical Synthesis of Graphene and Graphene Based Dispersions

3.1 Methods to Synthesize Graphene Sheets

Graphene's exceptional electrical, mechanical, and chemical mean that its thin films may be viable alternatives for design of flexible electronic devices. On the other hand, development of simple and scalable fabrication methods for G films is crucial for industry wide adoption.

Due to difficulties at industrial scaling of CVD and ST type fabrication methods, alternative means to synthesize large batches of G sheets are highly desired. Chemical methods are of interest due to their easy adaptation to industrial scale production volumes. First example of this was synthesis of GO where Gr can be oxidized in large batches and resulting in GO, which is naturally single layer. This contrasts methods such as CVD where films/sheets are formed atom-by-atom and ST where pristine sheets are cleaved mechanically. In this chapter, common methods of G synthesis and formulation of proposed G dispersion will be presented. Proposed synthesis method and characterization of resulting product will be discussed in detail.

Since its characterization, several different methods have been developed to synthesize or isolate thin sheets of G. First method to be developed was ST method, where a piece of ST was first placed on a small amount of Gr. Scotch tape, then, placed and removed on a clean substrate several times to mechanically cleave a viable sheet for analysis. Inability to isolate sheets with controllable dimensions has led researchers to develop CVD based methods for fabrication of thin G films atom-by-atom. In a typical CVD method, a carbon source is evaporated in one chamber and allowed to reassemble atom-by-atom on a substrate in a separate chamber. Due to high temperatures necessary for carbon to rearrange itself in graphitic form, substrates are usually common metals, such as copper. Initial samples fabricated through this method were susceptible to large number of defects introduced both by the process itself and the film transfer step. Through optimization of synthesis parameters, current CVD

fabricated films can achieve about 300 Ω/sq . CVD method has been limited to lab use due to its unscalable nature, high equipment cost, and high energy cost. In addition, CVD methods require careful optimization and control of process parameters which further complicates repeatability and reliability of this method.

Liquid phase exfoliation (LPE) was developed to address some of the technical and financial problems of CVD-like processes. LPE is a synthesis method where a cheap starting material (Graphite) is mechanically agitated by bath or probe sonication. Mechanical agitation happens due to generation and eruption of microscale air bubbles induced by high frequency sound energy. Choice of solvent, surfactants, and stabilizers depend on how the process is designed. Unlike CVD method, LPE method requires a liquid media and exfoliated sheets must be stable in this media to avoid eventual agglomeration. Once a stable colloidal dispersion is achieved, sheets must be deposited on desired substrate by other means. This adds flexibility to the choice of deposition method. Synthesized G sheets can be either used in initial media or can be dispersed in a different solvent through use of a solvent exchange method. Solvent exchange might be necessary if initial synthesis was conducted in a toxic or environmentally dangerous solvent.

It has been shown that only a few organic solvents can directly exfoliate G sheets from Gr through LPE. Organic solvents that show affinity to G can efficiently exfoliate thinner sheets. N-methylpyrrolidone (NMP), dimethylformamide (DMF), and dimethyl sulfoxide (DMSO) were shown to be good exfoliation solvents. Similar exfoliation behavior was also observed when surfactants were used in aqueous media. Experimental evidence suggests that direct exfoliation efficiency is affected by Hildebrand parameter (HDP), HSPs, and surface tension of a solvent. HDP precedes HSPs and is defined as square root of cohesive energy density

$$HDP = \left(\frac{U}{M}\right)^{1/2} \quad (3.1)$$

where U is the measurable energy of vaporization and M is the molar volume of the pure solvent (Hansen, 2012). Cohesive energy density is defined as the energy needed to fully remove unit volume of material to infinite separation. In the case of G, cohesive energy density means the amount of energy necessary to separate individual sheets far enough that sheet-to-solvent

interaction dominates over sheet-to-sheet attraction. Despite being occasionally used to determine solubility of materials, HDP has an important shortcoming. HDP does not account for individual impact of different types of interactions, such as polar and hydrogen bonding interactions. As a result, solutes with similar HDPs might exhibit starkly different affinities. For example, solute 1 and 2 might have same HDP yet solute 2 may exhibit very little hydrogen bonding compared to 1. In such a case, solute 1 could be hydrophilic while 2 could be hydrophobic.

Unlike HDP, HSPs define interactions between a solvent and solute in three components; dispersive (D), polar (P), and hydrogen-bonding (Hb). HSPs are related to HDP as they both define cohesive energy density of a material

$$HDP^2 = D^2 + P^2 + Hb^2 \quad (3.2)$$

Dispersive interactions derive from atomic interactions and are non-polar in nature. Hence, all solvents/solutes will exhibit D interactions to some degree. Polar interactions are molecular interactions. Polar type interactions arise from permanent dipole/permanent dipole interactions. These interactions are defined as “polar” interactions in a strict sense and high P parameter of a solute does not guarantee interaction with a polar solvent such as water. Finally, hydrogen interactions represent affinity of solute/solvent to establish hydrogen bonds. Hence, Hb interactions are molecular. Most hydrophilic solutes have large Hb parameter values. Based on G’s properties, as they were explained in Chapter 2, one can predict its possible HSPs. G is hydrophobic, it has weak bonds on basal plane that can interact with other material through van der waals forces (atomic forces) and is known to show affinity for non-polar organic solvents. Consequently, one would expect D interactions to be the dominant factor for G’s solubility. A high affinity for non-polar solvents mean low P parameter. Last, hydrophobicity of G should suggest a low Hb parameter. Indeed, based on current literature, G’s HSPs are predicted to be $D \approx 18$ MPa, $P \approx 9.3$ MPa, and $Hb \approx 7.7$ MPa (Hernandez, Lotya, Rickard, Bergin, & Coleman, 2010). Using equation 3.2, HDP of G is calculated as ~ 23 MPa. Based on solubility theory, ideal solvents would have to have HSPs and HDP that closely matches parameters of G.

An in depth look at the impact of each HSP components was made by Hernandez et al. (2010). Through short time bath sonication in various solvents, a rather loose trend was

observed for HSPs, HDP, and surface tension requirements of efficient exfoliation. Most efficient exfoliation tended to happen for solvents with ~ 40 mJ/m² surface tension (γ), ~ 23 MPa HDP, and $18 < D < 21$ MPa. Impact of γ , P , and Hb were less defined than rest of the parameters. While peak concentrations were indeed observed for $\gamma \approx 40$ mJ/m², $P \approx 12$ MPa, and $Hb = 6$ MPa, G exfoliation was still at measurable magnitudes for extreme γ , P , and Hb values. Evidence of exfoliation in solvents with very large γ (> 70 mJ/m²), P (> 25 MPa), and Hb (> 25 MPa) is especially startling considering hydrophobicity and non-polar nature of G. Hence, although correct HSP, HDP, and γ values are crucial to have high efficiency, exfoliation does not seem to seize for non-ideal solvents. TEM and AFM analysis of exfoliation products were supporting this conclusion. Ideal solvent in Hernandez's work (2010) was identified as cyclopentanone based on its solubility parameters. Yet, NMP outperformed cyclopentanone in all three criteria analyzed in the paper (mean # of G layers per sheet, # fraction of monolayer G sheets, and # fraction of few layer G sheets). More profoundly, acetone, a poor solvent based on solubility parameters and surface tension value, also outperformed cyclopentanone in all three criteria of exfoliation performance. Thus, it can be concluded that there may be unknown interactions taking place that influence solubility of G in solvents. Unfortunately, there yet to be a conclusive theory in this respect.

Direct exfoliation through use of organic solvents or through use of water/solvent blends is still the most common approach for LPE. Although G can be exfoliated in DI water, even in the lack of surfactants, exfoliation tends to take long hours of ultrasonication and produce only few layer sheets with diminished lateral dimensions. In addition, any exfoliated material agglomerates in a matter of hours due to very low affinity of water molecules towards G. Alternatively, researchers have identified large number of ionic and non-ionic surfactants that can manipulate solubility parameters of water to facilitate efficient exfoliation. Among these Tween 80, Pluronic 123 (Guardia et al., 2011), and sodium dodecylbenzene sulfonate (SDBS) (Lotya et al., 2009) were successful at exfoliating G at concentrations similar to solvent based exfoliation. Surfactant mediated exfoliation is generally undesirable due to non-volatile nature of these compounds. It is very difficult, or sometimes impossible, to efficiently remove surfactant residue from deposited films of LPE-G, even when surface adsorption did not take place. In such films, trapped surfactant molecules persist between individual G sheets as electrically non-conductive contaminants.

A more recent approach to LPE is to use of polymers to facilitate exfoliation and stabilization of G in liquid media. Although it is similar to surfactant-based exfoliation, polymer mediated exfoliation does not change solubility parameters and surface tension of the liquid media. Instead, polymers adsorb on G and act as a bridge between G and liquid media to exfoliate and stabilize individual sheets. This method can be used either aqueous or non-aqueous liquids, depending on solubility properties of polymer of interest. In a recent work, ethyl cellulose (EC) was used to stabilize G exfoliated in an ethanol/water solution (Secor et al., 2013). EC adsorption on G sheets was able to stabilize a higher concentration of G sheets in cyclohexanone/terpineol blend than ethanol/water solution could achieve. Although this method allows formulation of high concentration inks independent from exfoliation method, it requires removal of polymer in post processing. On the other hand, common polymers decompose quickly with thermal treatment. Thermal decomposition of ethyl cellulose in Secor's work (2013) had resulted in twice as higher conductivity compared to untreated samples.

3.1.1 Preparation of Aqueous Graphene Dispersion

Polymer based exfoliation presented in Secor's work (2013) can produce high number of single layer sheets and a higher concentration dispersion than direct solvent exfoliation methods. Yet, EC is not dispersible in water and water/ethanol solution is not inkjet printable. Hence, G nanosheets had to be exfoliated in a water/ethanol solution in the presence of EC, agglomerated using NaCl to salt out G-EC nanosheets, and then redispersed in an 85:15 mixture of cyclohexanone/terpineol.

In terms of health hazards regarding chemicals involved, development of a water-based dispersion is advantageous. LPE of G sheets using water soluble polyvinylpyrrolidone was proposed earlier which had resulted in stable dispersions (Wajid et al., 2012). In this work, a water soluble cellulose variant, Carboxymethyl Cellulose (CMC), was used to exfoliate and disperse G sheets in DI water. CMC is a non-toxic, high molecular weight, hydrophilic polymer that finds use in the industry as an emulsifier, stabilizer, and coating agent. It has a perfect safety track record and used in various food products. Due to its high solubility in water, use

CMC as a stabilizer in aqueous media can produce nontoxic dispersions hydrophobic nanoparticles.

Exfoliation of G sheets using CMC polymer is essentially similar to use of surfactants for G exfoliation. The CMC molecule has hydrophilic and hydrophobic functional groups spread along its polymer chain in a theoretically random but assumed to be homogenous in organization. The hydrophobic groups interact with the graphite edges and facilitate cleavage of sheets of G with the help of ultrasonication. Resulting dispersions have proved to be highly stable. Being a high molecular weight anionic polymer, CMC stabilizes G sheets by two different routes; electrostatic forces and steric forces. Stabilization by steric forces is highly desirable as ionic strength of the solvent has little impact on solubility of high molecular weight polymers. Consequently, monovalent and bivalent cations have no effect on stability of CMC functionalized G dispersions (G-CMC). Graphene-CMC ink can be synthesized directly from graphite flakes. Since G powders have become increasingly affordable, for this research, CMC was used to further exfoliate and stabilize a commercially available multilayer G powder.

To assess exfoliation performance of CMC, an exfoliation study was conducted based on bath sonication of G powder/CMC mixture in DI water and cycling of non-exfoliated material at the end of each synthesis cycle. The raw material cycling based approach was named cyclic liquid phase exfoliation (C-LPE). To prepare G-CMC dispersion, 2 mg/mL CMC (250 kDa, DS 0.7) was first dissolved in Milli-Q filtered DI water under magnetic stirring. Separately, 2 mg/mL multilayer G powder (Graphene Supermarket, A-12) was mixed with 100 mL Milli-Q water. Once CMC was completely dissolved, 100 mL CMC solution was mixed with 100 mL G-Water mixture. Three starting samples were prepared with exact same parameters as above and marked as A4, A8, and A24 representing 4-hour, 8-hour, and 24-hour bath sonication, respectively. A4 and A8 samples were further branched out in terms of cycle numbers as A4C1, A4C2, A4C3, A8C1, A8C2, and A8C3. For cycles 2 and 3 of each sample, raw material (RM) from previous cycle was recycled.

Each cycle was prepared using the following steps. Once bath sonication was done, samples were ultracentrifuged at 1000 G for 15 minutes. Suspended particles were poured into a separate container. Sedimented particles were reconstituted in DI water and ultracentrifuged a second time at 1000 G for 15 minutes. Again, suspended particles were poured in to a separate

container. Sedimented particles from both centrifuge steps were mixed DI water for a total volume 100 mL. This was mixed with a freshly prepared 100 mL CMC solution (2 mg/mL) and moved into the bathsonicator for the next cycle. Suspended particles were further ultracentrifuged at 20000 G for 15 minutes to separate G-CMC particles from free CMC left in the dispersion. Liquid in the tubes was decanted and sedimented particles were reconstituted in DI water. This step was repeated once more. Final product was reconstituted in 50 mL of DI water. Finished samples were allowed to sit for 24 hours before transferring into another container which resulted in very stable colloidal dispersions. It was observed that G-CMC particles can be reconstituted in smaller amounts of water to produce highly concentrate dispersions. During this study, stable dispersions were produced with up to 1/20th of the initial liquid volume without any observable reduction in stability.

3.1.2 Characterization of Liquid Phase Exfoliation Products

Based on literature and discussion on Chapter 2, high performing G films require G nanosheets with little to no defects, fewer layers per sheet, and larger lateral dimensions. On the contrary, subpar exfoliation performance may result in thicker than desired sheets, basal plane defects, and diminished lateral dimensions. Thus, exfoliation performance of any method must be characterized by analyzing defect status, sheet thickness, and lateral dimensions of its products. These properties can be characterized through well-established methods including TEM imaging, electron diffraction, and Raman Spectroscopy.

Three sonication protocols, A4 A8, A24, and their cycled products A4C1, A4C2, A4C3, A8C1, A8C2, A8C3, and A24 (single cycle) were characterized to assess effect of sonication length and re-cycling of RM on G sheet thickness, lateral dimensions, and defect status. In this section, characterization results for G-CMC, its consequences, and comparison to the available literature will be discussed.

3.1.2.1 TEM Imaging and Electron Diffraction

Transmission Electron Microscopy (TEM) is a crucial equipment in characterization of LPE-G. TEM works best with very thin samples (< 100 nm), such as G sheets, and can provide data

on expected lateral dimensions of sheets. Yet, due to limited field of view and operator manual analysis collected data may not be characteristic of the whole sample. In addition, TEM equipment without sample tilt function cannot provide any quantitative data for sample thickness. On the other hand, TEM imaging can provide conclusive data when combined with other characterization methods.

For samples prepared according to Section 3.1.1, visual confirmation was used to verify presence of thin G sheets, where multiple layers and folds on G sheets were easily observable (Fig. 3.1). It was observed that A4 inks included thicker sheets with visible clumping. Based on TEM image survey, individual edge lengths in A4 samples were ranged from 200 nm to 4 μm (Fig. 3.2). A4C1 sample also had large number of $< 1 \mu\text{m}$ sheets. This may indicate that RM already had very small sheets. Smaller sheets were also observed for A8C3 which is expected due to longer cumulative sonication process. A8C1 and A8C3 inks had thinner sheets compared to A4 samples. Observable sheet thickness was similar between A24 and A8C3 inks while lateral dimensions for A24 were below 1 μm for every sheet observed on the grid (Fig. 3.2d). It was also observed that individual sheets had no visible strands of CMC on them. Only visible strands were around the sheets and in contact with edges. This agrees with expected method of CMC functionalization. Pristine G sheets should have a defect free, hence chemically stable, basal plane. On the other hand, open bonds at the edges are active sites where CMC strands can attach.

Electron diffraction is a valuable tool for determining crystal structure of solid matter. In electron diffraction, electrons are fired at solid matter and interference from crystal/electron interaction results in an observable pattern of lattice structure. It is important to note that electron diffraction does not produce a pattern accurate enough for determination of atomic positions and lattice parameters. Instead, the pattern is a representation. Electron diffraction study was conducted to confirm film thickness and honeycomb structure of exfoliated sheets. For pristine G, electron diffraction pattern is expected to have rings of lattice positions with six lattice points in each circle. Additional lattice positions out of the rings may indicate impurities.

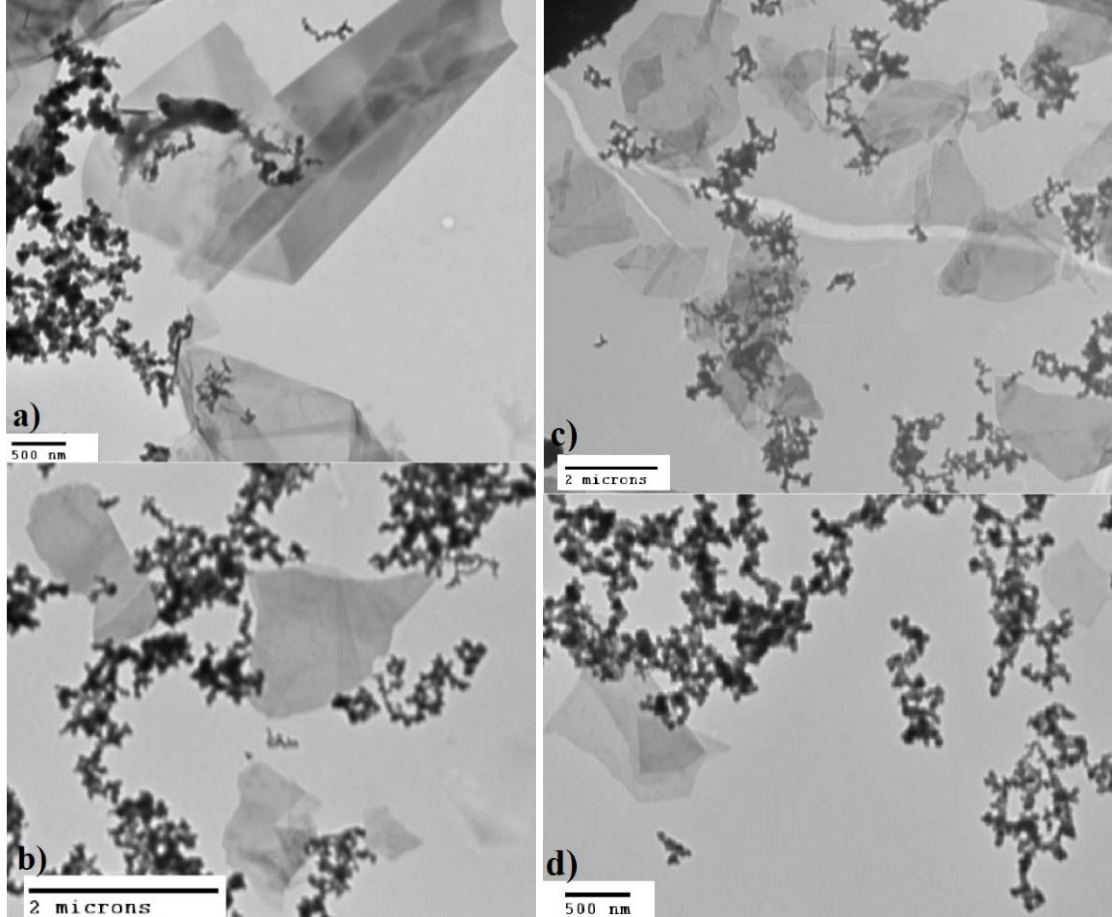


Figure 3.1 TEM images for A4C1 (a), A8C1 (b), A8C3 (c), and A24 (d) samples. A4 samples had large amount of clumped up sheets which indicate inefficient exfoliation. A24 sample had consistently thinner sheets than A8C1 but had smaller lateral dimensions. A8C3 sample had the optimal balance in terms of lateral dimensions and sheet thickness (Sinar & Knopf, 2018b).

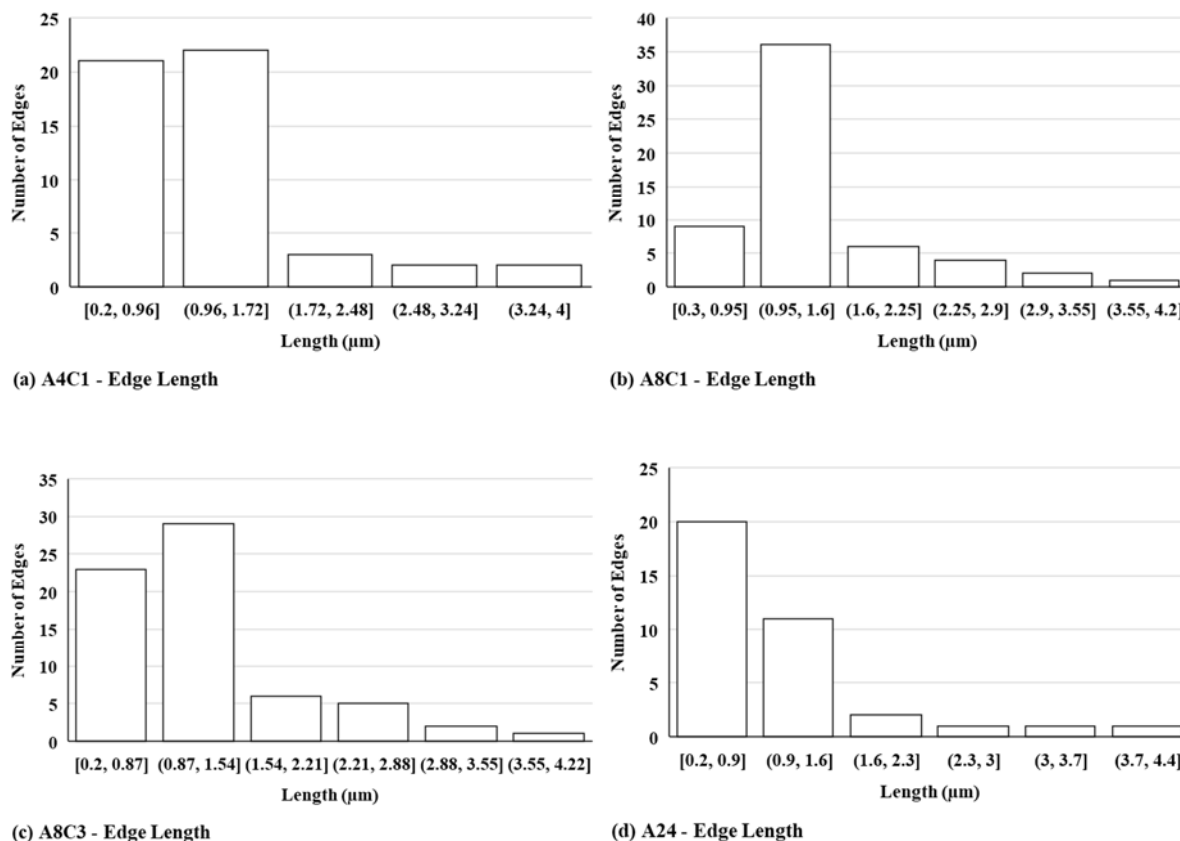


Figure 3.2 Edge length analysis of A4C1 (a), A8C1 (b), A8C3 (c), and A24 (d) revealed that shorter durations of repeated bath sonication preserves sheet lateral dimensions while 24 hour long single bath sonication resulted in reduced edge lengths (Sinar & Knopf, 2018b).

Intensity comparison between inner and outer ring of G diffraction pattern can distinguish between single and bilayer G sheets. In single layer sheets, $\{110\}$ and $\{210\}$ locations show comparable intensity. Higher intensity for $\{210\}$ position compared to $\{110\}$, as in the case of Figure 3.3a, indicates bilayer structure. Electron diffraction study showed that A8C3 sample predominantly had bilayer sheets (Fig. 3.3b). Due to equipment limitations, it was not possible to collect electron diffraction pattern for individual G-CMC sheets of every sample as interference from nearby particles ($\sim 5\text{-}10\ \mu\text{m}$ in every direction) can cause false reading. Instead, thin individual sheets that were isolated from other G sheets and CMC particles were analyzed.

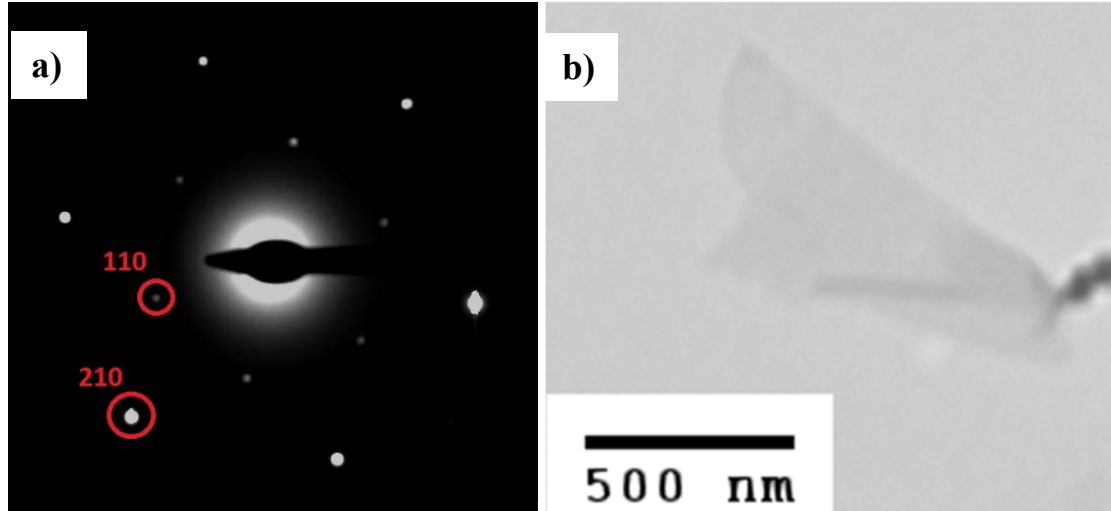


Figure 3.3 Electron diffraction pattern (a) and TEM image (b) for A8C3 sample. Intensity profile for $\{110\}$ and $\{210\}$ locations suggest bilayer sheets (Sinar & Knopf, 2018b).

3.1.2.2 RAMAN Spectroscopy

Raman Spectroscopy is an invaluable tool for characterizing structure of a material. In Raman Spectroscopy a monochromatic light source (i.e. laser) is directed on a transparent material. As light transverse through the material, most of the photons are elastically scattered (Rayleigh Scattering) in which case incident photons and scattered photons have the same energy. Contrary, a small portion of the photons are observed to scatter with an energy level that can be higher or lower than the incident photons. This change in the energy level and correlated change in frequency of the photons can be detected and isolated from Rayleigh Scattered photons. Resulting frequency shift (Raman Shift) provides a structural fingerprint for MUT by which unknown specimens can be identified. Further, analysis and comparison of characteristic vibrational modes of a material can provide important insight into lattice defects and impurities of a sample.

Most of the work on G's Raman spectra focuses on CVD fabricated or ST exfoliated samples with single to few layer thickness. Based on literature review, Raman spectra of an ideal G film has five characteristic peaks, D-mode (1350 cm^{-1}), G-mode (1583 cm^{-1}), D'-mode (1620 cm^{-1}), 2D-mode ($\sim 2680 \text{ cm}^{-1}$), and D+D'-mode (2947 cm^{-1}) (Das, Chakraborty & Sood, 2008). Note that center of these modes can change depending on excitation laser

wavelength and substrate on which G sheet deposited. Presence of both G-mode and 2D-mode at specified wavelengths is specific for G and commonly used to identify graphitic materials. D and D+D' modes are caused by disorder in sp² lattice structure of G. Open bonds at the edge of a G sheet also contributes to D-mode. D'-mode is sensitive to surface impurities. Since pristine G should be defect free, presence of D'-mode means that synthesis process is damaging to the basal plane. Determination of G sheet layer count is traditionally done by assessing I_{2D}/I_G ratio, 2D-mode wavelength, and component study of 2D-mode.

Differentiation of single layer G sheet from Gr is a simple task. Single layer G sheets exhibit strong 2D-mode where I_{2D}/I_G ratio can be between 2 to 5. On the other hand, I_{2D}/I_G ratio for Gr is usually around 0.5 or less (Das et al., 2008). Identification of layer numbers between single G to Gr can be a lot more complicated. As expected, I_{2D}/I_G ratio decreases according to number of layers. On the other hand, ratio differs depending on referenced literature. It is also observed that 2D-mode center shifts from 2680 cm⁻¹ beyond 2700 cm⁻¹. Exact start and end points of this shift can change up to 8 cm⁻¹ depending on experimental setup. Due to variations in I_{2D}/I_G ratio and 2D-mode center between available literature, it is a good practice to compare data in its own set instead of among different sources.

CVD fabricated and ST exfoliated samples are ideal cases for Raman spectra analysis. Both methods produce samples with low basal plane defects, free of impurities, and controllable layer count. Another aspect of samples produced by these methods is the fact that they do not have exfoliated yet stacked sheets. In the case of LPE-G, related deposition methods, most commonly drop casting, do not focus on ability of placing a single sheet at a specific position. Instead, unknown number of exfoliated sheets are allowed to self-assemble on a surface as solvent evaporates. In most cases, previously exfoliated sheets will stack on each other and impact perceived Raman spectra of the sample. Hence, it is crucial to review the literature carefully in order to accurately interpret Raman spectra of LPE-G samples that are deposited by drop casting.

It has been shown numerous times that 2D-mode of G red shifts with increasing layer count (Das et al., 2008; Ferrari, 2007; Ferrari & Basko, 2013). It was also shown by Ni, Wang, Yu, & Shen (2008) that if a single layer G film is folded, 2D-mode red shifts to approximate location of a 2D-mode for bilayer sheet without reduction in I_{2D}/I_G ratio unlike in the case of

higher layer number. This suggests that stacking and layer count do not impact I_{2D}/I_G ratio in the same way and if there are several sheets in a stack with varying layer counts, 2D-mode width would be widened.

The I_{2D}/I_G ratio is highly sensitive to stacking. On the contrary, red shift due to increasing layer count is observed to be universal for every G sample analyzed in the literature. Literature review has also revealed that components of 2D-mode for single, bilayer, few layer G, and Graphite (Gr) exhibit a similar trend where lower frequency components lose intensity as layer count is reduced. Hence, through comparison of high and low frequency components' intensity ratios among separate ink samples, it is possible to assess exfoliation performance. In addition, component pattern of 2D-modes can be compared to available literature to approximate layer number for each ink sample.

Raman spectrum of RM, A24, A8C3, A8C1, A4C3, and A4C1 samples are shown in Figure 3.4. Raman data was collected from four different locations on each sample. Raman spectra from different locations were not significantly different from each other. Hence, one reading for each sample was chosen and analyzed, instead of using an average of four measurements. It was also possible to locate a very faint sheet of about 1 μm lateral dimensions (A24-Thin). This sheet was characterized to be compared to other samples. A small D'-mode was evident for A24-Thin sample. Furthermore, a very small D'-mode signal was also observed for rest of the samples. Limited presence of D'-mode in Raman spectra suggests that proposed synthesis method does not cause extensive damage to the basal plane. Increase in D-mode intensity is an expected result of any LPE process. As lateral dimensions of sheets decrease due to ongoing exfoliation, edge-to-basal plane ratio shifts in favor of edges, which contributes to D-mode. I_{2D}/I_G ratio was around 0.35 to 0.5 for all samples except for A24-Thin and did not differ from RM. This ratio would normally indicate Gr rather than G. On the other hand, it is clear from general shape of 2D modes of RM and exfoliated samples that ink processing caused relative blue shift. This indicates generation of thinner sheets. A24-Thin had a I_{2D}/I_G ratio of 0.9 indicating a much thinner sheet although not in the ratio range expected of bilayer or single layer CVD-G sheets. Such discrepancies for LPE synthesized G have been observed in other studies as well (Hernandez et al., 2008; Paton et al., 2014). The I_{2D}/I_G ratio and 2D-mode wavelength are sensitive to stacking of G sheets and give better result for CVD-G or mechanically isolated sheets. Drop casted G films can suffer from stacking of sheets

which may skew Raman spectra and cause it to resemble Gr. As a result, it was concluded that I_{2D}/I_G ratio was not a reliable method for determining layer count due to non-ideal sheet assembly on substrates.

Components of 2D-modes for each sample was analyzed to compare exfoliation performance between synthesis protocols. First, 2-component curves were generated using Lorentzian method. Generation of 2-component elements in Lorentzian is the standard practice for analysis of the 2D-mode and it allows for easy comparison of its high and low frequency contributors. A clear trend was observed for longer sonication times (Fig. 3.5). In agreement with available literature, RM has the 2D-mode components typical of Gr. A4C3 and A4C1 samples had similar 2D-mode components which suggests 3 to 6-layer sheets (Zeng et al., 2015). This is in agreement with TEM images where large clumped G sheets were observed for all A4 samples.

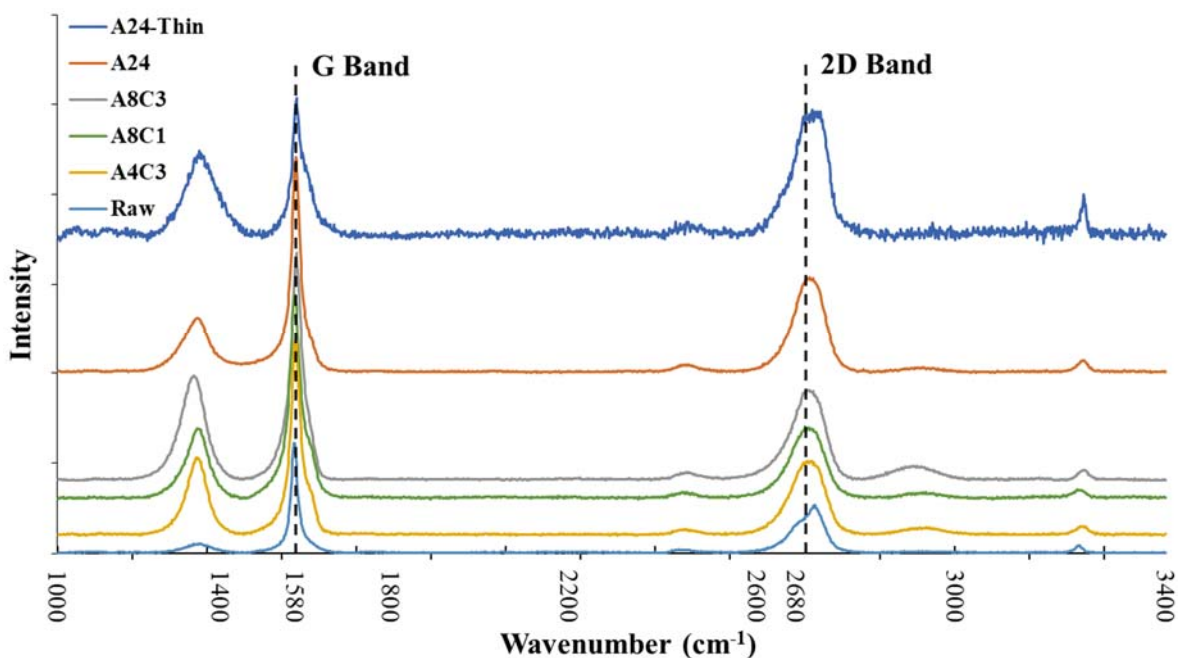


Figure 3.4 Raman spectra of select ink samples and raw material. Exfoliation is evident from Raman spectra of exfoliated sheets. Though, determination of layer count requires careful analysis of 2D-mode (Sinar & Knopf, 2018b).

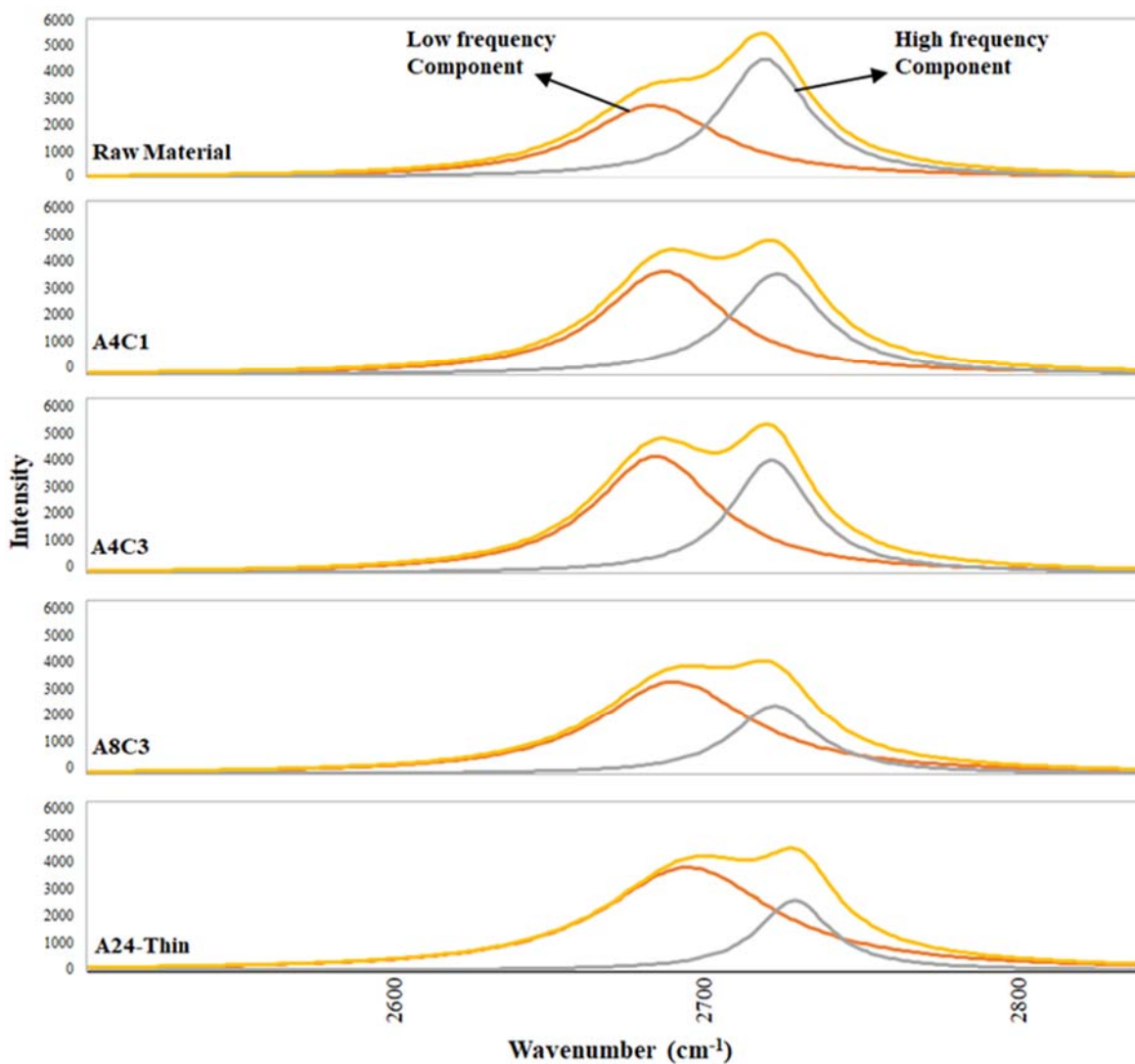


Figure 3.5 2-Component analysis of 2D-mode shows a clear trend for exfoliation performance of different protocols. For better exfoliated samples (A8C3 and A24-Thin), high frequency component is emphasized compared to stronger low frequency peak of raw material and A4 samples. Due to insufficient exfoliation during 4-hour sonication protocol of A4 samples, these inks were not included in the inkjet printing step (Sinar & Knopf, 2018b).

Based on this, it can be concluded that 4 hours is not enough for efficient exfoliation of G sheets and these ink samples were not included in inkjet printing step (Discussed in Chapter 4). 2D-mode components of A8C3 and A24-thin samples were identical. According to the 2-component fitting, A8C3 and A24-Thin samples can be either 2 or 3 layers. Layer count of these samples were further investigated by applying a 4-component analysis. Based on 4-component fitting both samples have 2D-mode components typical of bilayer sheets

(Fig. 3.6). Wider 2D-mode of A8C3 can be explained by the higher number of stacked sheets in the measurement area. Wider 2D-mode of A8C3 also means that some of the stacked sheets have more than 2 layers per sheet.

3.2 Graphene Oxide

Graphene Oxide is electrically insulating. Yet, thermal and chemical methods can be utilized to convert deposited GO films into conductive rGO. Although rGO is not as conductive as pristine G, ability to accurately tune the electrical resistivity of the rGO films by controlling the degree oxygen reduction through precision heating represents a novel method for fabricating a large variety of electrical components. It is known that carbon-to-oxygen ratio of GO or rGO samples are related to electrical properties where a higher ratio corresponds to stronger reduction and higher conductivity. In addition, the formation of rGO by removing oxygen molecules from the film is analogous to hole doping pristine graphene sheets. Prior chemical and electrical analysis has also shown that the energy band gap of rGO film is directly related to the level of oxygen content (Acik & Chabal, 2013). This observation supports the notion that controlled reduction of GO may allow adjustment of both conductivity and band gap energy of deposited films to create resistors or semiconductor components.

Wei et al. (2010) introduced a thermochemical nanolithography method to tune both the surface topographical and electrical properties of rGO film at a nanoscale resolution by performing local thermal reduction using a heated tip from an atomic force microscope (AFM). The thermal reduction of GO occurred using a heated AFM tip at 330°C and enabled tuning the current-voltage (I-V) characteristics of the reduced film. The authors also demonstrated that the rGO regions formed in this manner are up to four orders of magnitude more conductive than pristine GO. In addition, the researchers demonstrated that the rGO film had a transport gap greater than 0.5 eV at room temperature and, therefore, would behave like a semiconductor when appropriately reduced. The rGO film resembles the two-dimensional sheet structure of graphene but contains some residual oxygen and structural defects. These residual defects introduce electrical resistance and exhibits conductivity characteristics similar to doped conductive polymers (Wei et al., 2010).

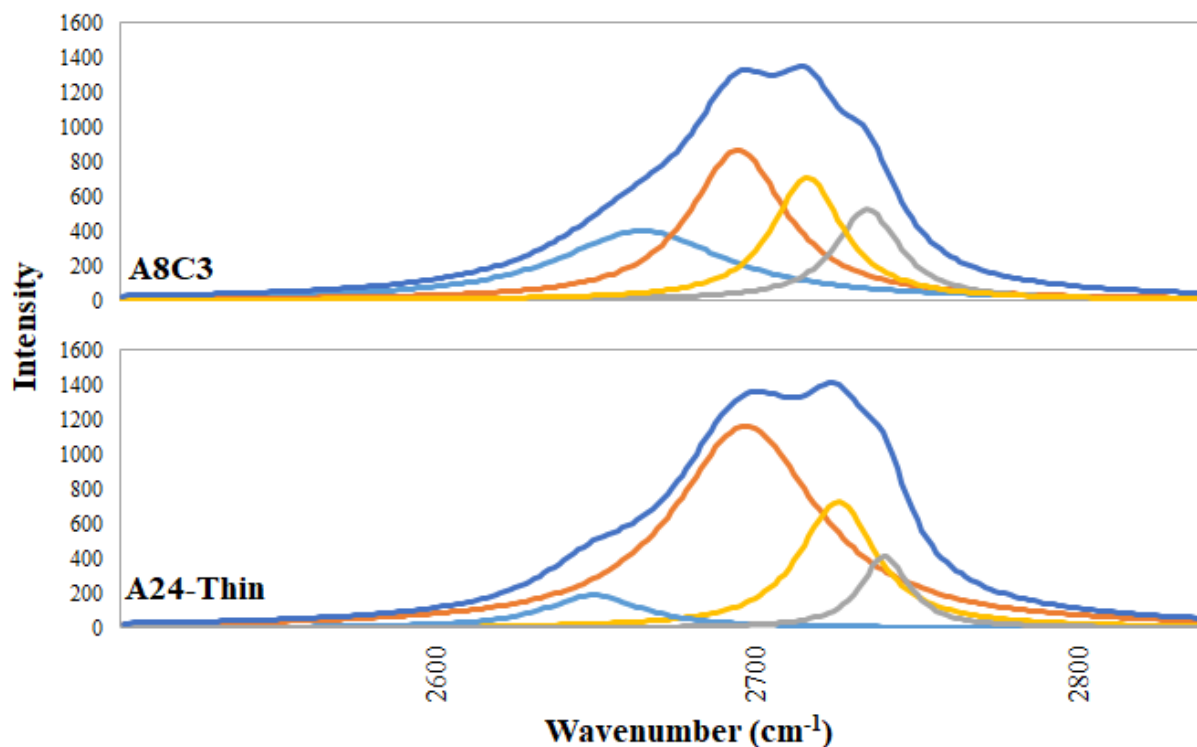


Figure 3.6 Both A8C3 and A24-Thin samples exhibited characteristic 4 components of bilayer G sheets (Sinar & Knopf, 2018b).

As mentioned in Section 2.1, GO can be easily synthesized directly from inexpensive graphite powders through the original procedure by Hummers & Offeman (1958) and its extensions (Becerril et al., 2008; Marcano et al., 2010). GO synthesis process is well established and highly controlled. Due to high demand, dry GO powder and its water based dispersion can be acquired for low cost. Hence, GO powder from Graphene Supermarket was used to prepare printable dispersions for this research.

3.2.1 Preparation of Aqueous Graphene Oxide Dispersion

Graphene Oxide is hydrophilic (Boukhvalov & Katsnelson, 2008) because of the oxygen functional groups (mainly as hydroxyl and carbonyl groups) located on the surface of the graphene sheets. Thus, additional solvent or surfactants are not necessary to ensure stability of a GO dispersion. On the other hand, printability of the dispersion can be improved with additional processing steps.

For a printable ink, it is necessary to ensure that the physical dimensions of the GO particles are sufficiently small so that they do not block the nozzle of the inkjet printer head. Several techniques have been described in the literature to reduce the size of the GO sheets (flakes). The simplest approaches use mechanical methods include ball milling, centrifuging or sieving to remove larger particles from the bulk material. Thermal shock and ultrasonication have also been explored as mechanisms to control the particle size. Chang et al. (2011) observed that superheating GO dispersion in an autoclave for 20 min at 120°C can reduce particle size down to $< 0.2 \mu\text{m}$. The researchers also showed that the heat required for this process was insufficient to reduce the oxygen and, therefore, the electrical properties of the original GO flakes were retained.

Chemical methods involving acids or polymers, such polyethylene glycol (PEG), have also been used to break-up the GO particles. PEG molecules have an affinity for water and readily attaches itself on the oxygen functional groups of GO. Once the PEG and GO are attached, sonication is used to break the GO sheets into smaller particles. As it is reported by Dua et al. (2010) PEG can be used to have a finer GO dispersion appropriate for inkjet printing. Alternatively, Sun and his colleagues were able to reduce the GO particle size between 20 – 50 nm range by using chloroacetic acid followed by sonication to activate epoxide and ester groups on GO particles, and to convert hydroxyl groups to carboxylic acid moieties allowing more sites to be available for PEGylation (Sun et al., 2008). In this research, a multi-arm PEG-Amine with very long chain was used. This type of PEG is rather expensive and not found to be a feasible option for mass manufacturing. Once broken into small particles, the dry GO is dispersed in an appropriate solvent. Water based inks are often required for thermal bubble actuated inkjet printers. Since graphene-oxide (GO) has a high affinity for water molecules it is possible to obtain a homogenous dispersion within deionized (DI) water without the need for any surfactants or additional solvents. Le, Ervin, Qiu, Fuchs, & Lee (2011) have shown that that GO ink made of simple dispersion of GO (2 mg GO per ml density) in DI water have a viscosity and surface tension of 1.06 mPa s and 68 mN/m, respectively. These values are similar to pure DI water (0.99 mPa s and 72 mN/m).

Although reduction of particle size is beneficial for sustained inkjet printing, excessively small particles commonly produce low performance films due to increasing number of sheet-to-sheet contact resistance. Hence, only mild bath sonication based methods

were employed during this research. For the preliminary experiments, the GO dispersion is prepared using 120 mg of GO per 15 mL of DI water followed by sonication for 0.5 h. Further, the dispersion is slightly diluted (up to 30 ml) to compensate for water losses during autoclave process. The diluted dispersion is autoclaved at 120°C for 15 min and then removed from the autoclave and allowed to cool down. Once the dispersion dries, any additional time the GO remains heated at elevated temperatures will cause oxygen reduction and the formation of rGO. After the cool down period, 0.2 mL PEG 400 is added to the dispersion. The sample is then sonicated for 20 min centrifuged at 6000 rpm for 15 min to remove large exfoliated particles. The remaining GO dispersion is filtered using a syringe filter of 0.45 μm pore size. The collected sample is then further sonicated for 15 min and injected into a cleaned printer cartridge.

3.3 Synthesis of Doped and Composite G-CMC Dispersions

Among carbon nanomaterials, pristine G thin films represent a good alternative to ITO films. Yet, even though G thin films fabricated by the CVD process represent the highest quality graphene films, these films tend to have significantly higher sheet resistances when compared to mechanically exfoliated G samples (Scotch Tape Method). During its early stages, G films fabricated by CVD method had high sheet resistance values in the order of $\text{k}\Omega$ per sq (Kasry et al., 2010). Recently, depending on the process parameters, a sheet resistance in the range of 700 to 350 Ω/sq can be expected from G samples. This is about 10 folds higher than ITO films of equivalent optical transmittance. Hence, effect of various dopants on G films have already been investigated to improve electrical performance of CVD-G. On the other hand, inkjet printed films universally perform worse than CVD-G films. Since, sheet-to-sheet contact resistance in an inkjet printed film cannot be eliminated by conventional methods, doping based alternative methods have been developed. As mentioned in Chapter 2, G's high conductivity is due to lack of major scattering in plane and not primarily due to large number of available free carriers – as is in the case of metals. This means that an increase in free carriers may result in higher conductivity even for inkjet printed films. In this section, two different routes employed in this research for increasing G film's free carriers are discussed; elemental doping and G/Nanoprism composites.

3.3.1 Elemental Doping of Films by Self-Assembly

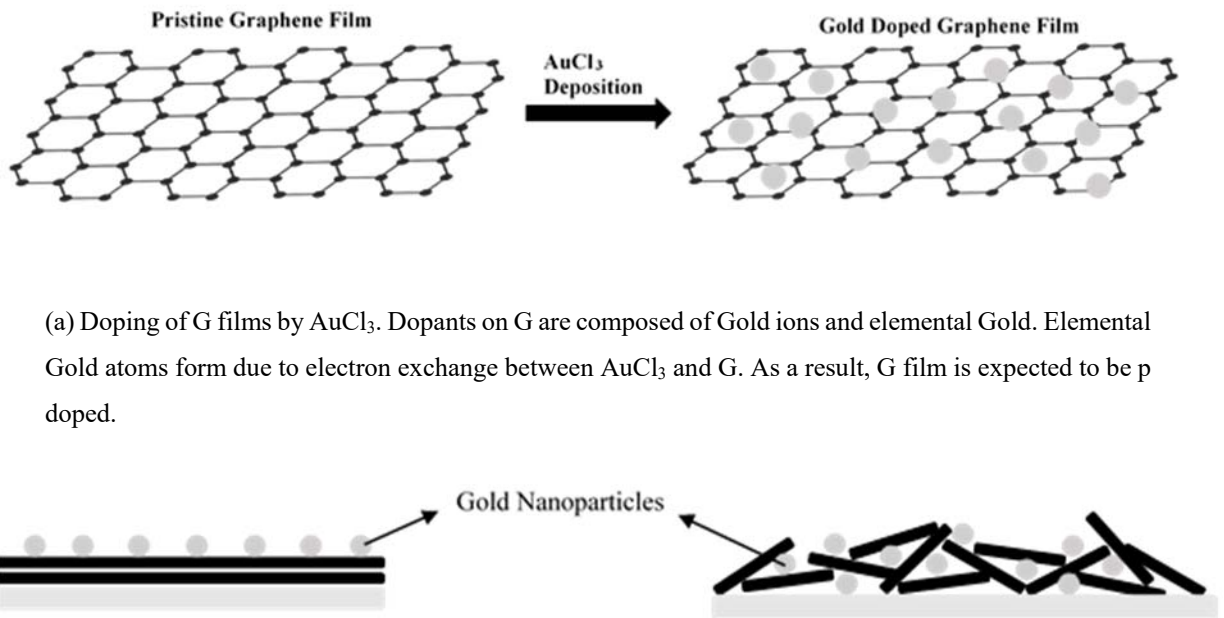
Graphene sheets can be doped with foreign atoms to increase available free carriers and improve electrical conductivity. Research has shown that after doping with either gold chloride (AuCl_3) or nitric acid (HNO_3), CVD grown graphene films were shown to be comparable to ITO films in terms of electrical conductivity and optical transparency (Kim, Reina, et al., 2010; Gunes et al., 2010). Doping through deposition of surface impurities (such as gold) on film surfaces is different than bulk deposition methods where inclusions or exclusions in lattice take place. Surface impurity doping is a non-destructive doping that does not change chemical structure of the material. Yet, due to electron transfer between the material and the dopant, electrical properties of the film changes. Various examples of surface impurity doping have been demonstrated during the last couple decades (Chen, Qi, Gao, & Wee, 2009; Ristein, 2006; Strobel, Riedel, Ristein, & Ley, 2004).

Doping of CVD grown G (CVD-G) with gold was investigated by Gunes et al. (2010) and results indicate that both top layer and layer-by-layer doping schemes can increase conductivity of CVD-G. Doping tends to have a diminishing return pattern as it was observed that layer-by-layer doping had only marginal improvement over top layer only doping. This is likely due to increased scattering from excess number of foreign atoms on G surface. Although promising, equipment and operational cost of CVD process and its inherently inflexible nature makes it a doubtful replacement for ITO process. But, it shows that under right conditions, high performance can be achieved with G. Although doping of CVD-G is a frequently visited subject, doping of inkjet printed G films has not been studied as often.

To investigate if doping with gold could result in similar performance improvements with injected printed films, G-CMC samples were prepared by the synthesis method explained in Section 3.1.1. A dopant solution was prepared by dissolving AuCl_3 in DI water at a concentration of 20 mM. AuCl_3 was chosen as an appropriate dopant for this study due to observed higher stability of doped samples, water solubility of the salt, and non-reactive properties of its solution. Gold is an electronegative element. When deposited on G film, gold ions receive electrons. As a result, G films are expected to p-doped when AuCl_3 is deposited (Pinto & Markevich, 2014). Also, due to charge transfer from G, elemental Au particles will form on film surface which increases carrier concentration of the film. As mentioned earlier,

surface absorbed dopants increase scattering and lower charge mobility with increasing doping concentration. To avoid excessive doping, doping time was limited. Samples were dipped in dopant solution for 30 minutes after annealing at 320°C, 420°C, or 540°C. Next, samples were removed from dopant solution and gently washed with DI water prior drying under forced air.

Different from CVD fabricated films which are spin coated a known amount of dopant, dipping samples allow self-assembly of gold atoms on film surface. As a result, there is less control over the magnitude of doping. Also, it is expected that this process will not result in an ordered top layer doping but a random surface adsorption and limited diffusion into deeper layers. Lack of diffusion for CVD-G is due to G's impermeable structure, which is not the case for inject printed films (Figs. 3.7a and 3.7b).



(a) Doping of G films by AuCl_3 . Dopants on G are composed of Gold ions and elemental Gold. Elemental Gold atoms form due to electron exchange between AuCl_3 and G. As a result, G film is expected to be p doped.

(b) CVD grown G is expected to have a uniform top layer doping structure (left). In comparison, inkjet printed G and Gold dopant will form a random mix of surface doping and limited diffusion (right).

Figure 3.7 Effect of different approaches to doping graphene films with AuCl_3 (Sinar et al., 2016).

Once annealing and doping steps were completed, all samples were characterized in terms of electrical and optical performance. For electrical performance, the sheet resistance of 40×1 mm electrodes was measured using 4-probe method. Optical transparency of doped and non-doped samples was measured and compared. Characterization data is presented in Chapter 4.

3.3.2 Dispersions Based on G-CMC/Silver Nanoprisms

During elemental doping, foreign atoms are randomly deposited along G sheet surface. Since deposited gold atoms are surface absorbents, excess number of atoms can negatively impact carrier mobility, which results in diminished return in electrical conductivity improvement. It has been suggested that G/Nanoparticle composites can circumvent this issue. Unlike elemental doping, the composite ink allows mixing of two nanoparticles at any desired ratio and is not expected to increase surface scattering any more than elemental doping. On the other hand, during this research, addition of silver spherical nanoparticles did not improve electrical conductivity more than that of AuCl_3 based elemental doping.

Silver Nanoprisms (AgNPs) are metal planar nanoparticles. Unlike spherical nanoparticles, a mixture of G-CMC and AgNPs may result in a composite ink where there is large area contact between AgNPs and G sheets (Fig. 3.8). Thus, it can be speculated that G-AgNP composite ink may allow deposition of higher conductivity thin films than otherwise would be possible with spherical nanoparticles. Moreover, triangular shape and large aspect ratio of AgNPs result in unique optical properties. UV/VIS spectra of AgNPs exhibit two prominent peaks corresponding to their thickness and edge length; transverse plasmon peak and longitudinal peak (Fig. 3.9). Transverse plasmon peak has been observed to occur around 330 nm wavelength and does not exhibit significant shift with increasing nanoprism thickness. On the contrary, longitudinal plasmon peak experiences significant shifts based on effective edge length. Effective edge length is defined as the straight edge that connect one corner to another. Since nanoprisms can experience truncation or rounding of the corners, effective edge length does not correspond directly to the lateral dimensions of the particle. In fact, if corners are extremely rounded, nanoprisms resemble a disc instead of a triangle and longitudinal plasmon peak is observed to blue shift significantly. This blue shift due to diminished effective

edge length is discussed in detail later in Chapter 4. If corners are well defined and effective edge length is large, it can be possible to push longitudinal plasmon peak beyond 750 nm. Hence, nanoprisms can be synthesized to absorb very little light in visible spectrum while contributing to enhanced conductivity.

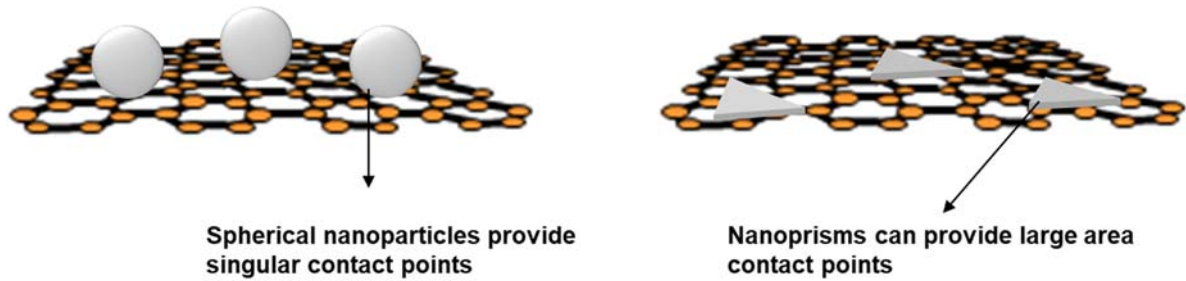


Figure 3.8 Synthesis of AgNPs start with reduction of silver nitrate salt. Presence of sodium citrate and etching effect of hydrogen peroxide forces elemental silver to assemble in a prismatic form (Sinar, Knopf, & Nikumb, 2017).

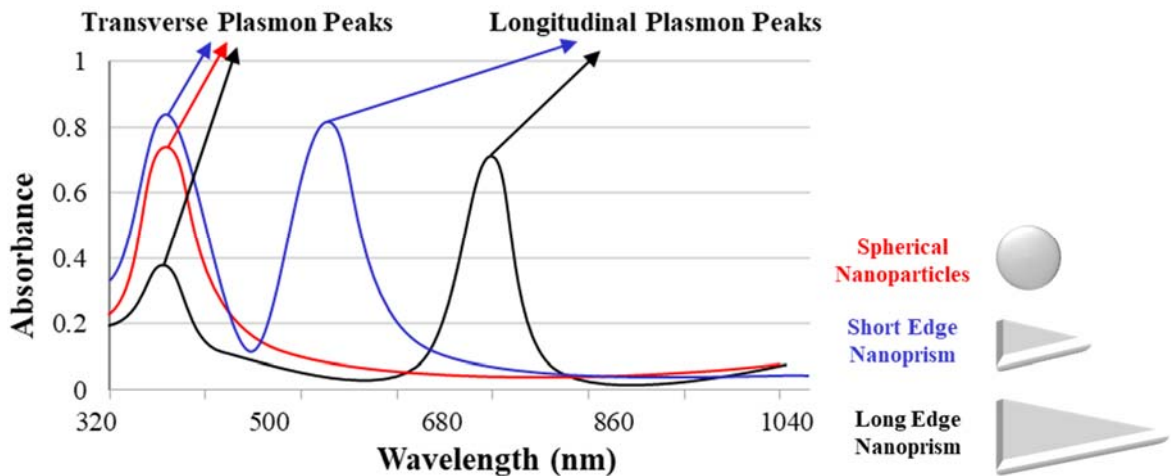


Figure 3.9 Typical UV-VIS spectra of AgNPs. Transverse plasmon peak intensity can change depending on nanoprism thickness, yet a significant shift on wavelength is not observed. On the other hand, longitudinal plasmon peak red shifts with increasing effective edge length (Sinar et al., 2017).

To investigate effect of AgNPs on inkjet printed G-CMC thin films, a composite ink was prepared (G-AgNP). G-CMC ink was prepared as detailed in Section 3.1.1. Silver nanoprisms were synthesized with a modified method based on the original study by Métraux & Mirkin (2005). Original method and its variations have been studied intensively (Zeng et al., 2010; Zhang, Li, Goebel, Lu, & Yin, 2011). For this research, the original method was modified to yield slightly larger nanoprisms in one step. In a regular synthesis 50 μL AgNO_3 (Silver nitrate, 100 mM), 50 μL $\text{Na}_3\text{C}_6\text{H}_5\text{O}_7$ (Trisodium citrate dihydrate - TCD, 750 mM), 50 μL Poly(vinylpyrrolidone) (PVP, 29000 Mw, 35 mM), and 60 μL H_2O_2 (Hydrogen peroxide, 30%) were mixed in 200 mL DI water at room temperature. Finally, ice cold 60 μL Na_4BH_4 (Sodium borohydride, 500 mM) was added to the mixture to start the reaction. In about 30 minutes, the solution changes colors to red, black, purple, and blue in quick successions, which indicate formation of nanoprisms. At this stage, additional 10 μL TCD, 10 μL PVP, and 30 μL Hydrogen Peroxide was added to the solution. It was quickly observed that the solution color changes to a light purple color in 5 minutes indicating the red shift and increase in effective edge length.

The main reaction for synthesizing AgNPs happens in two steps. The first step is the reduction of silver salt into elemental silver by the action of Sodium Borohydride. Resulting elemental silver nanoparticles are stabilized by Sodium Borohydride. Hence, they do not reassemble into larger particles and agglomerate. In the second step, nucleation of silver happens. Hydrogen peroxide is crucial for formation of nanoprisms. Silver nanoparticles are etched by hydrogen peroxide and self-assemble guided by selective absorption of capping agents on silver faces. Sodium citrate ions are preferably absorbed on twin $\{111\}$ planes of silver nanoparticles while PVP absorbs on the edges which causes in thin, triangular shaped nanoparticles to form (Fig. 3.10).

Based on TEM analysis, synthesized AgNPs have an aspect ratio of 7 to 25, effective edge length of up to 100 nm, and a uniform thickness of approximately 4 nm. Corners of AgNPs were robust with little truncation and only slight rounding of corners (Fig. 3.11). A small amount of the solution was removed for UV-VIS analysis. Spectrometer data shows the characteristic peaks at 330 nm and 850 nm (Fig. 3.12). The remaining mixture was centrifuged at high speed (45000 G for 15 minutes). Collected AgNPs were reconstituted in 25 mL DI water. It was observed that without free PVP in the solution, AgNPs start losing their geometry quickly as it was evident from their UV-VIS spectra. Hence, the centrifuge and wash were

done only once to remove by-products of silver nitrate reduction. Any free polymer left in the solution that would hinder conductivity is of no concern since PVP almost completely decomposes by 430°C along with CMC.

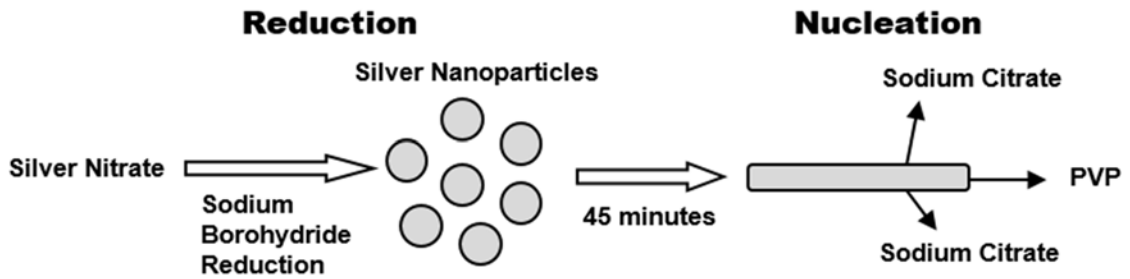


Figure 3.10 Synthesis of AgNPs start with reduction of silver nitrate salt. Presence of sodium citrate and etching effect of hydrogen peroxide forces elemental silver to assemble in a prismatic form (Sinar et al., 2017).

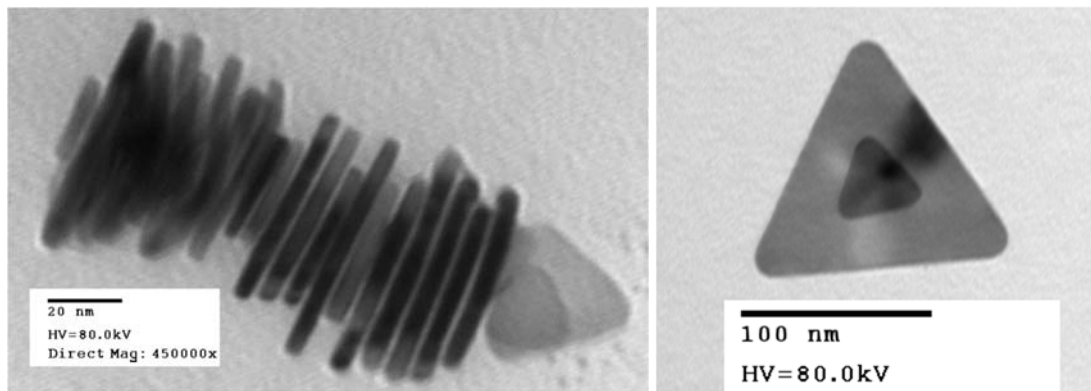


Figure 3.11 TEM Images of AgNPs synthesized with modified method. AgNPs have uniform thickness of ~4 nm. Sharp and robust corners contribute to red shift (Sinar et al., 2017).

3.4 Concluding Remarks

Synthesis of nondoped G-CMC dispersion and its modification through doping and metal nanoparticle addition was described in this chapter. G-CMC dispersion was synthesized using a bath sonicator as mechanical excitement source for layer-by-later exfoliation. There has been attempts at use of probe based sonication systems, yet results were not always satisfactory. Probe sonication had resulted in smaller particles with no significant increase in concentration. Bath sonication of G sheets in the presence of certain solvents was also investigated during the course of this project. It was observed that certain solvents (2-Butoxyethanol and Ethyl Diglyme) were susceptible to ultrasonic degradation which resulted in low performing inks. Bath sonication with a 1-Propanol/Water (50/50) mixture was also investigated. Although results were not included in this study, higher concentration and stable dispersions were achieved. Electrical performance of its thin films was also comparable.

Synthesized AgNPs have unique optical properties. On the other hand, edge truncation occurred with the composite G-AgNP ink caused significant blue shift. Exact reasons for this shift are not currently known. Future investigation into this subject could yield intriguing opportunities. If AgNPs can be tailored for a narrow bandwidth and mixed with G-CMC inks without edge deformation, transparent and semi-transparent conductive films with specific absorption bands can be inkjet printed on various surfaces.

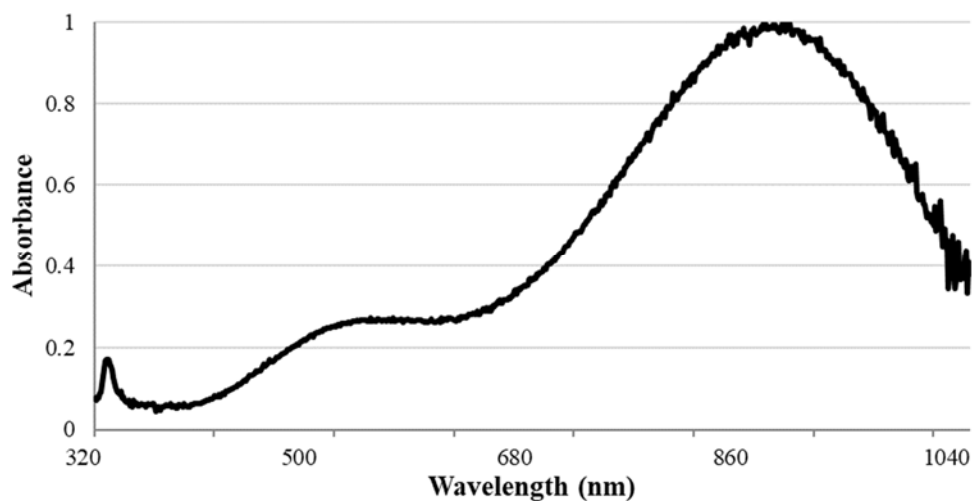


Figure 3.12 UV-VIS spectra of synthesized AgNPs. Due to long effective edge length, absorption in visible spectrum is minimal compared to absorption beyond 750 nm (Sinar et al., 2017).

Chapter 4

Thin Film Deposition of Graphene-Based Inks

4.1 Experimental Setup and Deposition Parameters

Liquid phase exfoliation (LPE) based preparation methods of either doped or non-doped G nanosheets allow large batch production of concentrated dispersions. Once a stable dispersion is established, suspended particles must be deposited on a viable surface to form a functional thin film. Although LPE process is the key step for fabrication of thin films, deposition process with inkjet printing presents its own unique set of challenges. In most cases, dispersion preparation step does not address these challenges and additional steps are necessary to ensure deposition of homogenous and robust thin films. In this chapter, custom built experimental inkjet printing setup, substrate treatment, preparation of inkjet printable inks, and post processing of fabricated films will be discussed.

Drop-on-demand deposition of thin films have been practiced in laboratory environment since early 1990s where either a metallic or polymer based dispersion was used (See Chapter 1). Once G was characterized, GO dispersions were inkjet printed on various substrates to be thermally or chemically reduced. Based on literature review, in most cases, inkjet printing equipment were simple office printers with or without CD/DVD tray capability. It is important to note that, in inkjet printing focused journal articles, difficulties at utilizing a commercial office printer for material deposition are usually neither discussed nor presented with required emphasis. This can lead to a false assumption that these printer units are viable fabrication equipment for critical research.

Prior to discussing the experimental DOD printer setup, it is beneficial to elaborate on shortcomings of commercial inkjet printers in terms of material deposition purposes. Entry level commercial office printers (COPs) can be roughly divided into two groups for the purposes of this study; paper feed COPs (P-COPs) and CD/DVD COPs (CD-COPs). P-COPs can be fed thin plastic sheets, such as polyimide, instead of paper to deposit functional materials on it. P-COPs cannot use rigid substrate since paper must be bend or rolled into the

paper feed mechanism. Regardless of paper feed route (front or back), once a pattern is printed, substrate goes through a series of rollers that are meant to keep paper in place (Fig 4.1). This can result in smudging of patterns or cross contamination from previous prints where trace amount of material could be left on rollers.

CD-COPs feature a CD/DVD tray (Fig. 4.2) that can load a rigid or flexible substrate of up to 2 mm thickness. This tray is usually front loaded into the printer where it is pulled in, printed on, and pushed back out. Although these printers allow rigid substrates, such as glass or silicon, to be printed on, they still use the paper feeding mechanism for controlling the tray, and rollers can get into contact with printed films. In addition, some printer models (such as Epson R2800) feature thin circular metal discs at paper feed entrance to push down plastic CD/DVD tray. During this research, severe scratching of films due to these metal pins was observed. Moreover, metal disc/thin film contact was not consistent, and any related issues occurred in a random fashion. Hence, it was possible to fabricate characterization worthy samples. Yet, rate of successful sample fabrication was low.



Figure 4.1 Paper feed mechanism of a Canon IP7220 inkjet printer. Office inkjet printers feature rollers to feed paper through and keep it in place during printing process. Regardless of feeding route, paper goes through rollers after inkjet printing.



Figure 4.2 Epson 2800 CD/DVD tray. CD/DVD trays allow use of both rigid and flexible substrates. Substrates must be fixed on the surface to avoid shifting during printing and keep flexible substrates from coming into contact with printhead.

Modern printhead technology can be regarded as the major roadblock at utilizing COPs for material deposition. As it was explained in Chapter 1, smallest feature that can be inkjet printed is determined by droplet size. For thermal printheads, a small nozzle diameter is the only way to reduce droplet size. Piezo printheads can deposit smaller droplets by manipulating driving signal, yet a smaller nozzle diameter is still needed to achieve droplets of few picolitres. Hence, in an attempt to improve printing resolution, manufacturers have been consistently reducing printhead nozzle diameters with each iteration of the technology. In 1990s, up to early 2000s, most printhead nozzles were around 60 to 80 μm diameter, on average. Current modern printheads can have nozzles between 20 to 40 μm diameter. In addition, depending on design, some printheads feature microfluidic channels to feed ink into the nozzle cavity. Size of these channels is currently unknown. Contaminants can accumulate in these channels or in the nozzle and interrupt printing process. Therefore, manufacturers universally employ cellulose or metal filters between ink reservoir and printhead. For printers that use dye inks, which are solutions, these filters are meant to retain all solids. For pigment loaded inks, filters are built to retain all but the smallest particles. Pigment based inks have suspended particles of less than 200 nm size. Considering larger G sheets are necessary for good electrical performance and most LPE-G exhibit 1-4 μm lateral dimensions, any attempt in printing G based inks fail if integrated

filters are intact. Removal of integrated filters usually involve destructive methods. For example, Epson R2800 filters are under plastic manifolds that are hot glue fixed into their positions (Fig. 4.3). To be able to remove these filters, manifolds must be either removed by heating up the glue or by breaking plastic manifold from its base. Regardless, due to small nozzle diameters, these printheads eventually fail. In this research, clogging of printheads have been a major challenge. Based on printhead model and related nozzle diameter, printheads were observed to clog between 100 to 400 prints.

Design philosophy of the custom printer focused on fulfilling following key requirements; contact free printing process, easy to access printhead with large nozzles, full control over droplet spacing and frequency, and stationary printhead/moving substrate arrangement. Although it can be thought as a daunting task, printers that can fulfill most of these needs have been built since 1960s. XY flatbed pen plotters, and later flatbed inkjet plotters, print patterns by moving the printhead (or pen) over a stationary substrate/paper. Since object to be printed on is stationary, there is no need for paper feeding mechanisms and rollers. A similar XY plotter setup can be built by using two linear stages and moving the substrate instead of the printhead.



Figure 4.3 Epson R2800 Printhead. Under the conical manifolds, there are thick cellulose filters to prevent contaminants from entering printhead assembly. To be able to use this printhead for inkjet print colloidal inks, cellulose filters must be removed.



Figure 4.4 C-Beam linear stages with NEMA 23 stepper motors (top). Linear stages can be fixed in 90-degree angle to each other to form an XY coordinate stage (bottom).

Two C-Beam linear stages were acquired from OpenBuilds with accompanying NEMA 23 stepper motors (1.8° Step Angle) (Fig. 4.4). Linear stages are driven by 8 mm acme lead screws (2 mm pitch, 8 mm lead). Two linear stages were fixed on each other in 90 degrees to complete the XY stage (Fig 4.4).

Stepper motors were driven by a pair of DQ542MA stepper motor drivers. Pulse and direction inputs to the stepper drivers were provided through an Arduino Uno connected a laptop. In order for the Arduino to communicate with stepper drivers, it was flashed with GRBL protocol. Finally, bCNC software was used to control the XY stage and run necessary gcode sequences for inkjet printing.

Quick access to printhead and full control over printing parameters require use of non-proprietary software and electronics. For this research, HP C6602 cartridge was chosen as the printhead since a third party driving circuit is available (Fig. 4.5). This cartridge has a relatively large nozzle diameter (60 μm) and large droplet volume (160 pl) which allows sustained printing without clogging. C6602 cartridge also has 12 nozzles that can be used as desired. To prep a cartridge for use, it was opened, ink sponge was removed, and whole printhead was thoroughly washed before bath sonication in DI water for 10 minutes. C6602 cartridge is designed for water based inks. Water based printer inks are composed of mainly water, pigments or dyes, and solvents/surfactants. Solvents or surfactants are usually added to improve wetting of the ink by reducing surface tension of water. Although there are innumerable variations to the formulation, expected composition of a water based ink is presented in Table 4.1.

Formulation of water based inks are usually done around the available equipment. In the case of inkjet printing, capabilities of the printhead cartridge determines the ink specifications. Since HP C6602 is water based thermal bubble printhead, viscosity requirements of the ink are expected to be in 1 to 5 cP range. Surface tension target value should be low to enable complete wetting on substrate. The relationship between surface

Table 4.1 Typical composition of water based printer inks (Seiko Epson Corp, 2004)

Component	Concentration Range (%)	Notes
Water	60 – 90	Main medium
Solvent	5 – 30	Viscosity control
Dye/Pigment	1 – 10	Coloring agent
Surfactants	0.1 – 10	Wetting promoter
Buffer	0.1 – 0.5	pH control
Other	~ 1	Crosslinking agent, lubricant

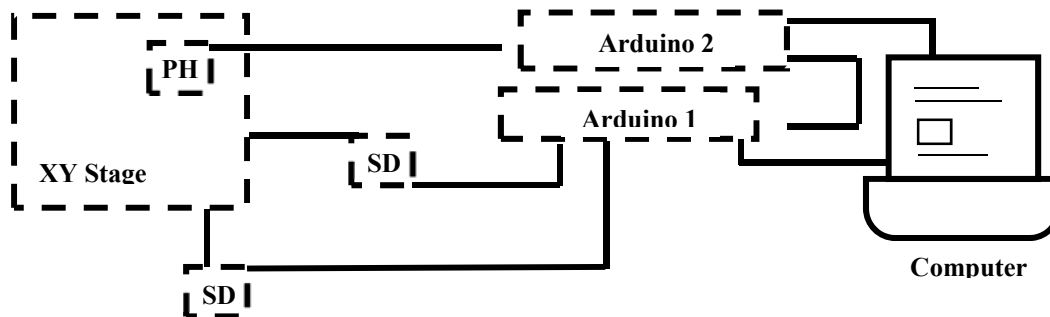
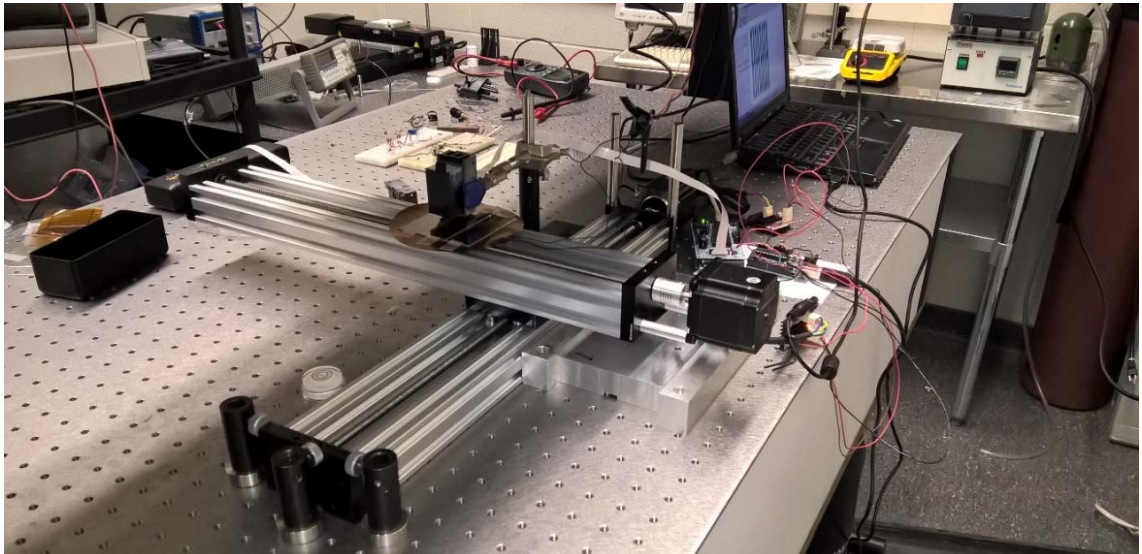
tension, viscosity, ink density and jettability was demonstrated by Jang, Kim, & Moon (2008). By using the proposed inverse Z of Ohnesorge number (Oh), one can calculate that a viscosity range of 1 to 5 cP and surface tension range of 25 to 35 mN/m would result in optimal printability. During the development of substrate treatment protocol (Section 4.2) and the formulation of printable G-CMC ink (Section 4.3), these requirements were taken into account.

This printer was set up as a single nozzle printer due to simplicity of necessary algorithm. Choice of nozzle and droplet frequency can be changed using Arduino IDE. It is a good practice to alternate between different nozzles as wear and tear can result in enlargement of already large nozzles. When this happens, uncontrolled leakage of ink through nozzles was observed. Droplet frequency must be chosen based on XY linear stage feedrate. During the course of this research, feedrate of Y linear stage was fixed to 4800 mm/min while X linear stage was fixed to 400 mm/min. Both linear stages were microstepped, although X linear stage had a more aggressive setup. To ensure precision, X linear stage step distance was set to 500 nm/step. Y linear stage step length was 2.5 $\mu\text{m}/\text{step}$. A more aggressive microstepping could also be used for Y linear stage. Yet, microstepping at high feedrate demands more torque than available NEMA 23 motors could provide. For the 4800 mm/min feedrate and 2.5 $\mu\text{m}/\text{step}$ setup, delay between each droplet was set to 2000 μs .



Figure 4.5 HP C6602 Printhead unit and carriage assembly (left). Inside of HP C6602 printhead (right). During this research, metal mesh filter was not removed as G-CMC sheets were small enough to pass through the filter without causing clogging.

Custom built system and a summary schematic of the experimental setup is presented in Figure 4.6. Communication between printhead and stepper motor drivers was established through a second Arduino board. An on/off signal, corresponding to the printhead, was produced when bCNC software executes a G01 code. This signal was picked up by the first Arduino and sent to the second one to be used as a variable in a “while” loop to enable/disable droplet jetting. All related codes and detailed wiring diagrams can be found in Appendix (A1).



**PH = Printhead; SD = Stepper Driver*

Figure 4.6 Experimental setup for custom XY plotter style printer. Printer was controlled through an Arduino Uno board. Designed circuits were translated into G-Code on the laptop (top). Summary schematic of experimental inkjet printing setup (bottom).

Due to large droplet volume of C6602 and non-absorbent substrates, deposited ink can take a few seconds to dry after each pass. Substrate heating methods have been commonly used for by MDSs such as Dimatix printers. On the other hand, radiating heat from substrate may cause ink to dry at the nozzle and clog it. Printer can be programmed to wait a predetermined number of seconds after each pass to allow ink evaporation. Yet, this method can substantially extend total printing time. An alternative method was used to upgrade system in Figure 4.6. Low pressure air was supplied from each side of the printhead by air blade outlets (Fig. 4.7). Through gentle air supply, ink was able to evaporate fast enough and the need for waiting time at the end of each pass was eliminated.

4.2 Substrate Treatment

In inkjet printing as a deposition method, jetted droplets land on a substrate (usually non-absorbent), spreads, and evaporates. During evaporation, suspended colloids self-assemble on substrate surface. Since it is impossible to directly control where each nanoparticle deposits on the substrate, film formation must be influenced indirectly. In this regard, surface treatment of substrates is critical.

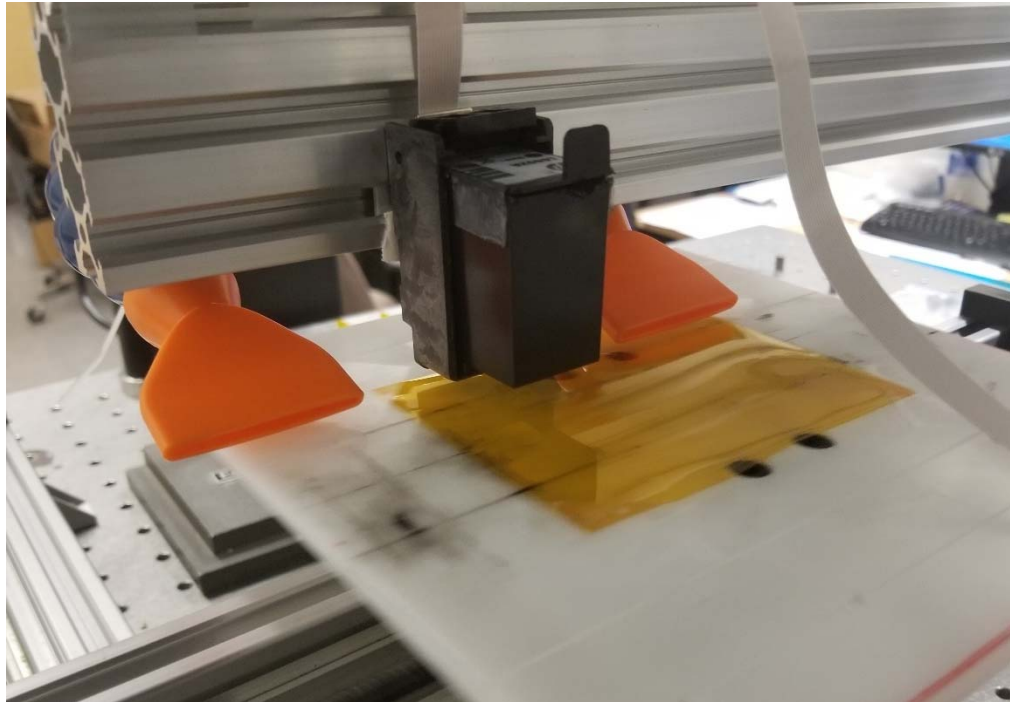


Figure 4.7 Low pressure air supply can facilitate quick evaporation of deposited ink.

There are two general routes for substrate surface treatment; hydrophobic or hydrophilic treatment. Hydrophobic treatments, such as hexamethyldisilazane (HMDS) treatment of glass and silicon substrates, create a water repelling surface by formation of methyl groups. Most flexible plastic substrates (e.g. PDMS, Kapton, and PET) are naturally hydrophobic, do not require further treatment, and can be used as is after thoroughly cleaned by various means. Due to limited spread, printed droplets can form very fine dots on printed surface. This phenomenon can be utilized to create features much smaller than inkjet printing equipment would otherwise allow. One of the early examples of this was demonstrated by van Osch, Perelaer, de Laat, & Schubert (2008). where silver conducting lines of 40 μm was inkjet printed on untreated plastic substrates. Nguyen, Yeo, Lok, & Lam (2014) further applied this method to inkjet print PEDOT/PSS films of 35 μm wide by forming hydrophilic, hydrophobic, and super-hydrophobic zones on the same substrate. On the other hand, investigated surface treatment requires a multistep approach to create desired surface energy pattern on the substrate. Surface energy pattern must match inkjet printing pattern which requires fabrication of a Ni mask. Need for a mask defeats the purpose of inkjet printed electronics as one of its strengths is its potential for fast prototyping without requiring custom mask designs.

Printing on a hydrophobic surface requires step size of the printer to be at least as small as dot diameter imprinted by jetted droplet. Another requirement for printing on hydrophobic surface is substrate heating. When substrate surface energy is much lower than ink surface tension, liquid-liquid attraction is stronger than solid-liquid attraction at ink-substrate interface. In such a case, deposited ink would recede until reaching a droplet-substrate contact angle that is thermodynamically stable. This would result in formation of disconnected dots. If droplet spacing is adjusted to be tight enough to avoid disconnected dots, it would mean deposition of a larger ink volume. This could result in broadening and consequent deformation of intended pattern. Due to presented limitations, heating of the substrate is a necessity. If the substrate is heated and droplet volume is sufficiently small, by the time a droplet is ejected, previous droplet will be evaporated on the surface. Thus, printed patterns will not experience deformation while retaining intended fine dimensions. Application of heat to a substrate can be a difficult task. To allow similar deposition characteristics all around, substrate temperature must be homogenous in deposition area. Only a few $^{\circ}\text{C}$ difference may result in surface energy gradients and negatively impact film formation. In addition, the temperature must be selected

carefully to avoid ink boiling on surface and droplet drying in nozzle due to emitted heat from substrate. Drying of ink in nozzle cavity is one of the two major reasons for a blocked printhead, other being nozzle blockage due to larger than ideal colloids in ink.

Alternatively, substrates can be treated to be hydrophilic. Hydrophilic surfaces have relatively high surface energy, thus can be wetted by water. To achieve highly hydrophilic surfaces, substrates must be thoroughly cleaned and treated by various means that include, but not limited to, oxygen plasma, UV/Ozone, chemical oxidizers, or corona stream. All these methods improve wettability by temporarily oxidizing substrate surface. When a water based liquid solution or suspension is placed on a treated substrate, surface OH functional sites interact with water molecules. Since solid-liquid interaction is strong relative to liquid-liquid interaction, liquid can spread and maintain a small angle (θ) at droplet-substrate interface. For a substrate to be considered wettable, θ angle must be less than 90 degrees. A perfect wetting condition occurs when θ is zero. When inkjet printing on a hydrophilic surface, disconnection between individual droplets is not a concern, unless droplet spacing is excessively large. On the other hand, deformation printing pattern can occur if droplets are allowed to spread uncontrollably. This would occur if θ is zero or close to zero. Hence, over treatment of substrates must be avoided. Deformation and over spread of patterns can also happen if too much ink is deposited. Since deposited liquid must maintain a small θ angle, when excess liquid is deposited, droplet will spread to compensate. This can result in budes, for example, on a straight electrode pattern. Yet, this can be easily corrected by reducing droplet volume or increasing droplet spacing.

In most cases, a surface treatment protocol starts with an Oxygen Plasma, UV/Ozone, oxidizing wet chemical (e.g. piranha solution), or corona process to clean the substrate and improve its wetting property. On the other hand, these processes do little to improve self-assembly of colloid particles. In fact, OH functional sites that develop on the treated surfaces are negatively charged, like the G-CMC particles in the proposed ink. Consequently, deposition of particles would be random. To promote better adhesion and orderly self-assembly, surfaces can be coated with certain charged molecules (Polyelectrolytes). Polyelectrolyte Coating (PEC) process involves deposition of oppositely charged polymers layer-by-layer to take advantage of a phenomenon called charge over-compensation. In a typical PEC process, a layer of positively charged polymer is deposited immediately following

a surface oxidizing process. If a negatively charged polymer is deposited on top of this layer, positive charge of the first polymer layer will be neutralized and a surplus of negatively charge on top surface will emerge due to charge over-compensation (Fig. 4.8). Depending on which polymer is coated last, a surface can be prepared to be either negatively or positively charged. Preparation parameters of coating solutions can affect thin film morphology. McAloney, Sinyor, Dudnik, & Goh (2001) demonstrated in his research that ionic strength of a solution impacts morphology and thickness of polyelectrolyte coatings. When a polyelectrolyte solution is prepared without salts, polymer strands tend to extend in a rod like shape as each unit (mer) of the polymer repel each other. As the ionic strength of a solution increases due to addition of salts, repulsive forces along chains of a polymer molecule become weaker. This leads to conformational changes on the polymer chain where a transition from rod-like to random coil form takes place. At sufficiently high ionic strength, polymer may completely collapse on itself and solution stability diminishes (Fig. 4.9). When a high ionic solution is used to deposit a polymer, random coil form allows for a denser immobilization on the surface. Hence, a thicker film can be achieved per coating step. On the other hand, it was shown that these thicker films have rougher morphologies and may have holes along the surface. McAloney had predicted that the conformational transition takes place at 0.2 M NaCl.

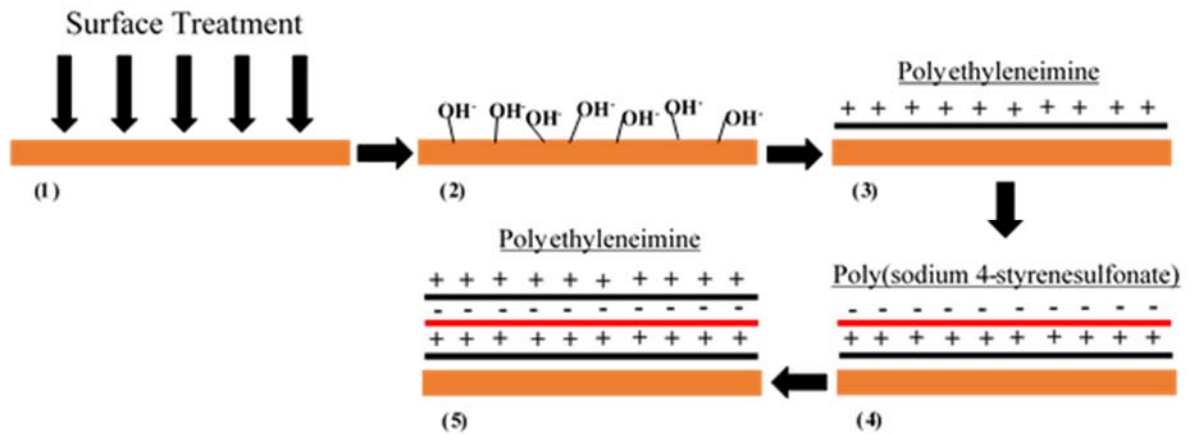


Figure 4.8 Polyelectrolyte coating process. Substrate is cleaned and treated to form negatively charged OH functional groups. Due to charge over compensation, there is a charge surplus after each polyelectrolyte deposition step (steps 3, 4, and 5).

In this study, all types of substrates were treated with the same protocol. Two aqueous polyelectrolyte solutions were prepared; negatively charged Polystyrene Sulfonate (PSS) (0.15 M NaCl, 7.5 mg/mL PSS) and positively charged Polyethyleneimine (PEI) (0.15 M NaCl, 8.1 mg/mL PEI - 50 wt% in water). Glass microscope slides were used for characterizing electrical and optical properties of printed films and flexible substrates (1-mil HN polyimide and PDMS) were used to investigate mechanical properties of deposited films. To prepare substrates for inkjet printing, substrates were cleaned with ethanol/water wash and dried with forced air. Clean substrates were treated with corona discharge for 1 min to improve wetting and form a negatively charged surface. The handheld corona device generates OH functional sites on the surface by ionization of surrounding air. Positively charged PEI solution was deposited first by submerging substrates into the solution for 20 minutes. After 20 minutes, substrates were removed from the PEI solution, briefly washed under DI water, dried under forced air, and submerged into the PSS solution for 20 minutes. The repeated coating process ensures complete coverage of substrate surface while forming a smooth positively charged upper layer. Substrate treatment protocol was not changed and applied in the same manner for each type of substrate.

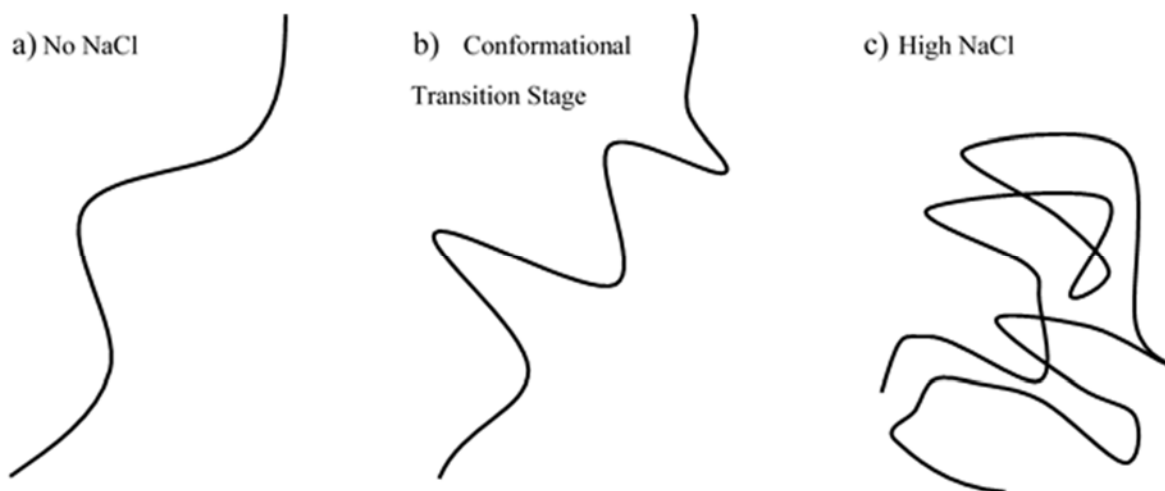


Figure 4.9 Conformational changes to a polymer strand can change its physical shape and properties. In a low ionic strength environment (no salt), polymer strands extend (a). Addition of salts masks opposing electrostatic charges on polymer subunits, which results in physical changes to polymer shape (b). If electrostatic charges are completely masked, polymer can collapse on itself and agglomerate (c).

4.3 Controlling Coffee Ring Effect During Drop-on-Demand Printing

When a colloidal ink is jetted on a hydrophilic substrate, it is often observed that colloid particles tend to deposit at the edges of droplets instead of forming a homogeneous film. Due to its resemblance to dried coffee stains, this phenomenon is commonly known as the coffee ring effect (CRE). Print deposition of colloidal inks form thin films in the form of random particulate networks. If CRE occurs, functional material is deposited at the edges instead of depositing homogeneously along printed pattern. Since electrical performance of such films is affected by efficiency of networking among constituent particles, to optimize electrical conductivity of deposited thin films, CRE must be addressed.

The coffee ring effect is a complex phenomenon where evaporation of a colloidal droplet is marked with edge heavy deposition of its particles. As it was stated by Deegan in his thesis, contact line pinning and evaporation are enough for coffee rings to develop (Fig. 4.10a) (Deegan, 1998). If a preceding condition is present, such as a high surface energy substrate or a low surface tension liquid, contact line will be temporarily pinned. Deposition of colloid particles on substrate surface causes the contact line to be permanently pinned. This means that droplet width will be constant during evaporation and angle θ will decrease. At this stage, evaporation at droplet edges is faster due to droplet geometry and evaporated volume must be resupplied by a flow from the center. This edge directed flow carries colloid particles and ultimately causes the coffee ring formation (Fig. 4.10b). Conversely, on hydrophobic surfaces where the contact line does not pin or is easily unpinned, edge directed flow is not necessary to preserve droplet width and angle θ will be constant during evaporation. Hence, formation of coffee rings is not observed. Deposition on hydrophobic surfaces result in receding/unpinned contact lines which would deform deposited patterns. Thus, deposition on hydrophobic surfaces is not a desirable solution and CRE must be addressed by a different approach.

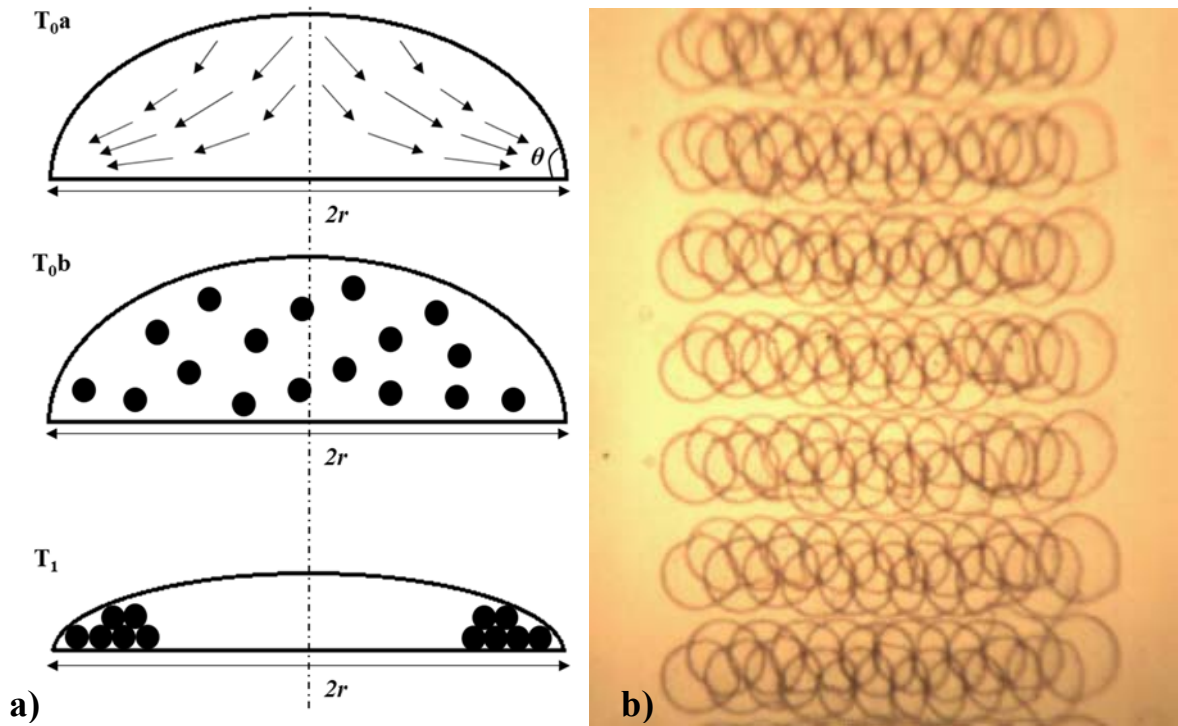


Figure 4.10 Marangoni flow (T_0a) and corresponding colloid movement (T_0b) inside a droplet at T_0 and T_1 (a). For a droplet with pinned contact lines, width ($2r$) does not change during evaporation. For larger θ , relative evaporation rate at the edges is larger than droplet center. Inkjet printing of solvent free aqueous inks on hydrophilic surfaces experience severe coffee ring effect (b) (Sinar & Knopf, 2018b).

Various methods have been investigated by researchers to develop a facile solution to CRE. Soltman & Subramanian (2008) demonstrated that strict control of printing parameters can substantially improve deposition quality of aqueous conductive polymer inks. On the other hand, the results of this work do not transfer well for non-polymer aqueous inks because inkjet printing of polymers can be a fundamentally different phenomenon. In a polymer solution, presence of entangling polymer chains means a network of polymers is being deposited, not individual particles which are constantly pushed away from each other by various means. Another method proposed by Yunker, Still, Lohr & Yodh (2011) involves control of geometrical shape of dispersed colloids. Yunker et al. (2011) have observed that unlike spherical colloids, ellipsoid colloids do not form coffee rings upon evaporation. Unfortunately, precise geometrical control of nanoparticles is impractical since necessary processes may be different for each material. In some cases, geometrical control may not even be possible. For

example, based on literature review, there has been no study to date on precise control of G sheet geometrical shape. Common batch processing methods, including LPE and Gr intercalation methods, are naturally random in their exfoliation of particles. Exfoliated sheets have been observed to be predominantly rectangular. Sheet dimensions exhibit a relationship between synthesis parameters only in a broad sense. As shown in Chapter 3, ultrasonication duration does affect sheet dimensions. Yet, in the same batch, sheet lateral dimensions can vary between 200 nm to 3 μm . Further refinements to dimensions require additional steps such as centrifuging and filtering.

A simple approach was proposed by Park & Moon (2006) where a binary solvent system was used to exploit surface tension difference between a low boiling point (LBP) and a high boiling point solvent (HBP). In a single solvent system, outward Marangoni flow is a consequence of constant droplet width. Outward flow is also mediated by cooling effect of solvent evaporation at the edges which generates a surface tension gradient across droplet. Hence, an outward dominant flow is common to all single solvent systems. Similarly, in a HBP/LBP binary solvent system, initial outward Marangoni flow in the droplet is initiated due to evaporation at the edges. Addition of an HBP solvent causes selective evaporation of LBP solvent at the edges. If HBP solvent has lower surface tension than the LBP solvent, resulting surface tension gradient introduces a second Marangoni flow in the opposite direction which in turn negates initial edge directed flow and disrupts formation of coffee rings (Fig. 4.11).

Surface tension forces that drive above mentioned flow can be related to the dimensionless Marangoni number (Ma) (Park & Moon, 2006);

$$Ma = -\frac{\Delta\gamma r}{\zeta\varphi} \quad (4.1)$$

where $\Delta\gamma$ is surface tension difference between solvents, r is droplet radius, ζ is viscosity, and φ is the diffusion coefficient for the solvent system. From (Eqn. 4.1), it can be deduced that for a large Marangoni flow, surface tension difference between HBP solvent and LBP solvent should be large while overall viscosity of the binary system should be low. In the context of this study, this would mean use of a low viscosity solvent with a higher boiling point and a lower surface tension value than of water. In addition, solvent must be miscible or highly soluble in water.

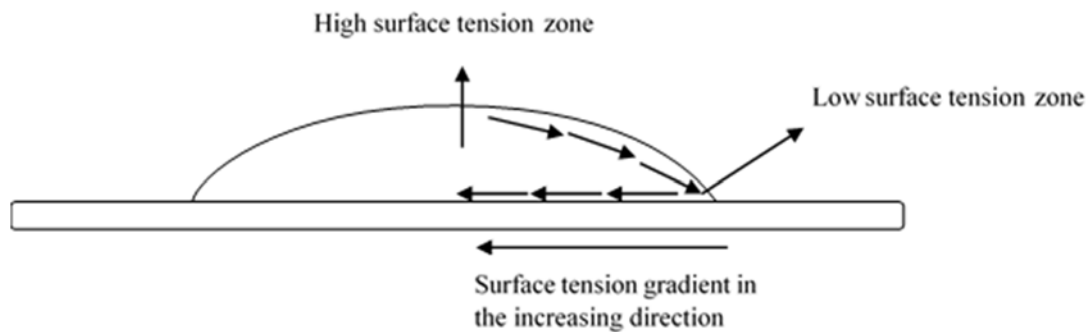


Figure 4.11 Reverse flow towards droplet center can carry dispersed particles and result in a more homogenous film formation. Dotted arrows show the direction of initial flow. Arrows inside the droplet show the reverse flow following the surface tension gradient.

During this research, it was observed that polyelectrolyte coating protocol discussed in Section 4.2 allows deposition of a homogeneous first layer without use of additional solvents or substrate heating. Inkjet printing of solvent free ink on treated and non-treated substrates clearly demonstrated impact of polyelectrolyte coating on thin film morphology (Fig. 4.12). Even though polyelectrolyte coating has no direct impact on Marangoni flow inside the droplet, electrostatic attraction between PEI (positively charged) and G-CMC (negatively charged) results in homogeneous self-assembly. In the lack of proper surface treatment, edge directed Marangoni flow hindered deposited films unusable (Fig. 4.12a). However, repeated inkjet printing using pure aqueous G-CMC ink, even on treated substrates, results in significant deterioration of film morphology as well (Fig. 4.12d). This deterioration happens due to changing surface properties and high surface tension of DI water. Initial substrate surface is clean, hydrophilic, and relatively smooth. Once an initial layer has been established, subsequent deposition happens on a rough surface which is harder to wet. Resultant, erratic spread of ink causes localized pools of ink, as well as displacement of previously deposited particles. A simple solution to this problem would be using a single low surface tension solvent system. Alternatively, mixing in a small amount of low surface tension solvent with water can provide enough wetting during deposition. This has been shown to result in films with good morphology (Park & Moon, 2006), if added solvent has a high boiling point.

Conversely, use of an LBP and low surface tension solvent in a water/solvent binary system has been traditionally associated with further exaggeration of CRE. At the droplet edge,

low boiling point solvent evaporates at a higher rate which results in a water rich region compared to the rest of the droplet. Resultant surface tension gradient contributes to already existing Marangoni flow. Due to this, HBP solvents are preferred in binary systems where water is the LBP component. Unfortunately, several HBP solvents are under scrutiny from Registration, Evaluation, Authorization, and Restriction of Chemicals (REACH) program in Europe. NMP, DMF, both used for LPE processes, and Formamide proposed by Park & Moon (2016) to eliminate CRE, are all categorized under Substances of Very High Concern (SVHC) and may soon be banned from import and use (ECHA, 2017).

It is proposed in this thesis that rate of change in surface tension of a binary solvent system is the determining factor for the magnitude of edge directed flow in a droplet, not the boiling point of its components. In fact, given that surface tension of the said binary solvent system is stable for a large range of its composition, an HBP solvent is not necessary to control coffee ring effect. To investigate viability of this approach, 1-Propanol/Water binary system was investigated. 1-Propanol is an environmentally friendly primary alcohol with low toxicity. It has a slightly lower boiling point than water (98°C). Compared to ideal liquid mixtures, 1-Propanol has a relatively flat region in its gas-liquid equilibrium near the azeotrope point. In fact, mass percentage of 1-Propanol in vapor is somewhat steady between 27 to 70 m% 1-Propanol mixtures. Moreover, surface tension of Water/1-Propanol mixture dips down to 27.84 mN/m at around 20 m% and does not change significantly up until 100 m% 1-Propanol (23.28 mN/m) (Vazquez, Alvarez, & Navaza, 1995). These have three important consequences for film formation. First, low surface tension means smaller angle θ and smaller difference in evaporation rates between the droplet center and edges. Second, flat region in 1-Propanol's gas-liquid equilibrium results in a linear evaporation. Finally, efficient suppression of surface tension at low m% leads to negligible surface tension gradient during evaporation. Figure 4.13 represents a case study where surface tension of two binary solvent droplets that evaporate predominantly from edge area is compared. Exponential increase in surface tension for Water/Methanol system means larger surface tension gradient between droplet center and edge. On the other hand, Water/1-Propanol shows subtle change in surface tension. Consequently, surface tension gradient and resulting Marangoni flow would be much less for Water/1-Propanol system. Thus, water/1-propanol binary system can reduce overall surface tension of an ink without inducing significant edge directed flow.

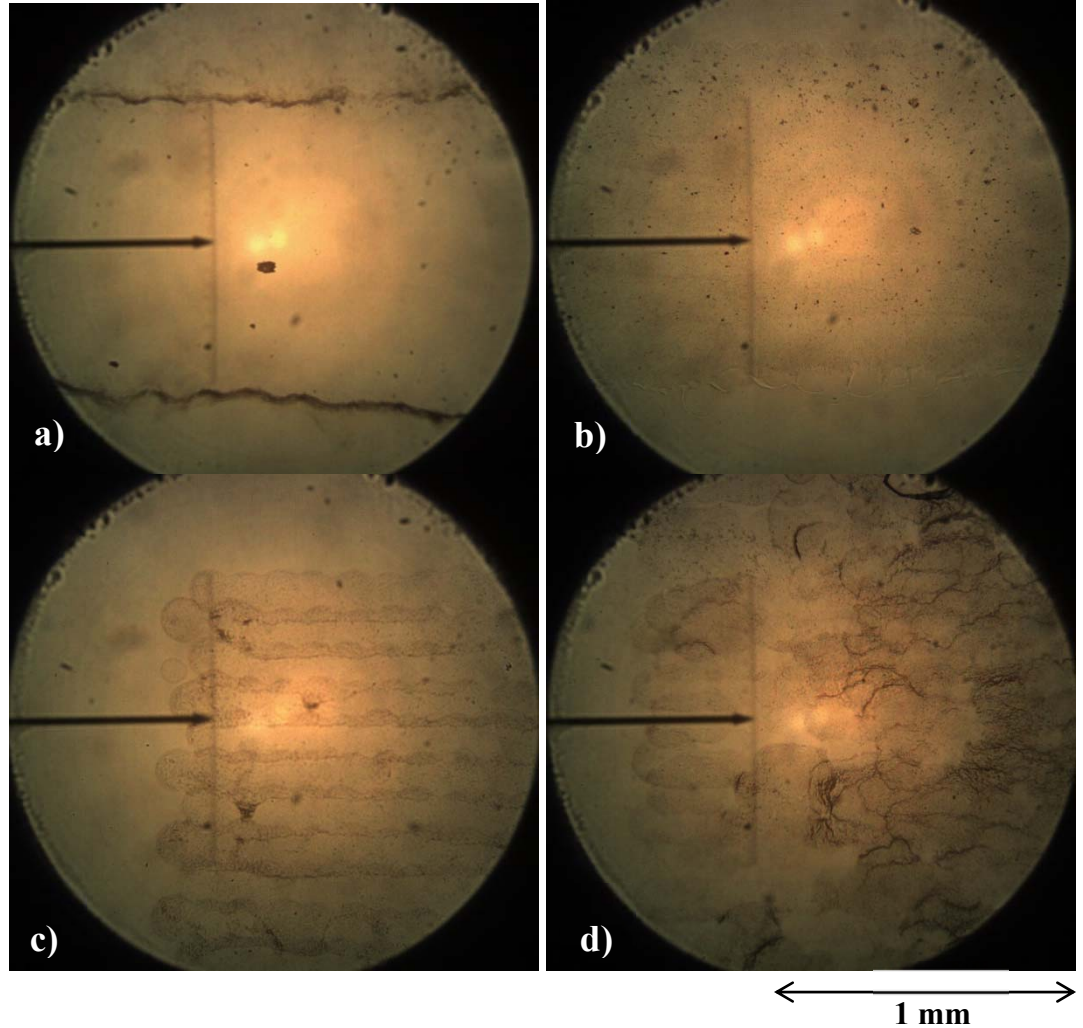


Figure 4.12 Repeated printing on previously deposited films result in degradation of film homogeneity. Thin films experience severe coffee ring effect when substrates are not treated with polyelectrolyte coating (a). During the first print cycle on a polyelectrolyte coating treated substrate, ink is deposited on a clean and treated surface, which results in acceptable film quality (b). Next print cycle happens on previously deposited film which has different surface properties than the substrate. High surface tension of aqueous ink results in poor wetting and large isolated droplets form. Resulting film shows very poor homogeneity (c: 2nd print; d: 6th print) (Sinar & Knopf, 2018b).

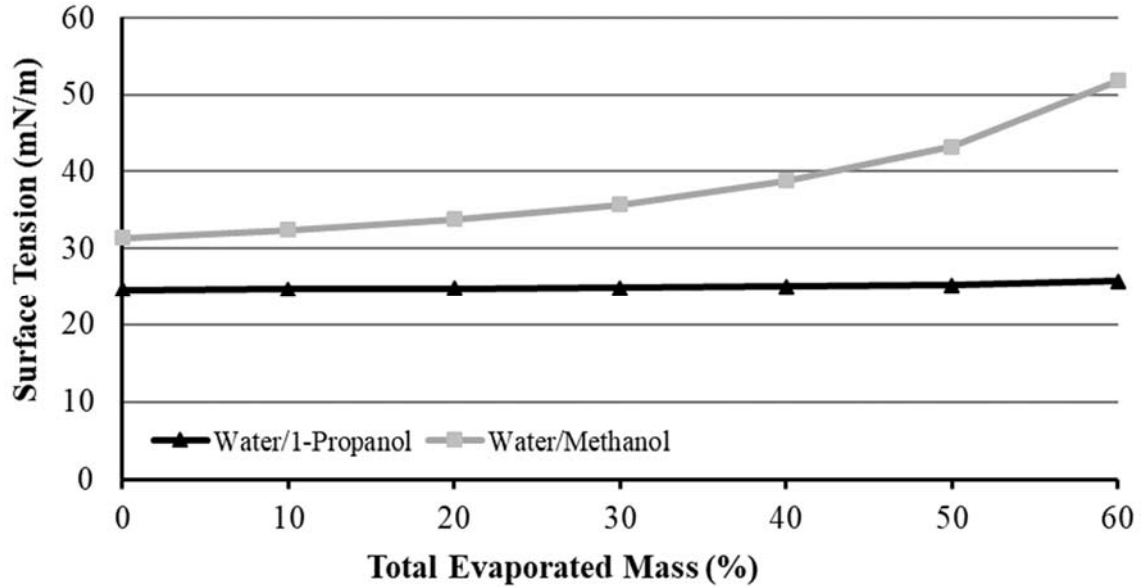


Figure 4.13 Comparison of Water/1-Propanol and Water/Methanol binary solvent systems. Water/1-Propanol system experience only subtle change in surface tension during evaporation. Lack of strong surface tension gradients mean less contribution to edge directed Marangoni flow (Sinar & Knopf, 2018b).

Inverse Z of Ohnesorge number was also taken into consideration. Using the known surface tension (Vazquez, Alvarez, & Navaza, 1995) and viscosity values for 1-Propanol/Water binary solvent mixtures (Tanaka, Matsuda, Fujiwara, Kubota & Makita, 1987), inverse Z of Oh was calculated to be in the jettable range of $4 < Z\text{-inverse} < 14$.

1-Propanol's impact on film formation was investigated in detail by comparing various solvent percentages (12, 17, 27, and 55 % m/m alcohol/G-CMC) on both non-treated and polyelectrolyte treated substrates using nondoped G-CMC ink. Treated substrates were prepared based on standard protocol presented in Section 4.2. Non-treated substrates were cleaned in the bath sonicator, air dried, and briefly corona discharge treated prior to inkjet printing. Inkjet printing of solvent free ink on treated and non-treated substrates clearly demonstrated impact of polyelectrolyte coating. 1-Propanol added samples have formed films with better morphology despite multiple prints on the same area at every percentage, although best results were achieved between 17 to 27% m/m (Fig. 4.14b and 4.14c, respectively). On the other hand, 55% m/m 1-Propanol added samples eliminated in-droplet Marangoni flow to such extent that partial center heavy deposition was observed for films deposited on both non-

treated and treated substrates (Fig. 4.14d). Effect of 27% m/m 1-Propanol on film morphology was further investigated through profilometry. Related topographic data is discussed in Section 4.4.

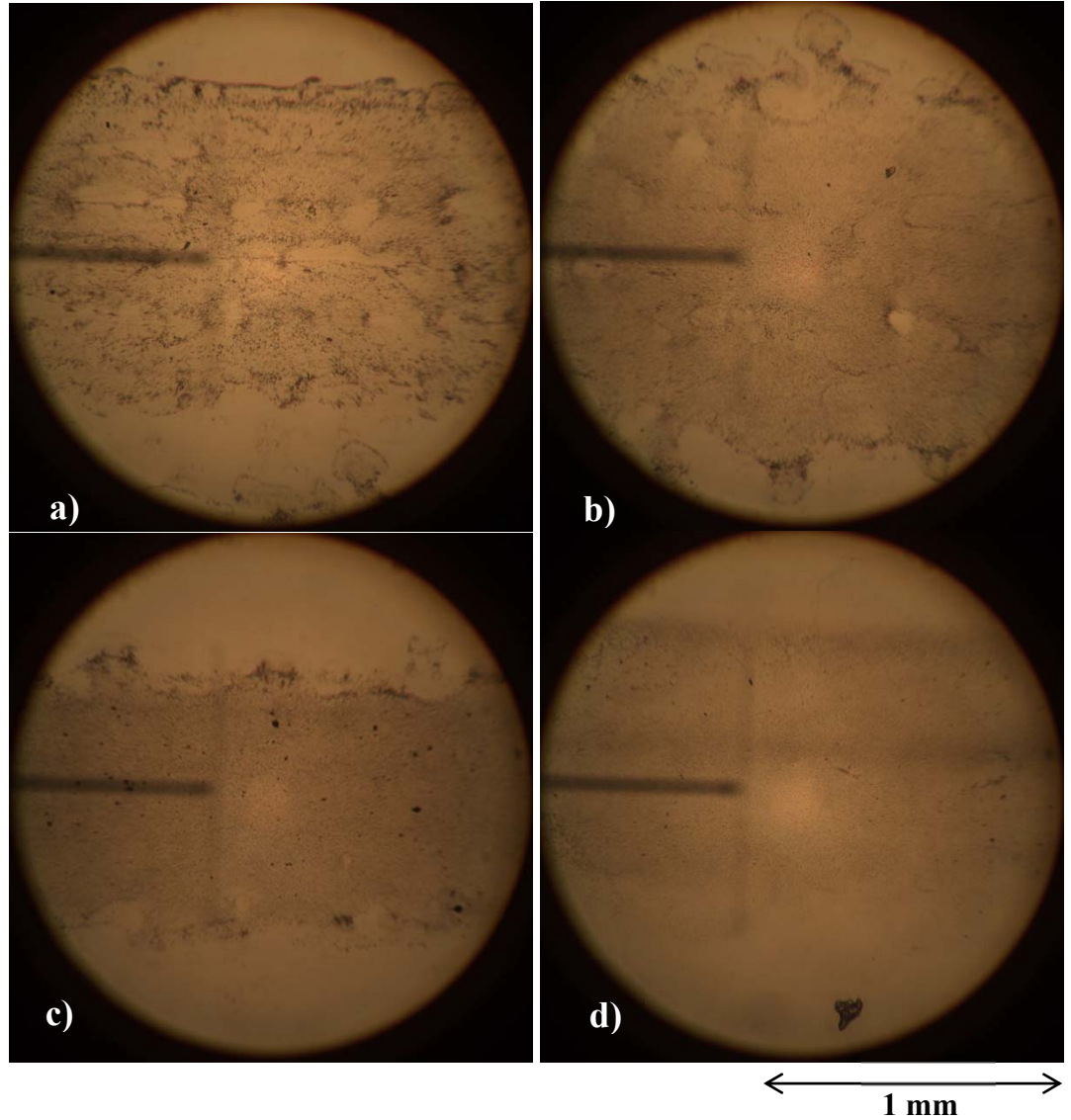


Figure 4.14 Microscope images of inkjet printed electrodes on PEC treated glass. Addition of 1-Propanol (12% m/m) resulted in slight improvement in homogeneity (a). Further improvements were observed for increasing 1-Propanol mass percentage; 17% m/m (b), 27% m/m (c), 55% m/m (d) (Sinar & Knopf, 2018b).

It is worth noting that use of 1-Propanol was mentioned by Kim et al (Kim, Jeong, Park, & Moon, 2006). It was listed among other low boiling point solvents that should not eliminate coffee ring effect, based on HBP solvent/water system approach. It is not clear if any hands-on experiments were conducted for the claim. Yet, it is shown here clearly that 1-Propanol can indeed eliminate coffee ring effect despite having an LBP.

4.4 Electrical and Physical Properties of Inkjet Printed G-CMC Films

To investigate electrical properties of A8C1, A8C3, and A24 ink samples, a separate set of electrodes (50×1 mm) were inkjet printed. For these electrodes, 1-Propanol mass percentage was 27% for all ink mixtures. Substrates were treated with the protocol detailed in Section 4.2. Printing was conducted with raster scanning method. Vertical and horizontal droplet spacings were 160 μm and 50 μm , respectively. For each ink sample, 10 electrodes were inkjet printed (Fig 4.15). Electrode thickness was adjusted through repeated printing. Thinnest electrode was printed 10 times while thickest electrode was printed 100 times. Printed electrodes were heat treated in Argon environment at 520°C for 15 minutes to partially decompose CMC.

Topographic scan of electrodes revealed that each printed layer was approximately 15-25 nm. Coffee ring effect was not observed at any film thickness (Fig. 4.16). A8C1 and A24 electrodes had similar thickness profiles while A8C3 electrodes was measurably thinner. This was expected as starting material for the third sonication cycle was less than the first sonication cycle, hence A8C3 ink was less concentrate. Thicker electrodes for all ink samples exhibited widening due to large droplet volume of C6602 cartridge. Thus, line thickness was closer to 1.3 mm rather than 1 mm as was specified by the design file. Widening of electrodes also resulted in slightly less thickness than expected, where thickest electrode was 1.75 μm instead of projected 2 μm . This issue was due to cartridge limitations and increased width was taken into account when calculating sheet resistance.

Sheet resistance of each electrode was measured with 4-point measurement method. As expected, sheet resistance of films decreased rapidly before reaching to a steady level (Fig. 4.17). A8C3 electrodes had lower sheet resistance values compared to A8C1, despite being thinner. A24 electrodes had higher sheet resistance than both A8C1 and A8C3 electrodes.

Relatively poor performance of A24 samples can be explained by diminished lateral dimensions of G sheets (Fig. 3.2). Small increase in conductivity for A8C3 samples can be explained by relatively higher number of thinner sheets due to removal of large particles during the first cycle and longer cumulative ultrasonic processing. Electrical and physical properties of 20, 60, and 100 print electrodes are summarized against their physical thickness for each sample in Table 4.1. Cyclic LPE products, A8C1 and A8C3, performed similarly and better than A24. This means that RM can be cycled to increase yield without sacrificing film performance.

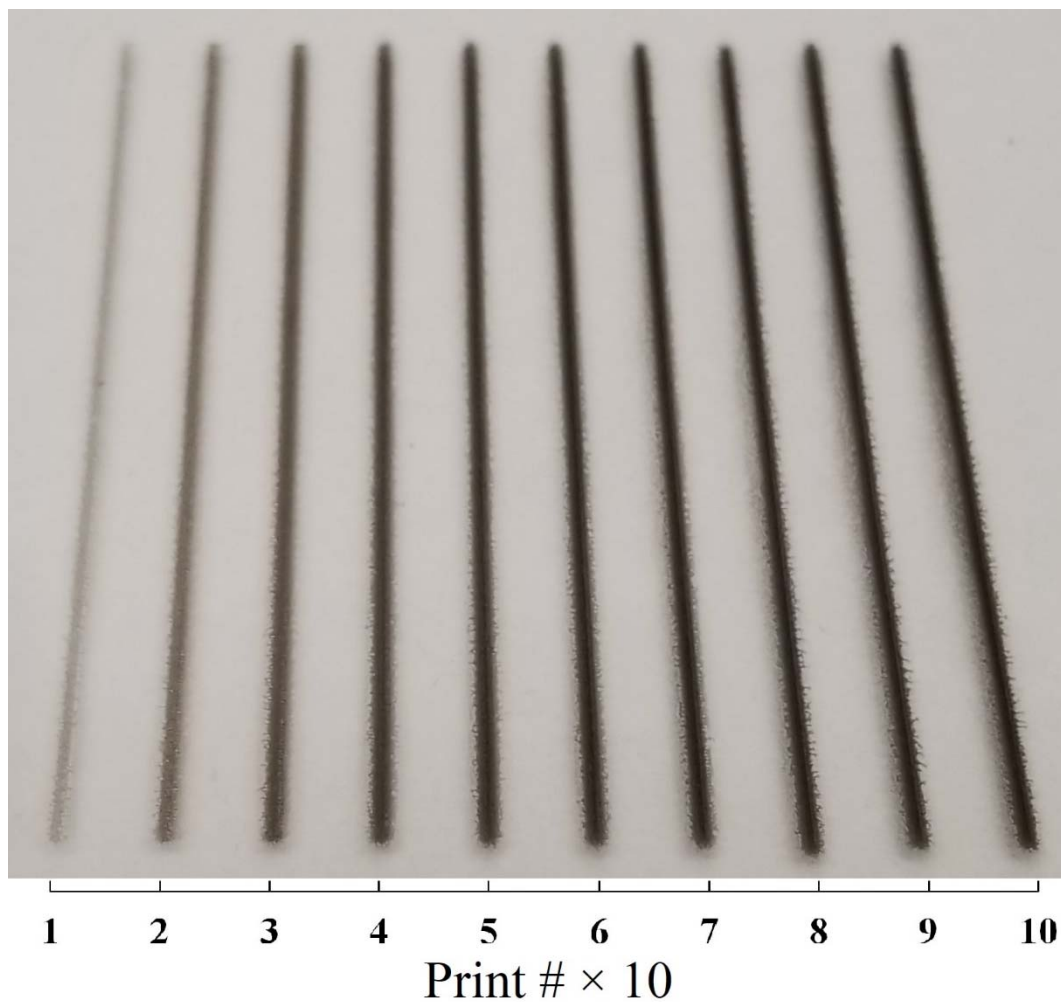


Figure 4.15 Electrodes inkjet printed using A8C3 ink. Electrode borders are less defined for thicker films due to large droplet volume of C6602 cartridges. Electrodes were printed 10 to 100 times (Sinar & Knopf, 2018b).

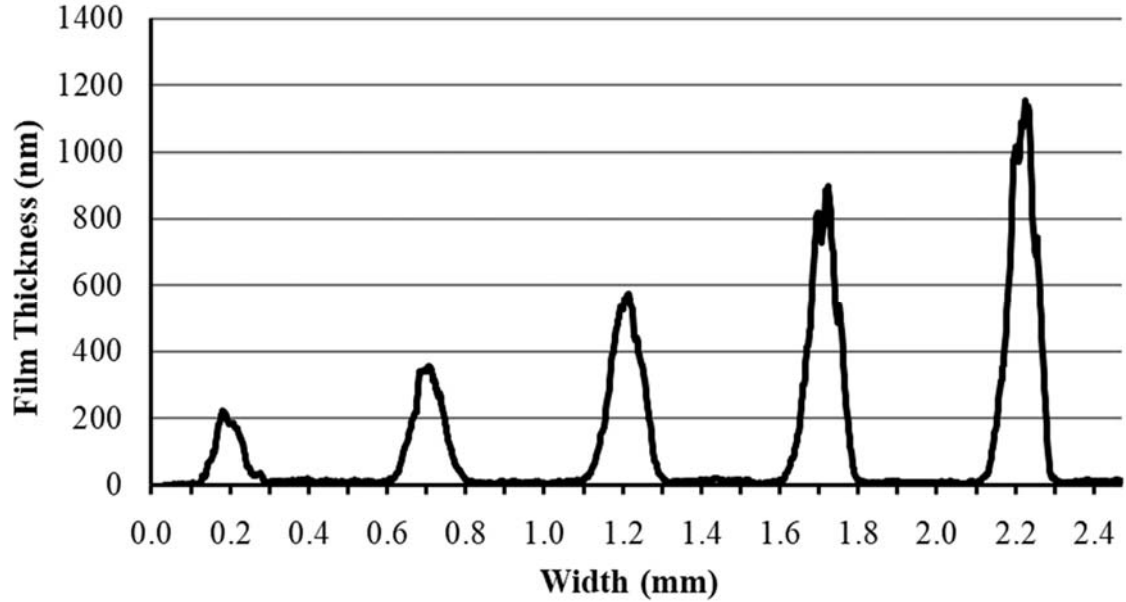


Figure 4.16 Full topographic scan of first four electrodes. Since LPE-G has lower conductivity than metals, it is important to demonstrate successful deposition of thicker films. Electrode profile shows that coffee ring effect was not present despite multiple printing cycles (Sinar & Knopf, 2018b).

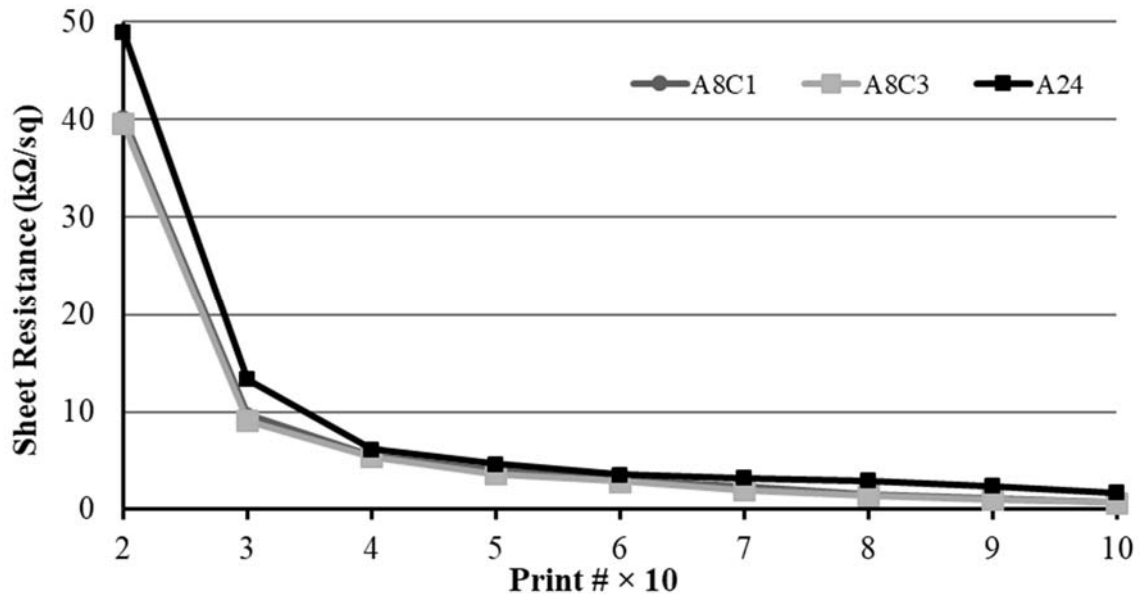


Figure 4.17 Sheet resistance of inkjet printed electrodes. Electrical performance of A8C1 and A8C3 electrodes were essentially the same. A24 electrodes exhibited measurably higher sheet resistance (Sinar & Knopf, 2018b).

Table 4.2 Comparison of film thickness (nm) and sheet resistance ($k\Omega/sq$) (Sinar & Knopf, 2018b).

Sample	20 Prints	60 Prints	100 Prints
A8C1	380 / 40.2	1352 / 3	1711 / 0.76
A8C3	340 / 39.6	1315 / 2.84	1682 / 0.66
A24	393 / 49	1372 / 3.56	1716 / 1.68

4.5 Impact of Au Doping on Film Properties

Gold doped G-CMC thin films were fabricated according to method detailed in Section 3.3.1. Nondoped G-CMC thin films performed as observed in Section 4.4. As expected, sheet resistance quickly decreases with each number of prints for both nondoped and gold doped G-CMC films. After 6 prints, decrease in sheet resistance is more linear per number of prints. Hence, it can be concluded that it takes approximately 6 prints to achieve an optimal conductive network of G sheets. At 70% transmittance (4 prints) sheet resistance of nondoped optically transparent (OTE) G-CMC films were measured as 8.2 $k\Omega$. For thicker films (10 prints), sheet resistance was below $k\Omega$ threshold but in the expense of transparency (35%) (Fig. 4.18).

Sheet resistance of films were further improved by dipping samples in $AuCl_3$ solution. Doping process reduced sheet resistance of the films in a range of 70 to 30% of original values. Changes were more pronounced in thinner films which is assumed to be due to gold particles diffusing deeper into thinner films and filling in gaps between G nanosheets, hence improving conductive network. Optical transmittance of the films was only marginally affected by doping (< 1.6%). For 70% transmittance, sheet resistance was reduced about 50% to 3.8 $k\Omega$. Highest conductivity that could be achieved was at 10 prints and 35% transmittance where sheet resistance was in the range of non-doped CVD-G (700 Ω). Doping by dipping was observed to be hard to control method, mainly due to unintended over deposition of gold particles.

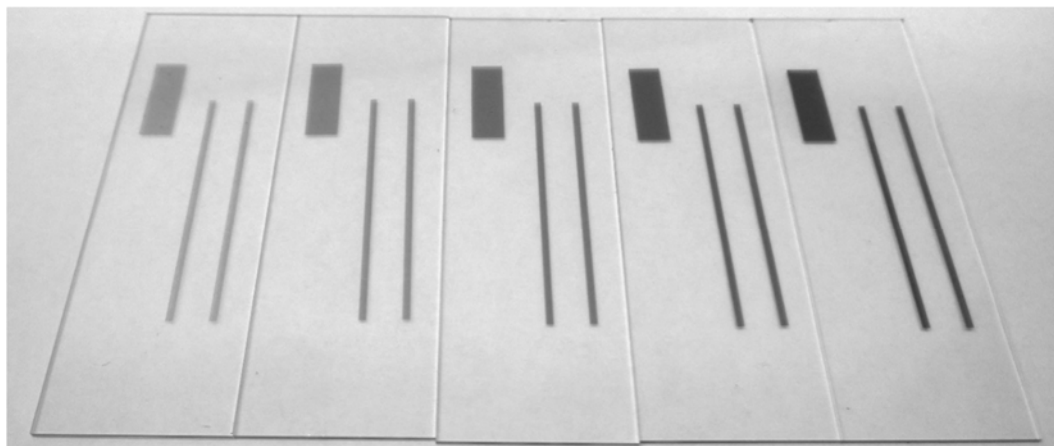
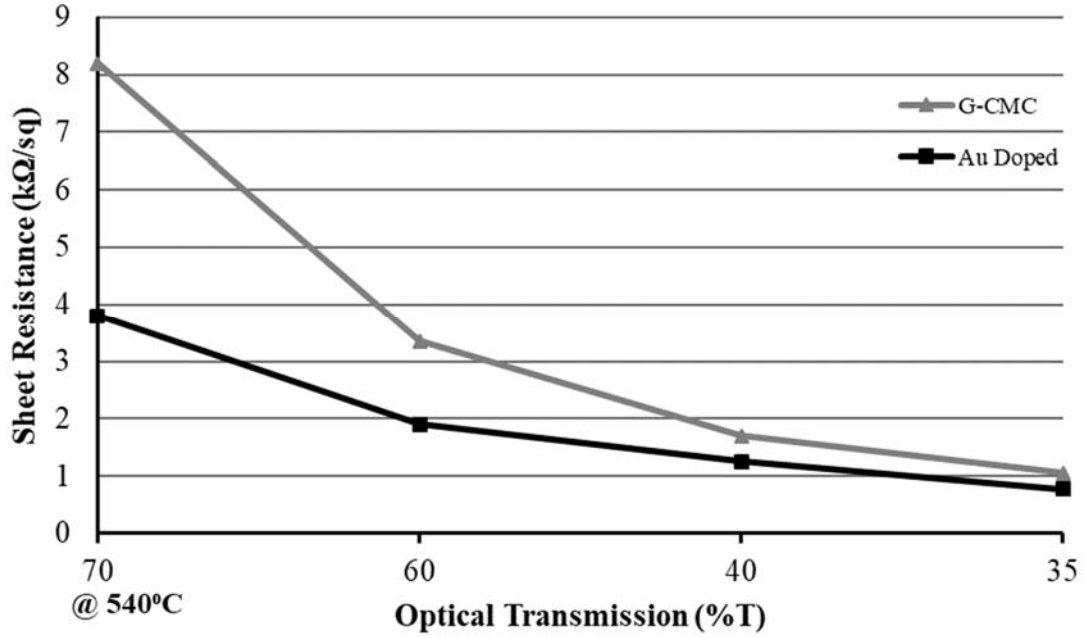


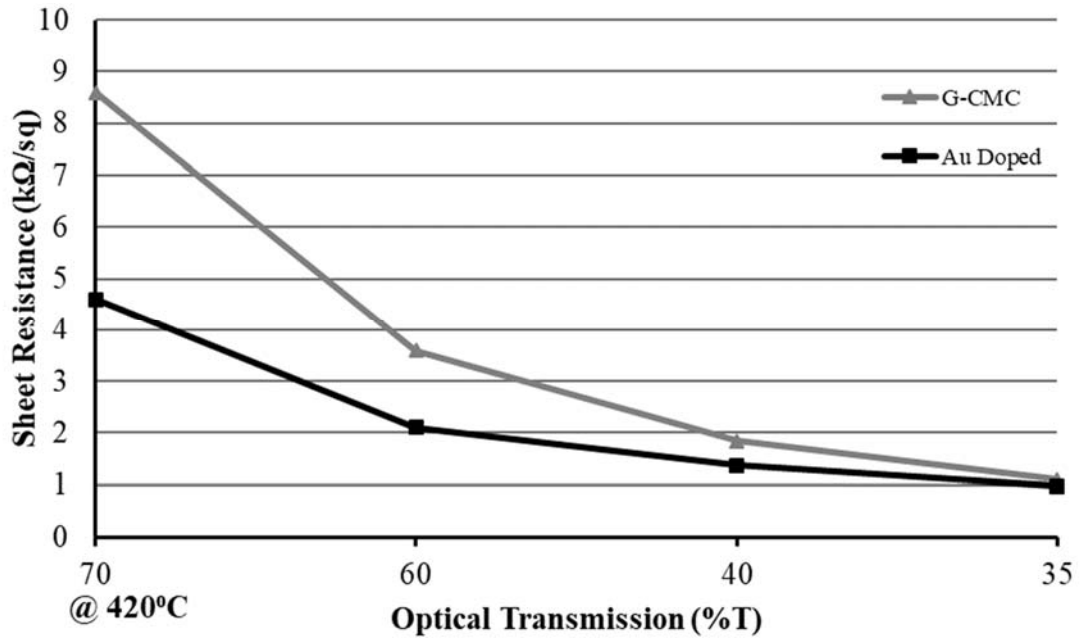
Figure 4.18 Inkjet printed Gold Doped G-CMC optically transparent electrodes (OTEs). From left to right; 2, 4, 6, 8, and 10 prints (Sinar et al., 2016).

It was also observed that for very long doping times (excess of 1 hour), there were clear signs of gold deposition on surface. It is known that G can adsorb elements which can cause changes to its properties. In the case of AuCl_3 , higher electronegativity of gold facilitates its self-assembly on the film surface. It is assumed that large amounts of open edges of G nanosheets further facilitates doping and makes self-assembly based gold doping hard to predict in terms of electrical performance. Optical transparency of samples was measured by using large area rectangular films. All measurements were done with a 550 nm light source. Deposition of particulate material differ from atom-by-atom deposition of CVD. It should be kept mind that, for sufficiently thin inkjet printed films, there are many holes in thin films that are microscopic in dimensions. Light can pass through these holes and increase perceived transparency. Once those holes are closed due to repeated printing, light transmission experiences a sudden drop while sheet resistance is reduced. It is theorized that initial prints do not assemble sheets on all available area and some amount of particle over particle stacking happens. Nevertheless, gold doping significantly reduced sheet resistance of printed films in a predictable manner. When compared, gold doped G-CMC films had 2 to 4 times less sheet resistance compared to nondoped G-CMC films (Fig 4.19).

Effect of annealing temperature was film thickness dependent, where thinner, more transparent films benefit from higher temperature at a greater magnitude. Despite diminishing return with increasing number of prints, higher temperature annealing (540°C) yielded lower sheet resistance for all thickness of films.



(a) Sheet resistance with respect to the number of prints (540°C)



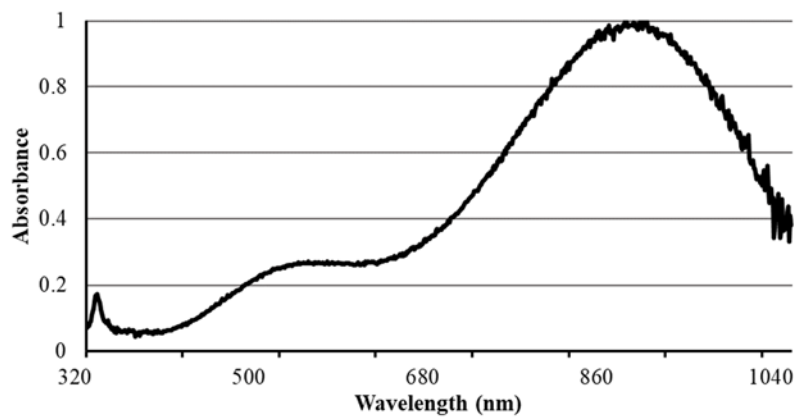
(b) Sheet resistance with respect to the number of prints (420°C)

Figure 4.19 Sheet resistance of films for high temperature treatment (540°C) decrease sharply with increasing film thickness (a). Similar changes were also observed for 420°C treatment (b) (Sinar et al., 2016).

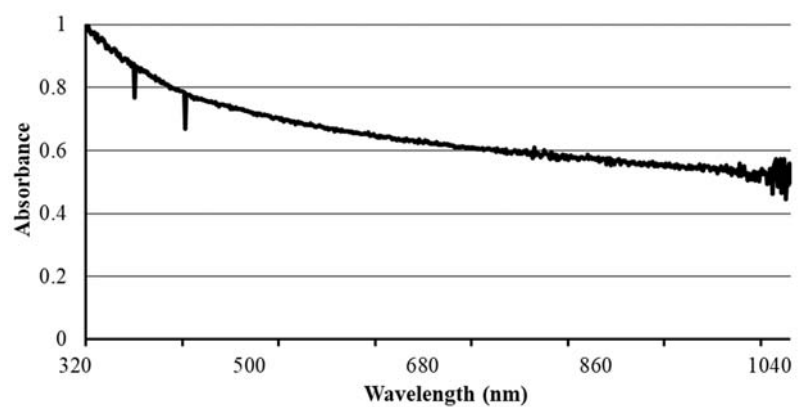
4.6 Electrical and Optical Properties of G-CMC/AgNP Films

AgNPs were synthesized according to the method detailed in Section 3.3.2. G-AgNP composite ink was prepared by slowly mixing of AgNPs into G-CMC ink under bath sonication. AgNP to G-CMC mixing ratio was 2:1. After 1 hour of bath sonication, G-AgNP composite ink was ready for inkjet printing.

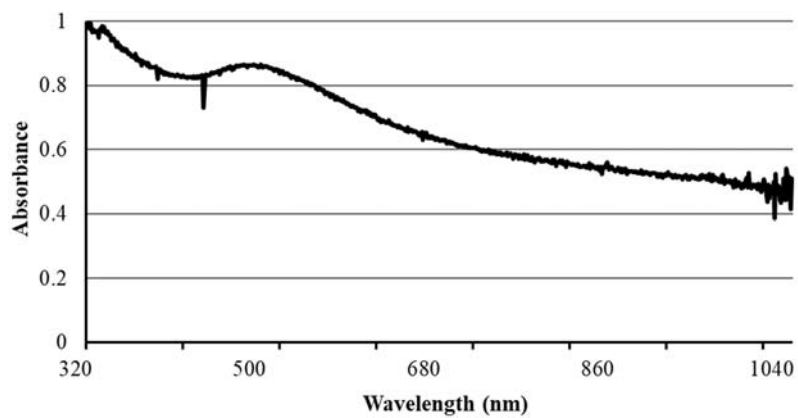
Prior the inkjet printing of films, UV-VIS spectra and TEM imaging of G-AgNP ink was conducted. Once AgNP solution was mixed with G-CMC ink (which does not have free PVP), a blue shift was observed (Fig. 4.20a and 4.20c). A similar blue shift was also observed when the solution was centrifuged and washed 3 times. It is not clear if adsorbed capping agents can be removed during centrifuge/wash step. It can be assumed from the observations that stability of AgNPs may be dependent on not only adsorbed but also presence of free capping agents (TCD and PVP) available in the system. On the other hand, blue shift in UV-VIS spectra does not mean that AgNPs were reduced to spherical nanoparticles. A blue shift in UV-VIS may mean either reassembly to polyhedral (spherical) form, reduction of lateral dimensions, or truncation of corners. TEM imaging was used to observe the geometrical changes to the AgNPs and determine the reason behind the blue shift. In this case, a truncation of corners was observed which resulted significant reduction in effective edge length (Fig. 4.21). Although effective edge length was diminished, AgNPs preserved the plate-like form.



(a) UV-VIS graph of the prepared AgNPs.



(b) UV-VIS graph of G-CMC ink.



(c) UV-VIS graph of G-AgNP composite ink.

Figure 4.20 UV-VIS spectra for AgNp, G-CMC and G-AgNP inks. Despite the blue shift, characteristic peaks at 330 nm and primary peak near 500 nm are visible (Sinar et al., 2017).

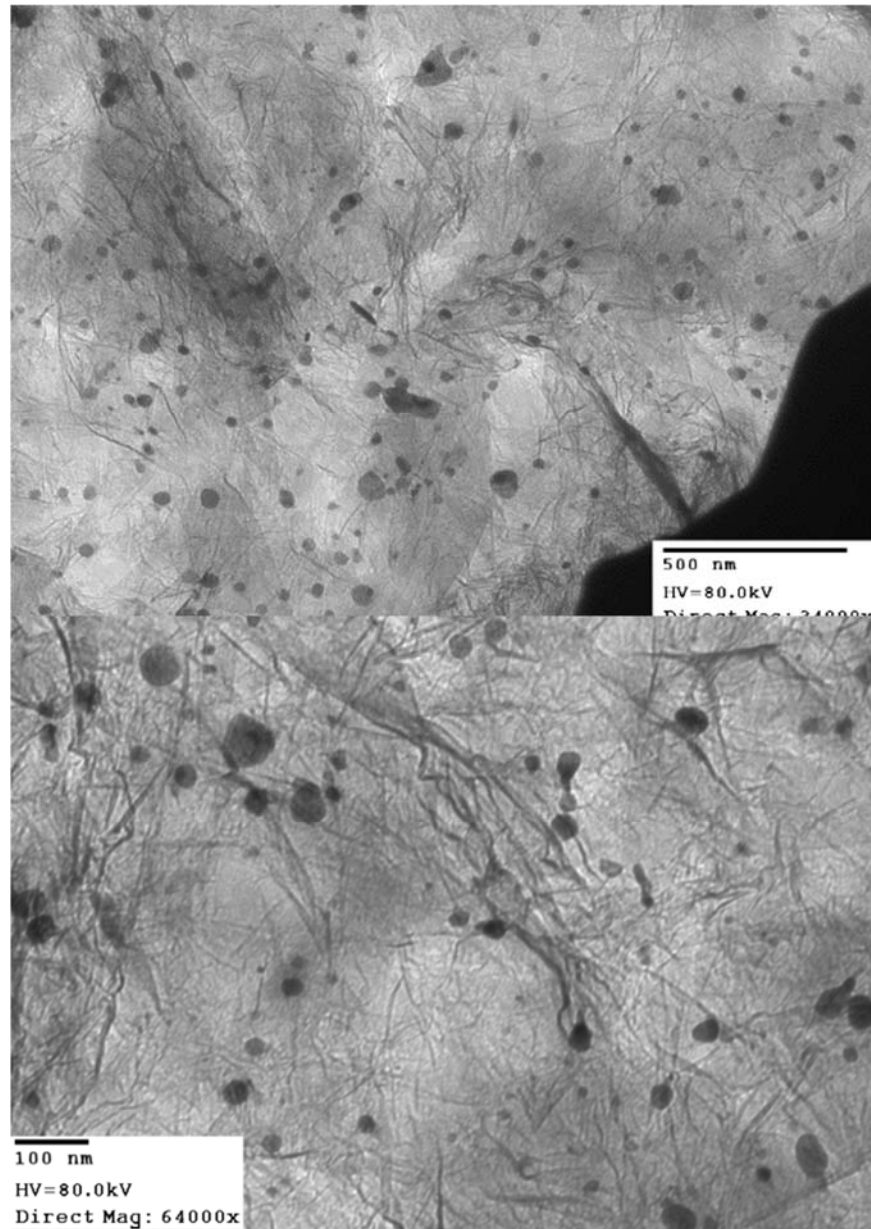
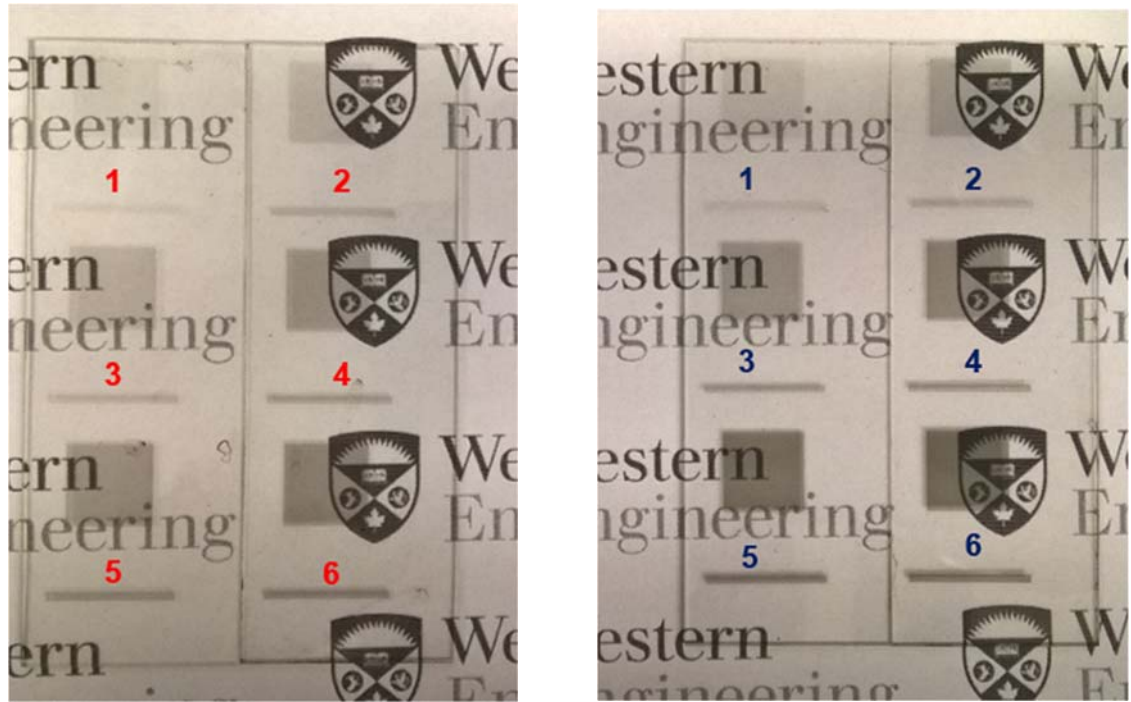


Figure 4.21 TEM Images of AgNPs synthesized with modified method. AgNPs have uniform thickness of ~ 4 nm. Sharp and robust corners contribute to red shift (top). Once mixed with G-CMC, AgNP experience truncation and resemble thin disks. Despite truncated corners, AgNPs preserve their plate-like form (bottom) (Sinar et al., 2017).

Prepared G-AgNP composite ink was inkjet printed using the methods detailed throughout this chapter. Optical transparency and electrical conductivity of inkjet printed G-AgNP and G-CMC thin films were measured and compared on soda lime glass substrates. Substrates were prepared using the method detailed in Section 4.2. Optical transparency was

measured using a 550 nm laser source. Laser power was measured before and after transmission through square shaped thin films (Fig. 4.22). In terms of film structure and mechanical behavior, no differences were observed between pure G-CMC films and G-AgNP films. Flexibility and durability tests yielded results within the expected margin of error ($\pm 5\%$ change in resistance values for electrodes). Particle deposition and film formation did not differ. A slight increase in absorption was observed for G-AgNP thin films compared to G-CMC films. This is in agreement with UV-VIS spectra of composite ink. As seen in Figure 4.20, G-AgNP ink exhibits an absorption peak around 500 nm due to truncation of AgNP edges during the process. On the other hand, transmission data suggested that contribution of AgNP were largely in electrical conductivity despite the larger size of AgNP compared to atom-by-atom elementally doped G-CMC films (Fig. 4.23).



(a) Printed G-CMC films.

(b) Printed G-AgNP films.

Figure 4.22 Inkjet printed G-CMC (left) and G-AgNP (right) films. The number of printed layers used to create the thin films are high-lighted in red and blue on the sample slides (Sinar et al., 2017).

Absorption discrepancy between G-AgNP and G-CMC thin films were consistent with increasing number of prints. This shows that addition of AgNPs does not negatively impact self-assembly of G sheets on substrate. It can be speculated that, if truncation had not happened, G-AgNP inks could be prepared without any significant impact to UV-VIS spectra in visible range.

Electrical conductivity of the inkjet printed lines was measured by four-point measurement method. Optical transmittance was measured by use of 550 nm laser diode. Transmittance values were corrected for absorbance of soda lime glass. Addition of AgNPs to G-CMC ink resulted in substantial increase of conductance (Fig. 4.23) At 50% transmittance (T-50%), conductance of G-AgNP was close to 6 times of G-CMC. Transmittance values were not substantially different between G-CMC and G-AgNP films (G-AgNP film was 5% less transparent). This was predicted due to low absorbance of AgNPs in 320nm to 700nm range. There was a stark increase in conductivity from T-75% to T-70%. This would suggest a lack of full network between G particles on the film. When particle number increase in the film by T-70%, better network results in higher conductivity. By the T-50%, rate of change in conductivity decreases which means that G particle coverage of print area closes to its optimum level. At T-50%, G-AgNP film had a sheet resistance of 374 Ω /sq.

4.7 Concluding Remarks

It is established in academic literature that dispersion based G films perform poorly compared to CVD-G films. Doping or metal nanoparticle addition can significantly improve performance of these films. Although doping can be a self-limiting process, addition of metal nanoparticles may be able to push conductivity of G-CMC films to a level where they could become viable as commercial OTEs. Especially, use of unique nanoparticles, such as the AgNPs presented in this study, is a rarely visited subject. Future work on optimization of G-AgNP composite ink and its films may help expanding application field for inkjet printed electronics.

On the other hand, presented data agrees that inkjet printed of G-CMC can be used to fabricate mechanically robust films. Unlike the available literature, this work demonstrates that much thicker films can be inkjet printed without deteriorating film morphology. Since sheet

resistance can be reduced simply by using thicker films, proposed methods can be used for a wide range of flexible circuit applications.

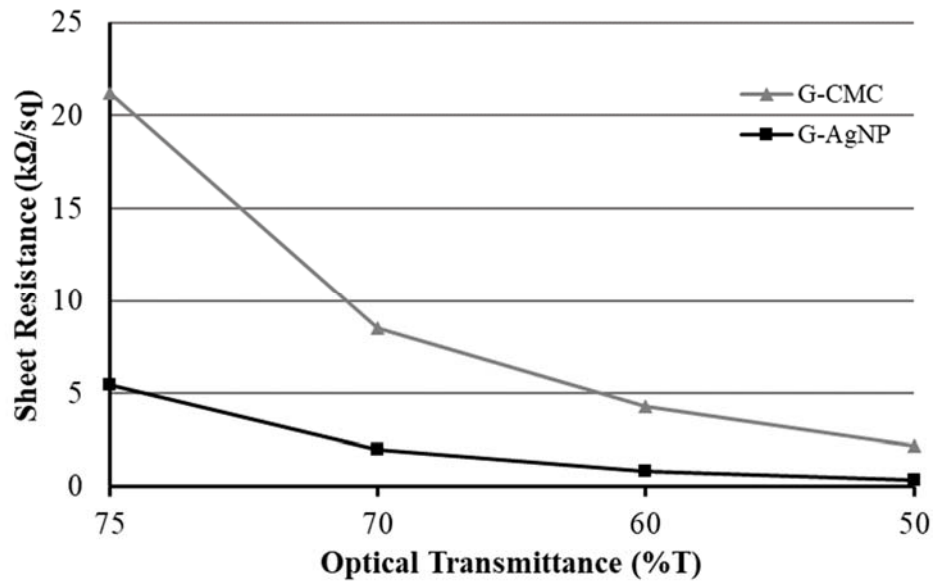


Figure 4.23 Sheet resistance of both G-CMC and G-AgNP steadily decreases as number of prints increases. At 6 prints, G-AgNP film is almost 6 times more conductive than G-CMC film (Sinar et al., 2017).

Chapter 5

Post Processing of Printed G-CMC and GO films

Thin film post processing is a fabrication step common to various deposition methods and functional materials. Post processing may be necessary in order to remove moisture, cure material, melt deposited nanoparticles, start a chemical reaction, remove less stable chemical compounds, decompose certain additives, or remove adsorbed functional groups from a material. Sintering of printed metal nanoparticles is an example of a heat based post processing step. Another example would be thermal treatment, chemical treatment, or thermal/chemical treatment of GO to remove functional groups of the basal plane and form rGO. In the case of G-CMC, thermal decomposition of CMC can be achieved by heating the thin film to a target temperature.

Another post processing step is micromachining of deposited thin films. This can be thought as analogous to photolithography step of thin films deposited by other means (e.g. spin coating or sputtering). One of the shortcomings of the inkjet printing method is the feature size. Achieving homogenous and continuous traces with very small width can be problematic as bleeding of separate traces into each other may occur due to several reasons. Very small feature sizes ($\sim 25\mu\text{m}$) can be achieved using specialized material deposition systems. But, these systems tend to be expensive and put harsh restrictions on ink properties such as surface tension, viscosity, and particle size. On the other extreme, large nozzle size results in very large droplet volume. HP C6602 printhead that was used during the initial stages of this research has a droplet volume of 160 pL compared to less than 10 pL that could be deposited by modern office and materials printers. Large droplet volume results in large area spread. On a treated surface (PEI/PSS coated), a single droplet was observed to spread to an area equivalent of 1 mm diameter disc.

In this chapter, methods of post processing for GO and G-CMC films will be discussed. Specifically, thermal treatment through furnace or laser assisted heating and pulsed laser micromachining of GO and G-CMC thin films will be presented.

5.1 Furnace Thermal Treatment

In this study, furnace heat treatment process was conducted with a muffle furnace capable of 1100°C maximum temperature (Fig. 5.1). Heating rate was set to 1°C per second throughout the research. Unless noted otherwise, high purity Ar gas was supplied into the furnace chamber to avoid combustion of treated samples.



Figure 5.1 Muffle furnace setup used for this research. Argon gas was supplied during treatment to remove oxygen from the furnace chamber.

As detailed in Chapter 3, proposed G dispersion is functionalized with hydrophilic CMC molecules. Since CMC is not electrically conductive, its presence can negatively impact conductivity. In fact, if purification step is not carried to remove free CMC from the G-CMC dispersion, deposited thin films exhibit very poor electrical performance.

Thermal processing parameters of G-CMC films depend on thermal decomposition dynamics of CMC. Li, Huang, & Bai (1999) studied thermal decomposition of CMC. It was observed that initial decomposition of CMC starts at $\sim 274^{\circ}\text{C}$. Previous to this temperature, any mass loss is due to humidity loss. Although decomposition starts at 274°C , maximum mass loss was observed at 322°C . Final decomposition temperature of CMC was reported as 341°C through extrapolation of data (Li et al., 1999). Based on this data, thermal treatment of G-CMC films on polyimide were conducted at 340°C while films on glass substrates were treated at 520°C , unless noted otherwise. PDMS substrates were treated at 200°C , only to remove moisture from deposited films. All treatments were 30 mins in duration at target temperature. At the end of post processing step, G-CMC films were observed to be 2 to 3 times more conductive. Difference in conductivity between 520°C and 340°C was small where 340°C treated samples were consistently 90-95% as conductive as 520°C treated films.

It should be noted that, G-CMC films demonstrate acceptable electrical conductivity prior to thermal treatment. Thus, they could be used as deposited when needed. As in the case of films deposited on PDMS, non-treated G-CMC films are able to function without a large penalty in performance. On the other hand, durability of films changes. Non-treated G-CMC films are water dispersible even after drying. Hence, these films tend to disintegrate when placed in water, but resist organic solvents. Once treated, G-CMC films become water resistant and their affinity to organic solvents increases. Since proposed G-CMC films can function without thermal treatment, this change in solvent affinity can be a valuable tool for altering film properties based on expected environmental exposure.

Furnace based thermal treatment of GO was also conducted. Yet, efficient thermal treatment of GO requires higher temperatures than CMC decomposition. As discussed in Chapter 2, efficient reduction of GO requires at least 600°C , which is beyond melting temperature of any plastic substrate. This temperature is also beyond annealing temperature of soda lime and borosilicate glass. If the treatment temperature is sufficiently above the

annealing temperature, glass substrates will deform due to softening. On the other hand, it is possible to limit heat diffusion depth into a thin film by applying short pulsed laser beams. In this concept, surface temperature of the thin film would reach the target value, yet heat would dissipate before substrate reaches the thermal equilibrium with the thin film. Hence, due to limited diffusion depth and HAZ, underlying substrate can be protected from thermal degradation. Next subsection provides further details on pulsed laser heating method applied on GO thin films.

5.2 Pulsed Laser Thermal Treatment

It has been previously shown in the literature and preliminary experimentation that a low power laser source can locally heat up GO traces and reduce the presence of oxygen molecules (El-Kady, Strong, Dublin, & Kaner, 2012). Kinetic studies of the GO reduction process have also suggested that continuous application of heat is not mandatory for reduction (Jung, Dikin, Piner, & Ruoff, 2008). Rather, repeated intermittent exposure to a heat source can also increase the electrical conductivity without the need to inadvertently increase the surface temperature of the film and substrate. Similar heating methodology can be applied through use of a pulsed laser system (Sinar, Knopf, & Nikumb, 2014). Each pulse would heat area under exposure up to a temperature point where GO would lose oxygen containing molecules. Between pulses, heat would dissipate, and film would cool down to ambient temperature. Depending on pulse length and gap, it should be possible to stop energy delivery before dissipated heat becomes too large for the underlying substrate. Hence, due to lack of heat accumulation, damage to substrate is not expected. Furthermore, unlike bulk application of heat, pulsed lasers can heat specific locations on the same film which would mean complete control on reduction location and magnitude. The ability to tune the film's electrical conductivity, or resistance, by controlling the thermal reduction process represents a novel method for fabricating a large variety of variable resistive components by tuning the degree oxygen reduction. The formation of rGO by removing oxygen molecules is also analogous to hole doping G. Chemical and electrical analysis of rGO films suggests that the oxygen content of rGO is directly related to band gap energy (Acik & Chabal, 2013). The tuning of band gap energy of rGO film suggests that this material can be used to produce a variety of semiconductor components. Although

this is an interesting concept to investigate, it will not be discussed in detail for being out of scope of this thesis.

To investigate pulsed laser thermal treatment process, GO films were deposited on polyimide substrates using the methods detailed in Chapters 3 and 4. Once deposition was completed, GO films were treated at 200°C for 30 mins in the muffle furnace under Ar gas to remove trapped water molecules. This pretreatment step also hardens GO films and makes it easier to adjust the printed structure's local resistivity characteristics. Non-pretreated GO films were observed to be ablated. Note that pretreatment temperature and duration must be kept low, otherwise treated sample may become too conductive due to inadvertent reduction. The darkening of the rGO films seen in Figure 5.2 is associated with partial loss of oxygen from GO and subsequent shift of absorbance band into visible range. Under these pretreatment conditions the film resistance is typically above 10 M Ω and resistivity was $\sim 5.6 \times 10 \Omega\text{-cm}$. Depending on the application, starting point for bulk resistance values can be decreased to any range by careful tweaking of annealing temperature and length. Alternatively, milder annealing conditions can be employed for very resistive films. It has been observed mild drying at 80°C for 12 hours can also increase film endurance for laser heating.



Figure 5.2 Ribbon GO electrodes before (left) and after (right) annealing. Electrodes lose their transparency due to removal of oxygen containing groups during thermal reduction process (Sinar, Knopf, & Nikumb, 2014).

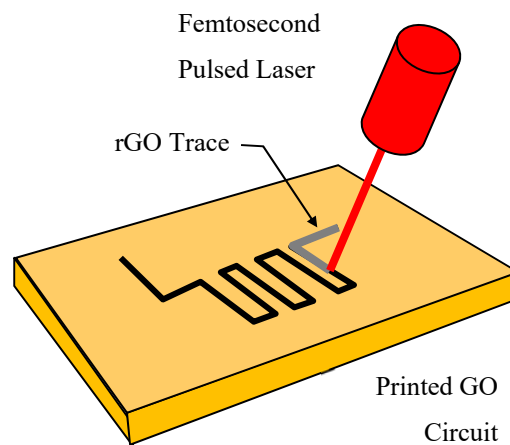
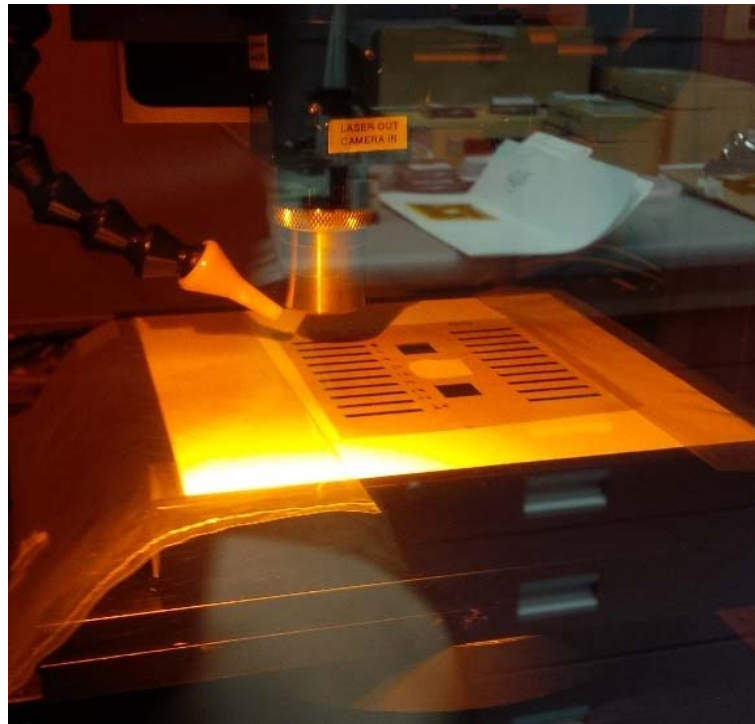


Figure 5.3 The 775 nm, 120 fs laser system used to reduce GO film to rGO (Sinar et al., 2013).

Pulsed laser thermal treatment of GO films was conducted with a 775 nm, 120 fs Gaussian beam pulsed laser system (Fig. 5.3). Treatment process was carried on in ambient air without an Ar gas supply. It is important to note that a small burst of high energy will produce a very small heat affect zone (HAZ) and, therefore, a stream of ultrashort pulses had minimal thermal impact on surrounding material compared to a long pulse or continuous wave laser system.

The laser system parameters used to modify or “tune” the electrical resistance of the annealed traces were: laser power (LP), material feed rate (FR) as determined by the positioning system, and the number of passes (NP) that the beam makes over the target area for thermal reduction. Due to Gaussian type form of laser beam, a threshold LP must be reached prior to starting the reduction process. Beyond this LP threshold, increasing LP impacts the instantaneous heating while changes to the FR affects the exposure time. Also, laser beam paths overlap to cover the whole film area. Figure 5.4 shows the overlapping of the laser beam paths as reduction process occur. As a result, certain areas of the film get exposed to laser beam 2 times more.

Several tests were performed with different power levels and material feed rates to investigate the impact of laser beam exposure on the film sheet resistance. The experimental power levels (LP) were set to: 18-19, 20-21, 23-24, 24-26, and 27-29 mW; and the material feed rates (FR) ranged from 1000, 1200, 1800 and 2000 mm/min. The exposure time was controlled by adjusting the number of passes over the target surface (NP). The NP values were set to 4, 6, 8, 10, 12, 14, 16, 18 and 20. More than one pass was necessary to observe a reduction in lower LP and/or high FR combinations. For laser heating process, laser optical setup was defocused to provide a Gaussian laser profile with an approximate spot diameter of 220 μm . The laser reduction process resulted on further darkening of the annealed film along the beam pathway (Fig. 5.5). The film thickness was measured using KLA Tencor P-10 surface profiler. For surface profilometry readings, GO films were printed on high quality microscope slides (Fig. 5.6). The profilometry results show a weak connection between film thickness and double exposed areas (Fig. 5.7). This suggests that material loss is limited during the process. On the other hand, average film thickness is lower at higher NP. Thickness variations of non-reduced film is due to limitations of inkjet printer.

The sheet resistance was determined by measuring bulk resistance and calculating resistivity using known dimensions. Figure 5.7 shows the sheet resistance of traces with increasing NP. GO traces on polyimide substrates gave high sheet resistance values for low NP among all LP and FR parameters used in this set of tests. Due to femtosecond pulse of the laser, underlying substrates did not experience thermal damage. More importantly, heated affected zone around treated area was negligible in size.

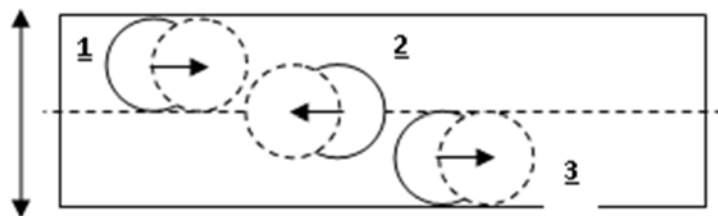


Figure 5.4 3-step reduction of a narrow film sample. Laser beam paths overlap as the beam travels from one end of the film to other (Sinar, Knopf, & Nikumb, 2014).

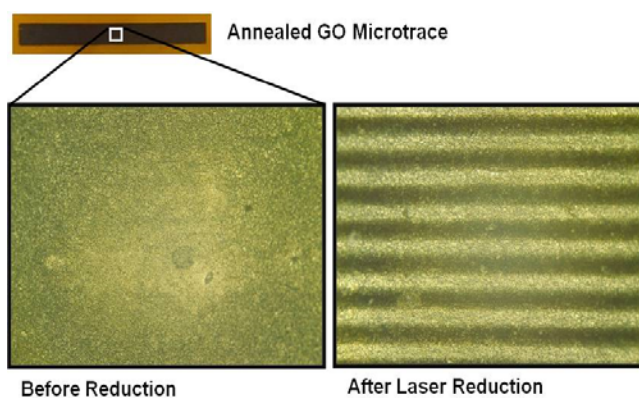
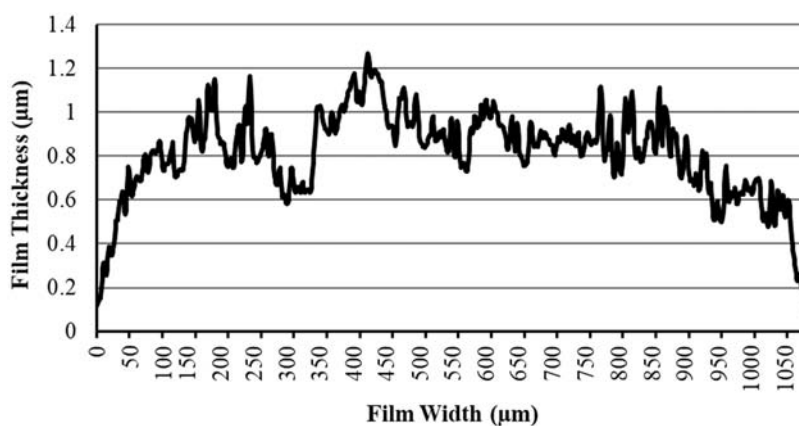
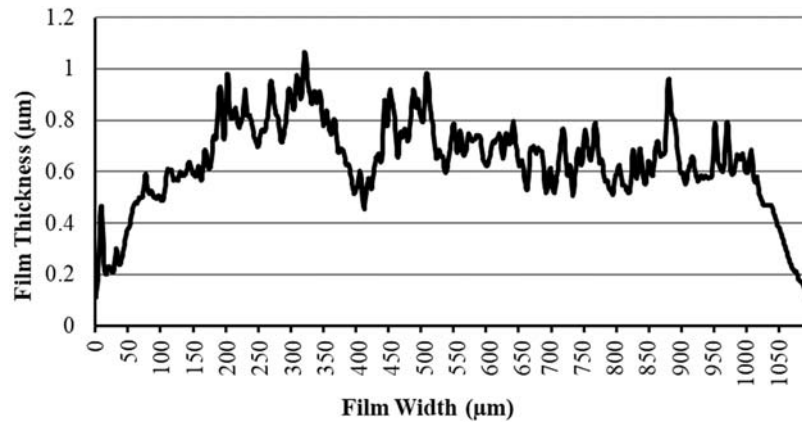


Figure 5.5 Midsection of GO trace before reduction and after laser reduction. Darker zones are due to overlap of laser beams (Sinar, Knopf, & Nikumb, 2014).



(a) Film thickness profile before reduction

Figure 5.6 (continued)



(b) Film thickness profile after reduction at ~ 19 mW LP, 1000 FR, and 20 NP

Figure 5.6 Film thickness is related to the degree of thermal reduction. The laser reduction caused decrease in overall film thickness (Sinar, Knopf, & Nikumb, 2014).

5.3 Pulsed Laser Micromachining

Localized micromachining is another advantage that a laser based system could provide. Laser micromachining can not only circumvent low resolution inherit to modest printhead technologies but also machine features finer than most advanced material printers can achieve. Hence, laser micromachining and DOD deposition can be complementary tools for fabrication of high precision thin film circuits.

Unlike laser heating, tuning of delivered power is not necessary for micromachining. Instead, success criteria were defined as lack of substrate damage and lack of non-ablated film patches in treated areas in a single pass. In this regard, first choice of LP (0.3 mW) and FR (100 mm/min) parameters was successful. For laser micromachining, laser optical setup was focused completely which yielded a spot size of approximately 8 μm .

A simple electrode (Fig. 5.8) was designed to be laser micromachined in a 2×2 mm simple square rGO film deposited using methods explained in Chapters 3 and 4. Electrode was designed to have a line width of approximately 3 μm . Electrode pattern was micromachined in ambient air. Smallest feature achieved was a 2.67 μm conductive trace, slightly off from planned 3 μm . As seen in Figure 5.9, features achieved through pulsed laser micromachining were far smaller in dimensions, even compared to state-of-the-art MDSs.

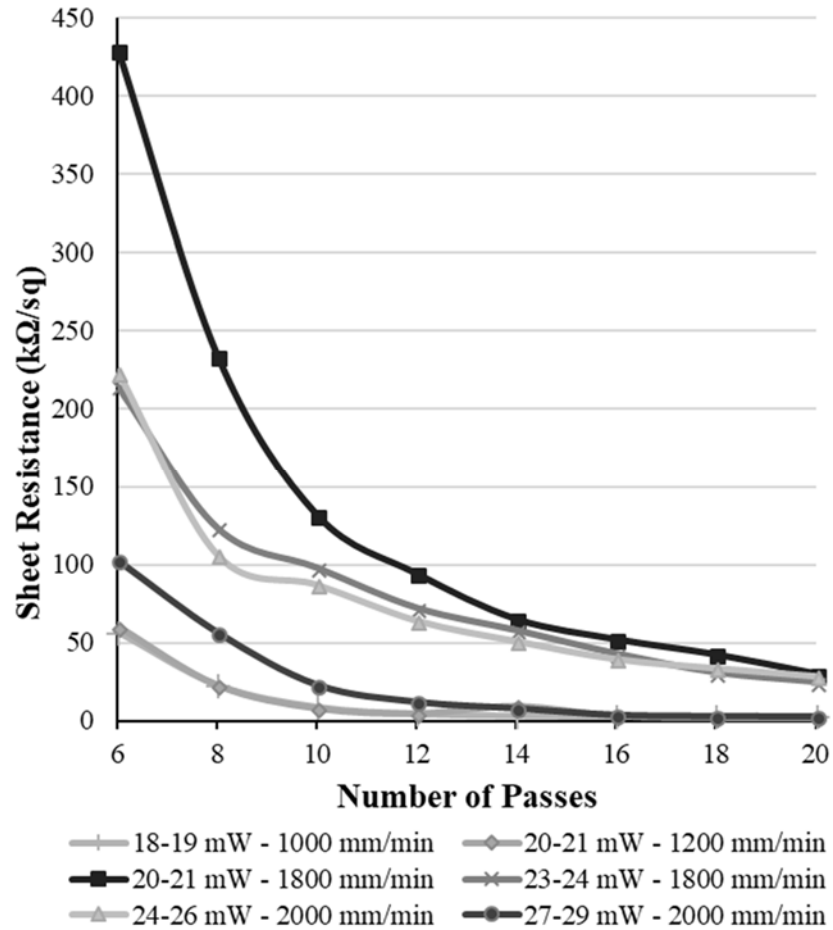


Figure 5.7 Sheet resistance values for GO traces. Higher NP is generally connected to smaller sheet resistance values while sheet resistance values for the same NP differs among different PO and FR parameters (Sinar, Knopf, & Nikumb, 2014).

Film ablation to create complex structures is less complicated in terms of tuning of laser parameters. With fine tuning of LP and beam diameter, high FR can be utilized to machine complex geometries at great speeds for mass manufacturing purposes. Furthermore, parameters used for GO micromachining were also effective at processing G-CMC films, which further simplifies use of pulsed laser micromachining as a complementary tool to DOD deposition.

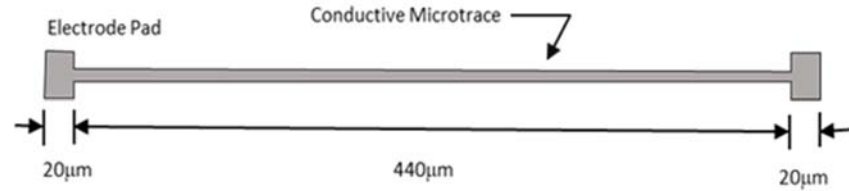


Figure 5.8 Basic design of microelectrode design.

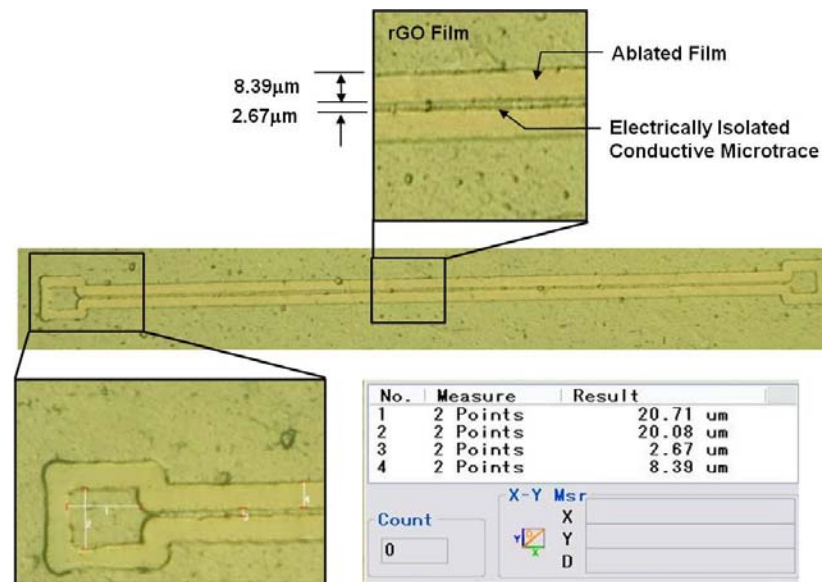


Figure 5.9 Microelectrode trace created by ablating the rGO film around the conductive line. The ablated regions have zero conductivity ($R \rightarrow \infty$). The width of the conductive microtrace is 2.67 μm (Sinar, Knopf, & Nikumb, 2014).

5.4 Concluding Remarks

Conventional muffle furnace and pulsed laser treatment routes for post process of G-CMC and GO films were discussed in this chapter. Pulsed laser thermal treatment and micromachining address two major criticisms of DOD deposition of functional materials: need for thermal treatment and large feature size.

Since ability to deposit on flexible plastic substrates is one of DOD systems' critical advantage, utilization of high temperature post-processing steps can be counter-productive. As mentioned, most printable functional materials require heating to either sinter to melt nanoparticles into a proper thin film, alter the material structure (i.e. GO), or decompose

additives inside deposited films (i.e. G-CMC). By using an ultrashort pulsed laser, HAZ can be limited to a few nanometers, which allow the precision treatment of extremely thin films without damaging underlying substrate.

Pulsed laser thermal treatment can also be useful for very high temperature alteration of material structure. An example of this would be carbonization and graphitization of G-CMC films. Carboxymethyl cellulose thermally decomposes around 341°C. By-products of this decomposition are intermediary compounds and NaCl, all of which are electrically poor conductors (Chen, Chen, et al., 2013). On the other hand, further heating of CMC up to 800°C for 2 hours under Ar gas results in amorphous carbon and sodium carbonate (Na_2CO_3). Compared to tar forms after CMC decomposition, amorphous carbon is a good conductor. Hence, it can be speculated that short (> 10 ps) pulsed laser treatment of G-CMC films could heat films above 800°C and significantly improve their conductivity, unlike what was observed for temperatures between 340°C and 520°C (Perry et al., 1999). If even higher LP was delivered with short (instead of ultrashort pulses of < 10 ps) pulses, instantaneous surface temperature of films can reach thousands of degrees (Zacharia, David, Vitek, & Debroy, 1989). This phenomenon has been utilized for pulsed laser welding and machining of metals. It should also be noted at few thousand of degrees, anything other than carbon would vaporize. If surface temperature of G-CMC films to reach $> 2000^\circ\text{C}$ under Ar gas, carbon's phase diagram suggests that rearranging of carbon atoms into graphitic structure would be observed (Bundy, 1989). This graphitization can be used to grow pristine G sheets. This growth and merging of G sheet may result in a true G thin film on plastic flexible films. Unfortunately, this concept wasn't investigated due to equipment and time limitations.

Another criticism of DOD systems is their low resolution and resulting large feature size. The 25 μm feature size that can be achieved with high end systems is still much larger than what can be achieved with photolithography. Although most device applications do not require very fine features, it is an enabling capability for a select, yet important, number of applications. For example, RFID antennas can be fabricated by DOD systems. Yet, frequency response of an RFID antenna is sensitive to dimensions of the antenna pattern. Lack of robustness and precision would result in large shifts from target resonance frequency and high variance between different samples of same design. A pulsed laser system can fix this issue through the high precision and robustness inherit to this equipment. Furthermore, feature size

of a pulsed laser machined thin film is determined by laser beam spot diameter. This diameter is theoretically limited to the optical setup of the equipment and wavelength of the emission. A 775 nm laser, in practice, can be focused to a few μm . On the other hand, use of a laser emitting at a much shorter wavelength could result in extremely fine features. An example of this would be utilization of x-ray laser systems which emit in nanometer range.

Chapter 6

Fabrication of Graphene Based Devices on Flexible Substrates

6.1 Introduction

Synthesis G-CMC colloidal ink, deposition and post-processing of nondoped and doped G-CMC films were detailed in Chapters 3 and 4. Resulting films exhibited acceptable conductance, mechanically robustness, and homogeneity on both rigid and flexible substrates. In order to illustrate these properties, several prototype thin film devices were fabricated during the course of this research using the novel G-CMC colloidal ink and DOD deposition. This chapter introduces the design theory, fabrication, and characterization of these devices.

6.2 Fabrication Thin Film Electronic Components

Fabrication of simple electrical components is a crucial step towards thin film flexible electronics. Although thin film active components, such as transistors, are still hard to achieve with DOD deposition, passive components such as electrodes, resistors, capacitors, inductors, and antennas can be fabricated using simple 2D patterns. In this section, use of G-CMC to construct various passive 2D components will be presented.

Non-metal thin film electrodes tend to have high sheet resistance. Hence, they can be used as resistors in a thin film circuit. In conventional electronics, resistance of conductive lines/electrodes can be ignored or represented as a small resistor load. When using printed G-CMC, intrinsic resistance of the electrode should not be ignored and must be represented as a resistor in circuit diagram. In terms of resistor fabrication, design parameters of deposited films should be simplified as much as possible to allow easy control over component values. For example, bulk resistance of a thin film is determined by material's resistivity, length of the trace, width of the trace, and thickness of the film. Relationship between these terms are

$$P = R \frac{w \times \eta}{s} \quad (6.1)$$

where P is resistivity, R is bulk resistance, w is width of the trace, η is the thickness of the film, and s is the length of the trace. Among these terms, the resistivity, P , is a constant for a known thickness of a film. Hence, by depositing G-CMC film the same thickness for each sample (same concentration ink, same number of prints), variables to tune bulk resistance can be reduced to trace width and length. In this scheme, increasing trace width will decrease the resistance while increasing the its length will increase the resistance (Fig 6.1).

Thin film inductors can also be fabricated by DOD systems and are considered as air-core inductors due to lack of a ferromagnetic core. Thin film inductors are less common in the literature compared to resistors and capacitors. This is mainly due to higher resistance of most DOD deposited thin film traces and low attainable inductance. On the other hand, different thin film capacitor designs have been demonstrated over the years. Most common examples of these are parallel plate capacitors (PPC) and interdigitated capacitors (IDCs). Parallel plate capacitors are designed as two conductive plates separated by an insulating layer with high resistance and high dielectric constant. Fabrication of PPCs is an on-going research in printed G electronics. Difficulty in PPC fabrication with DOD systems arise from the porous structure and rougher surface characteristics of deposited films. This results in diffusion of insulating layer into the first layer of conductor and diffusion of second conductor layer into the insulating layer, effectively shorting the capacitor. A simpler capacitor design, IDC avoids complications of layer-by-layer deposition of conducting and dielectric layers by depositing conductive electrodes with defined gaps (Fig. 6.2). In this design, whole IDC can be coated with a high dielectric constant layer to increase overall capacitance of the IDC.

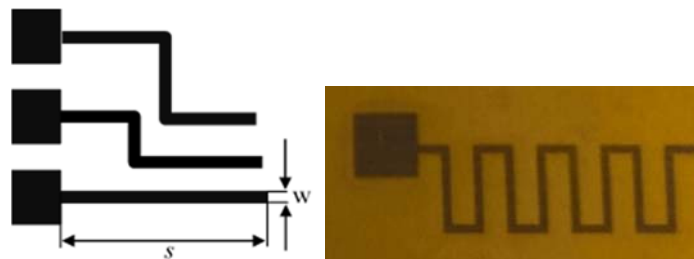


Figure 6.1 Three different resistor designs (left) and printed G-CMC resistor on polyimide (right) are represented. All resistors have the same width (w) but differing lengths (s). Consequently, resistance of lines decreases from top line to bottom.

IDCs can function as both capacitors and sensors. This will be discussed in more detail next section. However, PPC design can also be modified for use as a sensor. In the modified PPC design, a conductive first layer is deposited and covered with an insulating dielectric layer. A second conductive layer is not deposited. This device is called a self-capacitive sensor where capacitance of the whole surface area or trace is measured. This design is the foundation of capacitive touch screens used in early smart phones and tablets that featured capacitive touch screens.

Capacitance of a PPC sensor changes due to two reasons: dielectric and conductive properties of a foreign object. Initially, with no object in proximity of the sensor, device has a very low capacitance (C_I) as the PPC is configured in the form of conductive layer-dielectric-air (Fig. 6.3b). If a foreign object, such as human finger, approaches the dielectric layer, the overall capacitance of the sensor changes due to replacement of air ($\epsilon_a = \sim 1$) by human finger ($\epsilon_s = 41.4$) (Wasife, 2011). The large increase in the dielectric constant near by the sensor causes an increase in overall capacitance (C_T). The overall capacitance further increases with decreasing distance between the human finger and sensor surface. If the foreign object is conductive, as in the case of human finger, and makes contact with the dielectric layer, a PPC is formed. This results in the introduction of an additional capacitive component, C_F , that is in parallel to C_I . The total capacitance for two capacitors in parallel is simply the summation of the two terms. Hence, C_T of a sensor would be $(C_I + C_F)$. The change in C_T for both proximity and direct contact can be detected and quantified using a microcontroller unit (MCU) to construct a capacitive sensing device.

In order to illustrate G-CMC's electrical and mechanical capabilities, two different touch sensor devices were fabricated on polyimide and PDMS substrates: a simple touch sensor, based on circuit diagram in Figure 6.3, that turns on a surface mount LED on polyimide (Fig. 6.4) and a seven-key piano on PDMS substrate (Fig 6.5), which is an extension of the simple touchpad circuit in Figure 6.3. Both devices were controlled with an Arduino Uno prototyping board.

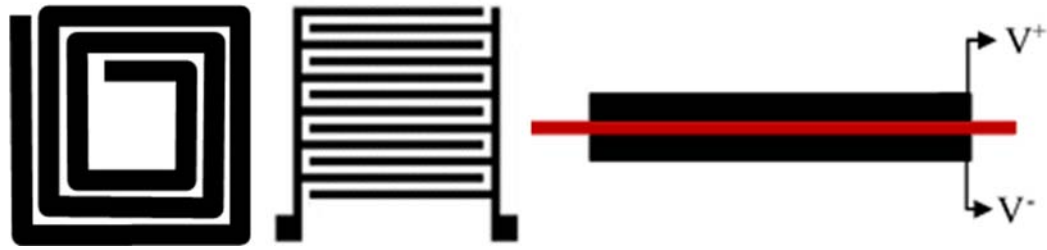
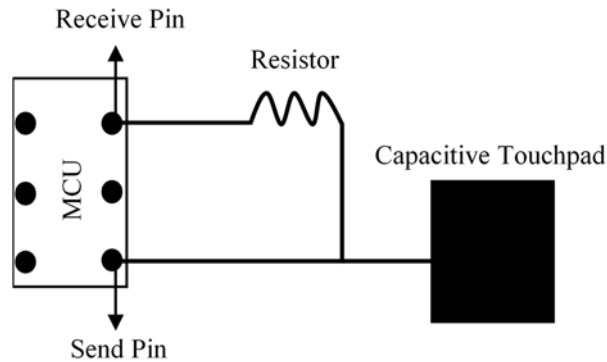
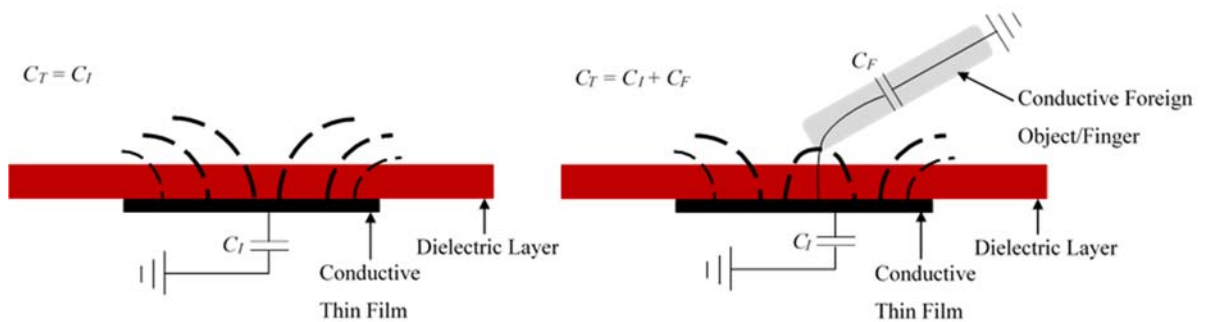


Figure 6.2 From left to right: thin film inductor, interdigitated capacitor, and parallel plate capacitor components.



(a) Circuit diagram of a touchpad sensor



(b) Capacitive touchpad sensor without and with a conductive object touching sensor area.

Figure 6.3 A simple capacitive sensor can be constructed using a modified parallel plate capacitor design (PPC) and controlled with a microcontroller unit (a). When a conductive foreign object touches the dielectric layer, total capacitance (C_T) of the PPC changes due to addition of C_F capacitive term in parallel to the initial stray capacitance (C_I) (b).

Since G-CMC has acceptable conductivity and can be deposited in the form of thin homogeneous films, it can be used as the conductor plate of PPC based touchpad design. To fabricate these touch sensor devices, G-CMC was DOD deposited on flexible substrates using the methods detailed in Chapter 4. For the LED circuit, G-CMC was deposited on polyimide, thermally treated in the muffle over at 340°C, and covered with a second layer of polyimide with silicone adhesive. Resulting capacitive touch pad (Fig. 6.4) was connected to an MCU and LED. Microcontroller unit was programmed to sense only the closest objects which allowed the LED to turn on only when a finger was pressed against the capacitive touch pad. A more sophisticated design, a seven-key piano, was fabricated on a PDMS substrate using the same methodology (Fig. 6.5). This circuit was covered with another layer of PDMS to act as the dielectric. In this design, seven G-CMC touchpads were connected to the MCU. Microcontroller unit was programmed to produce sound upon sensing a change in capacitance when a finger was pressed against the G-CMC piano keys (code used to run the inkjet printed flexible piano can be found in Appendix A2).

Fabricated G-CMC touchpads were also tested for mechanical durability. It was seen that both circuits were able to function under mechanical bending. Use of an MCU allowed for fine tuning of G-CMC touchpad sensitivity, hence mechanical bending or rolling did not cause false readings for either circuits.

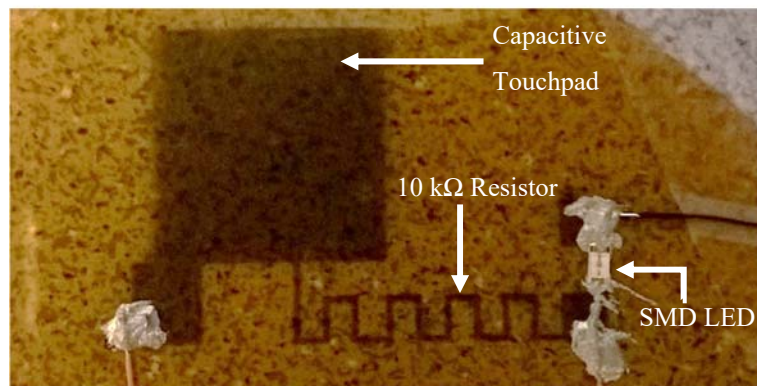


Figure 6.4 LED touchpad sensor on polyimide. Contact with touchpad area turns on the SMD LED.

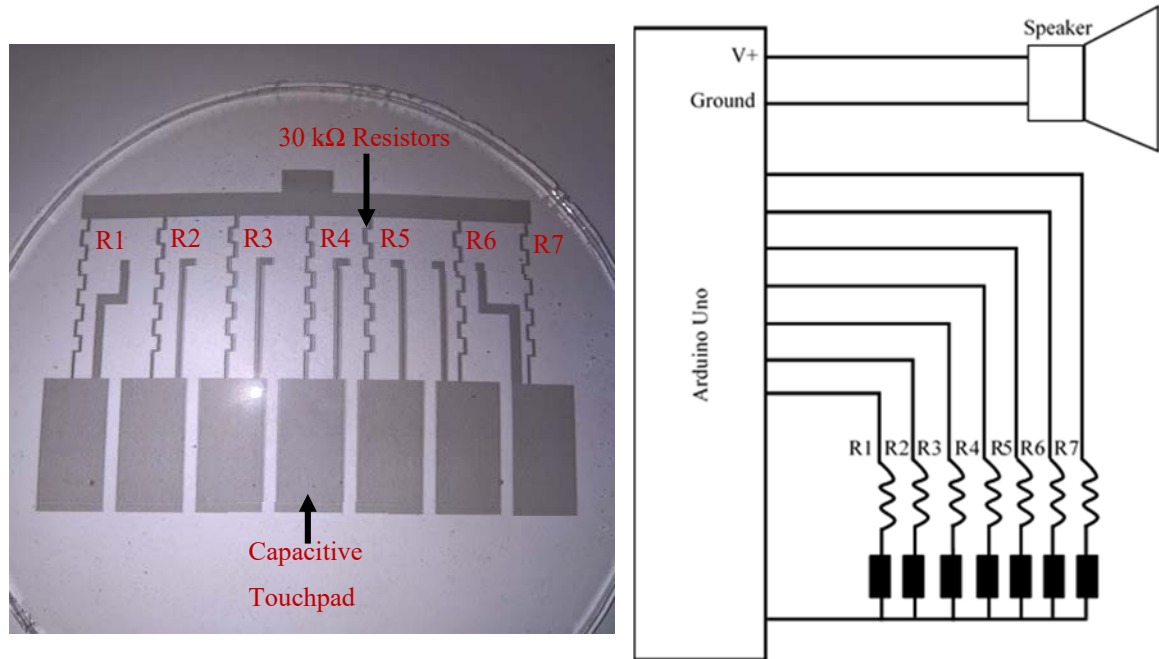


Figure 6.5 Printed seven-key flexible piano device PDMS substrate (left) and its circuit diagram (right). Black rectangles in the circuit diagram represent G-CMC touchpads. Another piano device was also fabricated on a polyimide substrate.

6.3 Fabrication and Characterization of Interdigitated Capacitive Sensor

Sensor devices represent one of the major fields where thin film technology can significantly improve device capabilities. Mechanical flexibility and ease of fabrication of thin film circuits can allow production of affordable and robust wearable devices. Capacitive sensing is a widely used technology for remote sensing of both metallic and non-metallic materials.

As mentioned in the previous section, IDCs can be used as capacitive sensing elements. Capacitive sensors based IDCs are simple circuits comprised of conductive patterned electrodes and can be fabricated through various methods (Hobdell, 1979; Endres & Drost, 1991; Berggren, Bjarnason, & Johansson, 2001). Some of the applications of IDC sensors include sensing of sugar content in water (Angkawisittpan & Manasri, 2012), water content in ethanol (Mendonca, Torikai, Ibrahim, Simoes, & Morimoto, 2008), harmful bacteria and toxins in the environment (Radke & Alocilja, 2005; Radke & Alocilja, 2004), and humidity content of environment or human skin (Laconte, Wilmart, Flandre, & Raskin, 2003; Laville & Pellet,

2002). Due to its ease of fabrication and wide range of functionality, proposed G-CMC ink was used to inkjet print IDC sensors of various dimensions on flexible polyimide substrates. Printed IDC sensors were used to sense ethyl alcohol percentage in DI water. This section summarizes the IDC design methodology, capacitive sensing theory, inkjet printing of proposed sensor devices, and experimental results for sensor performance.

Capacitive sensors take advantage of the changes in dielectric properties near the electrode surface when exposed to the analyte (i.e. substance undergoing analysis) or immersed in a solution. The interdigitated capacitive sensor has a planar structure where the consecutive fingers are connected to positive and negative electrodes as shown in Fig. 6.6a. The IDC electrodes can be printed directly on the substrate material and coated with a very thin passivation layer to prevent electrical shorting when encountering the MUT. Changes in the MUT dielectric constant will alter the capacitance that is measured by the sensor instrumentation.

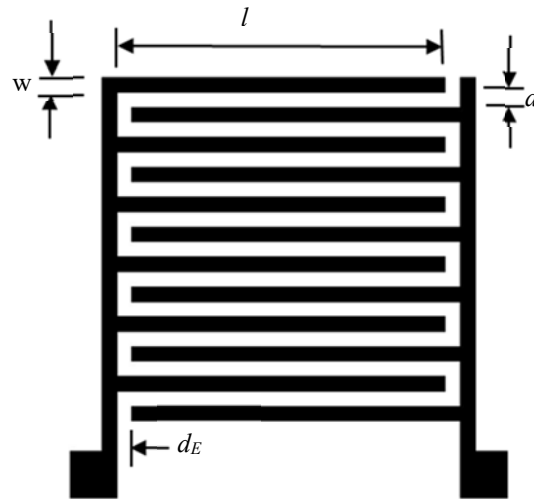
The IDC behaves similarly to a parallel plate capacitor that was introduced in previous section (Hobdell, 1979). The capacitance of a PPC is defined as

$$C = \frac{\epsilon\epsilon_0 A}{d} \quad (6.2)$$

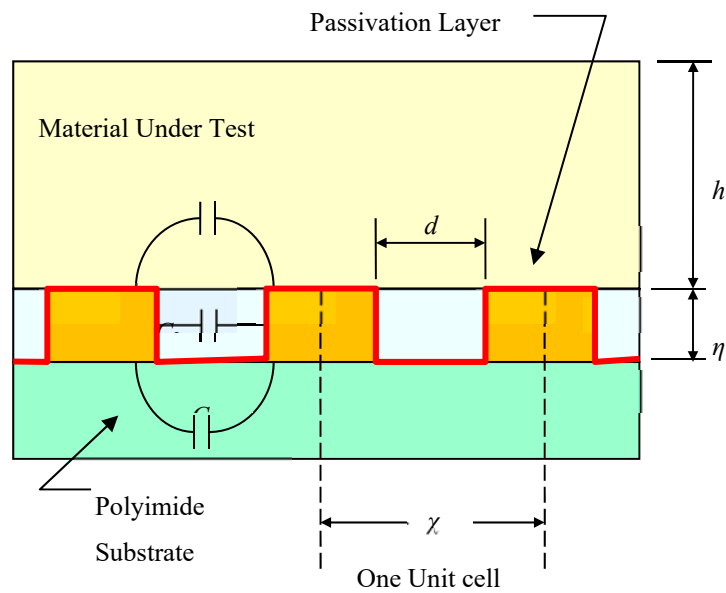
where ϵ is the dielectric constant of the medium located in the gap between the plates, $\epsilon_0 = 8.885419 \text{ pF/m}$ (permittivity of free space), A the area of the plates, and d the distance between them. The equation states that when there is a change in the dielectric property ϵ of the material in the gap between the plates there will be a corresponding change in capacitance. Furthermore, the capacitance and sensor sensitivity will increase as the distance between the 2 conductors decrease.

From a design perspective, the capacitance of the IDC increases as the gaps (d and d_E) are decreased but the size of the smallest repeatable gaps will be dictated by the manufacturing tolerances (i.e. the smallest reproducible feature size). Ideally, $d = d_E$. Decreasing the width of the fingers (w) will increase the characteristic impedance of the printed line but, simultaneously, lower the effective capacitance. Furthermore, increasing the length (l) of the fingers increases the capacitance but will enlarge the physical dimensions of the IDC sensor. The thickness of the conductor material (η) and its electrical resistivity (ρ) will also affect

circuit performance. Since the IDC is printed on a substrate, it may be necessary to consider the substrate material's dielectric constant (ϵ_r) and the thickness of the MUT layer (h).



(a) Top view of a planar IDC sensor



(b) Cross-sectional view of a planar IDC sensor.

Figure 6.6 Basic design of an IDC sensor that responds to dielectric changes in the material under test (MUT) (Sinar & Knopf, 2014).

The total capacitance of the IDC sensor, C_{IDC} , is determined by multiplying each unit cell capacitance, C_{Ucell} , by the number of digits (n) and length of the finger electrode (l) using the formula (Endres & Drost, 1991; Angkawisittpan & Manasri, 2012)

$$C_{IDC} = C_{Ucell}(n - 1)l \quad (6.3)$$

The capacitance of each unit cell, C_{Ucell} , is the summation of the two-dimensional capacitance over the entire cell and

$$C_{Ucell} = C_1 + C_2 + C_3 \quad (6.4)$$

Individual capacitance values can be calculated as

$$C_1 + C_3 = \epsilon_0 \left(\frac{\epsilon_1 + \epsilon_2}{2} \right) \frac{\psi \left[\sqrt{1 - \left(\frac{d}{x} \right)^2} \right]}{\psi \left[\frac{d}{x} \right]} \quad (6.5)$$

$$C_2 = \epsilon_0 \epsilon_2 \frac{\eta}{d} \quad (6.6)$$

where $\psi[x]$ is calculated using complete elliptic integral of the first kind because it provides a good model for magnetic fields, ϵ_0 is the permittivity of free space, ϵ_1 is the relative permittivity of the material under test, ϵ_2 is the relative permittivity of the material between the electrodes, and ϵ_3 is the relative permittivity of the substrate material.

Two different IDC patterns, Fig. 6.7, were deposited on glass slides and polyimide substrates. Both IDCs had the following dimensions: $l = 37$ mm, $w = 1.6$ mm and $d = 1.6$ mm. IDC #1 had $n = 12$ digits while IDC #2 had $n = 6$ digits. As mentioned before, increasing the evaporation rate can also substantially improve the thin film quality (Subramanian, Chang, Lee, Molesa, & Volkman, 2005). For this fabrication method, the substrates were preheated to $\sim 70^\circ\text{C}$ to control CRE as air supply system was not available at the time. After the patterns dried, the resultant G films were annealed on a hot plate for 40 minutes in ambient air at 320°C to decompose the CMC. Annealed patterns were covered with a second layer of polyimide coated with silicone adhesive.

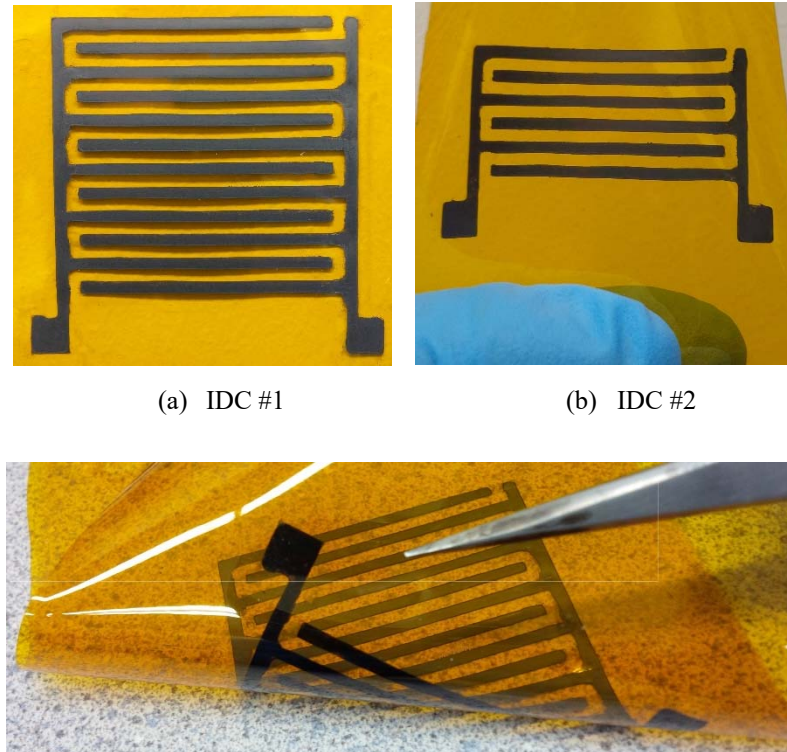


Figure 6.7 Printed G-CMC patterns on mechanically flexible polyimide substrates (Sinar & Knopf, 2014).

IDC sensors are often used to monitor environmental changes because exposure to materials with different dielectric constants produce clear changes in the capacitance values. One industrial application is to detect and measure the concentration of ethanol content in water (Mendonca et al., 2008). To assess printed IDC performance at ethanol detection in DI water, as simple experiment was conducted. Water/ethanol solution with different solution parameters were prepared. Each IDC sensor was completely submerged into solution and change in their capacitance values were recorded. Following section details the results of this experiment.

6.3.1 Experimental Results

Prior to measuring the capacitance of mixed water/ethanol solutions, several benchmark tests were performed to determine how the proposed IDC electrodes would respond to air, DI water, and pure ethanol. The sensor was connected to a HP 4284A LCR with a 1 V excitation source at operating frequencies of 1 kHz, 10 kHz, and 100 kHz. The experimental setup for measuring capacitance when the IDC is immersed in known and unknown liquids is shown in Fig. 6.8.

The capacitance measurements were made using HP 4284A LCR Meter. Table 6.1 show the average measured capacitance (pF) of IDC#1 for the three selected fluids taken over a 30 second time window. The variance from the mean was very small for each operating frequency. The time response from initial to steady-state, at 10 kHz, for DI water is shown in Figure 6.9.

Although the IDC sensor demonstrated high stability at all frequencies, at 1 kHz it was observed to be more sensitive to background noise. Further, the reduction in capacitance at the higher frequencies was not significant to impede sensing capabilities. The remainder of the experiments were carried out on 10 kHz at 1 V excitation voltage to reduce effects of background noise. It was also observed that capacitance values kept increasing as the IDC was kept in water, but not in air and pure ethanol, likely due to polyimide's capacity to absorb humidity. A slower but opposite trend was observed for ethanol measurements where capacitance was decreasing until a saturation point. This is due to the removal of humidity from polyimide and its subsequent mixing into the test sample. While this may be problematic for some applications, in the case of sensing the presence of water, it may provide additional information on the nature of contaminant.

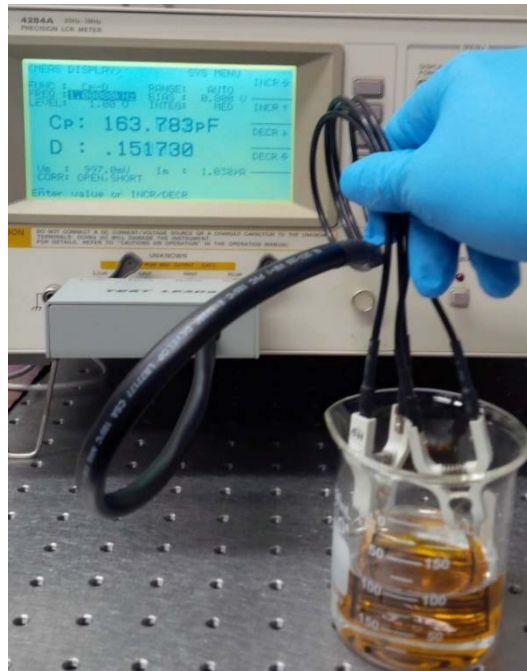


Figure 6.8 Experimental setup for measuring the capacitance of a printed G-CMC IDC submerged in a liquid (MUT) (Sinar & Knopf, 2014).

Table 6.1 Measured capacitance of several benchmark fluids using IDC#1 (Sinar & Knopf, 2014).

Measured Capacitance (pF)			
Frequency (kHz)	Air	DI Water	Ethanol
1	3.3	209.6	177.0
10	3.1	196.8	94.4
100	3.0	98.6	49.4

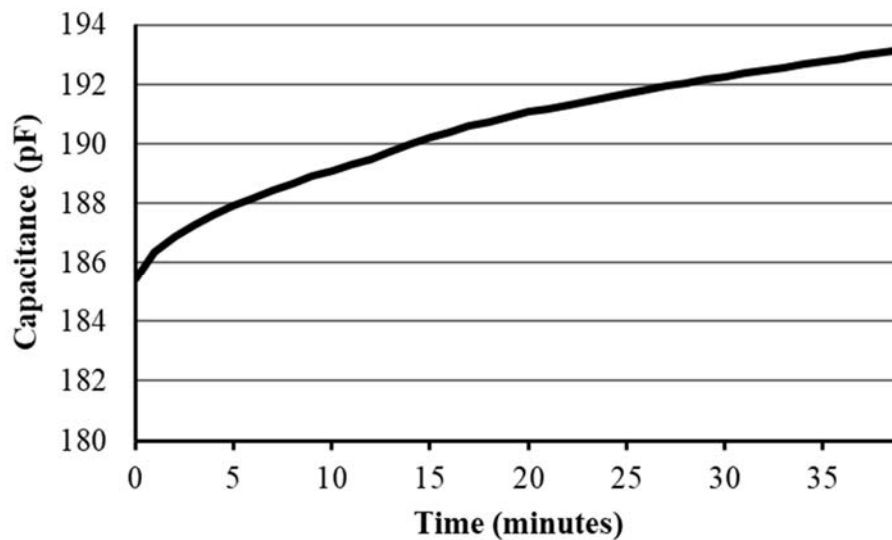


Figure 6.9 Time response of IDC #1 at the first 40 minutes of submerging into test liquid (DI water – 10 kHz). Capacitance fully stabilizes at 155th minute mark (not shown in the graph) (Sinar & Knopf, 2014).

To measure the sensor response of both IDC#1 and IDC #2 electrodes to the water content in ethanol, various water/ethanol solutions with 0, 5, 10, 15, 20, and 25% v/v water were prepared. The capacitance was measured for each test liquid at 10 kHz. Fig. 6.10 shows the change in capacitance for a period of 30 seconds according to water percentage for both IDC patterns. It can be clearly seen that capacitance values drop as ethanol percentage increases due to lower dielectric constant of ethanol. Moreover, both IDCs showed strong response to the change in liquid composition (Fig. 6.10).

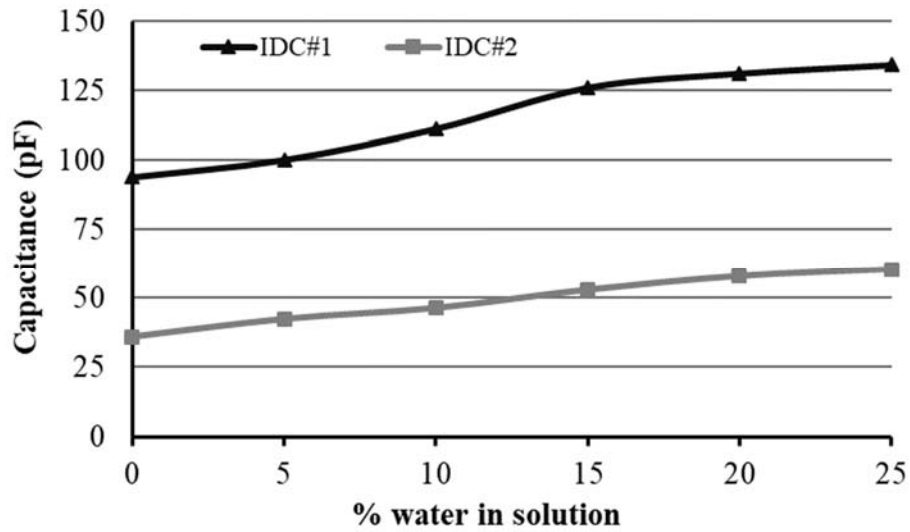


Figure 6.10 Capacitance values for IDC #1 and #2 for pure water, pure ethanol, and mixture of water/ethanol at varying percentages (Sinar & Knopf, 2014).

The frequency response of the two IDCs was analyzed from 100 Hz to 1 MHz. The results showed reliability of the conductive traces. As expected, smaller IDC showed higher capacitance at higher frequencies while large IDC showed high capacitance at lower frequencies due to inverse relation between capacitive reactance and capacitance (Fig. 6.11). Capacitive reactance decreases at a greater amount for larger capacitors than for smaller capacitors with increasing excitation frequency.

6.3.2 Mechanical Bending Performance

An important advantage of printed G-CMC IDCs manufactured in this study was the excellent mechanical flexibility of the films. To observe the effects of mechanical bending on resistance and capacitance of the IDCs, printed films were bent from one end to other 100 times. There was no significant change at resistance values between bent and unbent graphene films. Capacitance of the films showed change only at fully bent form due to changing geometry of capacitors. Yet, the change was marginal at less than 1% of unbent capacitance. Only permanent change in resistance values was observed in the case of extreme folding test where baseline resistance was increased about 8% (Fig. 6.12). For the extreme bending test, electrode was folded as seen in Figure 6.11 (left) and pressed by hand.

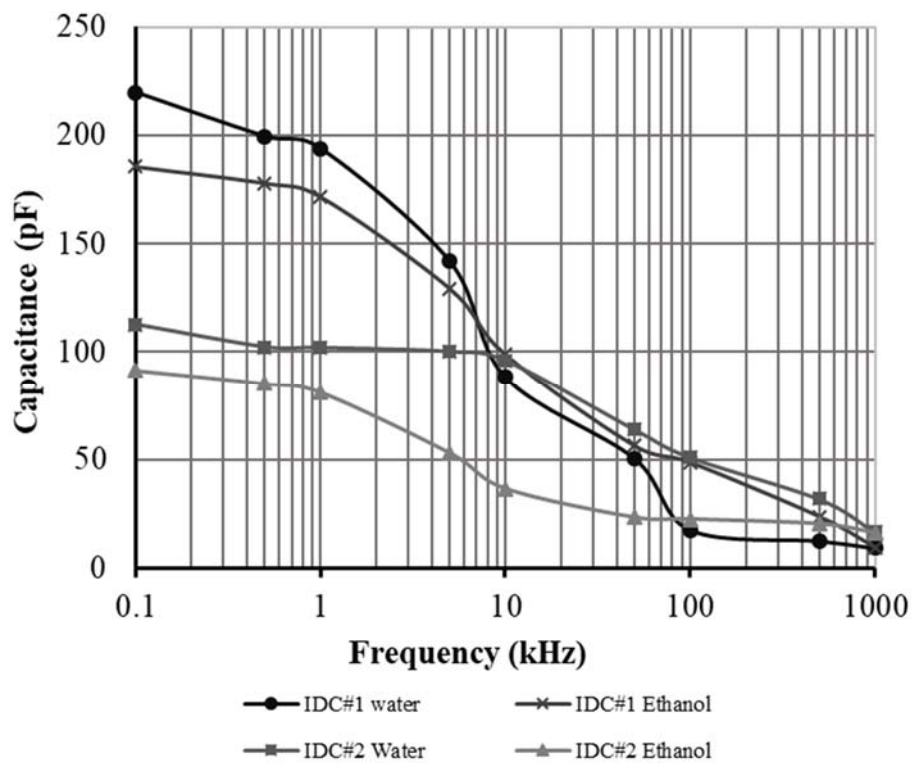


Figure 6.11 Frequency response of IDC #1 and #2 in pure water and pure ethanol. Frequency sweep range was 100 Hz to 1 MHz (Sinar & Knopf, 2014).

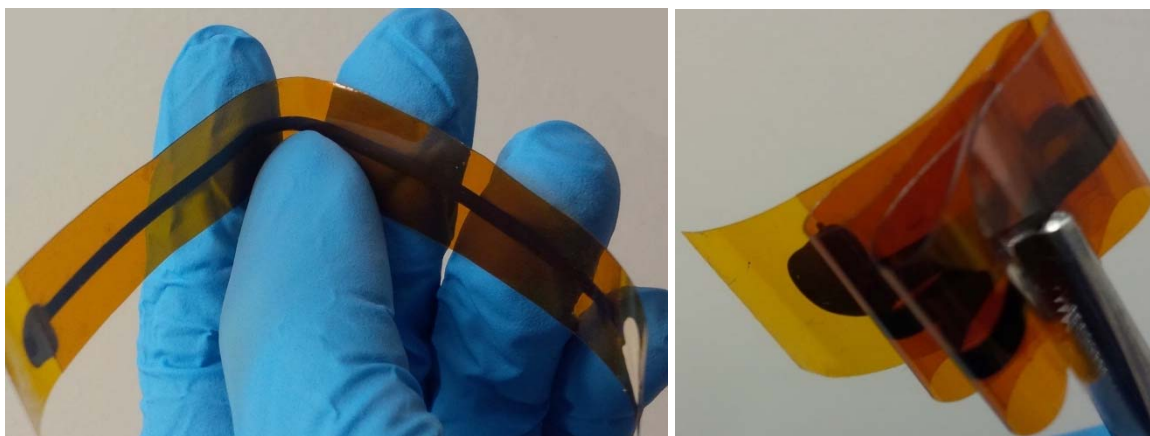


Figure 6.12 Extreme folding of 11 cm long Graphene electrode. Baseline sheet resistance was $66 \Omega/\text{sq}$ (Sinar & Knopf, 2014).

6.4 Fabrication and Characterization of Passive Electrical Filter Circuits

Electronic filters are crucial device components where they are used to remove noise or unwanted signal from output. Some of the common applications of filter circuits are audio equipment, RFID antennas, and other radio signal dependent devices, and sensors. Electronic filters are designed using either passive components (e.g. resistors, capacitors, inductors) or active components (e.g. transistors, FETs and Op-Amps). One of the most basic, and yet important, filters for communication and control circuits is the low-pass filter (LPF) that attenuates high frequency signals usually associated with carrier or noise. The cut-off frequency (f_c) depends upon the components used in the design. For example, in low frequency applications ($f < 100\text{kHz}$), passive filters are often constructed using simple resistor-capacitor (RC) circuits while for higher frequency low-pass filters ($f > 100\text{kHz}$) these circuits are usually constructed using passive resistors, capacitors and inductors (RLC). Since, construction of passive electrical filters requires combined use of more than one electrical component, it was determined to be a good demonstration for G-CMC's use for building thin film circuits. This section focuses on theory of passive electrical filters, fabrication of various G-CMC low pass filters, and characterization of fabricated passive filter devices.

The simplest LPF for low frequency applications is the 1st-order passive RC circuit shown in Fig. 6.13. The resistance is independent of frequency variations in the AC signal while the capacitance changes with frequency. Since the circuit has only one reactive component, the capacitor, the circuit is called a one-pole or first-order filter. The capacitor requires a specified amount of time to charge and discharge through the resistor. At low signal frequencies there is sufficient time for the capacitor charge up to the input voltage (V_{in}). However, at high frequencies the capacitor will not have enough time to fully charge before the input AC signal switches direction. To maintain the capacitance (C) value in the circuit, the capacitor will oppose these small fluctuations in current flow. The opposition to the current flow in the circuit is called impedance. In other words, the capacitive reactance (X_C) is inversely proportional to the frequency (f) applied to the circuit and can be described as

$$X_c = \frac{1}{2\pi fC} \quad (6.7)$$

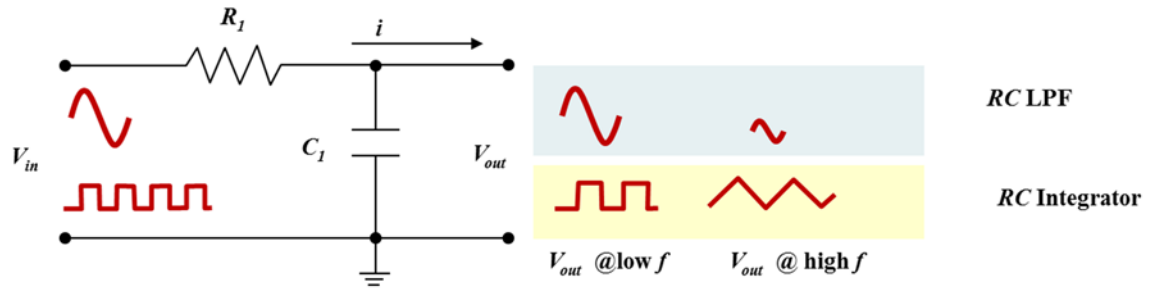


Figure 6.13 Passive 1st-order RC low-pass filter (RC-FO) for attenuating higher frequencies ($f > f_c$) or performing wave shaping (i.e. RC integrator circuit) (Sinar & Knopf, 2018a).

Since the 1st-order RC LPF (RC-FO) is constructed from one resistor (R) and one capacitor (C), the overall impedance (Z) impedance can be calculated as

$$Z = \sqrt{R^2 + X_C^2} \quad (6.8)$$

where impedance, resistance, and capacitive reactance are all given in ohms (Ω). Note that R is stable and fixed whereas the X_c varies with respect to the input voltage signal.

The voltage drop across the capacitor (V_{out}) is dependent on capacitive reactance and circuit impedance. The RC potential voltage divider equation can be given as

$$\frac{V_{out}}{V_{in}} = \frac{X_C}{\sqrt{R^2 + X_C^2}} = \frac{X_c}{Z} \quad (6.9)$$

where V_{in} is the input voltage signal. By using (Eqn. 6.9) it is possible to calculate V_{out} at any applied frequency (f).

The magnitude of the gain of the 1st-order RC LPF in decibels is given as $|f|_{dB}$ and can be calculated as

$$|f|_{dB} = 20 \log \frac{V_{out}}{V_{in}} \quad (6.10)$$

The output of the low pass filter in the frequency domain is constant until the frequency levels reach the cut-off frequency (f_c). The cut-off frequency depends on the values of resistor and capacitor and can be written as

$$f_c = \frac{1}{2\pi RC} \quad (6.11)$$

where C is given in Farads, R in Ohms and f_c in Hz. At f_c the output signal (V_{out}) is 70.7% of the input signal (V_{in}), and gradually decreases to zero as frequencies increase. This cut off point will occur when the resistance and the capacitive reactance are equal ($R = X_c$) and, at this point, the input signal is attenuated by -3dB/decade. The gain will further decrease along with the output voltage after the cut off frequency where the slope reaches a roll-off point that occurs at $\Delta L = -20$ dB/decade.

The time constant (τ) of a series RC circuit is defined as the time taken by the capacitor to charge up to 63.2% of the final steady state value and given by

$$\tau = \frac{1}{2\pi f_c} = RC \quad (6.12)$$

Note that the time constant is also defined as the time taken by the capacitor to discharge to 36.8% of steady state value.

In addition to attenuating high frequency sinusoidal signals, the basic RC LPF can act as a wave shaping circuit for a square wave input. This type of LPF circuit, sometimes called a RC integrator circuit, can convert the square wave to a triangular waveform. At low frequencies the output signal will emulate the square wave input. However, as the frequency increases the output waveform takes on a triangular shape because of the capacitor's inability to instantly charge and discharge. The amplitude of the output signal will also decrease. If the τ is long compared to the time period of the input waveform (V_{in}), then the resultant output waveform (V_{out}) will be triangular in shape and the higher the input frequency the lower will be the output amplitude compared to input.

Sometimes a single stage LPF may not enough to remove all unwanted frequencies, then second order (2nd-order) filters are used (Fig. 6.14). The 2nd-order RC low pass filters (RC-SO) are constructed by cascading two 1st-order RC LPFs. In contrast to a 1st-order RC LPF, this type of filter produces a slope of -40dB/decade. It is possible to create even higher-order filters by connecting more 1st-order RC LPFs resulting in a RC filter circuit known as an n th-order LPF with a roll-off slope of

$$\Delta L_{Total} = n\Delta L = n\left(-\frac{20dB}{decade}\right) \quad (6.13)$$

Unfortunately, these higher-order *RC* LPFs can introduce problems because the gain and accuracy of the final filter design declines with increasing order. When identical *RC* LPFs are cascaded in series, the output gain at the required cut-off frequency (f_c) is attenuated and the roll-off slope ΔL_{total} increases in relation to the number of stages (n). For example, the cut-off frequency of a 2nd-order *RC* low-pass filter (i.e. *RC-SO*) is given as

$$f_c = \frac{1}{2\pi\sqrt{R_1C_1R_2C_2}} \quad (6.14)$$

Note that cascading passive *RC* LPFs to produce larger-order filters is difficult to accurately create because the dynamic impedance of each constituent filter will affect the neighboring filters in the network. However, to reduce the impact of loading it is possible to adjust the impedance of each successive stage by a factor of 10

$$R_2 = 10 \times R_1 \quad (6.15)$$

$$C_2 = 10 \times C_1 \quad (6.16)$$

In terms of printable electronics, the resistors are often given as conductive traces where the resistivity varies with geometrical dimensions such as length, width and film thickness. Often, increase in electrical resistivity is achieved by increasing the length of the trace. It is important to realize, however, that the droplet deposition printing methods do not create uniform thin films similar to those achieved using photolithography or chemical vapor deposition (CVD) methods. Therefore, highly precise resistance values are nearly impossible to obtain with inkjet printing. Yet, based on (Eqn. 6.11), impact of low precision components can be small if a sufficiently low margin of error can be achieved. Capacitor components of an *RC* LPF circuit are traditionally ceramic types with double plate format. Double plate capacitive components are especially difficult to fabricate due to pin holes. Inkjet printed thin films are formed by smaller particles and are permeable. Their surfaces are also rougher as individual sheets/particles can stick out in an angle or even in vertical orientation (See Figure 2.7). If second layer of different material, such as an insulator, is inkjet printed over this first layer, second layer will diffuse into first layer and some of the particles from first layer will

stick through. This phenomenon will repeat if a third layer, such as a conductive layer, is inkjet printed over the second layer. Due to diffusion of third layer into second (and even the first layer, if layers are very thin) and sheets/particles sticking through layers, capacitor device will short circuit. Hence, for this research, IDC presented in Section 6.1 was used as the capacitive component.

6.4.1 Low Pass Filter Fabrication

All G-CMC LPF circuitry was inkjet printed 10 times using the methods detailed in Chapter 3 and 4. Substrates (HN polyimide) were prepared according to Section 4.2. Based on previous data, this would correspond to approximately 250 to 300 nm film thickness. Printed circuits were heat treated in an Argon environment at 320°C for 30 mins to partially decompose the CMC. Note that decomposition of CMC increases conductivity roughly 2 times. Once heat treatment was finished, circuits were covered with a second layer of polyimide with silicone adhesive on the side facing the RC components. Exposed contact pads were covered with small amount of silver paste to allow stable connection to Agilent arbitrary waveform generator and Agilent DSO oscilloscope.

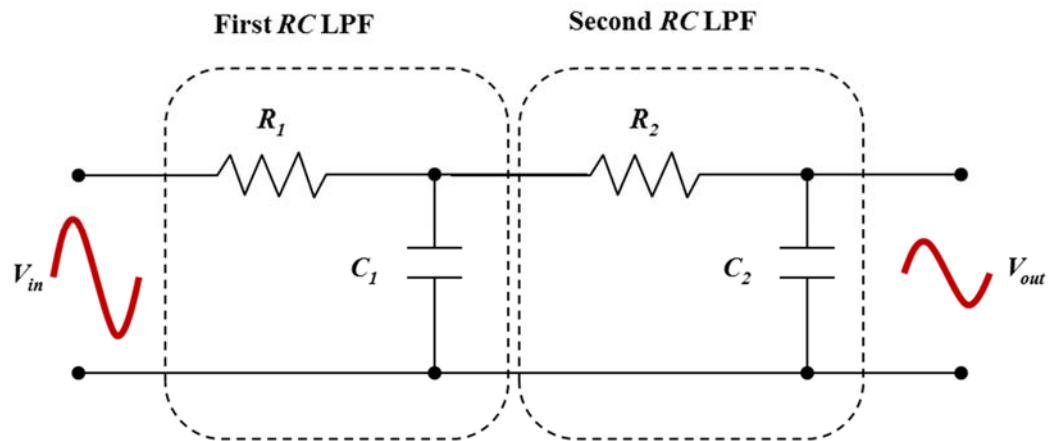
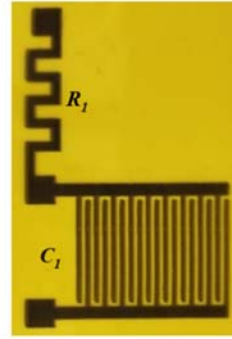
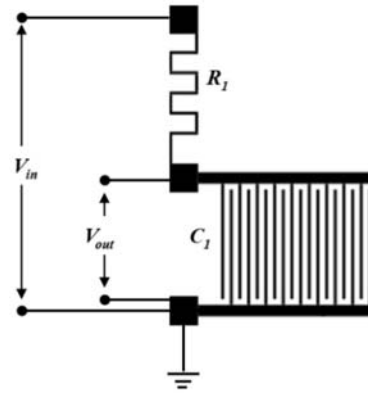


Figure 6.14 Illustration of cascading two 1st-order RC low pass filters (RC-FO1 and RC-FO2) to obtain a 2nd-order RC low pass filter (RC-SO) (Sinar & Knopf, 2018a).

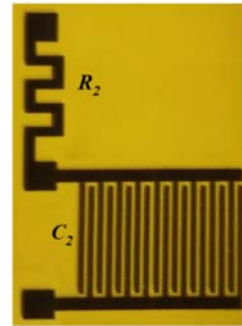
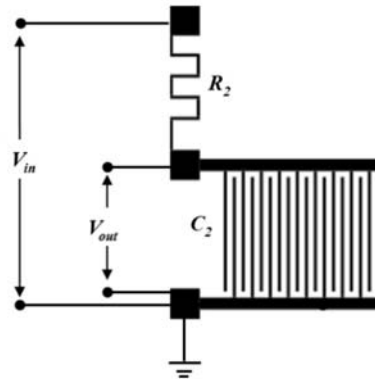
Several passive filters were inkjet-printed for analysis: 1st-order G-CMC low pass filter #1 (G-FO1), 1st-order G-CMC low pass filter #2 (G-FO2), and 2nd-order G-CMC low pass filter (G-SO). The two first-order LPFs were variant designs. For G-FO2 and G-SO, filter circuits were fabricated with a different R values to demonstrate degree of control on f_c . The R , C , τ and f_c values for each inkjet-printed G-CMC filter are summarized in Table 6.2. Schematics of these all filter circuits are depicted in Figure 6.15. The R for variant designs was adjusted simply increasing length of the resistive trace. Note that the trace resistance increases with increasing length and decreasing width or film thickness. Additional two circuits were constructed on a breadboard using conventional R and C components. R and C component values of these circuits were chosen to closely match the R and C components of G-CMC based devices.

Table 6.2 Resistance (R), capacitance (C), time constant (τ) and cut-off frequency (f_c) for printed G-CMC passive filters

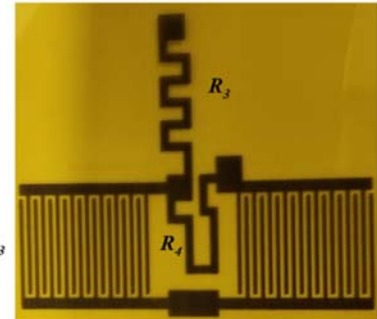
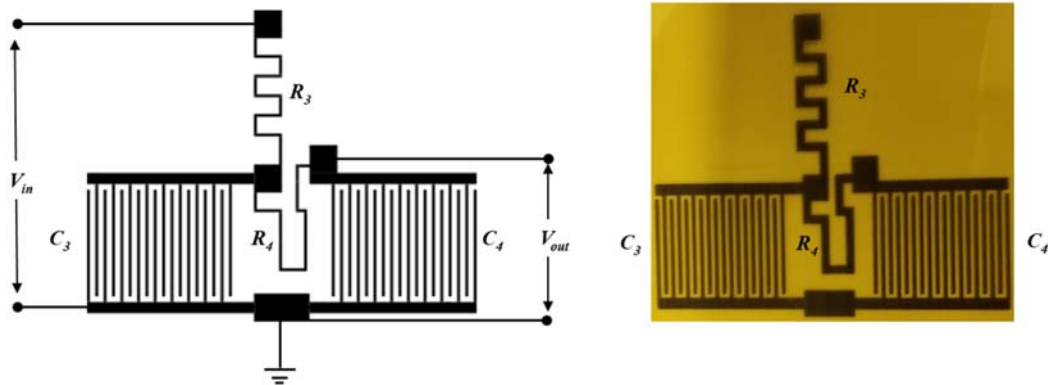
Component	G-FO1	G-FO2	G-SO
R (k Ω)	290	317.5	520
C (pF)	18	18	18
τ (μ sec)	5.22	5.72	9.36
f_c (kHz)	30.5	27.8	8



(a) 1st-order G-CMC low pass filter #1 (G-FO1)



(b) 1st-order G-CMC low pass filter #2 (G-FO2)



(c) 2nd-order G-CMC low pass filter (G-SO)

Figure 6.15 First-order G-CMC low pass filters (a) G-FO1 and (b) G-FO2, and second-order G-CMC low pass filter (c) G-SO circuits and the corresponding inkjet-printed devices based on these designs (Sinar & Knopf, 2018a).

6.4.2 Experimental Results

The frequency response of the passive filter circuits was analyzed by supplying a sinusoidal signal with 1 V_{pp} amplitude. Output Voltage was measured with the oscilloscope and mean V_{out} was recorded for each data point (10 Hz to 1 MHz). G-CMC based low pass filters exhibited diminishing V_{out} at their designated cutoff frequency (f_c). G-FO1 had a calculated f_c of ~30.5 kHz while the variant G-FO2 was fabricated with a different R value to observe sensitivity of device to changing component parameters. The f_c of G-FO2 was calculated to be 27.8 kHz. Measured f_c of filter G-FO2 was shifted as expected due to larger R . Both G-FO1 and G-FO2 filters performed as expected from passive electrical filters in low pass configuration (Fig. 6.16).

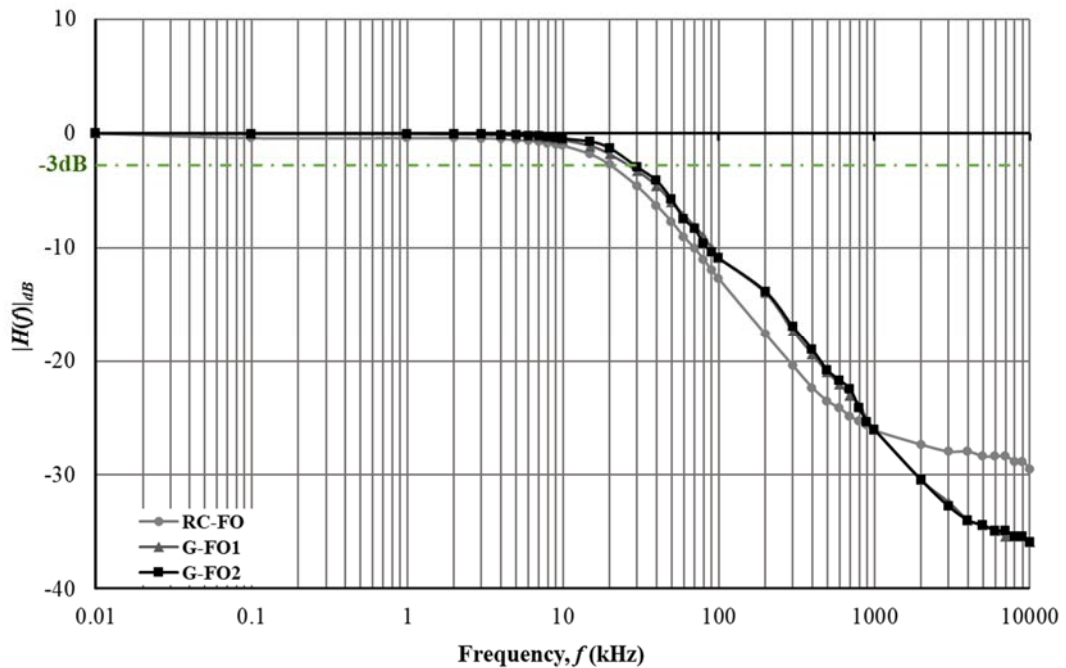


Figure 6.16 First order low pass filter performance of RC-FO, G-FO1 and G-FO2. Note that the f_c was same for both G-CMC circuits and roll off rate was lower than the conventional RC low pass filter (Sinar & Knopf, 2018a).

A conventional RC passive filter was also constructed using the same R and C values for G-FO1. Frequency response of RC-FO and G-FO1 did not differ significantly with both filters exhibiting diminishing V_{out} at near their designated f_c . Roll-off rate was essentially identical for both G-FO1 and G-FO2 and slightly less than RC-FO (Table 6.3). For G-FO1 and G-FO2, a small irregularity in frequency response was observed at around 120 kHz. Since same C design was used for both filters, this is thought to be a consequence of IDCs frequency dependent capacitance value.

A second order passive filter (G-SO) was also fabricated and characterized separately (Fig. 6.17). Calculated f_c of G-SO was around 8 kHz. A small decrease was observed for G-SO V_{out} . Similar irregularity was also observed for second order filter constructed from conventional RC components (RC-SO) as well, albeit at a smaller magnitude. Roll-off rate of G-SO and RC-SO filters were 15.2 and 18.8 db/decade, respectively. The f_c of G-SO showed slight shift (approximately 1 kHz) compared to RC-SO despite similar component values.

The transient response of both G-CMC and conventional passive electrical filters was also investigated using a square wave with 1 V amplitude. Transient response was observed for both low (1 kHz) and high frequency regimes. For high frequency regime, which is defined here as frequencies at and beyond f_c , square wave inputs were effectively converted to triangular signals for both G and RC conventional filters. Hence, all filters performed as expected from RC integrator circuits. Change in waveform below and above f_c can be observed in Figure 6.18.

Table 6.3 Roll-off rate comparison of G-CMC passive electrical filters (Sinar & Knopf, 2018a).

ΔL (db/decade)	G-FO	G-SO
Off-the-Shelf RC Circuit	15.8	18.8
G-CMC Printed RC Circuit	14.4	15.2

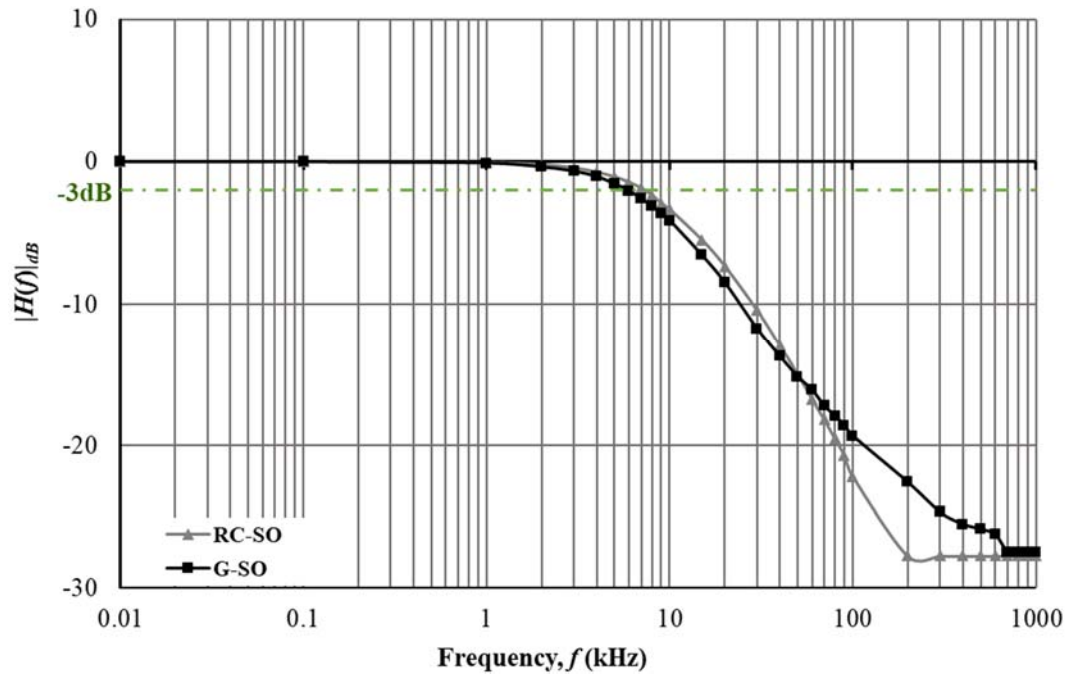
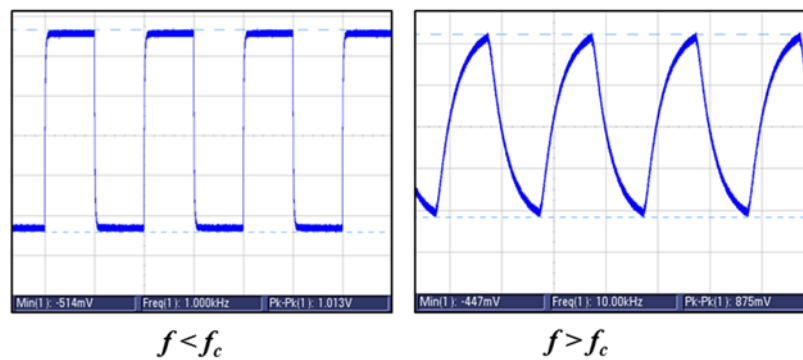
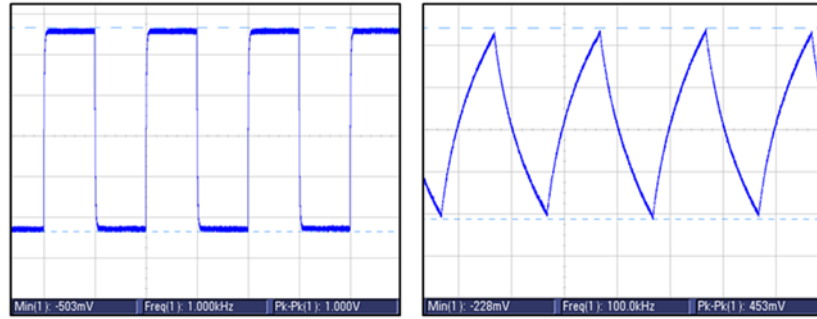


Figure 6.17 Comparison of 2nd-order G-CMC low pass filter performance with equivalent conventional RC circuit. Note that the second order filter roll-off rate was roughly twice of first order circuit. As expected, f_c value did not differ between first and second order low pass filters (Sinar & Knopf, 2018a).



(a) 1st-order RC integrator (RC-FO)

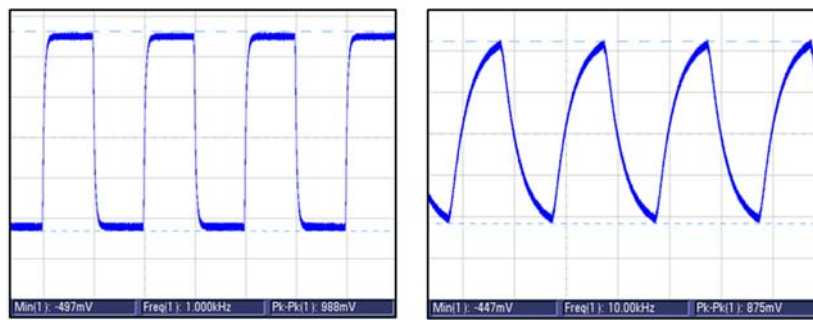
Figure 6.18 (continued)



$$f < f_c$$

$$f > f_c$$

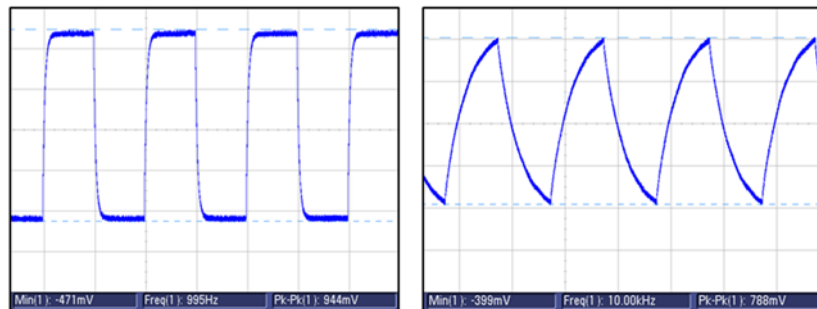
(b) 1st-order G-CMC integrator (G-FO1)



$$f < f_c$$

$$f > f_c$$

(c) 2nd-order RC integrator (RC-SO)



$$f < f_c$$

$$f > f_c$$

(d) 2nd-order G-CMC integrator (G-SO)

Figure 6.18 Comparison of transient response for (a) 1st-order RC integrator, (b) 1st-order G-CMC integrator, (c) 2nd-order RC integrator, and (d) 2nd-order G-CMC integrator. As expected, output signal was a square wave (left-side) below f_c . Beyond f_c , signal was converted to a triangular wave (right-side) (Sinar & Knopf, 2018a).

6.4.3 Mechanical Bending Performance

Shape conformable and wearable electronics should not only perform under mechanical stress but also behave in an expected way. In the case of passive filters, a large variation in capacitance and/or resistance of the circuit would cause a large shift at f_c during strain. This could potentially cause device failures. To assess the f_c error margins due to bending stress, each device was analyzed while being rolled into a cylinder. The frequency response of each device was analyzed to observe the magnitude of shift at V_{out} values. No measurable change was observed in the frequency response for any G based filter device. On the other hand, it was possible to manipulate frequency response by placing a finger, or a foreign object, on the IDC capacitor. This behavior is expected as IDCs can capacitively sense nearby objects based on their dielectric constants. In this case, f_c was observed to shift to 5 kHz for G-FO1 which was also supported by mathematical calculations (Fig. 6.19). Since flexible microcontrollers are beyond current technological capabilities, ability to manipulate f_c of filters by remote sensing could provide a unique opportunity to fabricate active filter circuits with simple RC components.

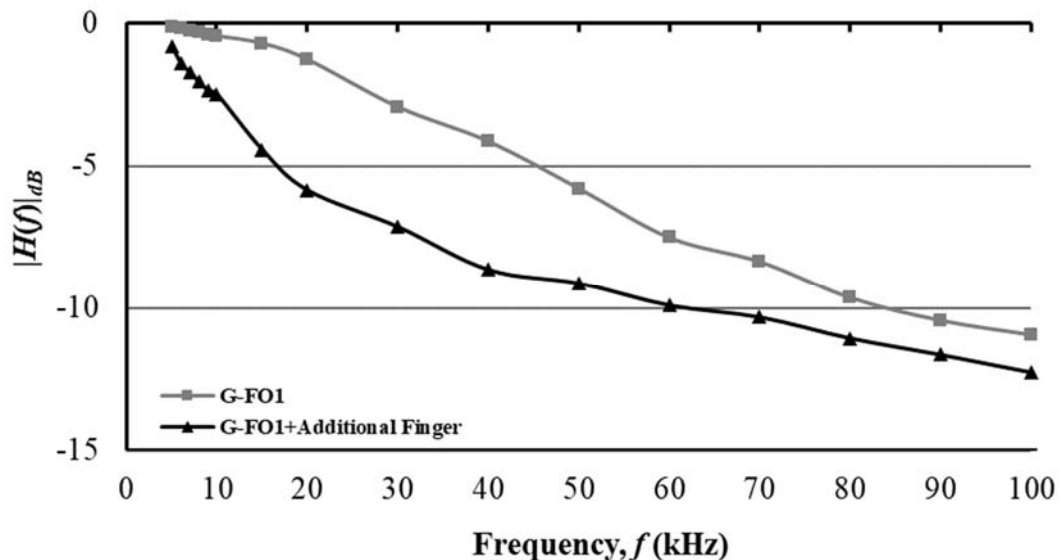


Figure 6.19 Due to increase in capacitance of component C (i.e. a foreign object or finger), the frequency response of the G-FO1 changes. With a finger on C component, f_c of G-FO1 shifted from 30.5 kHz to 5 kHz (Sinar & Knopf, 2018a).

6.5 Fabrication and Characterization of G-CMC pH Sensor

In recent years, researchers have been working on developing methods for fabrication of wearable technologies that can monitor users for various health conditions. Monitoring of bodily fluids, namely urine, sweat, and saliva, can provide hints about the health status of the user without use of invasive procedures. In order to incorporate biochemical sensors into wearable devices, they need to be affordable, mechanically robust, and easy to fabricate. In addition, the electronic circuitry and signal transducers for creating these disposable bio-sensing devices must be biocompatible. Finally, wearable biosensors are expected to adhere to non-rigid bendable surfaces such as a bandage or drainage bag. This means repeated bending/unbending due to user body movement.

Wearable biosensing technology is one of the areas where G devices can make an impact due to G's mechanical robustness and biocompatibility. Furthermore, proposed G-CMC and DOD deposition methods can fulfill the affordability and easy fabrication requirements. Hence, a simple pH sensor was designed to be fabricated on PDMS substrates. Following sections provide details on impact of disease status on pH of bodily fluids, synthesis of a pH sensitive hydrogel, use of this hydrogel to fabricate the pH sensing G-CMC sensor, and device performance.

6.5.1 Hydrogel Synthesis and Device Assembly

All biochemical processes in the body are influenced by the level of acidity (pH). Changes in the pH of a body fluid can indicate a chronic condition or the onset of infection. For example, high or low urine pH can be indication of serious medical conditions such as acidosis, diabetes, dehydration, urinary tract obstruction, chronic renal failure, and respiratory diseases. Furthermore, consistently low urine pH has been suggested as a possible indication for metabolic syndrome in otherwise healthy adults (Maalouf, Cameron, Moe, Adams-Huet, & Sakhaee, 2007). In this regard, the continual monitoring of the skin pH during wound healing and tracking the changes in pH of fluid excretions captured in a urinary catheter drainage bag represent two clinical applications for pH responsive biosensors.

One of the important drawback of biosensors is their functional longevity. Many bioactive molecules and/or enzymes quickly degrade in room temperature which causes biosensor to malfunction. In this study, alternative approach was used. In this approach, a pH sensitive hydrogel membrane was placed upon a G-CMC IDC sensor. With change in pH, hydrogel is expected to expand or contract, indirectly affecting capacitance of the underlying IDC in the process. This change in capacitance can be detected and related to a pH value.

Due to its biocompatibility, PDMS was the material of choice as the substrate. PDMS substrates were produced using SYLGARD 184 elastomer kit. After mixing the base and curing agent at 10:1 ratio, mixture was mixed for 5 minutes and then degassed. Next, degassed mixture was poured into a circular non-stick pan and placed onto a hot plate at 85°C. Cured PDMS substrates were removed from non-stick pan after 3 hours without use of removal agents. Surface treatment of PDMS substrates present a unique challenge. PDMS has a low surface energy (20.4 dyne/cm) which must be addressed before G-CMC IDC can be deposited. In addition, PDMS is a self-healing material. When PDMS surface is treated with one of the common methods, such as plasma treatment (Kim & Jeong, 2011), corona treatment (Zhu, Otsubo, Honda, & Tanaka, 2006), and surface silanization (Sui et al., 2006), hydrophilic functional groups form on the surface as expected. On the other hand, due to its self-healing properties, PDMS molecules shift towards the surface and replace functional groups with hydrophobic silicone. During this study, it was observed that even the most aggressive treatment with corona discharge was reversed in about 30 minutes. PDMS surface can rapidly heal itself, because layer of functional groups from treatment is atomically thin. Yet, PDMS self-healing process can be significantly slowed down, if applied layer is sufficiently thick.

Thus, substrate treatment previously used for glass and polyimide substrates was especially effective at functionalizing PDMS substrate. The surface wettability of the PDMS substrate was improved in this research by treating substrates according to the method detailed in Section 4.2. No additional modifications were done to the original substrate treatment method. Once the PDMS substrate was treated, G-CMC IDC was inkjet printed using the methods detailed in Section 4.1. Conductive silver epoxy was used to connect metal cabling to the designated contact points on IDC. After drying the silver epoxy on the hot plate, another SYLGARD 184 mixture was prepared with the same base/curing agent ratio. After degassing this mixture, it was poured over the printed surface and allowed to spread evenly on the whole

substrate surface. During this step, a metal mold was pressed against non-cured PDMS to form a circular area for hydrogel placement and anchoring surface to hold the hydrogel in place (Fig. 6.20). This second PDMS layer was allowed to be cured for three hours.

Hydrogels are cross-linked polymer networks that swell (enlarge) or deswell (shrink) in response to changes in moisture, salinity, temperature, glucose concentration, and pH. The expansion mechanism of the hydrogel to variations in pH can be described by principles of Fickian and anomalous diffusion (Goycoolea et al., 2003; Ostrowska-Czubenko, Gierszewska, & Pierog, 2015; Wei, Luo, Fu, Zhang, & Ma, 2012) because the gel swelling arises from water molecular diffusion into the network causing the gap between two cross-linked chains to increase (Wei, Luo, et al., 2012; Qu, Wirsén, & Albertsson, 1999). A simple pH sensitive biosensor can, therefore, be created by placing a hydrogel layer above the conductive IDC electrodes such that the expansion/contraction of the gel changes the circuit capacitance or inductance. During experimental testing, the hydrogel would swell/de-swell in response to changes in pH and, correspondingly, modify the gel's coverage over the interdigitated electrodes. The changes in surface coverage are detected as measurable changes in circuit capacitance.

Once the G-CMC IDC structure was ready, a biocompatible pH-sensitive chitosan hydrogel was chemically synthesized to be fixed on top of the sensor area. The hydrogel was created by dissolving 0.2 gr chitosan (medium M_w) in a diluted acetic acid solution (1% vol.). After a brief bath sonication (< 5 mins) N,N'-Methylene-bisacrylamide (MBa) was added to the solution as the crosslinking agent. The hydrogel was then cast onto the 3D patterned area on the IDC to anchor the gel to the device. The hydrogel was allowed to dry on the IDC sensor for 6 hours. Once dry, the hydrogel was removed and submersed in methanol for 5 hours. Finally, the hydrogel was submerged in DI water for 30 mins and dried on a hot plate. It was observed that 3D molded anchor was able to keep hydrogel in place even after its complete drying and shrinkage (Fig. 6.21). Methanol bath step removes non-crosslinked polymers from hydrogel, improves its performance and durability.

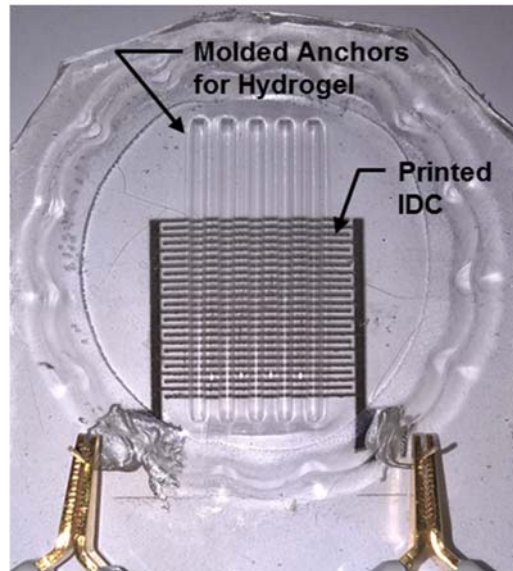


Figure 6.20 The pH sensitive hydrogel was poured over the IDC area and allowed to anchor the 3D molded zone. After the pour, hydrogel was allowed to crosslink on the hot plate for 6 hours (Knopf & Sinar, 2017).

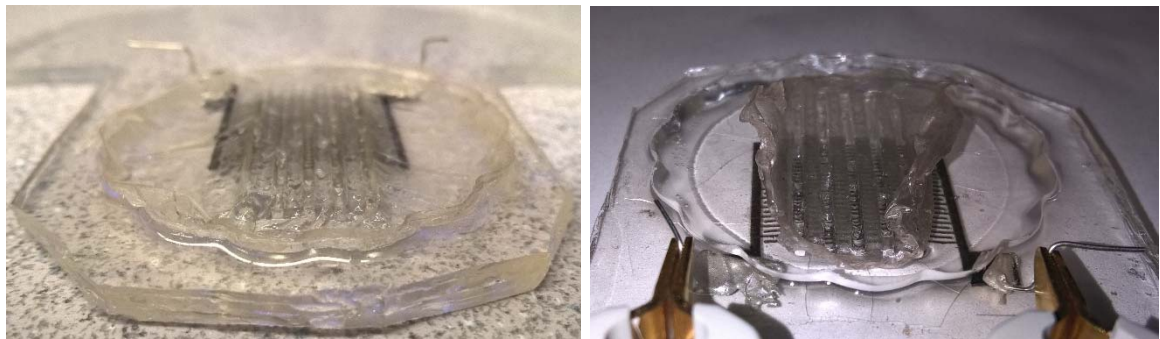


Figure 6.21 The pH sensitive hydrogel on G-CMC IDC before (left) and after (right) drying on hot plate. Anchoring pattern keep hydrogel in place even when hydrogel was completely dry (Knopf & Sinar, 2017).

6.5.2 Experimental Results

The experimental prototype of the hydrogel actuated G-CMC biosensor consists of a twelve electrode interdigitated capacitor where $l = 20$ mm, $w = 0.5$ mm, and $d = 0.5$ mm. The number of unit cells in the IDC design is $(n-1) = 11$. The capacitance and frequency response characteristics for the biosensor were investigated for a number of different environmental

conditions with and without the pH responsive hydrogel layer. All measurements were acquired using an HP 4284a LCR meter with 1 V excitation at a frequency range of 100 Hz to 1 MHz. Before the PDMS passivation layer was deposited on the electrodes, the air exposed IDC sensor had a measured capacitance of 9.2 pF at 1 kHz.

The first set of experiments on the G-CMC IDC biosensor was performed without the presence of the hydrogel layer acting as a pH transducer. The tests involved exposing the biosensor to air, DI water, and three standardized buffer solutions (pH 4, 7 and 10). The DI water and buffer solutions were injected directly into the sensor channels. Each channel accommodates 55 μL of liquid before overflowing. A total of 275 μL was used for each test. A separate baseline test was also performed to examine the capacitance when a dry hydrogel was placed directly onto the IDC electrodes.

The measured capacitance of the biosensor, without the hydrogel transducer, to these various baseline conditions and solutions is shown in Fig. 6.22. In general, the IDC response for all test samples exhibited similar frequency behavior with a higher capacitance at lower frequencies and a significant drop at ~ 20 kHz. Only slight changes in capacitance from air-only were observed when liquid was directly deposited on the IDC electrodes. The slight increase in capacitance at low frequencies for liquids was $< 6\%$. However, at high frequencies (~ 1 MHz) the deviation from air-exposed capacitance value was more pronounced (35%). Furthermore, filling the areas around the IDC with additional liquid did not affect capacitance values at any frequency. Finally, the dry hydrogel layer showed only minor differences in capacitance.

The second set of experiments required the hydrogel to be immobilized over the electrodes of the G-CMC IDC biosensor. The hydrogel actuated biosensor was then exposed to several buffer solutions with different pH values (pH 4, 7, and 10). Each pH solution was carefully spread at a volume of 1.5 mL onto the active sensor area. The chitosan hydrogel reacted to pH quickly and, therefore, change in capacitance was measurable within a few minutes after the solution was introduced. To prevent cross-contamination after each test, the hydrogel was washed with DI water and left to dry on a hot plate at low temperature (50°C) before reuse. The measured capacitance of the hydrogel actuated biosensor to the buffer solutions is shown in Fig. 6.23. As expected, the volume of the hydrogel significantly increased

(i.e. swell) for low pH and the measured capacitance was much higher at low frequencies (< 10 kHz) than a solution with a high pH.

Table 6.4 provides a summary of the capacitive behavior of the proposed G-CMC IDC biosensor at specific frequencies. Although changes in capacitance were measurable at every frequency, the sensor response was stronger for lower frequencies (< 10 kHz). This is an expected result for IDC based sensors. The frequency response of the IDC is also dependent on geometrical parameters of the design where physically smaller sensors provide higher capacitance values at high frequency excitation compared to larger IDCs at the same frequency. The fabrication methods discussed in this paper are scale independent and can be used to fabricate these smaller sensors. Another way to improving sensitivity would be through increasing number of electrodes that IDC has. This can be achieved through either a higher resolution printhead or through laser micromachining fine features using the methods detailed in Chapter 5.

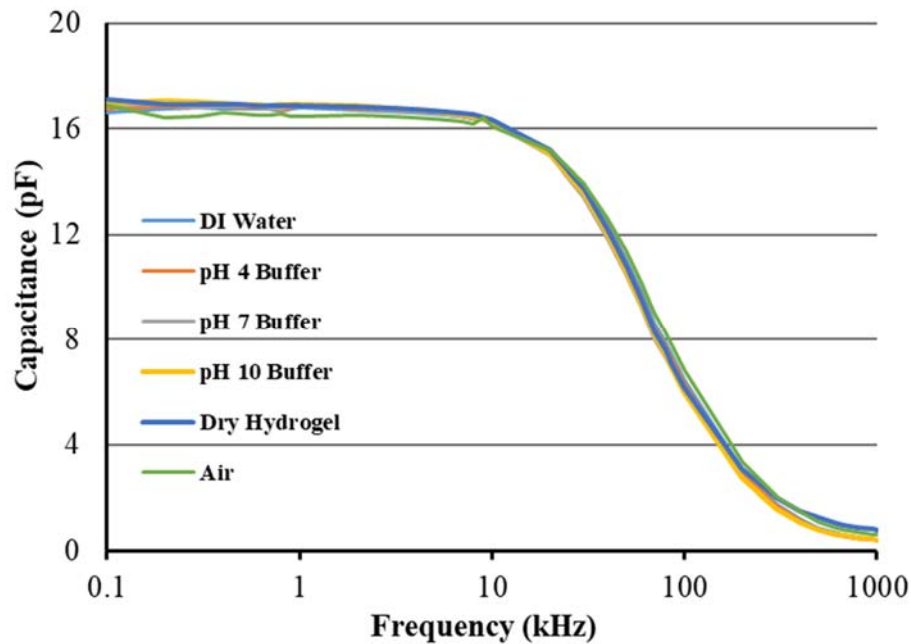


Figure 6.22 Frequency response of IDC biosensor, without the pH responsive hydrogel, to various baseline conditions and solutions (Knopf & Sinar, 2017).

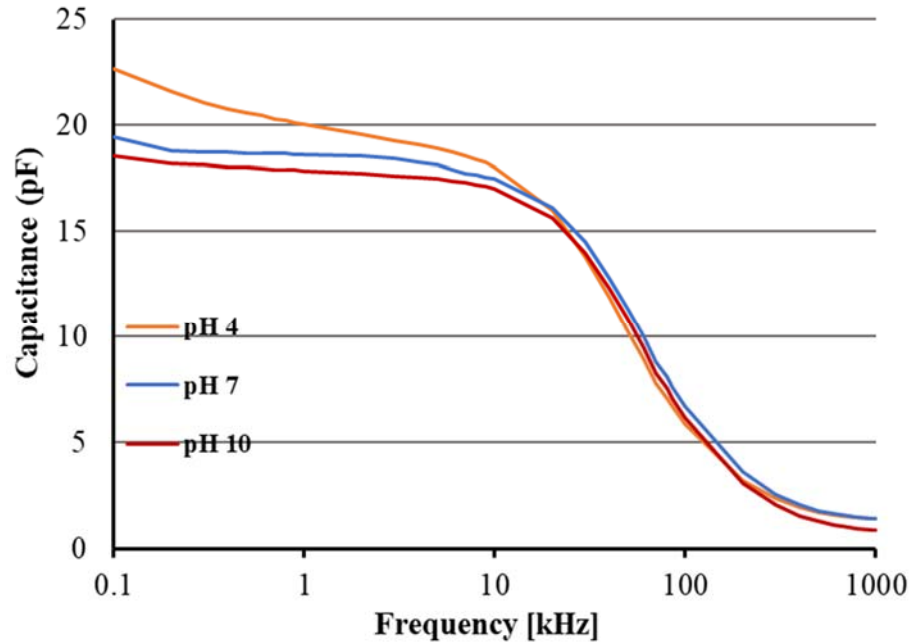


Figure 6.23 Frequency response of hydrogel actuated G-CMC IDC biosensor to standardized buffer solutions with various pH (Knopf & Sinar, 2017).

Table 6.4 Measured capacitance of fluids using G-CMC IDC (Knopf & Sinar, 2017).

Freq. (kHz)	Measured Capacitance (pF)					
	Air	DI Water	Dry Hydrogel	pH 4	pH 7	pH 10
0.10	16.91	16.59	17.09	22.68	19.42	18.57
1	16.45	16.80	16.87	20.21	18.63	17.85
10	16.06	16.24	16.35	18.03	17.46	17
100	6.81	6.43	6.18	5.87	6.71	6.16
1000	0.60	0.42	0.79	1.42	1.42	0.87

6.6 Concluding Remarks

The various devices presented in this study performed as expected when compared to circuits constructed from traditional discrete components. On the other hand, major benefit of these devices was mechanical flexibility and ability to function under mechanical stress. As a result, all device examples could be viable as a part of a wearable technology.

Through utilizing methods explained in Chapters 3 to 5, it was possible to fabricate capacitive touchpads, resistors and IDCs. Graphene-CMC capacitive touchpads were successfully used to simulate touch buttons to operate an LED and to operate piano buttons to produce sound. Graphene-CMC resistors were fabricated with $< 1000 \Omega$ to $\sim 1 \text{ M}\Omega$ bulk resistance, depending on circuit requirements. The resistance values were adjusted by depositing G-CMC traces with varying lengths and widths. Interdigitated capacitors with various sizes and number of electrodes were fabricated to be used as sensors and capacitors. The IDCs usually exhibited low capacitance ($< 20 \text{ pF}$) without a foreign object in proximity or contact. When a foreign object approached, capacitance was observed to rise in agreement to the theory explained in Section 6.2. This phenomenon was utilized to sense and quantify ethanol percentage in DI water and pH values of various buffer solutions. Finally, combined use of resistors and capacitors (IDCs) was demonstrated by fabrication and characterization of first and second order passive electrical filters. The low pass filters (LPFs) exhibited similar performance to RC circuits assembled from traditional discrete components. Furthermore, illustrated LPFs were able to function while under mechanical stress.

Possible applications of DOD deposited G-CMC films are not limited with these simple examples. A number of other prototypes were also investigated during this project. Omni-directional RFID antenna is one such device. Although not presented here due to its preliminary nature, an omni-directional thin film RFID antenna was inkjet printed using G-CMC. The antenna featured a narrow band at around 1.5 GHz. Ringing was observed at other frequency ranges. In the same manner, planar waveguides can also be designed by G-CMC thin films. When it comes to thin film antenna fabrication, laser micromachining would have an emphasis due to dimensional accuracy and precision necessary for these devices to function as intended. Overall, this can be an interesting subject for a future study.

Chapter 7

Conclusions

7.1 Thesis Summary

This thesis presented a novel aqueous G ink for drop-on-demand deposition of thin film circuits and sensors on flexible and rigid substrates. Graphene is touted as an extraordinary material, which is true to an extent. However, harnessing of its true potential is out of reach for current technology. High performing G films produced by CVD can rival ITO films, yet they are technically and economically not feasible for mass production. On the other hand, G's mechanical, electrical, chemical, and optical properties can still be utilized to fabricate electronic devices through use of batch synthesis route known as liquid phase exfoliation (LPE). Liquid phase exfoliation method is a compromise where ease of ink synthesis, affordability, and flexible fabrication of thin films are emphasized over mechanical, chemical, electrical, and optical perfection of G films. Chapter 2 discussed the structure and properties of G and how it translates to inkjet printed films in detail.

Graphene is a hydrophobic material and shows affinity to a very select number of solvents. Some of these solvents are highly toxic to human health and dangerous for the environment. From an industrial point of view, solvency of a liquid must also be considered. For example, in the case of NMP, superior solvency of the chemical means swelling of plastic parts, dissolving of adhesives, and leeching of unknown chemicals from deposition system's parts into the G ink. Yet, through use of certain polymers it is possible to functionalize G surface and disperse its sheets in water. Use of an anionic polymer, Carboxymethyl Cellulose (CMC), to exfoliate and disperse G in water was described in Chapter 3. Unlike the solvents commonly used for exfoliating and dispersing G, CMC is non-toxic. In fact, it is used in food industry as a coating agent and emulsifier. Since, LPE-G is a low performer when compared to CVD-G, atomic doping and metal nanoparticle composite methods were also introduced in Chapter 3. Both methods improve electrical properties of G-CMC film without significantly

changing its optical properties. Characterization data for exfoliation products, doped films, and G-AgNP composite ink were presented in this chapter.

Liquid phase exfoliated graphene must be deposited using a DOD method. For this research, inkjet printing was chosen. Capabilities required from an inkjet printer for material deposition, necessary substrate treatment, and formulation of inkjet printable colloidal ink were detailed in Chapter 4. Requirements of a material deposition system is different than what is expected from an office inkjet printer. Hence, details for a building a custom XY plotter inkjet printer was described in this chapter. Printed films of colloidal inks often suffer from severe inhomogeneity as suspended particles tend to deposit towards droplet edges. This phenomenon is known as the Coffee Ring Effect (CRE). Tackling CRE requires a combination of effective surface treatment and ink formulation. A simple substrate treatment protocol was introduced and successfully used for preparing glass, polyimide, and PDMS surfaces for inkjet printing. Formulation of the ink directly impacts film morphology. In most cases, water's surface tension is too high for consistent wetting of surfaces. More importantly, insufficient pinning and resulting recession of water droplets causes displacement of previously deposited layers. Technical background on this subject and practical concerns were discussed and use of a simple primary alcohol (1-Propanol) to eliminate CRE was demonstrated in this chapter. Finally, electrical, mechanical, and optical performance of inkjet printed films were presented.

Post processing of deposited G-CMC and GO thin films was presented in Chapter 5. Deposited G-CMC films are functional as printed. Yet, through thermal treatment, their conductivity can be improved and solvent affinity can be altered. Graphene Oxide films require heat treatment to be functional, unless they are to be used as insulators. Since GO require high temperatures to become conductive, pulsed laser thermal treatment is preferred. Experimental results on both G-CMC and GO thermal post processing steps are detailed in this chapter. In addition, pulsed laser micromachining of thin films was introduced. Pulse laser micromachining can form fine features on deposited thin films that would not be possible through inkjet printing. Pulsed laser micromachining of a sample electrode was presented.

Chapter 6 presents several mechanically flexible capacitive sensors and electrical passive filter circuits fabricated through methods described in Chapters 3 and 4. Demonstration of device performance is crucial for novel functional inks and methodologies. First

demonstration was done by fabrication of simple Interdigitated Capacitive (IDC) sensor. This sensor was used to determine alcohol percentage in DI water systems. IDC sensor was highly sensitive to changes in alcohol-to-water ratio and provided stable and repeatable data for a large frequency range (100 kHz to 1 MHz). A biosensor was constructed using the same IDC technology and combining it with a pH sensing hydrogel. This sensor was fabricated in PDMS. The pH sensitive hydrogels subtle expansion and contraction was sensed through the IDC sensor and related to the pH of the buffer solution. Proposed sensor was able to distinguish between dry hydrogel and pH 4, 7, and 10. Finally, an RC electrical passive circuit was fabricated on polyimide substrates. Proposed passive filter was effective at removing unwanted signal in designated frequency range. It also showed mechanical robustness where it performed as expected when mechanically bend. Design methodologies of these devices and experimental results for their performance were presented in this chapter.

7.2 Thesis Contribution

The major contributions of this dissertation are synthesis of a novel non-toxic aqueous graphene ink (G-CMC) and development of methods for drop-on-demand deposition of G-CMC and its derivative inks (Au Doped and G-AgNP) in thin film form on rigid and flexible substrates. To achieve this, a complete fabrication methodology was designed from ground up that can allow fabrication of mechanically flexible thin film sensors and electrical circuitry. Presented methodology is composed of synthesis of the novel aqueous G dispersion, substrate treatment protocol, formulation of inkjet printable ink, determination of inkjet printing parameters, and post-fabrication heat treatment. Successful synthesis of novel ink and its inkjet printing required several technical developments. In addition, presented pH sensor and passive electrical filter circuit are novel additions to the field of inkjet printed G devices.

Every component of this research was developed, built, or produced in-house. Aqueous G-CMC ink was synthesized in the laboratory. Ink characterization was conducted using facilities available on Western Campus. XY plotter inkjet printer was built from scratch using the parts detailed in Chapter 4. Proposed devices were fabricated and tested in the laboratory. The major contributions of the thesis are categorized and presented in the following sections.

7.2.1 Synthesis of Aqueous Graphene and Graphene Derivative Inks

The thesis presented a novel functional ink (G-CMC) and a novel LPE method, Cyclic LPE (C-LPE), for exfoliation and dispersion of G sheets. The principle objectives in synthesis of the novel ink were summarized in Section 1.7: use of water as the solvent, use of a non-toxic and environmentally friendly polymer/surfactant for high dispersion stability, and increase of the ink yield. In addition, proposed methods had to be scalable, industry friendly, and affordable while resulting in a functional material with acceptable electrical conductivity that can produce mechanically robust thin films. Carboxymethyl cellulose functionalized G dispersion was able to fulfill these objectives in combination with C-LPE method. Carboxymethyl cellulose is a non-toxic, low-cost cellulose derivative which is used in various fields, including food industry where it is used as an emulsifier or a coating agent. Since CMC is a large molecular weight anionic polymer, it allowed highly stable dispersions of graphene. Liquid phase exfoliation is a scalable method, which is crucial for industrial adoption. Yet, yield of LPE method is low due to disposal of non-exfoliated material at the end of exfoliation cycle. Compared to LPE method, C-LPE increased final ink yield by reducing exfoliation time to 8 hours and recycling left over material at the end of each cycle. The magnitude of lattice defects as determined by Raman spectroscopy was comparable between LPE and C-LPE, while C-LPE resulted in sheets with larger lateral dimensions. Consequently, recycled raw material used for C-LPE resulted in electrically better performing inks compared to LPE. Summary of synthesis process and its comparison to other methods from the literature are presented in Chapter 3.

In addition, two different methods to improve G-CMC film electrical performance was introduced. Among these two methods, gold doping through AuCl_3 was applied to an inkjet printed G film for the first time through this research. It was seen that magnitude of improvement in electrical performance was comparable to gold doping of CVD-G. Second method, G-AgNP composite ink has the potential to be an alternative to ITO electrodes for low performance devices. It was observed that AgNPs were able to improve electrical performance more than gold doping. At 50% transparency, G-AgNP films had $374 \Omega/\text{sq}$ sheet resistance (6 prints). Composite ink preparation is not self-limiting like the gold doping process. Hence, it may be possible to deposit thicker (non-transparent) films of G-AgNP which would exhibit lower sheet resistance.

7.2.2 Inkjet Printing of Homogeneous Thin Films

Inkjet printing of homogeneous thin films can be a difficult task. This is mainly due to coffee ring effect (CRE). There are many different methods in the literature for addressing CRE. Some of these methods are very specific to dispersed material while others require strict control of nanoparticle geometry, which can be difficult. Elimination of CRE and development of deposition parameters that allow fabrication of both thinner and thicker films were part of the objectives of this research (Section 1.7).

In this research, 1-Propanol was proposed for a water/1-Propanol binary solvent system to address CRE and facilitate inkjet printing of thicker films. 1-Propanol is a primary alcohol with low toxicity and effects similar to ethanol in living beings. Homogeneous films using this solvent system was demonstrated in Chapter 4. It was possible to deposit thinner (20 nm thick at 1 print) and thicker (2000 nm thick at 100 prints) films without occurrence of CRE.

Proposition of water/1-Propanol binary solvent system is a major contribution because use of 1-Propanol in this scheme is against commonly accepted theories of binary solvent use for CRE elimination. Based on traditional thought, 1-Propanol was supposed to further deteriorate film morphology, not improve it. A theory on why water/1-Propanol binary system works and how it could be applied to other binary systems were presented in Chapter 4.

7.2.3 Fabrication of Flexible Capacitive Sensors

DOD deposition of thin film electrodes and other electronic components have been demonstrated many times in the literature. On the other hand, demonstration of thin film electronic components used for a specific task is crucial to prove viability of proposed methods. In this research, thin film capacitors in the form of Interdigitated Capacitor (IDC) as sensing elements and an IDC-Hydrogel device for pH sensing were fabricated to illustrate capabilities of G-CMC films and DOD deposition.

First, IDC remote sensors was fabricated on flexible polyimide substrates which were used to detect and quantify presence of ethanol in DI water samples. Surprisingly, capacitance of fabricated sensors and their capacitive response to ethanol/water solution were larger than

electroplated thin film metal IDCs on rigid plastic substrates. Polyimide's dielectric constant is not large (~ 3.4), hence it is thought that G's dielectric properties are the reason for this high performance.

A second IDC based sensor was fabricated on PDMS. This sensor used a pH sensitive hydrogel to indirectly measure pH of sample liquids. Based on literature review, this study is the first of its kind to feature an all G capacitive sensor that can sense the subtle changes in hydrogel dimensions to measure pH of a sample. Furthermore, proposed design can be optimized through employment of pulsed laser micromachining to increase sensitivity of the IDC sensor, which would increase sensor resolution.

7.2.4 Fabrication of RC Electrical Passive Filters for Signal Control

As it was shown in Chapter 6, it is possible deposit functioning discreet conductive/resistive traces and capacitors using G-CMC and DOD deposition. On the other hand, illustration of all G circuits featuring more than one component is a crucial step at encouraging use of proposed methods to fabricate sophisticated circuits. In this research, all Graphene first order and second order low pass filters (LPF) were demonstrated for the first time. Presented LPFs were designed as resistor-capacitor (*RC*) passive filters and performed as expected. Graphene-CMC LPFs performed comparable to solid state *RC* LPFs in the tested frequency ranges and adhered to the well established mathematical equations used for modeling passive filters. In addition, proposed filter devices were fabricated on flexible polyimide substrates and exhibited excellent mechanical robustness. Thus, proposed devices and their iterations can be parts of wearable technology applications. Passive and active electrical filters are crucial for all types of consumer electronics. These devices are used to eliminate unwanted signals from the output signal and are part of virtually any electronic device.

7.3 Limitations and Recommendations for Future Work

Current work has produced a novel non-toxic and environmentally friendly aqueous G dispersion that can be formulated with 1-Propanol to deposit both thin and thick functional films. Developed methods have been used to fabricate novel sensors and electrical filter circuits

on rigid and flexible substrate. All proposed devices performed as expected and showed excellent mechanical robustness under repeated bending. However, there are several limitations that can be addressed in future iterations of proposed methods.

7.3.1 Feature Size and Prospect of Laser Machining/Heating of Thin Films

Large droplet size and resulting large feature size of the custom XY plotter printer was the major setback in this study. Modern printheads have several hundreds of nozzles which are driven by less than 50 signal contacts (exact number depends on printhead model). Individual control of each nozzle is possible as they are connected in a multiplexed array. Consequently, it is not possible to know which contacts must receive a signal to turn on each nozzle, unless detailed pinout diagram and control matrix array are provided. In comparison, HP C6602 printhead has 12 nozzles and 13 contact points: one contact point per nozzle and one contact point for the ground. Hence, due to availability, HP C6602 was chosen as the printhead. However, thin film homogeneity, precision, and accuracy can be significantly improved by upgrading printhead of the XY plotter printer. The custom plotter printer's linear actuators are capable of moving less than 1 μm per step, hence whole system would benefit from a printhead upgrade.

In addition, pulsed laser micromachining can be employed for fabricating circuits and components. Simple square thin films can be deposited and subsequently micromachined by a pulsed laser system. This would allow fabrication of fine features beyond the capabilities of any DOD system ever built to day. For example, it would be possible to fabricate a 1 cm \times 1 cm IDC with more than 500 electrodes. With such high number of electrodes, fabricated IDC would exhibit superior sensitivity compared to printed IDCs. The prospect of pulsed laser micromachining of components had to be indefinitely postponed due to lack of access to critical equipment.

If necessary equipment can be accessed, x-ray laser micromachining can be another research field. Micromachining of submicron feature would be beneficial for sensor and RFID applications.

7.3.2 Optimization of AgNP Geometry

Proposed G-AgNP exhibited high electrical performance compared to G-CMC films due to large surface area of AgNPs. Yet, there is room for optimization in this concept. There has been reports of AgNPs as large as 4 μm lateral dimensions (Zhang, Hu, Guo, Goebel, & Yin, 2010). Composite inks with extra large AgNPs might exhibit superior electrical properties. In addition, edge truncation issue was not resolved in this study. If edge truncation can be avoided, use of extra large AgNPs may improve thin film electrical performance without increasing optical absorption. This could lead to development of a viable ITO alternative.

7.3.3 Optimization of pH sensitive Hydrogel Sensor

Proposed pH sensor proved that it is possible to sense subtle changes in hydrogel dimension with a G-IDC and related the change in capacitance to a pH values. On the other hand, signal difference between pH 4, 7, and 10 were not as large as desired. As a result, pH values in between cannot be reliably measured. It is believed that this issue can be solved through two routes. First, sensitivity of G-IDC can be improved by increasing electrode number and reducing gap between the electrodes. Second, hydrogel design can be improved. Anchor points were found to be covering too large of an area over the IDC. It is believed that a cross shaped anchor would work better by allowing hydrogel to move freely over the sensor.

7.4 Final Thoughts

The presented results demonstrate the feasibility of G-CMC/GO for DOD fabrication of flexible thin film devices. However, optimization of fabrication parameters is recommended which would significantly improve performance of proposed circuits and sensors. In particular, further research into AgNPs may allow fabrication of thin films with wavelength specific properties. Yet, methods must be developed for better control on AgNP dimensions. In addition, laser assisted post-processing of DOD deposited G-CMC films present an interesting opportunity for altering material structure and modify geometrical parameters of deposited films. This may allow fabrication of single crystal graphene films on various substrates.

Bibliography

- Acik, M., & Chabal, Y. (2012). A review on reducing graphene oxide for band gap engineering. *Journal of Materials Science Research*, 2(1), 101-112. <http://dx.doi.org/10.5539/jmsr.v2n1p101>
- Ambrosi, A., Chua, C., Bonanni, A., & Pumera, M. (2012). Lithium aluminum hydride as reducing agent for chemically reduced graphene oxides. *Chemistry of Materials*, 24(12), 2292-2298. <http://dx.doi.org/10.1021/cm300382b>
- Angkawisittpan, N., & Manasri, T. (2012). Determination of sugar content in sugar solutions using interdigital capacitor sensor. *Measurement Science Review*, 12(1), 8-13. <http://dx.doi.org/10.2478/v10048-012-0002-0>
- Axelevitch, A., Gorenstein, B., & Golan, G. (2012). Investigation of optical transmission in thin metal films. *Physics Procedia*, 32, 1-13. <http://dx.doi.org/10.1016/j.phpro.2012.03.510>
- Bagri, A., Mattevi, C., Acik, M., Chabal, Y., Chhowalla, M., & Shenoy, V. (2010). Structural evolution during the reduction of chemically derived graphene oxide. *Nature Chemistry*, 2(7), 581-587. <http://dx.doi.org/10.1038/nchem.686>
- Barone, V., Hod, O., & Scuseria, G. (2006). Electronic structure and stability of semiconducting graphene nanoribbons. *Nano Letters*, 6(12), 2748-2754. <http://dx.doi.org/10.1021/nl0617033>
- Becerril, H., Mao, J., Liu, Z., Stoltenberg, R., Bao, Z., & Chen, Y. (2008). Evaluation of solution-processed reduced graphene oxide films as transparent conductors. *ACS Nano*, 2(3), 463-470. <http://dx.doi.org/10.1021/nn700375n>
- Bepete, G., Anglaret, E., Ortolani, L., Morandi, V., Huang, K., Pénicaud, A., & Drummond, C. (2016). Surfactant-free single-layer graphene in water. *Nature Chemistry*, 9(4), 347-352. <http://dx.doi.org/10.1038/nchem.2669>
- Berggren, C., Bjarnason, B., & Johansson, G. (2001). Capacitive biosensors. *Electroanalysis*, 13(3), 173-180. [http://dx.doi.org/10.1002/1521-4109\(200103\)13:3<173::aid-elan173>3.0.co;2-b](http://dx.doi.org/10.1002/1521-4109(200103)13:3<173::aid-elan173>3.0.co;2-b)
- Boukhalov, D., & Katsnelson, M. (2008). Modeling of graphite oxide. *Journal of The American Chemical Society*, 130(32), 10697-10701. <http://dx.doi.org/10.1021/ja8021686>
- Bundy, F. (1989). Pressure-temperature phase diagram of elemental carbon. *Physica A: Statistical Mechanics and Its Applications*, 156(1), 169-178. [http://dx.doi.org/10.1016/0378-4371\(89\)90115-5](http://dx.doi.org/10.1016/0378-4371(89)90115-5)
- Candidate List of substances of very high concern for Authorization - ECHA. (2017). Echa.europa.eu. Retrieved 26 September 2017, from <https://echa.europa.eu/candidate-list-table>

- Chang, Y., Yang, S., Liu, J., Dong, E., Wang, Y., & Cao, A. et al. (2011). In vitro toxicity evaluation of graphene oxide on A549 cells. *Toxicology Letters*, 200(3), 201-210. <http://dx.doi.org/10.1016/j.toxlet.2010.11.016>
- Chen, J., Jang, C., Xiao, S., Ishigami, M., & Fuhrer, M. (2008). Intrinsic and extrinsic performance limits of graphene devices on SiO₂. *Nature Nanotechnology*, 3(4), 206-209. <http://dx.doi.org/10.1038/nnano.2008.58>
- Chen, X., Chen, C., Zhang, Z., & Xie, D. (2013). Synthesis and capacitive performance of nitrogen doped porous carbons derived from sodium carboxymethyl starch. *Powder Technology*, 246, 201-209. <http://dx.doi.org/10.1016/j.powtec.2013.05.023>
- Chen, W., Qi, D., Gao, X., & Wee, A. (2009). Surface transfer doping of semiconductors. *Progress in Surface Science*, 84(9-10), 279-321. doi: 10.1016/j.progsurf.2009.06.002
- Chung, M., Kim, D., Lee, H., Kim, T., Choi, J., & Seo, D. et al. (2012). Highly sensitive NO₂ gas sensor based on ozone treated graphene. *Sensors and Actuators B: Chemical*, 166-167, 172-176. <http://dx.doi.org/10.1016/j.snb.2012.02.036>
- Collins, G., & Buckley, L. (1996). Conductive polymer-coated fabrics for chemical sensing. *Synthetic Metals*, 78(2), 93-101. [http://dx.doi.org/10.1016/0379-6779\(96\)80108-1](http://dx.doi.org/10.1016/0379-6779(96)80108-1)
- Das Sarma, S., Adam, S., Hwang, E., & Rossi, E. (2011). Electronic transport in two-dimensional graphene. *Reviews of Modern Physics*, 83(2), 407-470. <http://dx.doi.org/10.1103/revmodphys.83.407>
- Das, A., Chakraborty, B., & Sood, A. (2008). Raman spectroscopy of graphene on different substrates and influence of defects. *Bulletin of Materials Science*, 31(3), 579-584. <http://dx.doi.org/10.1007/s12034-008-0090-5>
- Deegan, R., Bakajin, O., Dupont, T., Huber, G., Nagel, S., & Witten, T. (1997). *Nature*, 389(6653), 827-829. <http://dx.doi.org/10.1038/39827>
- Dirac, P. (1958). *The principles of quantum mechanics*. Oxford: Clarendon Press.
- Dreyer, D., Park, S., Bielawski, C., & Ruoff, R. (2010). The chemistry of graphene oxide. *Chem. Soc. Rev.*, 39(1), 228-240. <http://dx.doi.org/10.1039/b917103g>
- Dua, V., Surwade, S., Ammu, S., Agnihotra, S., Jain, S., & Roberts, K. et al. (2010). All-organic vapor sensor using inkjet-printed reduced graphene oxide. *Angewandte Chemie International Edition*, 49(12), 2154-2157. <http://dx.doi.org/10.1002/anie.200905089>
- Duch, M., Budinger, G., Liang, Y., Soberanes, S., Urich, D., & Chiarella, S. et al. (2011). Minimizing Oxidation and Stable Nanoscale dispersion improves the biocompatibility of graphene in the lung. *Nano Letters*, 11(12), 5201-5207. <http://dx.doi.org/10.1021/nl202515a>
- Eda, G., Fanchini, G., & Chhowalla, M. (2008). Large-area ultrathin films of reduced graphene oxide as a transparent and flexible electronic material. *Nature Nanotechnology*, 3(5), 270-274. <http://dx.doi.org/10.1038/nnano.2008.83>

El-Kady, M., Strong, V., Dubin, S., & Kaner, R. (2012). Laser scribing of high-performance and flexible graphene-based electrochemical capacitors. *Science*, *335*(6074), 1326-1330. <http://dx.doi.org/10.1126/science.1216744>

Endres, H., & Drost, S. (1991). Optimization of the geometry of gas-sensitive interdigital capacitors. *Sensors and Actuators B: Chemical*, *4*(1-2), 95-98. [http://dx.doi.org/10.1016/0925-4005\(91\)80182-j](http://dx.doi.org/10.1016/0925-4005(91)80182-j)

Ferrari, A. (2007). Raman spectroscopy of graphene and graphite: Disorder, electron-phonon coupling, doping and nonadiabatic effects. *Solid State Communications*, *143*(1-2), 47-57. <http://dx.doi.org/10.1016/j.ssc.2007.03.052>

Ferrari, A., & Basko, D. (2013). Raman spectroscopy as a versatile tool for studying the properties of graphene. *Nature Nanotechnology*, *8*(4), 235-246. <http://dx.doi.org/10.1038/nnano.2013.46>

Fleischmann, M., Mengoli, G., Musiani, M., & Pagura, C. (1985). An electrochemical and Raman spectroscopic investigation of synergetic effects in the corrosion inhibition of copper. *Electrochimica Acta*, *30*(12), 1591-1602. [http://dx.doi.org/10.1016/0013-4686\(85\)87004-3](http://dx.doi.org/10.1016/0013-4686(85)87004-3)

Fuller, S., Wilhelm, E., & Jacobson, J. (2002). Ink-jet printed nanoparticle microelectromechanical systems. *Journal of Microelectromechanical Systems*, *11*(1), 54-60. <http://dx.doi.org/10.1109/84.982863>

Geim, A. (2009). Graphene: Status and prospects. *Science*, *324*(5934), 1530-1534. <http://dx.doi.org/10.1126/science.1158877>

Goycoolea, F., Heras, A., Aranaz, I., Galed, G., Fernández-Valle, M., & Argüelles-Monal, W. (2003). Effect of chemical crosslinking on the swelling and shrinking properties of thermal and pH-responsive chitosan hydrogels. *Macromolecular Bioscience*, *3*(10), 612-619. <http://dx.doi.org/10.1002/mabi.200300011>

Le, L., Ervin, M., Qiu, H., Fuchs, B., & Lee, W. (2011). Graphene supercapacitor electrodes fabricated by inkjet printing and thermal reduction of graphene oxide. *Electrochemistry Communications*, *13*(4), 355-358. doi: 10.1016/j.elecom.2011.01.023

Griffiths, D. (2005). *Introduction to quantum mechanics*. Upper Saddle River, NJ: Pearson Education.

Guardia, L., Fernández-Merino, M., Paredes, J., Solís-Fernández, P., Villar-Rodil, S., Martínez-Alonso, A., & Tascón, J. (2011). High-throughput production of pristine graphene in an aqueous dispersion assisted by non-ionic surfactants. *Carbon*, *49*(5), 1653-1662. <http://dx.doi.org/10.1016/j.carbon.2010.12.049>

Güneş, F., Shin, H., Biswas, C., Han, G., Kim, E., & Chae, S. et al. (2010). Layer-by-layer doping of few-layer graphene film. *ACS Nano*, *4*(8), 4595-4600. <http://dx.doi.org/10.1021/nn1008808>

Hansen, C. (2012). *Hansen solubility parameters*. Hoboken: Taylor and Francis.

- Hebner, T., Wu, C., Marcy, D., Lu, M., & Sturm, J. (1998). Ink-jet printing of doped polymers for organic light emitting devices. *Applied Physics Letters*, 72(5), 519-521. <http://dx.doi.org/10.1063/1.120807>
- Hernandez, Y., Lotya, M., Rickard, D., Bergin, S., & Coleman, J. (2010). Measurement of multicomponent solubility parameters for graphene facilitates solvent discovery. *Langmuir*, 26(5), 3208-3213. <http://dx.doi.org/10.1021/la903188a>
- Hernandez, Y., Nicolosi, V., Lotya, M., Blighe, F., Sun, Z., & De, S. et al. (2008). High-yield production of graphene by liquid-phase exfoliation of graphite. *Nature Nanotechnology*, 3(9), 563-568. <http://dx.doi.org/10.1038/nnano.2008.215>
- Hobdell, J. (1979). Optimization of interdigital capacitors. *IEEE Transactions on Microwave Theory and Techniques*, 27(9), 788-791. <http://dx.doi.org/10.1109/tmmt.1979.1129730>
- Holgate, S. (2010). *Understanding solid state physics*. Boca Raton: CRC Press.
- Huang, H., Li, Z., She, J., & Wang, W. (2012). Oxygen density dependent band gap of reduced graphene oxide. *Journal of Applied Physics*, 111(5), 054317. <http://dx.doi.org/10.1063/1.3694665>
- Huang, L., Huang, Y., Liang, J., Wan, X., & Chen, Y. (2011). Graphene-based conducting inks for direct inkjet printing of flexible conductive patterns and their applications in electric circuits and chemical sensors. *Nano Research*, 4(7), 675-684. <http://dx.doi.org/10.1007/s12274-011-0123-z>
- Huang, P., Ruiz-Vargas, C., van der Zande, A., Whitney, W., Levendorf, M., & Kevek, J. et al. (2011). Grains and grain boundaries in single-layer graphene atomic patchwork quilts. *Nature*, 469(7330), 389-392. <http://dx.doi.org/10.1038/nature09718>
- Huang, X., Zhi, C., Jiang, P., Golberg, D., Bando, Y., & Tanaka, T. (2012). Temperature-dependent electrical property transition of graphene oxide paper. *Nanotechnology*, 23(45), 455705. <http://dx.doi.org/10.1088/0957-4484/23/45/455705>
- Hummers, W., & Offeman, R. (1958). Preparation of graphitic oxide. *Journal of The American Chemical Society*, 80(6), 1339-1339. <http://dx.doi.org/10.1021/ja01539a017>
- Hwang, E., Adam, S., & Sarma, S. (2007). Carrier transport in two-dimensional graphene layers. *Physical Review Letters*, 98(18). <http://dx.doi.org/10.1103/physrevlett.98.186806>
- Kim, H. J., Maleki, T., Pinghung Wei, & Ziaie, B. (2009). A biaxial stretchable interconnect with liquid-alloy-covered joints on elastomeric substrate. *Journal of Microelectromechanical Systems*, 18(1), 138-146. <http://dx.doi.org/10.1109/jmems.2008.2011118>
- Jang, D., Kim, D., & Moon, J. (2009). Influence of fluid physical properties on ink-jet printability. *Langmuir*, 25(5), 2629-2635. doi: 10.1021/la900059m
- Jin, R. (2001). Photoinduced conversion of silver nanospheres to nanoprisms. *Science*, 294(5548), 1901-1903. <http://dx.doi.org/10.1126/science.1066541>

Jones, C., & Grainger, D. (2009). In vitro assessments of nanomaterial toxicity. *Advanced Drug Delivery Reviews*, 61(6), 438-456. <http://dx.doi.org/10.1016/j.addr.2009.03.005>

Jönsson, S., Birgersson, J., Crispin, X., Greczynski, G., Osikowicz, W., & Denier van der Gon, A. et al. (2003). The effects of solvents on the morphology and sheet resistance in poly(3,4-ethylenedioxythiophene)–polystyrenesulfonic acid (PEDOT–PSS) films. *Synthetic Metals*, 139(1), 1-10. [http://dx.doi.org/10.1016/s0379-6779\(02\)01259-6](http://dx.doi.org/10.1016/s0379-6779(02)01259-6)

Jung, I., Dikin, D., Piner, R., & Ruoff, R. (2008). Tunable electrical conductivity of individual graphene oxide sheets reduced at “low” temperatures. *Nano Letters*, 8(12), 4283-4287. <http://dx.doi.org/10.1021/nl8019938>

Kaiser, A., & Skákalová, V. (2014). *Graphene*. Woodland Publishing.

Kaniyankandy, S., Achary, S., Rawalekar, S., & Ghosh, H. (2011). Ultrafast relaxation dynamics in graphene oxide: evidence of electron trapping. *The Journal of Physical Chemistry C*, 115(39), 19110-19116. <http://dx.doi.org/10.1021/jp206923q>

Karim, M., Hatakeyama, K., Matsui, T., Takehira, H., Taniguchi, T., & Koinuma, M. et al. (2013). Graphene oxide nanosheet with high proton conductivity. *Journal of The American Chemical Society*, 135(22), 8097-8100. <http://dx.doi.org/10.1021/ja401060q>

Kasry, A., Kuroda, M., Martyna, G., Tulevski, G., & Bol, A. (2010). Chemical doping of large-area stacked graphene films for use as transparent, conducting electrodes. *ACS Nano*, 4(7), 3839-3844. <http://dx.doi.org/10.1021/nn100508g>

Kim, D., Jeong, S., Park, B., & Moon, J. (2006). Direct writing of silver conductive patterns: Improvement of film morphology and conductance by controlling solvent compositions. *Applied Physics Letters*, 89(26), 264101. <http://dx.doi.org/10.1063/1.2424671>

Kim, D., Xiao, J., Song, J., Huang, Y., & Rogers, J. (2010). Stretchable, curvilinear electronics based on inorganic materials. *Advanced Materials*, 22(19), 2108-2124. <http://dx.doi.org/10.1002/adma.200902927>

Kim, H., & Jeong, O. (2011). PDMS surface modification using atmospheric pressure plasma. *Microelectronic Engineering*, 88(8), 2281-2285. <http://dx.doi.org/10.1016/j.mee.2011.02.084>

Kim, K., Reina, A., Shi, Y., Park, H., Li, L., Lee, Y., & Kong, J. (2010). Enhancing the conductivity of transparent graphene films via doping. *Nanotechnology*, 21(28), 285205. <http://dx.doi.org/10.1088/0957-4484/21/28/285205>

Knopf, G., & Sinar, D. (2017). Flexible hydrogel actuated graphene-cellulose biosensor for monitoring pH. 2017 *IEEE International Symposium on Circuits and Systems (ISCAS)*. 1-4. <http://dx.doi.org/10.1109/iscas.2017.8050613>

Knopf, G., Sinar, D., Andrushchenko, A., & Nikumb, S. (2016). Flexible electrical circuits printed on polymers using graphene-cellulose inks. 2016 *IEEE International Symposium on Circuits and Systems (ISCAS)*. 854-857. <http://dx.doi.org/10.1109/iscas.2016.7527375>

- Krishnamurthy, A., Gadhamshetty, V., Mukherjee, R., Chen, Z., Ren, W., Cheng, H., & Koratkar, N. (2013). Passivation of microbial corrosion using a graphene coating. *Carbon*, *56*, 45-49. <http://dx.doi.org/10.1016/j.carbon.2012.12.060>
- Krishnamurthy, A., Gadhamshetty, V., Mukherjee, R., Natarajan, B., Eksik, O., & Ali Shojaee, S. et al. (2015). Superiority of graphene over polymer coatings for prevention of microbially induced corrosion. *Scientific Reports*, *5*(1). <http://dx.doi.org/10.1038/srep13858>
- Kumar, K., Pittala, S., Sanyadanam, S., & Paik, P. (2015). A new single/few-layered graphene oxide with a high dielectric constant of 106: contribution of defects and functional groups. *RSC Adv.*, *5*(19), 14768-14779. <http://dx.doi.org/10.1039/c4ra10800k>
- Kunzmann, A., Andersson, B., Thurnherr, T., Krug, H., Scheynius, A., & Fadeel, B. (2011). Toxicology of engineered nanomaterials: Focus on biocompatibility, biodistribution and biodegradation. *Biochimica Et Biophysica Acta (BBA) - General Subjects*, *1810*(3), 361-373. <http://dx.doi.org/10.1016/j.bbagen.2010.04.007>
- Laconte, J., Wilmart, V., Flandre, D., & Raskin, J. High-sensitivity capacitive humidity sensor using 3-layer patterned polyimide sensing film. *Proceedings of IEEE Sensors 2003 (IEEE Cat. No.03CH37498)*. 372-377. <http://dx.doi.org/10.1109/icsens.2003.1278961>
- Laville, C., & Pellet, C. (2002). Interdigitated humidity sensors for a portable clinical microsystem. *IEEE Transactions on Biomedical Engineering*, *49*(10), 1162-1167. <http://dx.doi.org/10.1109/tbme.2002.802052>
- Le Harzic, R., Huot, N., Audouard, E., Jonin, C., Laporte, P., & Valette, S. et al. (2002). Comparison of heat-affected zones due to nanosecond and femtosecond laser pulses using transmission electronic microscopy. *Applied Physics Letters*, *80*(21), 3886-3888. <http://dx.doi.org/10.1063/1.1481195>
- Le, L., Ervin, M., Qiu, H., Fuchs, B., & Lee, W. (2011). Graphene supercapacitor electrodes fabricated by inkjet printing and thermal reduction of graphene oxide. *Electrochemistry Communications*, *13*(4), 355-358. <http://dx.doi.org/10.1016/j.elecom.2011.01.023>
- Leenaerts, O., Partoens, B., & Peeters, F. (2009). Water on graphene: Hydrophobicity and dipole moment using density functional theory. *Physical Review B*, *79*(23). 235440. <http://dx.doi.org/10.1103/physrevb.79.235440>
- Lerf, A., He, H., Forster, M., & Klinowski, J. (1998). Structure of graphite oxide revisited. *The Journal of Physical Chemistry B*, *102*(23), 4477-4482. <http://dx.doi.org/10.1021/jp9731821>
- Li, X., Huang, M., & Bai, H. (1999). Thermal decomposition of cellulose ethers. *Journal of Applied Polymer Science*, *73*(14), 2927-2936. [http://dx.doi.org/10.1002/\(sici\)1097-4628\(19990929\)73:14<2927::aid-app17>3.3.co;2-b](http://dx.doi.org/10.1002/(sici)1097-4628(19990929)73:14<2927::aid-app17>3.3.co;2-b)
- Liu, J., Galpaya, D., Notarianni, M., Yan, C., & Motta, N. (2013). Graphene-based thin film supercapacitor with graphene oxide as dielectric spacer. *Applied Physics Letters*, *103*(6), 063108. <http://dx.doi.org/10.1063/1.4818337>

- Liu, Z., Robinson, J., Sun, X., & Dai, H. (2008). PEGylated nanographene oxide for delivery of water-insoluble cancer drugs. *Journal of The American Chemical Society*, *130*(33), 10876-10877. <http://dx.doi.org/10.1021/ja803688x>
- Lotya, M., Hernandez, Y., King, P., Smith, R., Nicolosi, V., & Karlsson, L. et al. (2009). Liquid phase production of graphene by exfoliation of graphite in surfactant/water solutions. *Journal of The American Chemical Society*, *131*(10), 3611-3620. <http://dx.doi.org/10.1021/ja807449u>
- Lv, Y., Yu, L., Jiang, C., Chen, S., & Nie, Z. (2014). Synthesis of graphene nanosheet powder with layer number control via a soluble salt-assisted route. *RSC Advances*, *4*(26), 13350. <http://dx.doi.org/10.1039/c3ra45060k>
- Maalouf, N., Cameron, M., Moe, O., Adams-Huet, B., & Sakhaee, K. (2007). Low urine pH: A novel feature of the metabolic syndrome. *Clinical Journal of The American Society Of Nephrology*, *2*(5), 883-888. <http://dx.doi.org/10.2215/cjn.00670207>
- Marcano, D., Kosynkin, D., Berlin, J., Sinitskii, A., Sun, Z., & Slesarev, A. et al. (2010). Improved synthesis of graphene oxide. *ACS Nano*, *4*(8), 4806-4814. <http://dx.doi.org/10.1021/nn1006368>
- Mathkar, A., Tozier, D., Cox, P., Ong, P., Galande, C., & Balakrishnan, K. et al. (2012). Controlled, stepwise reduction and band gap manipulation of graphene oxide. *The Journal of Physical Chemistry Letters*, *3*(8), 986-991. <http://dx.doi.org/10.1021/jz300096t>
- McAloney, R., Sinyor, M., Dudnik, V., & Goh, M. (2001). Atomic force microscopy studies of salt effects on polyelectrolyte multilayer film morphology. *Langmuir*, *17*(21), 6655-6663. <http://dx.doi.org/10.1021/la010136q>
- Mélinon, P., Masenelli, B., Tournus, F., & Perez, A. (2007). Playing with carbon and silicon at the nanoscale. *Nature Materials*, *6*(7), 479-490. <http://dx.doi.org/10.1038/nmat1914>
- Mendonca, L., Torikai, D., Ibrahim, R., Simoes, E., & Morimoto, N. (2008). Interdigitated capacitive sensor to verify the quality of ethanol automotive fuel. *ABCM Symposium Series in Mechatronics*, *3*, 580 - 585.
- Métraux, G., & Mirkin, C. (2005). Rapid thermal synthesis of silver nanoprisms with chemically tailorable thickness. *Advanced Materials*, *17*(4), 412-415. <http://dx.doi.org/10.1002/adma.200401086>
- Mohanty, N., Nagaraja, A., Armesto, J., & Berry, V. (2010). High-throughput, ultrafast synthesis of solution- dispersed graphene via a facile hydride chemistry. *Small*, *6*(2), 226-231. <http://dx.doi.org/10.1002/sml.200901505>
- Myers, H. (2002). *Introductory solid state physics*. Boca Raton: CRC Press.
- Nguyen, P., Yeo, L., Lok, B., & Lam, Y. (2014). Patterned surface with controllable wettability for inkjet printing of flexible printed electronics. *ACS Applied Materials & Interfaces*, *6*(6), 4011-4016. <http://dx.doi.org/10.1021/am4054546>

- Ni, Z., Wang, Y., Yu, T., & Shen, Z. (2008). Raman spectroscopy and imaging of graphene. *Nano Research*, 1(4), 273-291. <http://dx.doi.org/10.1007/s12274-008-8036-1>
- Nilsson, J., Neto, A., Guinea, F., & Peres, N. (2006). Electronic properties of graphene multilayers. *Physical Review Letters*, 97(26), 266801. <http://dx.doi.org/10.1103/physrevlett.97.266801>
- Novoselov, K., Geim, A., Morozov, S., Jiang, D., Katsnelson, M., & Grigorieva, I. et al. (2005). Two-dimensional gas of massless Dirac fermions in graphene. *Nature*, 438(7065), 197-200. <http://dx.doi.org/10.1038/nature04233>
- Novoselov, K., Geim, A., Morozov, S., Jiang, D., Zhang, Y., & Dubonos, S. et al. (2004). Electric field effect in atomically thin carbon films. *Science*, 306(5696), 666-669. <http://dx.doi.org/10.1126/science.1102896>
- Ogata, C., Kurogi, R., Awaya, K., Hatakeyama, K., Taniguchi, T., Koinuma, M., & Matsumoto, Y. (2017). All-graphene oxide flexible solid-state supercapacitors with enhanced electrochemical performance. *ACS Applied Materials & Interfaces*, 9(31), 26151-26160. <http://dx.doi.org/10.1021/acsami.7b04180>
- Ostrowska-Czubenko, J., Gierszewska, M., & Pieróg, M. (2015). pH-responsive hydrogel membranes based on modified chitosan: water transport and kinetics of swelling. *Journal of Polymer Research*, 22(8), 153. <http://dx.doi.org/10.1007/s10965-015-0786-3>
- Park, J., & Moon, J. (2006). Control of colloidal particle deposit patterns within picoliter droplets ejected by ink-jet printing. *Langmuir*, 22(8), 3506-3513. <http://dx.doi.org/10.1021/la053450j>
- Park, S., & Ruoff, R. (2009). Chemical methods for the production of graphenes. *Nature Nanotechnology*, 4(4), 217-224. <http://dx.doi.org/10.1038/nnano.2009.58>
- Paton, K., Varrla, E., Backes, C., Smith, R., Khan, U., & O'Neill, A. et al. (2014). Scalable production of large quantities of defect-free few-layer graphene by shear exfoliation in liquids. *Nature Materials*, 13(6), 624-630. <http://dx.doi.org/10.1038/nmat3944>
- Perry, M., Stuart, B., Banks, P., Feit, M., Yanovsky, V., & Rubenchik, A. (1999). Ultrashort-pulse laser machining of dielectric materials. *Journal of Applied Physics*, 85(9), 6803-6810. <http://dx.doi.org/10.1063/1.370197>
- Phair, J., & Badwal, S. (2006). Review of proton conductors for hydrogen separation. *Ionics*, 12(2), 103-115. <http://dx.doi.org/10.1007/s11581-006-0016-4>
- Pinto, H., & Markevich, A. (2014). Electronic and electrochemical doping of graphene by surface adsorbates. *Beilstein Journal of Nanotechnology*, 5, 1842-1848. <http://dx.doi.org/10.3762/bjnano.5.195>
- Ponomarenko, L., Yang, R., Mohiuddin, T., Katsnelson, M., Novoselov, K., & Morozov, S. et al. (2009). Effect of a high-temperature environment on charge carrier mobility in graphene. *Physical Review Letters*, 102(20), 206603. <http://dx.doi.org/10.1103/physrevlett.102.206603>

- Qu, X., Wirsén, A., & Albertsson, A. (1999). Structural change and swelling mechanism of pH-sensitive hydrogels based on chitosan and D,L-lactic acid. *Journal of Applied Polymer Science*, 74(13), 3186-3192. [http://dx.doi.org/10.1002/\(sici\)1097-4628\(19991220\)74:13<3186::aid-app22>3.0.co;2-y](http://dx.doi.org/10.1002/(sici)1097-4628(19991220)74:13<3186::aid-app22>3.0.co;2-y)
- Radke, S., & Alocilja, E. (2004). Design and fabrication of a microimpedance biosensor for bacterial detection. *IEEE Sensors Journal*, 4(4), 434-440. <http://dx.doi.org/10.1109/jsen.2004.830300>
- Radke, S., & Alocilja, E. (2005). A microfabricated biosensor for detecting foodborne bioterrorism agents. *IEEE Sensors Journal*, 5(4), 744-750. <http://dx.doi.org/10.1109/jsen.2005.848138>
- Ren, P., Yan, D., Ji, X., Chen, T., & Li, Z. (2010). Temperature dependence of graphene oxide reduced by hydrazine hydrate. *Nanotechnology*, 22(5), 055705. <http://dx.doi.org/10.1088/0957-4484/22/5/055705>
- Ristein, J. (2006). PHYSICS: Surface transfer doping of semiconductors. *Science*, 313(5790), 1057-1058. doi: 10.1126/science.1127589
- Salomão, F., Lanzoni, E., Costa, C., Deneke, C., & Barros, E. (2015). Determination of high-frequency dielectric constant and surface potential of graphene oxide and influence of humidity by kelvin probe force microscopy. *Langmuir*, 31(41), 11339-11343. <http://dx.doi.org/10.1021/acs.langmuir.5b01786>
- Schrand, A., Dai, L., Schlager, J., Hussain, S., & Osawa, E. (2007). Differential biocompatibility of carbon nanotubes and nanodiamonds. *Diamond and Related Materials*, 16(12), 2118-2123. <http://dx.doi.org/10.1016/j.diamond.2007.07.020>
- Secor, E., Prabhumirashi, P., Puntambekar, K., Geier, M., & Hersam, M. (2013). Inkjet printing of high conductivity, flexible graphene patterns. *The Journal of Physical Chemistry Letters*, 4(8), 1347-1351. <http://dx.doi.org/10.1021/jz400644c>
- Seiko Epson Corp. (2004). Water-based pigment ink composition. USA. US 7,307,110 B2
- Seung Hun Huh. (2011). *Thermal Reduction of Graphene Oxide*. INTECH Open Access Publisher.
- Shankar, R. *Principles of quantum mechanics*. Springer US.
- Shearer, C., Slattery, A., Stapleton, A., Shapter, J., & Gibson, C. (2016). Accurate thickness measurement of graphene. *Nanotechnology*, 27(12), 125704. <http://dx.doi.org/10.1088/0957-4484/27/12/125704>
- Shimoda, T., Morii, K., Seki, S., & Kiguchi, H. (2003). Inkjet printing of light-emitting polymer displays. *MRS Bulletin*, 28(11), 821-827. <http://dx.doi.org/10.1557/mrs2003.231>

Shin, H., Kang, S., Koo, J., Lee, H., Kim, J., & Kwon, Y. (2014). Cohesion energetics of carbon allotropes: Quantum Monte Carlo study. *The Journal of Chemical Physics*, *140*(11), 114702. <http://dx.doi.org/10.1063/1.4867544>

Sinar, D., & Knopf, G. (2014). Printed graphene interdigitated capacitive sensors on flexible polyimide substrates. *14Th IEEE International Conference on Nanotechnology*. 538-542. <http://dx.doi.org/10.1109/nano.2014.6968041>

Sinar, D., & Knopf, G. (2018a). Printed graphene derivative circuits as passive electrical filters. *Nanomaterials*, *8*(2), 123. <http://dx.doi.org/10.3390/nano8020123>

Sinar, D., & Knopf, G. (2018). Cyclic liquid phase exfoliation of electrically conductive graphene-derivative inks. *IEEE Transactions on Nanotechnology*, 1-1. doi: 10.1109/tnano.2018.2849264

Sinar, D., Knopf, G., & Nikumb, S. (2013). Graphene-based inkjet printing of flexible bioelectronic circuits and sensors. *Micromachining and Microfabrication Process Technology XVIII*. 861204. <http://dx.doi.org/10.1117/12.2003936>

Sinar, D., Knopf, G., & Nikumb, S. (2014). Laser assisted reduction of printed GO films and traces. *14Th IEEE International Conference on Nanotechnology*. 549-553. <http://dx.doi.org/10.1109/nano.2014.6968086>

Sinar, D., Knopf, G., & Nikumb, S. (2017). Graphene and silver-nanoprism dispersion for printing optically-transparent electrodes. *Organic Photonic Materials and Devices XIX*. 101010L. <http://dx.doi.org/10.1117/12.2252248>

Sinar, D., Knopf, G., Nikumb, S., & Andrushchenko, A. (2014). Laser micromachining of oxygen reduced graphene-oxide films. *Micromachining and Microfabrication Process Technology XIX*. 89730K. <http://dx.doi.org/10.1117/12.2038423>

Sinar, D., Knopf, G., Nikumb, S., & Andrushchenko, A. (2016). Printed optically transparent graphene cellulose electrodes. *Organic Photonic Materials and Devices XVIII*. 974515. <http://dx.doi.org/10.1117/12.2208790>

Singh Raman, R., Chakraborty Banerjee, P., Lobo, D., Gullapalli, H., Sumandasa, M., & Kumar, A. et al. (2012). Protecting copper from electrochemical degradation by graphene coating. *Carbon*, *50*(11), 4040-4045. <http://dx.doi.org/10.1016/j.carbon.2012.04.048>

Sirringhaus, H., Kawase, T., Friend, R., Shimoda, T., Inbasekaran, M., Wu, W., & Woo, E. (2000). High-resolution inkjet printing of all-polymer transistor circuits. *Science*, *290*(5499), 2123-2126. <http://dx.doi.org/10.1126/science.290.5499.2123>

Soltman, D., & Subramanian, V. (2008). Inkjet-printed line morphologies and temperature control of the coffee ring effect. *Langmuir*, *24*(5), 2224-2231. <http://dx.doi.org/10.1021/la7026847>

Stankovich, S., Dikin, D., Dommett, G., Kohlhaas, K., Zimney, E., & Stach, E. et al. (2006). Graphene-based composite materials. *Nature*, 442(7100), 282-286. <http://dx.doi.org/10.1038/nature04969>

Strobel, P., Riedel, M., Ristein, J., & Ley, L. (2004). Surface transfer doping of diamond. *Nature*, 430(6998), 439-441. doi: 10.1038/nature02751

Subramanian, V., Chang, P., Lee, J., Molesa, S., & Volkman, S. (2005). Printed organic transistors for ultra-low-cost RFID applications. *IEEE Transactions on Components and Packaging Technologies*, 28(4), 742-747. <http://dx.doi.org/10.1109/tcapt.2005.859672>

Sui, G., Wang, J., Lee, C., Lu, W., Lee, S., & Leyton, J. et al. (2006). Solution-phase surface modification in intact poly(dimethylsiloxane). *Microfluidic Channels. Analytical Chemistry*, 78(15), 5543-5551. <http://dx.doi.org/10.1021/ac060605z>

Sun, X., Liu, Z., Welsher, K., Robinson, J., Goodwin, A., Zaric, S., & Dai, H. (2008). Nano-graphene oxide for cellular imaging and drug delivery. *Nano Research*, 1(3), 203-212. <http://dx.doi.org/10.1007/s12274-008-8021-8>

Tanaka, Y., Matsuda, Y., Fujiwara, H., Kubota, H., & Makita, T. (1987). Viscosity of (water + alcohol) mixtures under high pressure. *International Journal of Thermophysics*, 8(2), 147-163. doi: 10.1007/bf00515199

Teng, K., & Vest, R. (1987). Liquid ink jet printing with mod inks for hybrid microcircuits. *IEEE Transactions on Components, Hybrids, And Manufacturing Technology*, 10(4), 545-549. <http://dx.doi.org/10.1109/tchmt.1987.1134794>

Teng, K., & Vest, R. (1988). Mathematical models of ink jet printing in thick-film hybrid microelectronics. *Applied Mathematical Modelling*, 12(2), 182-188. [http://dx.doi.org/10.1016/0307-904x\(88\)90010-8](http://dx.doi.org/10.1016/0307-904x(88)90010-8)

van Osch, T., Perelaer, J., de Laat, A., & Schubert, U. (2008). Inkjet printing of narrow conductive tracks on untreated polymeric substrates. *Advanced Materials*, 20(2), 343-345. <http://dx.doi.org/10.1002/adma.200701876>

Vazquez, G., Alvarez, E., & Navaza, J. (1995). Surface tension of alcohol water + water from 20 to 50°C. *Journal of Chemical & Engineering Data*, 40(3), 611-614. <http://dx.doi.org/10.1021/jc00019a016>

Venugopal, S., Allee, D., Quevedo-Lopez, M., Gnade, B., Forsythe, E., & Morton, D. (2010). Flexible Electronics: What can it do? What should it do?. *2010 IEEE International Reliability Physics Symposium*. 644-649. <http://dx.doi.org/10.1109/irps.2010.5488757>

Wajid, A., Das, S., Irin, F., Ahmed, H., Shelburne, J., & Parviz, D. et al. (2012). Polymer-stabilized graphene dispersions at high concentrations in organic solvents for composite production. *Carbon*, 50(2), 526-534. <http://dx.doi.org/10.1016/j.carbon.2011.09.008>

- Wang, D., Zhang, X., Zha, J., Zhao, J., Dang, Z., & Hu, G. (2013). Dielectric properties of reduced graphene oxide/polypropylene composites with ultralow percolation threshold. *Polymer*, *54*(7), 1916-1922. <http://dx.doi.org/10.1016/j.polymer.2013.02.012>
- Wang, S., Ang, P., Wang, Z., Tang, A., Thong, J., & Loh, K. (2010). High mobility, printable, and solution-processed graphene electronics. *Nano Letters*, *10*(1), 92-98. <http://dx.doi.org/10.1021/nl9028736>
- Wang, Z., Nelson, J., Hillborg, H., Zhao, S., & Schadler, L. (2012). Graphene oxide filled nanocomposite with novel electrical and dielectric properties. *Advanced Materials*, *24*(23), 3134-3137. <http://dx.doi.org/10.1002/adma.201200827>
- Wasife, K. (2011). Power density and SAR in multi-layered life tissue at global system mobile (GSM) frequencies. *Journal of Electromagnetic Analysis And Applications*, *03*(08), 328-332. <http://dx.doi.org/10.4236/jemaa.2011.38052>
- Wei, Q., Luo, Y., Fu, F., Zhang, Y., & Ma, R. (2012). Synthesis, characterization, and swelling kinetics of pH-responsive and temperature-responsive carboxymethyl chitosan/polyacrylamide hydrogels. *Journal of Applied Polymer Science*, *129*(2), 806-814. <http://dx.doi.org/10.1002/app.38788>
- Wei, Z., Wang, D., Kim, S., Kim, S., Hu, Y., & Yakes, M. et al. (2010). Nanoscale tunable reduction of graphene oxide for graphene electronics. *Science*, *328*(5984), 1373-1376. <http://dx.doi.org/10.1126/science.1188119>
- Williams, D. (2008). On the mechanisms of biocompatibility. *Biomaterials*, *29*(20), 2941-2953. <http://dx.doi.org/10.1016/j.biomaterials.2008.04.023>
- Wu, X., Sprinkle, M., Li, X., Ming, F., Berger, C., & de Heer, W. (2008). Epitaxial-graphene/graphene-oxide junction: An essential step towards epitaxial graphene electronics. *Physical Review Letters*, *101*(2), 026801. <http://dx.doi.org/10.1103/physrevlett.101.026801>
- Yamada, Y., Murota, K., Fujita, R., Kim, J., Watanabe, A., & Nakamura, M. et al. (2014). Subnanometer vacancy defects introduced on graphene by oxygen gas. *Journal of The American Chemical Society*, *136*(6), 2232-2235. <http://dx.doi.org/10.1021/ja4117268>
- Yousefi, N., Sun, X., Lin, X., Shen, X., Jia, J., & Zhang, B. et al. (2014). Highly aligned graphene/polymer nanocomposites with excellent dielectric properties for high-performance electromagnetic interference shielding. *Advanced Materials*, *26*(31), 5480-5487. <http://dx.doi.org/10.1002/adma.201305293>
- Yunker, P., Still, T., Lohr, M., & Yodh, A. (2011). Suppression of the coffee-ring effect by shape-dependent capillary interactions. *Nature*, *476*(7360), 308-311. <http://dx.doi.org/10.1038/nature10344>
- Zacharia, T., David, S., Vitek, J., & Debroy, T. (1989). Heat transfer during Nd: Yag pulsed laser welding and its effect on solidification structure of austenitic stainless steels. *Metallurgical Transactions A*, *20*(5), 957-967. <http://dx.doi.org/10.1007/bf02651661>

- Zeng, J., Liu, J., Zhang, S., Zhai, P., Yao, H., & Duan, J. et al. (2015). Irradiation effects of graphene and thin layer graphite induced by swift heavy ions. *Chinese Physics B*, 24(8), 086103. <http://dx.doi.org/10.1088/1674-1056/24/8/086103>
- Zeng, J., Xia, X., Rycenga, M., Henneghan, P., Li, Q., & Xia, Y. (2010). Successive deposition of silver on silver nanoplates: lateral versus vertical growth. *Angewandte Chemie*, 123(1), 258-263. <http://dx.doi.org/10.1002/ange.201005549>
- Zhan, D., Ni, Z., Chen, W., Sun, L., Luo, Z., & Lai, L. et al. (2011). Electronic structure of graphite oxide and thermally reduced graphite oxide. *Carbon*, 49(4), 1362-1366. <http://dx.doi.org/10.1016/j.carbon.2010.12.002>
- Zhang, Q., Hu, Y., Guo, S., Goebel, J., & Yin, Y. (2010). Seeded growth of uniform ag nanoplates with high aspect ratio and widely tunable surface plasmon bands. *Nano Letters*, 10(12), 5037-5042. <http://dx.doi.org/10.1021/nl1032233>
- Zhang, Q., Li, N., Goebel, J., Lu, Z., & Yin, Y. (2011). A systematic study of the synthesis of silver nanoplates: Is citrate a “magic” reagent? *Journal of The American Chemical Society*, 133(46), 18931-18939. <http://dx.doi.org/10.1021/ja2080345>
- Zhou, S., Gweon, G., Fedorov, A., First, P., de Heer, W., & Lee, D. et al. (2007). Substrate-induced bandgap opening in epitaxial graphene. *Nature Materials*, 6(10), 770-775. <http://dx.doi.org/10.1038/nmat2003>
- Zhu, Y., Otsubo, M., Honda, C., & Tanaka, S. (2006). Loss and recovery in hydrophobicity of silicone rubber exposed to corona discharge. *Polymer Degradation and Stability*, 91(7), 1448-1454. <http://dx.doi.org/10.1016/j.polymdegradstab.2005.10.014>

Appendices

Appendix A - Printhead Control Code

Printhead control code initiates droplet jetting as required to deposit G-CMC colloidal ink. The XY plotter's linear actuators are run by an Arduino Uno board. The G-code G01 automatically enable a digital output meant to start a laser. This output was repurposed to send an initiation signal to the printhead control board. Once the digital signal (+ 5V) is received to pin 23 on the printhead control board, printActivePin variable is set to HIGH. The If-Else conditional reads this variable and initiated droplet ejection while at the same to time setting the nozzle in hexadecimals (e.g. 0x800). Droplet ejection happens through supplying and cutting power to a certain nozzle in quick succession. For this purpose, pulsePin is set to HIGH and then set to LOW with 5 μ s delay in between. Droplet spacing on substrate surface is determined in combination with feedrate and delay between each nozzle ON/OFF signal. In the code provided below, this delay is set to 2000 μ s.

```
#include <InkShieldLite.h>

//initialize shield on pin 2
const byte pulsePin = 2;
int printActivatePin = 23;
int printActivateStatus = 0;

void setup() {
  setABCDPinMode(abcdA0A3, OUTPUT); //set the abcd pins as outputs
  pinMode(pulsePin, OUTPUT); //set the pulse pin as output
  pinMode(printActivatePin, INPUT);
  digitalWrite(printActivatePin, LOW);
}
void loop() {

  printActivateStatus = digitalRead(printActivatePin);
  if (printActivateStatus == HIGH) {
    spray_ink(0x0800);
```

```
    }  
  }  
  void spray_ink(word strip)  
  {  
    for(byte i = 0; i <= 11; i++){  
      if(strip & 1<<i){  
        fastABCDDigitalWrite(abcdA0A3, i, HIGH); //set abcd (nozzle address)  
        fastDigitalWrite(pulsePin, HIGH); delayMicroseconds(5);  
        fastDigitalWrite(pulsePin, LOW); //pulse pin low  
        fastABCDDigitalWrite(abcdA0A3, i, LOW); //reset abcd  
      }  
    }  
    delayMicroseconds(2000);  
  }
```

Appendix B – Printed Piano Device Code

Piano device code monitors and compares capacitance of printed touchpads and produces sounds. In the code below, most of the commands are for setting up monitoring of each touchpad for manual calibration. During the first run, values for each touchpad with and without finger pressing were observed. Then, sensitivity value was changed to ensure that touchpads produce sound only when pressed. A very high sensitivity can result in touchpads sensing user's finger from up to 5 cm away.

```
/* DIY Piano
```

- This project using the concept of capacitive sensor, so no switch/button is required for it.
- Here is the link of capacitive sensor. For better understanding, please visit the page.
<http://playground.arduino.cc/Main/CapacitiveSensor?from=Main.CapSense>

```
Created by:
```

```
Oh Hai Seng || Junny Oh 07 November 2013
```

```
Modified by:
```

```
Dogan Sinar || June 2015
```

```
*/
```

```
// Import the CapacitiveSensor Library.
```

```
#include <CapacitiveSensor.h>
```

```
// Name the pin as led.
```

```
#define speaker 11
```

```
// Set the Send Pin & Receive Pin.
```

```
CapacitiveSensor cs_2_3 = CapacitiveSensor(2,3); // Resistor between pins 3 & 2. A  
large resistor (>1 Mohm) is necessary for enough touch sensitivity
```

```
CapacitiveSensor cs_2_4 = CapacitiveSensor(2,4);
```

```
CapacitiveSensor cs_2_5 = CapacitiveSensor(2,5);
```

```
CapacitiveSensor cs_2_6 = CapacitiveSensor(2,6);
```

```
CapacitiveSensor cs_2_8 = CapacitiveSensor(2,8);
```

```
CapacitiveSensor cs_2_9 = CapacitiveSensor(2,9);
```



```

CapacitiveSensor cs_2_10 = CapacitiveSensor(2,10);

void setup()
{
  cs_2_3.set_CS_Autocal_Millis(0xFFFFFFFF); // turn off autocalibrate on channel 1 - just
  as an example

  // Arduino start communicate with computer.
  Serial.begin(9600);
}

void loop()
{
  // Set a timer.
  long start = millis();

  // Set the sensitivity of the sensors.
  long total1 = cs_2_3.capacitiveSensor(55);
  long total2 = cs_2_4.capacitiveSensor(55);
  long total3 = cs_2_5.capacitiveSensor(55);
  long total4 = cs_2_6.capacitiveSensor(55);
  long total5 = cs_2_8.capacitiveSensor(55);
  long total6 = cs_2_9.capacitiveSensor(55);
  long total7 = cs_2_10.capacitiveSensor(55);

  Serial.print(millis() - start); // check on performance in milliseconds
  Serial.print("\t"); // tab character for debug window spacing

  Serial.print(total1); // print sensor output 1
  Serial.print("\t"); // Leave some space before print the next output
  Serial.print(total2); // print sensor output 2
  Serial.print("\t"); // Leave some space before print the next output
  Serial.print(total3); // print sensor output 3
  Serial.print("\t"); // Leave some space before print the next output
  Serial.print(total4); // print sensor output 4
  Serial.print("\t"); // Leave some space before print the next output
  Serial.print(total5); // print sensor output 5
  Serial.print("\t"); // Leave some space before print the next output
  Serial.print(total6); // print sensor output 6
  Serial.print("\t"); // Leave some space before print the next output

```

```
Serial.println(total7);           // print sensor output 7
                                   // "println" - "\n" represent as "line", system will jump to next
                                   // line after print the output.

// When hand is touched the sensor, the speaker will produce a tone.
// I set a threshold for it, so that the sensor won't be too sensitive.
if (total1 > 150) tone(speaker,523);
if (total2 > 150) tone(speaker,587);
if (total3 > 150) tone(speaker,659);
if (total4 > 150) tone(speaker,698);
if (total5 > 150) tone(speaker,784);
if (total6 > 150) tone(speaker,880);
if (total7 > 150) tone(speaker,988);

// When hand didn't touch on it, no tone is produced.
if (total1<=150 & total2<=150 & total3<=150 & total4<=150 & total5<=150 &
total6<=150 & total7<=150)
    noTone(speaker);

delay(10);                         // arbitrary delay to limit data to serial port
}
```

Curriculum Vitae

Name **Dogan SINAR**

Post-secondary Education

- 2018 Doctor of Philosophy (Ph.D.) in Mechanical Engineering,

 The University of Western Ontario, London, Ontario, Canada
- 2009 M.Eng. in Mechanical Engineering (University of Western Ontario) M.Eng.
 project title is “Carbon Nanotube based Vibration Sensors.”
- 2007 B.Sc. in Mechatronics Engineering (Sabanci University)

Published Peer Reviewed Papers

- Sinar, D. and Knopf, G.K. (2018). Cyclic Liquid Phase Exfoliation of Electrically Conductive Graphene-Derivative Inks. *IEEE Transactions on Nanotechnology*, Accepted on June 11, 2018. doi: 10.1109/tnano.2018.2849264
- Sinar, D. and Knopf, G.K. (2018). Printed Graphene Derivative Circuits as Passive Electrical Filters. *Nanomaterials*, 8, 123. doi:10.3390/nano8020123

Book Chapters

- Sinar, D. (2018). Printable Electronics for Biosensing. *Smart Biosensor Technology*, Knopf, G.K. and Bassi, A.S., CRC Press, submitted for publishing (2018).

Published Conference Proceedings Papers

- Knopf, G.K. and Sinar, D. (2017). Flexible hydrogel actuated graphene-cellulose biosensor for monitoring pH. *IEEE Int'l Symposium on Circuits & Systems, Baltimore MD*, May 28-31.

- Sinar, D., Knopf, G., & Nikumb, S. (2017). Graphene and silver-nanoprism dispersion for printing optically-transparent electrodes. *Organic Photonic Materials and Devices XIX*. <http://dx.doi.org/10.1117/12.2252248>
- Sinar, D., Knopf, G., Nikumb, S., & Andrushchenko, A. (2016). Printed optically transparent graphene cellulose electrodes. *Organic Photonic Materials and Devices XVIII*. <http://dx.doi.org/10.1117/12.2208790>
- Knopf, G., Sinar, D., Andrushchenko, A., & Nikumb, S. (2016). Flexible electrical circuits printed on polymers using graphene-cellulose inks. *2016 IEEE International Symposium on Circuits and Systems (ISCAS)*. <http://dx.doi.org/10.1109/iscas.2016.7527375>
- Knopf, G.K., Sinar, D., Andrushchenko, A. and Nikumb, S. (2015) “Variable conductive micro-patterns printed on flexible substrates”, *2015 Canadian Printable Electronics Symposium*, Montreal, QC.
- Sinar, D., Knopf, G., Nikumb, S., & Andrushchenko, A. (2014). Laser micromachining of oxygen reduced graphene-oxide films. *Micromachining and Microfabrication Process Technology XIX*. <http://dx.doi.org/10.1117/12.2038423>
- Sinar, D. and Knopf, G. (2014). Printed graphene interdigitated capacitive sensors on flexible polyimide substrates. *14Th IEEE International Conference on Nanotechnology*, Toronto, ON.
- Sinar, D., Knopf, G., & Nikumb, S. (2014). Laser assisted reduction of printed GO films and traces. *14Th IEEE International Conference on Nanotechnology*, Toronto, ON.
- Sinar, D., Knopf, G., & Nikumb, S. (2014). Microfabrication of passive electronic components with printed graphene-oxide deposition. *Micromachining and Microfabrication Process Technology XIX*. <http://dx.doi.org/10.1117/12.2038411>
- Sinar, D., Knopf, G., & Nikumb, S. (2013). Graphene-based inkjet printing of flexible bioelectronic circuits and sensors. *Micromachining and Microfabrication Process Technology XVIII*. <http://dx.doi.org/10.1117/12.2003936>

Conference Presentations

- Sinar, D. and Knopf, G. (2014). Printed graphene interdigitated capacitive sensors on flexible polyimide substrates. *14Th IEEE International Conference on Nanotechnology*. <http://dx.doi.org/10.1109/nano.2014.6968041>

Full Time Work Experience

- Quality Engineer at Ford Motor Company (Nov 2007 – May 2008)
 - Analyzed quality data systematically, reporting and documenting in appropriate format for bi-weekly inter-departmental meetings, resulting in smooth functioning of company procedures
 - Led Variety Reduction Team (Locks & Mechanisms), coordinating solutions of both major and minor manufacturing and supplier related problems of mechanical origin
 - Supervised Quality Warning System for Ford Motor Company Turkey's transition from hard to digital documents for inter-departmental communication for quality issues, making system functional and recovering stuck and due files
 - Inspected quality issues of different vehicle models on a daily basis, gaining first-hand experience in potential quality issues and their possible root causes; helped quality testers by reporting several quality problems that were missed on occasion

Part Time Work Experience

- Engineering Project Assistant at Gentek Building Products Canada (June 2010 – Aug 2010)
 - Analyzed and reviewed of process flow in Grid Department and created SOP's in ISO designated format for standardization of labor
 - Wrote new Grid Department software on VB.Net for manufacturing related calculations that doubles the productivity and makes it easier for new workers to learn the procedure. For this purpose, learned VB.
 - Cooperated with workers to learn process details for future problem solving regarding manufacturing and quality control errors.
- Mechanical Maintenance Supervisor at Sentek Rubber (June 2004 – July 2007)

- Mechanical Maintenance Supervisor at KROS Automotive (July 2007 – Sept 2007)
 - Supervised construction of new cutting edge high technology full manufacturing line being built. Worked constantly together with German engineers and supervised local engineers and workers, resulting in completion of the line in designated time frame
 - Worked and researched on technical aspects of new manufacturing line; reported on major mistakes before the first test run preventing incapacitation of line.